THE UNIVERSITY *of* EDINBURGH

Understanding Molecular Crystal Structures at Extreme Conditions

Nicholas P. Funnell

A Thesis submitted in fulfilment of the requirements for the degree of Doctor of Philosophy to the School of Chemistry, University of Edinburgh

March 2012

Declaration

I declare that this Thesis has been written by me and that the work carried out is my own, or I have made a substantial contribution towards it except where specific reference is made to another. This work has not been submitted for another degree or professional qualification.

Nicholas P. Funnell

Abstract

Understanding the structure of matter in the solid state could be considered as being one of 'the big questions' in chemistry. Whereas the structural behaviour of molecules in the gas phase is relatively well-understood, this is not the case for the condensed phase due to the complexity of short and long-range intermolecular interactions. The purpose of the work in this thesis is to examine the structural response of solid molecular materials to stimuli of extreme pressure and temperature.

L-alanine crystallises as a zwitterion in the space group $P2_12_12_1$. Neutron powder diffraction and X-ray single crystal diffraction data show that the *a* and *c*-axes are very similar in length. The *a*-axis is more compressible than the *c*-axis, and at *ca.* 2 GPa the cell becomes metrically tetragonal, however the underlying symmetry is still orthorhombic. The structure remains in a compressed form of the ambient phase up to 9.87 GPa. Previous Raman and energy dispersive powder diffraction studies have interpreted changes in spectra at *ca.* 2 and 9 GPa as phase transitions. The diffraction data and DFT calculations described here suggest that these are in fact due to changes in conformation of the ammonium group.

L-alanine shows remarkable resistance to the effects of pressure but something must happen to the structure if pressure continues to be increased. Neutron powder diffraction has been used to obtain high-pressure data for L-alanine up to 15.46 GPa. These are the highest-pressure diffraction data reported for any amino acid. Above *ca.* 15 GPa, L-alanine undergoes a reversible transition to an amorphous phase through volume collapse of the crystal, driven by the need to minimise the *PV* term in the Gibbs free energy equation, as opposed to relieving destabilising contacts. It is currently the only amino acid known to undergo a transition of this type.

The co-crystal of methylpyridine and pentachlorophenol (MP-PCP) forms in the space group *P*-1. When the phenolic proton is deuterated (MP-PCP-*d*) it exhibits isotopic polymorphism, crystallising in the space group *Cc*. Structures of the two other combinations of isotope and space group, i.e MP-PCP in *Cc* and MP-PCP-*d* in *P*-1 have not yet been determined. We demonstrate that these polymorphs can be obtained using high-pressure and low-temperature conditions predicted by thermodynamics. The use of in-situ crystallisation at pressure has driven MP-PCP to pack with *Cc* symmetry, minimising the *PV* term in the Gibbs free energy equation. Low-temperature crystallisation causes MP-PCP-*d* to form in *P*-1 due to this phase being favoured by vibrational enthalpic and entropic contributions.

Aniline is a liquid under ambient conditions but freezes at 267 K in the monoclinic space group $P2_1/c$. It can also be frozen by pressure (*ca.* 0.8 GPa) in the orthorhombic space group $Pna2_1$. Neutron powder diffraction shows that on decompression the orthorhombic form transforms to the monoclinic phase at 0.3 GPa, owing to the monoclinic packing being less dense. PIXEL calculations provide an insight into the intermolecular energies of the orthorhombic crystal up to 7.301 GPa. They show that dispersive forces are more dominant than the hydrogen bonds, one of which becomes destabilising at higher pressure. Thermodynamic calculations estimating the relative stabilities of the two polymorphs prove inconclusive owing to improper treatment of dispersion interactions by Density Functional Theory calculations.

The structural behaviour of cyclohexane in the crystalline ($P2_1/c$) and plastic phases ($Fm3m$) has been studied using neutron total scattering data and Reverse Monte Carlo (RMC) modelling. Atomistic models show that the molecules exhibit correlated motion as they prepare to undergo transformation on heating. Inclusion of $I(t)$ data in the RMC refinements is shown to be important as when it is not accounted for, the RMC method is incapable of distinguishing the form of the disorder in the plastic phase. Molecular motion in this phase is shown to be correlated through the avoidance of short intermolecular D···D contacts.

The ordered and disordered solid phases of oxalyl chloride (space groups $P2_1/c$ and $Pbca$ respectively) have been studied by neutron total scattering and modelled using a Reverse Monte Carlo approach. Atomistic models show that on heating, the atoms vibrate out of the plane of the molecule until 245 K where they show approximately isotropic vibration owing to reduced steric restriction. This may provide the molecules with the freedom they require to rotate and undergo the solid-solid transition. The onset of disorder has also been partially predicted by molecular dynamics simulations. RMC modelling does not provide satisfactory atomic configurations of the disordered solid phase due to an unrealistic distribution of intermolecular chlorine-chlorine contacts. This study presents an example of a flexible, 3-atom-type system that may be too complex for analysis by the RMC method.

Publications

N. P. Funnell, A. Dawson, D. Francis, A. R. Lennie, W. G. Marshall, S. A. Moggach, J. E. Warren, and S. Parsons, *CrystEngComm*, 2010, **12(9)**, 2573-2583

N. P. Funnell, W. G. Marshall and S. Parsons, *CrystEngComm*, 2011, **13(19)**, 5841-5848

P. J. Bailey, N. L. Bell, L. Y. Gim, N. Funnell, F. White and S. Parsons, *Chem. Commun.*, 2011, **47(42)**, 11659-11661

Acknowledgements

I would like to begin by thanking my supervisor Prof. Simon Parsons. Simon – you've been a brilliant supervisor and I'm really grateful to you for giving me the opportunity to do a PhD in your group. I've not only learned a lot about crystallography, but also history, dangerous insects, the marvels of Margaret Thatcher and how to spot when you're trying to wind me up! I will miss being a part of your group.

Thanks to my second supervisor, Dr. Stephen Moggach for all the general every-day help you've given me, be it crystallography-related or helping me move flat. You've gone out of your way many times to help me, and it has been really appreciated. (You've got lots of good stories too!)

Thanks very much to Dr. Matt Tucker and Dr. Carole Morrison for all your help in the respective areas of total scattering and computational chemistry. I've asked a lot of questions and you've both been very patient in explaining the answers to me.

To all the members of the group that have been here since I began – Russell, Pete, Fraser, Anna, Laura, Alex 1, Alex 2, Pat, Paul, Andy, Chris and Gary. You've all made this group fun to be a part of. Thanks especially to Russell for showing me how to do everything in my first year. I've only really appreciated this year just how busy you would have been and so I'm very grateful for your help.

Thanks to my old flatmates Nikki and Katherine for putting up with me for three years. You guys have been great flatmates and even better friends.

The fact I am here writing this Thesis is only possible because of my Mum. You have always been very supportive of whatever I choose to do. I'm really grateful for all those times you pushed me with schoolwork and university applications. I doubt I thanked you at the time for it, but I wouldn't have ended up where I am now if you hadn't. Thank you.

Finally to my girlfriend, Ailsa - thank you for putting up with me for the last five years and for all the support you've given me whilst I've been writing up. I promise I'll stop stressing all the time now!

Abbreviations

The following abbreviations have been used throughout this Thesis:

Experimental techniques and equipment:

ToF	-	Time of Flight
INS	-	Inelastic Neutron Scattering
DSC	-	Differential Scanning Calorimetry
DTA	-	Differential Thermal Analysis
DAC	-	Diamond Anvil Cell
PE	-	Paris-Edinburgh (cell)
CCR	-	Closed Cycle Refrigerator

Computational modelling

MD	-	Molecular Dynamics
QM	-	Quantum Mechanical
RMC	-	Reverse Monte Carlo
DFT	-	Density Functional Theory
DFT+D	-	Density Functional Theory + Dispersion (correction)
L-J	-	Lennard-Jones (potential)
MP	-	Møller-Plesset
DNP	-	Double Numerical basis set with Polarisation
BLYP	-	Becke, Lee, Yang and Parr (density functional)
B3LYP	-	Becke (three parameter), Lee, Yang and Parr (density functional)
PBE	-	Perdew, Burke and Ernzerhof (density functional)
PW91	-	Perdew–Wang (density functional)

Abbreviations (continued)

Other

BM	-	Birch Murnaghan (equation of state)
K_0	-	Bulk modulus
K'	-	Bulk modulus first derivative
ADP	-	Atomic Displacement Parameter
ZPE	-	Zero Point Energy
RMSD	-	Root Mean Square Deviation
PDF	-	Pair Distribution Function
CSD	-	Cambridge Structural Database
ESI	-	Electronic Supplementary Information

Contents

1. Introduction

1.1 Phase Transitions and Polymorphism in the Solid State 2
1.2 Pressure-Induced Phase Transitions; the *PV* Term 6
1.3 Experimental Determination of Lattice Enthalpy 10
1.4 Computational Derivation of Lattice Energies 13
1.5 The Contribution of Vibrational Modes to Free Energy 22
1.6 Thesis Outline 24
1.7 References 25

2. The Effect of Pressure on the Crystal Structure of L-Alanine

2.1 Introduction 31
2.2 Experimental 34
2.3 Results 40
2.4 Discussion 45
2.5 Conclusions 55
2.6 References 56

3. Alanine at 13.6 GPa and its Pressure-Induced Amorphisation at 15 GPa

3.1 Introduction 63
3.2 Experimental 64
3.3 Results 69
3.4 Discussion 72
3.5 Conclusions 79
3.6 References 80

4. Using Pressure to Direct Polymorph Formation: Overcoming Isotopic Polymorphism in the 4-Methylpyridine-Pentachlorophenol Co-Crystal

4.1 Introduction 87
4.2 Experimental 91
4.3 Results and Discussion 96
4.4 Conclusions 104
4.5 References 105

5. The Phase Behaviour of Aniline at High Pressure and Low Temperature

5.1 Introduction 109
5.2 Experimental 110
5.3 Results 116
5.4 Discussion 123
5.5 Conclusions 132
5.6 References 133

6. The Crystalline-Plastic Phase Transition in Cyclohexane Examined by Neutron Total Scattering
6.1 Introduction 139
6.2 Experimental 141
6.3 Results and Discussion 145
6.4 Conclusions 162
6.5 References 163

7. A Neutron Total Scattering Study of Crystalline Oxalyl Chloride
7.1 Introduction 167
7.2 Experimental 170
7.3 Results and Discussion 173
7.4 Conclusions 185
7.5 References 186

8. Conclusion
8.1 Conclusion 190

Chapter 1

Introduction

1.1 Phase transitions and polymorphism in the solid state

1.1.1 The importance of understanding phase behaviour

Predicting the packing arrangement and symmetry elements of crystal structures under a given set of crystallisation conditions is arguably the greatest challenge facing crystallographic research groups. The ability to do so is hindered only by our understanding of the solid state which is dependent on the accurate description of intermolecular interactions. Adding to this complex problem is the phenomenon of polymorphism; the ability for a chemical compound to possess more than one crystal structure, and in some cases interconvert between these solid phases through variation of temperature and/or pressure. Some materials can possess many different crystal packing arrangements - for instance there are currently 16 known crystalline forms of ice.[1] Conversely other structures show a remarkable robustness; the α-glycine crystal structure persists to 23 GPa despite the fact that the glycine molecule is known to pack in five additional forms.[2, 3]

Understanding how and why phase transformations occur is an active area of academic and industrial research. At the academic level, much interest is focussed towards the prediction of crystal packing, mostly using quantum mechanical (QM) computational methods and database mining in a complementary manner to identify correlations between molecular and crystalline structures. Notable work in this field includes the Crystal Structure Prediction (CSP) blind tests conducted by the Cambridge Crystallographic Data Centre.[4, 5] The prediction methods used in these studies evaluate the thermodynamic influence on crystal packing by associating the most likely crystal structures with the lowest lattice energy, predicted by the conformation of the molecule and the interactions it forms with its nearest neighbours. However, the true crystal structure of a given molecule may not be the most thermodynamically favourable but could be kinetically stable. The role of kinetic stability on the aforementioned glycine polymorphs has been investigated by He *et al* who found that the kinetic effect could be suppressed by a slow evaporation growth method where the thermodynamically stable γ polymorph was yielded in preference to the kinetically-favoured α-glycine.[6] The suggestion was made that slower growth enabled an aqueous glycine solution to sample more energy states

instead of becoming trapped in a metastable α form. To predict kinetically-driven crystal packing successfully, the effect of temperature has to be included in the calculation which necessitates the use of molecular dynamics (MD) simulations. MD results reported by Hamad and Catlow suggest that the glycine molecules do not arrange themselves into a favourable hydrogen-bonded dimer reminiscent of the packing arrangement seen in α-glycine as had previously thought to be the case.[7] A case study of a chemical system that shows kinetic dependence is discussed in Chapter 4.

Industrial interest in this area tends to be concerned with the relationship between structure and function. In pharmaceutical science, controlling the crystalline form of therapeutic molecules is essential, as solubility can vary between polymorphs and drug delivery is dependent on dissolution of the capsule in the desired target area. If the crystal has multiple polymorphic forms, then each of these should be identified and tested to ensure similar solubility and therapeutic activity. The anti-HIV agent, Ritonavir, possessed unidentified polymorphic forms: the drug precipitated out of the final semi-solid formulated product into a more thermodynamically-stable crystal structure. The precipitate showed markedly lower solubility, reducing its therapeutic activity. However, its existence was not realised until two years after the drug had been launched.[8] Identifying stability and activity of solid-state forms is not only important for bioavailability and safety issues but also for protection of intellectual property rights; polymorph-specific patents prevent rival companies marketing an unprotected polymorph as their own product.

The work described in this Thesis outlines the investigation of the effects of extreme pressure, P, and temperature, T, on simple molecular, organic solids. Variation of P and T, which is achieved easily in a laboratory environment, enables identification of the driving forces responsible for packing arrangements at these conditions, in the context of one or more of the thermodynamic terms.

The overriding aim is to identify why phase transitions occur and how molecules prepare to undergo a transition.

1.1.2 Classification of phase transitions

Commonly crystalline phase transformations are referred to as being reconstructive or displacive. The reconstructive process occurs between crystal forms that do not need to possess a group-subgroup relation between their respective space groups and this is characterised by an abrupt change in cell volume. The transition involves breaking and reforming bonding interactions between molecules (e.g. hydrogen bonds) such that the molecular packing arrangement is changed. An example of a pressure-induced reconstructive transition can be seen in serine monohydrate, where the ammonium group undergoes a 52° rotation at 5.2 GPa, destroying existing hydrogen bonds and creating a new one.[9] The new packing arrangement showed a more favourable, smaller unit cell volume. However, it has been observed that crystallinity cannot always be maintained following a transition, sometimes transforming the sample to a micro-crystalline powder or an amorphous phase. The structure of benzene has been reported to undergo a transition above 20 GPa, where both crystallinity and molecular structure are disrupted due to transformation into an amorphous phase of hydrogenated carbon.[10]

Displacive transitions occur through symmetry-mode distortions. This is the case where the initial and final crystal packing forms must be symmetry-related, where one is a sub-group of the other – i.e. the lower symmetry form is a distorted version of the higher symmetry phase. This process can usually be attributed to softening of phonon modes – long-range, low energy vibrations that decrease in frequency due to weakening of the force constant as the transition is approached. If the force constant becomes negative then this equates to an imaginary frequency. The crystal structure becomes energetically unstable with respect to that vibration and the packing arrangement transforms to a lower energy form. The origin and examples of displacive transitions have been reviewed by Dove.[11] Examples of such transitions can be seen in as quartz, cristobalite and strontium titanate.[12-14] It is thought that lattice defects play an important role in displacive transitions and a comprehensive study has been carried out on the effect of oxygen defects on the thermally-induced transition in strontium titanate.[15] Measurement and calculation of phonon modes are discussed in Section 1.1.3.

A further categorisation of phase transitions is whether they are first or second-order, according to Ehrenfest's classification. A first-order transition is where the first derivative of free energy changes at the point of transformation which can be seen as a step-change in a plot of volume versus pressure or temperature. Pressure-induced phase transformations tend to be first-order as the new resulting crystal structure frequently possesses a smaller volume than the lower pressure polymorph in order to minimise free energy. A second-order transition is where the first derivative of free energy does not change but the second derivative does. This is usually the case where the initial and final structures are related by symmetry; where one crystallises in a sub-group of the other.

1.1.3 Calculation and measurement of phonon modes

Lattice vibrations can be divided into two types: acoustic and optical. The latter correspond to molecular vibrations which are, in principle, detectable experimentally by IR and Raman spectroscopy. Acoustic modes are low in energy (typically less than 300 cm^{-1}) and are associated with whole unit-cell vibrations. Calculation of phonon modes can be readily accomplished with modern computational packages, such as CASTEP, which require a geometry-optimised set of coordinates, from which vibrational frequencies can be calculated.[16] The calculations are performed within the Brillouin zone – a reciprocal representation of the unit cell containing a complete classification of available energy levels to the crystal system. The vibrational frequencies are usually only calculated at the centre of the zone, the gamma point, in the interest of minimising computational cost. At the gamma point the whole-unit-cell acoustic vibrations have zero frequency, as all the molecules vibrate 'in-phase' with each other, and only the optical modes are observable. One method that can be used to measure the acoustic modes is to re-cast the unit cell as a supercell so that the acoustic vibrations appear as optical modes. Alternatively, calculation at non-gamma points in the Brillouin zone means the acoustic modes have a positive frequency. A diagrammatic representation of acoustic and optical modes is shown in Figure 1.1.

Acoustic phonon modes cannot be observed by IR and Raman spectroscopy as the vibrations are measured at the gamma point but they can be detected with

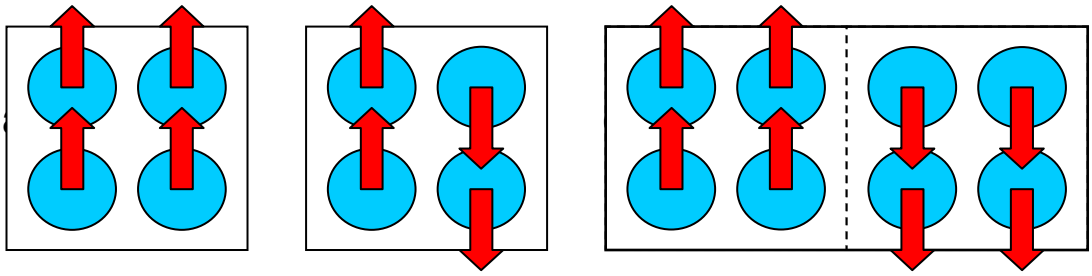

Figure 1.1. The schematic of an acoustic mode (**a**) and an optical mode (**b**). To measure an acoustic mode, it is recast as an optical mode by measuring the vibration over a supercell (**c**).

inelastic neutron scattering (INS). As a neutron possesses mass it interacts with all vibrational events, including those at non-gamma points, which can be measured by calculating the energy loss that occurs during the inelastic collision process. The role of phonon modes in the phase transition between α- and β-quartz has been reported by Axe *et al*, obtained via INS.[17]

1.2 Pressure-induced phase transitions; the PV term

1.2.1 The thermodynamic pathway for a pressure-induced transition

The packing arrangement of molecules in the solid state is governed by Gibbs free energy, *G*, given in Equation 1.1. A phase transition between one crystal polymorph to another is induced by a change in one or more of these thermodynamic terms such that it results in a more favourable value of *G*.

$$G = U + PV - TS \qquad 1.1$$

The internal energy, *U*, is a state function that represents the cohesive energy within the crystal lattice. The *PV* term gives the energetic contributions of the system pressure and volume and the *TS* term accounts for temperature and entropy. At ambient pressure, $P \approx 0$ GPa and thus the *PV* contribution to free energy is negligible. The remaining *U* and *TS* terms then determine the thermodynamic stability of the polymorph. However, the influence of the *PV* term on *G* can be significantly increased with the use of high-pressure environments, such as the Merrill-Bassett diamond anvil cell (DAC), shown in Figure 1.2 .[18] This can result in

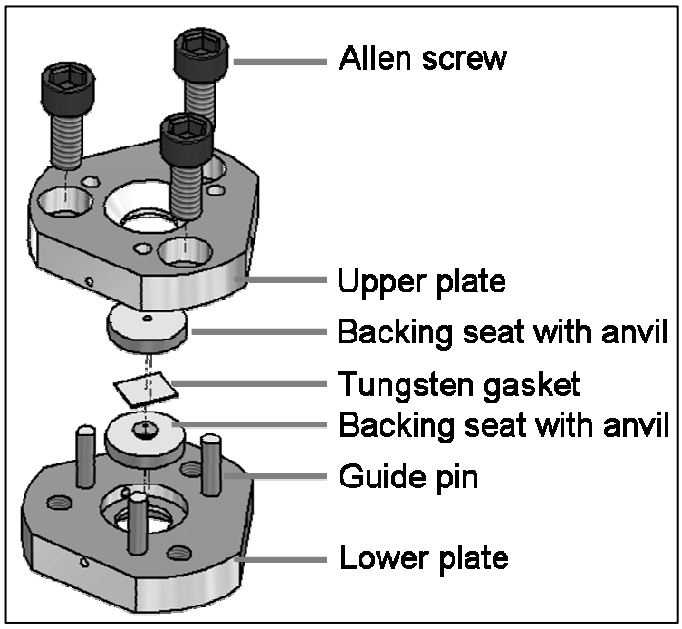

Figure 1.2. Exploded schematic of a Merrill-Bassett diamond anvil cell

PV exerting great influence over *G*, affecting whether a phase transition to another crystalline form occurs or not. If the *P* term increases, it becomes important for the cell volume to minimise in order to maintain a favourable value of *G*.

Figure 1.3, reproduced from Figure 2.5 in ref [19] shows *U* as a function of V/V_0 for two hypothetical polymorphs. If the assumption is made that the *TS* contribution to *G* is negligible for solid materials then the relationship

$$P = -\left(\frac{\partial U}{\partial V}\right)_T \qquad 1.2$$

can be derived, allowing the pressure to be calculated for any position on the curves in Figure 1.3. In principle, the pressure at which a transition between polymorphs occurs can be predicted. At the transition pressure, the polymorphs are in equilibrium where $\Delta G = 0$ and therefore, $\Delta U = -P\Delta V$. The two curves will share a common tangent where this condition is met and Equation 1.3 can be used to find the transition pressure. If the above conditions are fulfilled then an increase in pressure is equivalent to a decrease in V/V_0. Starting at the equilibrium point of structure 1 in

Figure 1.3, an increase in pressure causes a rapid increase in ΔU. Eventually a region of the potential is reached that is higher in energy than the equilibrium point for structure 2. Therefore, any pressure increase of structure 1 beyond the point where the two potentials share the common tangent (dotted line) will induce a phase transition to structure 2. The penalty for the increase in U is outweighed by the minimisation of the PV term.

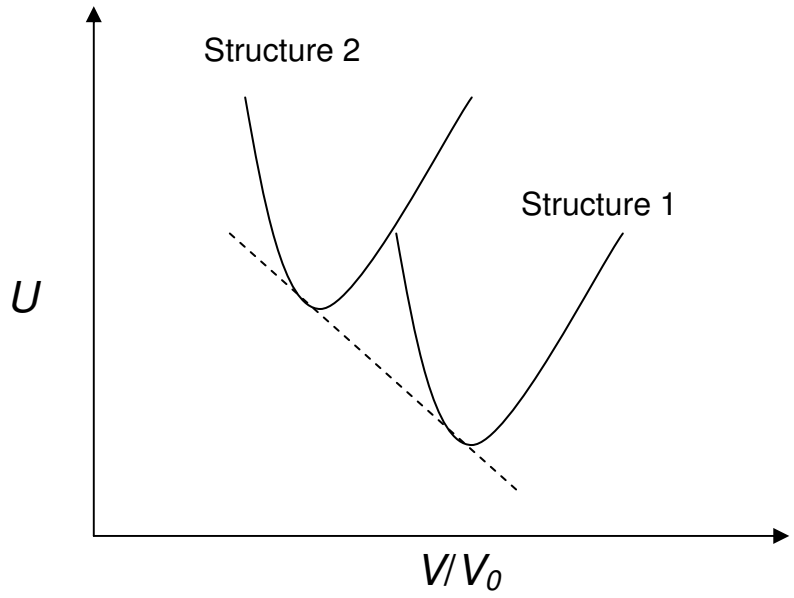

Figure 1.3. Plot of internal energy against V/V_0. The dotted line shows the common tangent shared by the potentials of the two structures. Reproduced from Ref. 19.

1.2.2 Experimentally obtaining the pressure-volume contribution to free energy

The PV term is the most easily calculated thermodynamic variable. The crystallographic unit cell volume, V, is obtained by diffraction and the calculation of P is dependent on the experimental setup. If a Merrill-Basset DAC is used, then the crystal sample is loaded with a small ruby chip from which the internal pressure can be deduced through the ruby fluorescence method. High-pressure neutron powder diffraction experiments require the use of a Paris-Edinburgh (PE) cell, shown in Figure 1.4.[20] The sample chamber is loaded with a pressure marker (lead, MgO or CaF_2 has been used in this Thesis) for which the equation of state is known. Its refined lattice parameter then enables calculation of the pressure. The upper attainable pressure limit varies depending on the exact cell setup and choice of

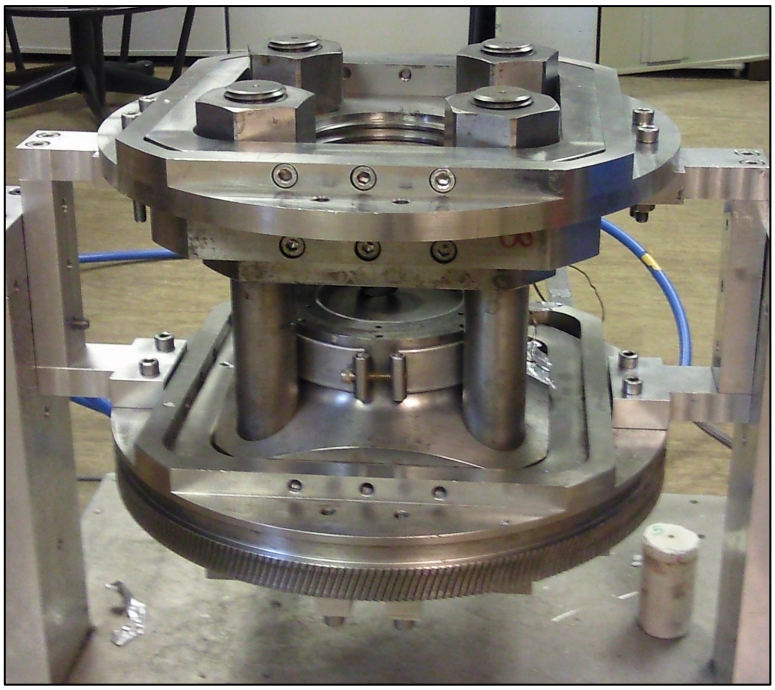

Figure 1.4. The Paris-Edinburgh high-pressure cell

hydrostatic medium. Commonly used hydrostatic media and their respective pressure limits are given in Table 1.1, taken from Ref 21. The high-pressure work described here focuses on the 0-15 GPa pressure regime, where the maximum pressures reached are either due to the limitations of the experimental configuration or it is not the purpose of the investigation to observe the sample behaviour beyond the reported pressure.

The high-pressure experiment allows structural characterisation of the sample, including its cell constants and volume. Determination of the energetic contribution of the *PV* term to free energy is relatively straightforward compared with the other thermodynamic terms. It is given by

$$E_{PV} = (P\Delta V)0.6 \qquad 1.3$$

where P is in units of GPa, V is in units of Å^3 and multiplication by 0.6, derived from Avogadro's constant, gives E_{PV} in units of kJ mol^{-1}. It is frequently found that the *PV* term is responsible for pressure-induced phase transitions, as opposed to the *U* term; there have been several instances where an abrupt decrease in unit cell volume has

accompanied a phase change, such as those seen in serine monohydrate and S-4-sulfo-L-phenylalanine monohydrate[9, 22]

Table 1.1 Hydrostatic media

Hydrostatic medium	Upper limit of quasi-hydrostatic pressure (GPa)
Silicon oil	< 2.0
Water	2.5
Isopropyl alcohol	4.3
Glycerine:water (3:2)	5.3
Petroleum ether	6.0
Pentane:isopentane (1:1)	7.4
Methanol	8.6
Methanol:ethanol (4:1)	10.4
Methanol:ethanol:water (16:3:1)	14.5
Hydrogen	177.0
Helium	60-70
Neon	16.0
Argon	9.0
Xenon	55.0
Nitrogen	13.0

1.3 Experimental determination of lattice enthalpy

1.3.1 Ionic and molecular materials

The lattice enthalpy in an ionic complex corresponds to the enthalpy change on going from ions in a gaseous state to the formation of a crystal lattice. It is determined by constructing a Born-Haber cycle from known thermodynamic quantities, an application of Hess's Law. The cycle applies for isolated systems where energy cannot be transmitted to or from the surroundings. This means that the total sum of

all enthalpy changes within the closed cycle must equal zero. For example, the lattice enthalpy of potassium chloride (ΔH_{Latt}) can be found by:

$$\Delta H_{Latt} = \Delta H_{sub[K]} + \Delta H_{bondCl} + I.E._K + eaff_{Cl} - \Delta H_{fKCl} \qquad 1.4$$

where ΔH_{subK} and ΔH_{bondCl} are the enthalpies of sublimation and bond dissociation for K and Cl_2 respectively. $I.E._K$ is the first ionisation energy of K, $eaff_{Cl}$ is the electron affinity of Cl and ΔH_{fKCl} is the enthalpy of formation of solid KCl. The appropriate Born-Haber cycle is shown in Figure 1.5. This method of lattice energy determination has been demonstrated for the methylammonium halides and ethylammonium halides.[23, 24] In both cases isoperibol calorimeters were used to measure the enthalpy of reaction between the alkylammonium salt and hydroxide ions. The remaining required enthalpy changes were obtained from other literature values. Derakhshan *et al* report a good agreement between the experimentally determined enthalpies with calculated values, finding a discrepancy of only 5-12%.

In organic molecular materials, the 'enthalpy of sublimation' is often quoted as the enthalpy change between gaseous molecules and the crystal structure. It is essentially the molecular equivalent of lattice enthalpy which is given by:

$$\Delta H_{sub} = -U_{latt} - 2RT \qquad 1.5$$

The discrepancy between the two is estimated to be $2RT$ which accounts for the difference in $P\Delta V$ between the gaseous and solid states. It is thought that the assumption of ideal gas behaviour, only gives a systematic error of 5% at worst for

crystals that have sublimation energies of *ca.* 100 kJ mol^{-1} at 298 K.[25] There are many methods by which sublimation enthalpy can be determined experimentally, several have been listed by Chickos and Acree, Jr. (Table 5 in ref. [26]) along with a compilation of sublimation enthalpies for over 1200 references.[26] One possible approach, often referred to as an 'indirect' method involves the use of a Knudsen effusion cell and determining the temperature dependence of a substance's

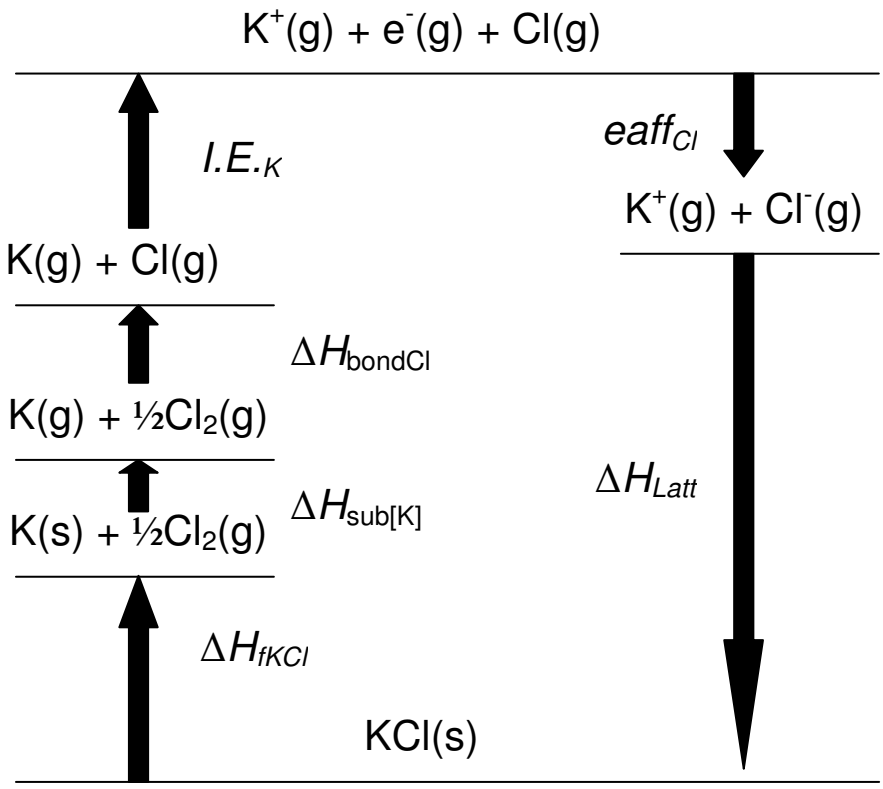

Figure 1.5. Born-Haber cycle for calculating the lattice enthalpy of potassium chloride.

equilibrium vapour pressure. The vapour pressure can then be related to sublimation enthalpy by the Clausius-Clapeyron equation. An example of this procedure is given by Taulelle *et al* for the pharmaceutical Irbesartan.[27] Pfefer *et al* have used an alternative, 'direct' approach instead to determine the sublimation enthalpy of 3-(3,4-dichlorophenyl)-1,1-dimethylurea.[28] A Tian-Calvet calorimeter was used where the enthalpy of sublimation could be found by calculating the area under the resulting voltage-time thermogram.

1.3.2 Detecting changes in lattice energy

Differential scanning calorimetry (DSC) is a useful tool for making relatively quick assessments of phase behaviour as a function of temperature. DSC instruments operate on the principle of measuring the quantities of heat energy simultaneously transferred to the sample under investigation and a reference. The sample and reference are maintained at the same temperature and vary linearly with time. When an exothermic or endothermic process occurs, the amount of heat supplied to the

sample to maintain the linear temperature-time relationship must differ from the reference material at the transition point. This is reflected in the DSC trace as a negative or positive peak. The sensitivity of the technique means the peaks are very well-defined; broad peaks represent quite sluggish transitions and sharper peaks indicate transitions occurring over a shorter time period.

A common variation of the DSC method is differential thermal analysis (DTA) which works in a similar manner except the heat flow to the sample and reference remains the same and the change in temperature is measured.

For a DSC experiment, the enthalpy of a given transition can be found from the area, A, under the corresponding peak in the trace

$$\Delta H = KA \qquad 1.6$$

where K is the calorimetric constant. The changes seen in the trace are indicative of whether the transition is first or second order, according to the Ehrenfest classification, discussed in Section 1.1.2. A peak or trough corresponds to a first-order transition and a shift in the base level of the trace is evidence of a second-order transition.

1.4 Computational derivation of lattice energies

1.4.1 The atom-atom model in lattice energy calculation

Computational modelling of chemical structure is useful as a complementary tool to investigations that aim to observe chemical structure experimentally and/or verify it. Common applications include geometry optimisations, calculation of spectral, electronic and thermodynamic properties and lattice energy calculation.[29-34]

There are two common approaches to modelling chemical structure. One is to obtain a near-solution of the Schrödinger equation, which forms the basis of quantum mechanical (QM) methods. QM methods are discussed in more detail in Section 1.4.3. However, QM calculations can be computationally expensive – excessively so if there are a large number of atoms. For larger simulations, determination of lattice energies by summation of individual atom-atom interactions is more appropriate. This approach does not deal with solution of the Schrödinger equation but instead

estimates a potential energy curve as a function of approach distance between the nuclei of pairs of non-bonded atoms, achieved by empirical weighting of attractive and repulsive force terms. The Lennard-Jones (L-J) and Buckingham potentials form the basis of the common atom-atom potential models.[35] The L-J potential has the form

$$E_{ij} = A(R_{ij})^{-12} - B(R_{ij})^{-6} \qquad 1.7$$

where R_{ij} is the distance between atoms i and j and A and B are empirical parameters. Polarisation and dispersive attractive forces are accounted for by the R^{-6} term, and repulsive interactions by R^{-12}. The Buckingham potential is an improvement on the L-J model by dealing with repulsion using an exponential term instead:

$$E_{ij} = A\exp(-BR_{ij}) - C(R_{ij})^{-6} \qquad 1.8$$

In both formulae, the A, B and C parameters determine the depth of the potential energy well, the curvature of the surface and the position of the minimum. These are calibrated against experimental thermodynamic, structural and vibrational data. Finally, the inclusion of a fourth term can be used to account for Coulombic interactions.

$$E_{ij} = A\exp(-BR_{ij}) - C(R_{ij})^{-6} + \frac{q_i q_j}{4\pi\varepsilon_0 R_{ij}} \qquad 1.9$$

In principle, the shape of the potential becomes more accurate with additional parameters although Gavezzotti warns that the chemical relevance of each term decreases and no real physical significance should be placed on the individual components – i.e. the attractive and repulsive terms do not truly represent these forces.[36]

Due to the empirical nature of the potentials, or forcefields, their performance varies for different systems and thus most forcefields are optimised for particular sets of atoms.[37] The success of the method can only be judged against experimental data;

how closely the calculated lattice enthalpy agrees with the experimentally determined sublimation energy. The recently-developed atom-atom Coulomb-London-Pauli (AA-CLP) forcefield has been tested against the sublimation enthalpies of 154 different organic crystal structures.[38] It was shown that, on average, the calculated lattice energy was within 8% of the experimentally determined value (using the relationship in Equation 1.8) and that it never exceeded an error greater than 15%. The individual Coulombic, polarisation, dispersion and repulsive interactions were compared with those calculated by the PIXEL method (discussed in the next Section). The AA-CLP forcefield underestimated both Coulombic and repulsive forces to the extent that cancellation of errors actually gave the correct lattice energy. This further illustrates the point that the four energy terms as calculated by atom-atom forcefields are individually meaningless; however their sum results in an accurate lattice energy.

1.4.2 The PIXEL method

The semi-classical density sums (PIXEL) method, developed by Gavezzotti, is a computational technique for assessing lattice energies and specific intermolecular energies on the basis of molecule-molecule rather than atom-atom interactions.[36, 39] This approach offers the clear advantage over atom-atom based methods in that electron density is defined over many more sites (*ca.* 10^4) instead of a few localised points corresponding to the atomic nuclei. This means that the individual Coulombic, polarisation, repulsive and dispersive contributions to lattice energy are physically meaningful. The terms can then be ascribed to structural features in molecules, thus showing how they differ between polymorphs or how they change over the course of, e.g. heating or compression. Furthermore, Coulombic energies calculated by PIXEL are much more accurate than those derived from atom-atom methods as it takes into account the effects of electron cloud overlap with nuclear charges. The overriding advantage offered by PIXEL, is the speed at which the energies can be calculated as it is not computationally demanding.

The calculations themselves are carried out with the program OPiX which uses a pre-calculated electron density map of a molecule in its experimentally-determined crystal-structure geometry performed by a program such as

GAUSSIAN09, using the MP2/6-31G** level of theory.[40, 41] The density map is split into pixels, and subsequently super-pixels, the size of which depend on a user-defined 'condensation' level. The charges are screened, and any that fall below a specified threshold (typically 10^{-6} eÅ^{-3}) are deemed to be negligible and set to equal zero. All the remaining pixels are then renormalized so that the overall charge is neutral. The calculation of each energy term is performed on pairs of pixels between a reference molecule and a symmetry-related equivalent within a cluster radius. The energy terms used by PIXEL, listed below, are defined with the same formalisms and descriptions as those given in Ref. 36. In order to calculate the lattice energy, the four individual energy contributions, noted above, must first be found. The total lattice energy is then the sum of all the individual contributions.

$$E_{tot} = E_{Coul} + E_{pol} + E_{disp} + E_{rep} \qquad 1.10$$

The Coulombic energy is calculated as sums of pixel-pixel, pixel-nucleus and nucleus-nucleus terms. It is given by

$$E_{Coul} = \frac{q_1 q_2}{4\pi\varepsilon^{\circ} r} \qquad 1.11$$

where q_1 and q_2 are charges separated by distance, r. For two molecules in close proximity, there can potentially be some overlap in the electron density. PIXEL does not treat this as partial bonding but instead treats the regions of density separately. To avoid overlap, PIXEL employs a 'collision avoidance' procedure, resetting pixel-pixel distances below half the stepsize of the pixel mesh to half the stepsize.

The polarisability at pixel i, α_i, is given by

$$\alpha_i = (q_i / Z_{atom})\alpha_{atom} \qquad 1.12$$

where α_{atom} and Z_{atom} are the polarisability and atomic charge respectively for an atom in pixel i. An electric field, ε_i is calculated, employing the 'collision avoidance' procedure (see above) by weighting it with an adjustable empirical damping

parameter, ε_{max}, to prevent unrealistically high values of the electric field arising from density overlap. If $\varepsilon > \varepsilon_{max} \cdot \varepsilon_{max}$ then the polarisation energy, E_{pol}, is set to zero. E_{pol} then takes the form:

$$E_{pol} = -1/2\alpha_i[\varepsilon_i d_i]^2 \quad \text{for } \varepsilon < \varepsilon_{\max} \tag{1.13}$$

$$d_i = \exp(\varepsilon_i / (\varepsilon_{\max} - \varepsilon_i)) \tag{1.14}$$

The remaining attractive force, the dispersion energy can be found with the formulae:

$$E_{disp} = \frac{(-3/4)\sum_{i,A}\sum_{j,B} E_{OS} f(R)\alpha_i \alpha_j}{(4\pi\varepsilon_0)^2 (R_{ij})^6} \tag{1.15}$$

$$f(R) = \exp[-(D/R_{ij} - 1)^2] \tag{1.16}$$

Where $f(R)$ is, again, a damping function, made adjustable by an empirical parameter, D. E_{OS} is the 'oscillator strength', a quantity that is analogous to a quantum mechanical vibrational energy for the electrons. It can be calculated using the ionisation potential for pixel i, I_i, which in turn can be found from the ionisation potential of the atom of which the pixel is part, $I°$. This is dependent on β, a value that is effectively a dispersion energy coefficient that varies with atom type.

$$E_{OS} = (I_i I_j)^{1/2} \tag{1.17}$$

$$I_i = I° \exp(-\beta R_i) \tag{1.18}$$

Finally, the repulsive energy is calculated by first finding the total overlap integral, S, between the charge densities of molecules A and B.

$$S_{AB} = \sum_{i,A}\sum_{j,B} [\rho_i(A)\rho_j(B)]V \tag{1.19}$$

This is then divided into contributions from atomic pairs, S_{mn}. The repulsive energy can then be found for each pair:

$$E_{rep} = (K_1 - K_2 \Delta\chi_{mn}) S_{mn} \qquad 1.20$$

χ_{mn} is the difference in electronegativities between the atoms. K_1 and K_2 are parameters that account to some extent for electronic reorganisation when atoms with different electronegativities come into close contact by reducing the repulsion term. Table 1.2 contains a list of all the parameters used in this Thesis, for the atom types $C_{aliphatic}$, $C_{aromatic}$, N, O and H.

When setting up a PIXEL calculation, one must consider the size of the cluster radius to be used. This is somewhat system-specific; for chemical species where the strongest interactions are dispersive forces, such as the noble gases or alkanes, there is a drop-off in dispersive energy on increasing r by a factor of $1/r^6$ (where r is cluster radius). Whereas systems such as the amino acids, which crystallise as zwitterions, possess Coulombic interactions which are more significant at long range as these only drop off by a factor of $1/r$. Typically a cluster radius of 18 Å is used for calculating the lattice energy of uncharged molecules whereas a radius of *ca.* 40 Å would be more appropriate for the amino acid series. Defining a fixed radius for calculation can present problems for experiments where the cell volume changes significantly – frequently the case for high pressure investigations – as at higher pressure the same cluster radius could contain more molecules than at ambient conditions.

Table 1.2. Default parameters for the atom types used in all PIXEL calculations reported here.

atom	ε_{max} / Vm^{-1}	D / Å	K_1	K_2	β	$I°$ / au	α / $Å^{-3}$	χ	radius / Å
H	150 x 10^{10}	3.00	4800	1200	0.4	0.500	0.39	2.1	1.10
C_{aliph}	150 x 10^{10}	3.00	4800	1200	0.8	0.414	1.05	2.5	1.77
C_{arom}	150 x 10^{10}	3.00	4800	1200	0.9	0.414	1.35	2.5	1.77
N	150 x 10^{10}	3.00	4800	1200	0.5	0.534	0.95	3.0	1.64
O	150 x 10^{10}	3.00	4800	1200	0.4	0.500	0.75	3.5	1.58

An assessment of the performance of the PIXEL method was carried out by Gavezzotti where it was shown that the experimental sublimation enthalpies of 172 organic crystals were reproduced accurately (linear fit $y = 0.96x$, $R^2 = 0.79$).[36] Additional comparisons with lattice energies calculated by DFT-D methods and dimer energies derived from ab initio techniques also revealed good agreements.[42] The strength of PIXEL lies in the relatively short computation times, especially compared with high-level quantum mechanical calculations.

PIXEL is particularly useful for quantifying relative lattice energies between polymorphs in pressure-induced phase transitions. Although it has been observed more frequently for PV to be primarily responsible for most first-order phase changes, the U term has been reported to contribute towards transformations as well. If the transition is driven by the need to relieve repulsive contacts then this will be reflected by an increase in stability of the lattice energy. This was seen to be the case for L-serine, where PIXEL calculations showed an increase lattice energy, following a transition between phases II and III when an O-H···O H-bond adopted a more favourable conformation.[43]

1.4.3 Quantum mechanical calculations: density functional theory

The alternative to modelling structure in terms of atom-atom potentials is to find the energetic minima of a system via the near-solution of the Schrödinger equation. This is known as the quantum mechanical (QM) method. The simplified form of the Schrödinger equation is

$$H\Psi = E\Psi \qquad 1.21$$

which can only be solved completely for the hydrogen atom. The Hamiltonian operator, H, contains terms that account for the kinetic energy of electrons, electron-nuclei interactions and electron-electron interactions. All of these must be known in order to obtain the energy of the electronic wavefunction, $E\Psi$.

The most significant obstacle to solving the equation completely is the difficulty in ascertaining the electron-electron interaction term. In order to find this quantity, the wavefunctions for every electron would have to be considered

simultaneously as the electrostatic effects of one electron influences the position of its neighbouring electrons. For modern computers, it would require an unfeasibly large number of calculations to determine the electron-electron contribution to the Hamiltonian operator exactly.

Several considerations need to be made when running a QM calculation as the setup depends very much on the aim and complexity of the investigation. The initial decisions that must be made are, 1) the level of theory to use, and 2) the choice of basis set. Both of these influence the speed and accuracy of the calculation.

The simplest level of theory is the Hartree-Fock method which neglects to model the electron-electron interaction term completely. The more complex methods in the hierarchy of levels of theory go to greater lengths to predict this term accurately, making fewer approximations at the expense of increased computational cost. The PIXEL method, previously described in Section 1.4.1, is optimised for use with the 'MP2' level of theory – part of the Møller-Plesset (MP) perturbation theory series. However, geometry optimisation of a periodic system, i.e. a solid-state lattice, is generally too complex a problem to be solved by approximation of the wavefunction. Instead, it is usually more appropriate to model the electron density over 3-dimensional spatial coordinates, and this is the underlying principle of density functional theory (DFT). A further impetus for using DFT is that accurate lattice energies are more likely to be obtained from a large periodic model rather than a smaller finite one as it is difficult to calculate long-range Coulombic interactions from the latter model.

The quantity and type of functions that are used to describe the electron density are dependent on the choice of basis set. For levels of theory other than DFT, functions that give localised models of electron density are used, such as Gaussians. Whilst DFT can also make use of these basis sets, commonly it is used in conjunction with plane waves for modelling solid-state structures as the periodic nature of these functions makes them appropriate for use with crystal lattices.[44] The quality of the basis set is directly related to the number of plane waves used to model electron density.

A drawback of DFT is that the term corresponding to exchange-correlation interactions between electrons is unknown and so the use of an exchange-correlation

(XC) functional is necessary to fill in the missing information. The majority of the DFT calculations described in this Thesis utilise the PBE XC functional. The choice of functional is not straightforward as there are many available and it is hard to know whether the functional being used is the 'best' one for the task. Many programs only allow the use of a few selected functionals anyway. No one functional performs equally well for a range of systems as often they have been developed to tackle specific problems. A particularly useful overview of several DFT functionals is given by Boese *et al*, assessing their performance with the cc-pVTZ and TZ2P basis sets.[45] The accuracy of a QM calculation will, naturally, affect the predicted lattice energy. DFT calculations generally struggle to adequately account for dispersion energies which will affect the lattice energy, and so empirical corrections can be employed to correct for this (DFT+D). Dispersion interactions are particularly important in organic molecular systems as H-H contacts and π-π interactions are more prevalent than in inorganic complexes. Grimme showed that when using a damping potential of C_6R^{-6} (where R is distance and C_6 is a tuneable parameter) that calculated interaction energies were accurate within 10-30% of the experimental values for a sample of 29 organic molecules.[46] Feng *et al* carried out a similar investigation on 31 organic molecules, firstly obtaining lattice energies in good agreement with the experimental sublimation energy and then secondly showing that for all the molecules investigated, the dispersion energy contribution was between 40 and 65% of the total lattice energy.[25] A different approach was used by Tsuzuki *et al* where periodic DFT was used in combination with MP2, to describe dispersion accurately, in order to evaluate the lattice energies of urea and hexamine.[47] The former is predominantly H-bonded in the crystal structure whereas molecules of the latter primarily interact through dispersive forces. The experimental sublimation energies of urea and hexamine are 87.4-98.7 kJ mol^{-1} and 74.1-78.7 kJ mol^{-1} respectively and these were calculated as being 88.7 and 83.7 kJ mol^{-1}. The role of the basis set was also shown to be important here as smaller basis sets underestimated the lattice energy.

QM studies will likely play an increasingly important part of investigations into solid-state structure at non-ambient conditions as the accuracy and reliability of calculations improve. High-pressure crystallographic studies are time-consuming to

perform and produce datasets that are currently non-trivial to process. Being able to predict high-pressure structures reliably (and similarly structures at non-ambient temperatures) without the need to experimentally verify the results will represent a huge step forward in this field.

1.5 The contribution of vibrational modes to free energy

1.5.1 Zero point energy and vibrational enthalpy

The ability to evaluate various thermodynamic variables is convenient for identifying driving forces in phase transitions through assessment of polymorph stabilities, as described for the *PV* term in Section 1.2. Molecular vibrational frequencies can be calculated readily using a computational package such as CASTEP or DMOL.[48] The frequencies are found by displacing atoms from their ground-state positions and then calculating the resultant forces acting upon the atom. This corresponds to the first derivative of the potential energy surface. The second derivative of the surface gives the force constant, which can be used to calculate the frequency, where μ is the reduced mass of the atoms in the bond

$$\nu = \frac{1}{2\pi}\left(\frac{k}{\mu}\right)^{1/2} \qquad 1.22$$

The frequencies obtained are based on a harmonic approximation. The level of accuracy diminishes for vibrations that are excited from their groundstate as these show increasing anharmonic character with energy.[49] It is then straightforward to calculate the zero point energy; the energy of the lowest vibrational level,

$$ZPE = \sum \frac{1}{2} h\nu \qquad 1.23$$

The vibrational contribution to enthalpy is given by [50]

$$H_{vib}(T) = N_A h\nu \frac{\exp(-\theta_{vib}/T)}{1-\exp(-\theta_{vib}/T)} \qquad 1.24$$

$$\text{where} \quad \theta_{vib} = \frac{h\nu}{k_B} \tag{1.25}$$

1.5.2 Calculation of statistical entropy

A Boltzmann interpretation of entropy, *S*, defines it as the number of quantized energy levels that can be occupied or, equivalently, the number of ways a chemical system can organise itself. Boltzmann's constant, k_B, describes the distribution of the system over the energy levels – typically the more energetic levels are less densely populated; exhibiting an exponential decay in population as energy increases. Solid materials have fewer energetic states that can be occupied as crystal packing forces the loss of translational freedom that gases and liquids exhibit and, with the exception of plastic phases and cases of dynamic disorder, also lose any significant rotational freedom. Therefore, only vibrational levels remain accessible. If the frequency of a vibrational mode (measured using IR, Raman or neutron spectroscopy) as a function of temperature is known, then it is straightforward to calculate the vibrational contribution to entropy, using the expression, [50]

$$S_{vib} = \left[\frac{\theta_{vib}/T}{\left(\exp(\theta_{vib}/T) - 1\right)} - \ln\left(1 - \exp(-\theta_{vib}/T)\right) \right] \times R \tag{1.26}$$

Thus changes in vibrational spectra reveal the level of contribution the *TS* term makes towards driving a phase transition. Only neutron spectroscopy is capable of measuring all vibrational modes as IR and Raman are limited by selection rules that potentially preclude the measurement of specific vibrations. The assumption is made in Equation 1.29 that the vibrations are harmonic, which is true for low temperatures. At higher temperatures, the bond stretching process starts to deviate from the harmonic region of the Morse potential, and if enough energy is supplied, the bond will break.

In general, for high pressure experiments, bond-stretching frequencies tend to shift to higher wavenumber when pressure is increased. This is due to the bond-stretching process being more likely to be hindered by the close proximity of neighbouring atoms and so the bond length oscillates about the equilibrium position

more often. A plot of wavenumber versus pressure, in principle, should show some degree of linearity. Phase transitions can disrupt this relationship by, e.g. mode-softening, as described in Section 1.1.3. Some studies have identified phase transitions on the basis of slope discontinuity, seen in the metal complexes $Mn(CO)_5Br$ and $Re(CO)_5Cl$ where a decrease in the axial CO stretching mode was observed.[51] However, it is important to note that slope discontinuities are not exclusively indicative of phase transformations (see Chapter 2).

1.6 Thesis outline

The structural responses of the molecular materials L-alanine, 4-methylpyridine pentachlorophenol, aniline, cyclohexane and oxalyl chloride to non-ambient environments have all been investigated. Although the solid-state structures of these specific materials are not of commercial importance *per se*, they form a representative range of small molecular systems that all display some kind of interesting structural behaviour as a function of pressure or temperature. The fundamental observations made here may help to tackle the various industrial and academic challenges that have been discussed in Section 1.1.1.

L-alanine, one of the naturally occurring amino acids, is an attractive system to study owing to the wealth of different intermolecular interactions present in the crystal between relatively small molecules. Its resistance to pressure-induced change, until amorphisation at *ca.* 15 GPa, can be explained thermodynamically namely in terms of the *PV* variable and the importance of efficient packing.

4-methylpyridine pentachlorophenol and aniline both present examples where polymorphism achieved previously through isotopic substitution and low temperature respectively can also be driven using pressure. These studies demonstrate the potential of pressure use in the field of crystal engineering as both phase transitions were predicted to occur based on the *PV* term.

Complementary computational analysis has been performed on all the structures reported here as it provides an insight into the main energetic contributions towards lattice (in)stability and also a source of meaningful data to aid experimental refinements. Assessment of intermolecular energies at extreme conditions not only

helps to explain observed structural changes but also tests the limits of the computational method itself.

Although the relative stability of polymorphs can be explained thermodynamically, this approach provides little insight as to how molecules physically undergo a transition. Experimental research in this area is scarce and so the total scattering experiments reported in Chapters 6 and 7 represent early work on understanding how small organic molecules prepare to undergo order-disorder transitions. Reverse Monte Carlo algorithms have been employed to model large atomistic configurations, reproducing the instantaneous crystal structure. The idea is to monitor the onset of disorder in the samples and identify whether it is localised or randomly distributed throughout the lattice.

1.7 References

1. M. Cogoni, B. D'Aguanno, L. N. Kuleshova and D. W. M. Hofmann, *Journal of Chemical Physics*, 2011, **134**, 204506/204501-204506/204510.
2. C. Murli, S. M. Sharma, S. Karmakar and S. K. Sikka, *Physica B: Condensed Matter (Amsterdam, Netherlands)*, 2003, **339**, 23-30.
3. S. V. Goryainov, E. V. Boldyreva and E. N. Kolesnik, *Chemical Physics Letters*, 2006, **419**, 496-500.
4. G. M. Day, T. G. Cooper, A. J. Cruz-Cabeza, K. E. Hejczyk, H. L. Ammon, S. X. M. Boerrigter, J. S. Tan, R. G. Della Valle, E. Venuti, J. Jose, S. R. Gadre, G. R. Desiraju, T. S. Thakur, B. P. van Eijck, J. C. Facelli, V. E. Bazterra, M. B. Ferraro, D. W. M. Hofmann, M. A. Neumann, F. J. J. Leusen, J. Kendrick, S. L. Price, A. J. Misquitta, P. G. Karamertzanis, G. W. A. Welch, H. A. Scheraga, Y. A. Arnautova, M. U. Schmidt, J. van de Streek, A. K. Wolf and B. Schweizer, *Acta Crystallographica. Section B, Structural Science*, 2009, **65**, 107-125.
5. D. A. Bardwell, C. S. Adjiman, Y. A. Arnautova, E. Bartashevich, S. X. M. Boerrigter, D. E. Braun, A. J. Cruz-Cabeza, G. M. Day, R. G. Della Valle, G. R. Desiraju, B. P. van Eijck, J. C. Facelli, M. B. Ferraro, D. Grillo, M. Habgood, D. W. M. Hofmann, F. Hofmann, K. V. J. Jose, P. G. Karamertzanis, A. V. Kazantsev, J. Kendrick, L. N. Kuleshova, F. J. J.

Leusen, A. V. Maleev, A. J. Misquitta, S. Mohamed, R. J. Needs, M. A. Neumann, D. Nikylov, A. M. Orendt, R. Pal, C. C. Pantelides, C. J. Pickard, L. S. Price, S. L. Price, H. A. Scheraga, J. van de Streek, T. S. Thakur, S. Tiwari, E. Venuti and I. K. Zhitkov, *Acta Crystallographica, Section B: Structural Science*, 2011, **B67**, 535-551.

6. G. He, V. Bhamidi, S. R. Wilson, R. B. H. Tan, P. J. A. Kenis and C. F. Zukoski, *Crystal Growth & Design*, 2006, **6**, 1746-1749.
7. S. Hamad and C. R. A. Catlow, *CrystEngComm*, 2011, **13**, 4391-4399.
8. S. R. Chemburkar, J. Bauer, K. Deming, H. Spiwek, K. Patel, J. Morris, R. Henry, S. Spanton, W. Dziki, W. Porter, J. Quick, P. Bauer, J. Donaubauer, B. A. Narayanan, M. Soldani, D. Riley and K. McFarland, *Organic Process Research & Development*, 2000, **4**, 413-417.
9. R. D. L. Johnstone, D. Francis, A. R. Lennie, W. G. Marshall, S. A. Moggach, S. Parsons, E. Pidcock and J. E. Warren, *CrystEngComm*, 2008, **10**, 1758-1769.
10. L. Ciabini, F. A. Gorelli, M. Santoro, R. Bini, V. Schettino and M. Mezouar, *Physical Review B: Condensed Matter and Materials Physics*, 2005, **72**, 094108/094101-094108/094107.
11. M. T. Dove, *American Mineralogist*, 1997, **82**, 213-244.
12. M. G. Tucker, M. T. Dove and D. A. Keen, *Journal of Physics: Condensed Matter*, 2000, **12**, L723-L730.
13. A. P. Giddy, M. T. Dove, G. S. Pawley and V. Heine, *Acta Crystallographica, Section A: Foundations of Crystallography*, 1993, **A49**, 697-703.
14. Q. Hui, M. G. Tucker, M. T. Dove, S. A. Wells and D. A. Keen, *Journal of Physics: Condensed Matter*, 2005, **17**, S111-S124.
15. H. Hunnefeld, T. Niemoller, J. R. Schneider, U. Rutt, S. Rodewald, J. Fleig and G. Shirane, *Physical Review B: Condensed Matter and Materials Physics*, 2002, **66**, 014113/014111-014113/014114.
16. S. J. Clark, M. D. Segall, C. J. Pickard, P. J. Hasnip, M. I. J. Probert, K. Refson and M. C. Payne, *Zeitschrift für Kristallographie*, 2005, **220**, 567-570.

17. J. D. Axe and G. Shirane, *Physical Review B: Solid State*, 1970, **1**, 342-348.
18. L. Merrill and W. A. Bassett, *Review of Scientific Instruments*, 1974, **45**, 290-294.
19. D. S. Sholl and J. A. Steckel, *Density Functional Theory: A Practical Introduction*, John Wiley and Sons, Hoboken, USA, 2009.
20. J. M. Besson and R. J. Nelmes, *Physica B: Condensed Matter (Amsterdam)*, 1995, **213&214**, 31-36.
21. R. Miletich, D. R. Allan and W. F. Kuhs, *Reviews in Mineralogy and Geochemistry*, 2000, **41**, 445-519.
22. D. L. Johnstone Russell, R. Lennie Alistair, S. Parsons, E. Pidcock and E. Warren John, *Acta Crystallographica. Section B, Structural Science*, 2009, **65**, 731-748.
23. J. W. Wilson, *Journal of the Chemical Society, Dalton Transactions: Inorganic Chemistry (1972-1999)*, 1976, 890-893.
24. B. M. Derakhshan, A. Finch, P. N. Gates and M. Stephens, *Journal of the Chemical Society, Dalton Transactions: Inorganic Chemistry (1972-1999)*, 1984, 601-603.
25. S. Feng and T. Li, *Journal of Chemical Theory and Computation*, 2006, **2**, 149-156.
26. J. S. Chickos and W. E. Acree, Jr., *Journal of Physical and Chemical Reference Data*, 2002, **31**, 537-698.
27. P. Taulelle, G. Sitja, G. Pepe, E. Garcia, C. Hoff and S. Veesler, *Crystal Growth & Design*, 2009, **9**, 4706-4709.
28. G. Pfefer, R. Sabbah and R. Boistelle, *Journal of Applied Crystallography*, 1997, **30**, 527-531.
29. N. P. Funnell, A. Dawson, D. Francis, A. R. Lennie, W. G. Marshall, S. A. Moggach, J. E. Warren and S. Parsons, *CrystEngComm*, 2010, **12**, 2573-2583.
30. D. C. Sorescu, J. A. Boatz and D. L. Thompson, *Journal of Physical Chemistry A*, 2001, **105**, 5010-5021.
31. M. Mohr, J. P. McNamara, H. Wang, S. A. Rajeev, J. Ge, C. A. Morgado and I. H. Hillier, *Faraday Discussions*, 2003, **124**, 413-428.

32. R. P. Stoffel, C. Wessel, M.-W. Lumey and R. Dronskowski, *Angewandte Chemie, International Edition*, 2010, **49**, 5242-5266.

33. C. A. Morrison and M. M. Siddick, *Chemistry - A European Journal*, 2003, **9**, 628-634.

34. A. D. Fortes, J. P. Brodholt, I. G. Wood and L. Vocadlo, *Journal of Chemical Physics*, 2003, **118**, 5987-5994.

35. R. A. Buckingham, *Proceedings of the Royal Society of London, Series A: Mathematical, Physical and Engineering Sciences*, 1938, **168**, 264-283.

36. A. Gavezzotti, *Molecular Aggregation: Structure Analysis and Molecular Simulation of Crystals and Liquids*, Oxford University Press, Oxford, UK, 2007.

37. J. C. Osborn and P. York, *Journal of Molecular Structure*, 1999, **474**, 43-47.

38. A. Gavezzotti, *New Journal of Chemistry*, 2011, **35**, 1360-1368.

39. A. Gavezzotti, *Zeitschrift für Kristallographie*, 2005, **220**, 499-510.

40. A. Gavezzotti, *OPiX: A computer program package for the calculation of intermolecular interactions and crystal energies*, 2003.

41. M. J. Frisch, G. W. Trucks, H. B. Schlegel, G. E. Scuseria, M. A. Robb, J. R. Cheeseman, G. Scalmani, V. Barone, B. Mennucci, G. A. Petersson, H. Nakatsuji, M. Caricato, X. Li, H. P. Hratchian, A. F. Izmaylov, J. Bloino, G. Zheng, J. L. Sonnenberg, M. Hada, M. Ehara, K. Toyota, R. Fukuda, J. Hasegawa, M. Ishida, T. Nakajima, Y. Honda, O. Kitao, H. Nakai, T. Vreven, J. A. Montgomery Jr., J. E. Peralta, F. Ogliaro, M. Bearpark, J. J. Heyd, E. Brothers, K. N. Kudin, V. N. Staroverov, R. Kobayashi, J. Normand, K. Raghavachari, A. Rendell, J. C. Burant, S. S. Iyengar, J. Tomasi, M. Cossi, N. Rega, J. M. Millam, M. Klene, J. E. Knox, J. B. Cross, V. Bakken, C. Adamo, J. Jaramillo, R. Gomperts, R. E. Stratmann, O. Yazyev, A. J. Austin, R. Cammi, C. Pomelli, J. W. Ochterski, R. L. Martin, K. Morokuma, V. G. Zakrzewski, G. A. Voth, P. Salvador, J. J. Dannenberg, S. Dapprich, A. D. Daniels, Ö. Farkas, J. B. Foresman, J. V. Ortiz, J. Cioslowski and D. J. Fox, *Gaussian 09 , Revision B.01, Gasussian, Inc.*, 2009.

42. L. Maschio, B. Civalleri, P. Ugliengo and A. Gavezzotti, *Journal of Physical Chemistry A*, 2011, **115**, 11179-11186.

43. P. A. Wood, D. Francis, W. G. Marshall, S. A. Moggach, S. Parsons, E. Pidcock and A. L. Rohl, *CrystEngComm*, 2008, **10**, 1154-1166.

44. R. Dovesi, R. Orlando, B. Civalleri, C. Roetti, V. R. Saunders and C. M. Zicovich-Wilson, *Zeitschrift für Kristallographie*, 2005, **220**, 571-573.

45. A. D. Boese, J. M. L. Martin and N. C. Handy, *Journal of Chemical Physics*, 2003, **119**, 3005-3014.

46. S. Grimme, *Journal of Computational Chemistry*, 2004, **25**, 1463-1473.

47. S. Tsuzuki, H. Orita, K. Honda and M. Mikami, *Journal of Physical Chemistry B*, 2010, **114**, 6799-6805.

48. B. Delley, *Journal of Chemical Physics*, 1990, **92**, 508-517.

49. W. A. Richards and P. R. Scott, *Energy Levels in Atoms and Molecules*, Oxford University Press, Oxford, UK, 1994.

50. A. Maczek, *Statistical Thermodynamics,* Oxford University Press, Oxford, UK, 1998

51. D. M. Adams, P. D. Hutton and A. C. Shaw, *Journal of Physics: Condensed Matter*, 1991, **3**, 6145-6158

Chapter 2

The Effect of Pressure on the Crystal Structure of L-Alanine*

*Nicholas P. Funnell, Alice Dawson, Duncan Francis, Alistair R. Lennie, William G. Marshall, Stephen A. Moggach, John E. Warren and Simon Parsons, *CrystEngComm,* (2010), 12(9), 2573-2583

2.1 Introduction

The use of high pressure is becoming an increasingly popular method with which to study polymorphism in molecular crystals.[1-5] It has been shown that high-pressure phase transitions are driven by the need to fill space efficiently,[6, 7] and in some cases also by relief of destabilising contacts.[8] Effectively the two driving forces can be considered to operate respectively via the *PV* or *U* terms in the equation $G = U + PV - TS$, where the symbols have their usual thermodynamic meanings.

One class of molecules which has been subject to systematic investigation by us and other groups is the amino acids. A number of these are known to undergo pressure-induced phase transitions, and crystal structures have been obtained for high pressure polymorphs of glycine,[9-12] L-serine,[13-15] cysteine,[16] cystine[17] and L-serine monohydrate.[7] A new form of leucine has also been grown from solution at 0.4 GPa and recovered.[18] By contrast, other amino acid phases are remarkably robust: α-glycine for example is stable up to 23 GPa.[19] The purpose of this paper is to describe the effect of pressure on the crystal structure of another amino acid, L-alanine (Scheme 2.1).

The crystal structure of L-alanine has been well characterised at ambient pressure, and there are 15 entries originating from nine different groups in the Cambridge Database[20] with refcodes LALNINxx. The crystal structure was first determined in two simultaneous studies by Simpson and Marsh[21] and by Dunitz and

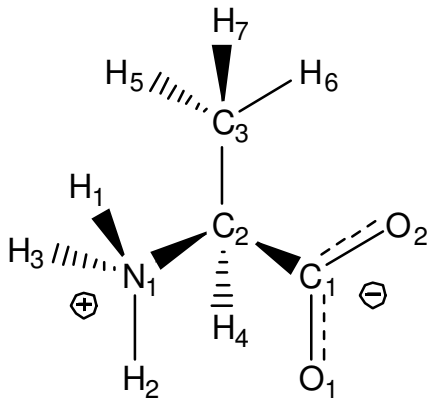

Scheme 2.1 Chemical structure diagram of L-alanine showing the numbering scheme.

Ryan.[22] The structure was studied by Lehmann *et al.* a few years later by neutron diffraction.[23] Other structural investigations have included testing of a variety of charge density models,[24] and a study of the surface structure with atomic force microscopy.[25] There is no evidence for a low-temperature transition[26, 27] which had been suggested by Wang.[28]

L-alanine crystallises as a zwitterion, possessing charged ammonium and carboxylate moieties, in space group $P2_12_12_1$. Each molecule forms three conventional intermolecular hydrogen bonds originating from the ammonium terminus, which are all accepted by carboxylate oxygen atoms on three separate symmetry-related molecules. The molecules are connected in a head-to-tail fashion through primary-level C(5) chains [N1-H2···O2, 1.704(12) Å] along the *c*-axis.[29] Each chain is H-bonded by N1-H3···O2 interactions [1.875(12) Å] to a neighbouring anti-parallel chain generated by a 2_1 screw operation about the *a*-direction. Repetition of this motif along **a** generates a layer in the form of a pleated layer which features a network of secondary-level $R_4^3(14)$ rings (Figure 2.1*i*). Successive sheets are stacked along the *b*-axis, and are interconnected with N1-H1···O1 H-bonds [1.819(12) Å], so that the overall structure is a three-dimensional H-bond network (Figure 2.2*i*).

The vibrational spectra of L-alanine have been studied at high pressure by Freire and co-workers, and phase transitions have been proposed for both the protonated and deuterated forms of the molecule.[30, 31] Orthorhombic to tetragonal phase transitions are reported to occur at 2.2 GPa and 1.5 GPa for the -h_7 and -d_7 forms, respectively. A further transition was identified above 9 GPa for the h_7-form.[32, 33] We describe below our attempts to obtain crystal structures of these new phases for both the h_7 and d_7 forms of L-alanine using single crystal X-ray and neutron powder diffraction supported by periodic DFT calculations.

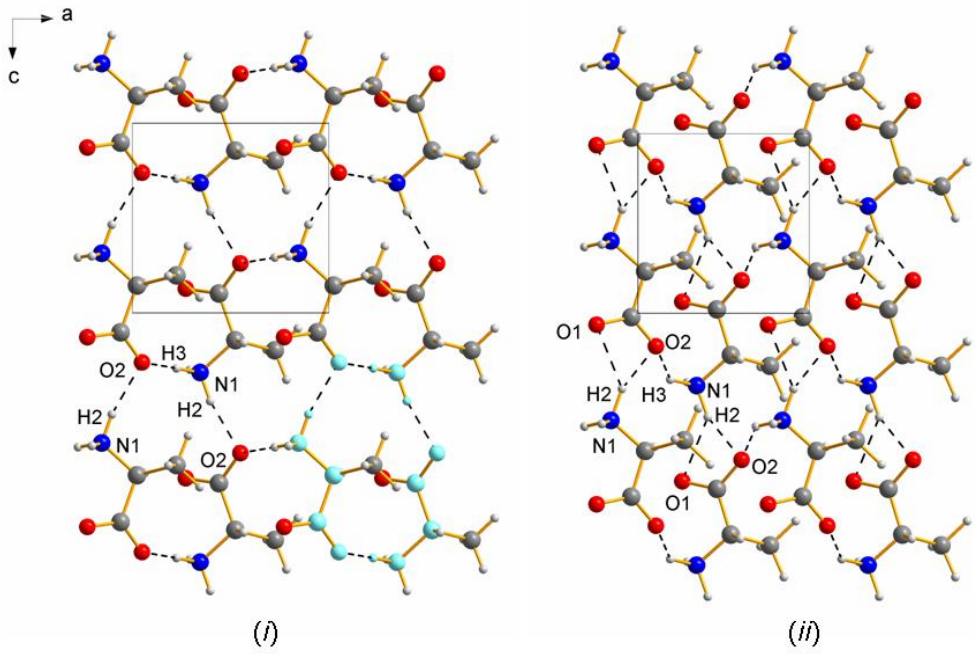

Figure 2.1 L-alanine layers, formed in the *ac*-planes, and constructed of anti-parallel chains. (*i*) Ambient pressure. (*ii*) 9.87 GPa. The view is along the *b*-axis, where black dotted lines represent H-bonds. The cyan coloured atoms in (*i*) define the $R_4^3(14)$ motif. Both figures are on the same scale.

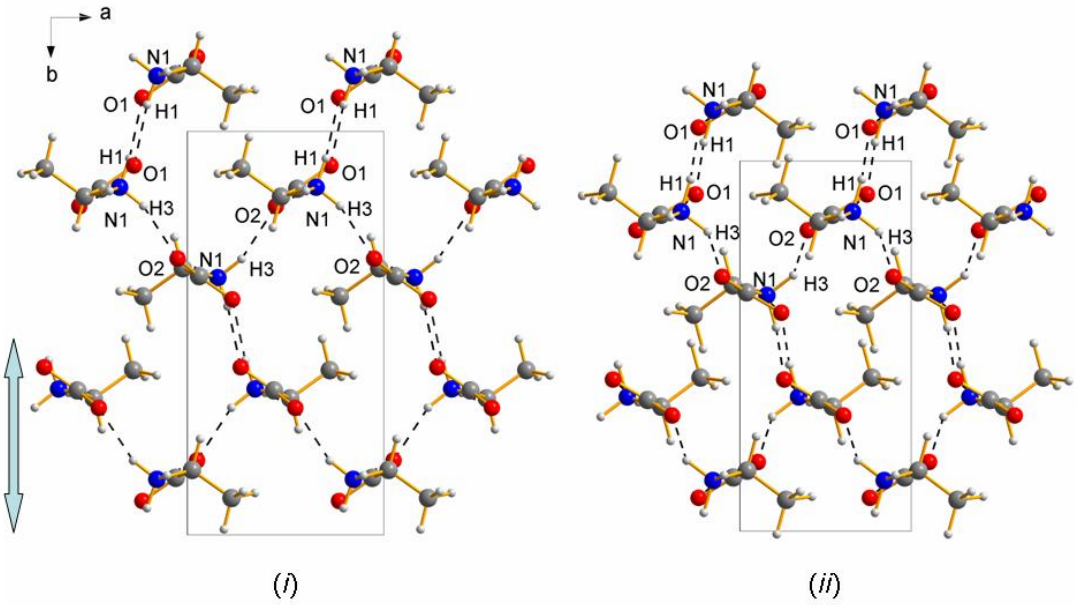

Figure 2.2 L-alanine (*i*) at ambient pressure and (*ii*) at 9.87 GPa viewed along the *c*-axis. The block arrow on the left indicates one layer as shown in Figure 2.1 and discussed in the text. Both diagrams are on the same scale.

2.2 Experimental

2.2.1 Sample preparation

Single crystal X-ray diffraction measurements were carried out using L-alanine-h_7 (99%) purchased from Sigma-Aldrich, and recrystallised from deionised water and ethanol. Neutron powder diffraction measurements were carried out with L-alanine-d_7 obtained from CDN Isotopes and used as supplied.

2.2.2 High-pressure single-crystal X-ray measurements

Three separate crystals of L-alanine-h_7 were used for the X-ray diffraction measurements in the ranges: ambient pressure to 2.1 GPa, 1.4 to 5.7 GPa and 5.3 to 8.1 GPa. In each case a single crystal was loaded into a Merrill-Bassett diamond anvil cell (half opening angle 40°), equipped with brilliant-cut diamonds with 400 μm culets, a tungsten gasket and tungsten carbide backing plates.[34, 35] A mixture of 4:1 methanol and ethanol was used as the pressure-transmitting medium. A small ruby chip was used as a pressure calibrant, using the ruby fluorescence method to measure the pressure[36]

Diffraction data were collected on a Bruker-Nonius APEX-II diffractometer with silicon-monochromated synchrotron radiation (λ = 0.4767 Å) on Station 9.8 at the SRS, Daresbury Laboratory. Data collection and processing procedures followed Ref. 37. Data were integrated using dynamic masking of the regions of the detector shaded by the pressure cell with the programme SAINT.[38] Absorption corrections were carried out with the program SADABS.[39] Data were merged using SORTAV.[40]

2.2.3 High-pressure neutron powder diffraction measurements

Neutron data were collected using the time-of-flight technique at the PEARL beamline high-pressure diffractometer (HiPr) at ISIS.[41, 42] Data sets between ambient pressure and 9.87 GPa were collected in the range $0.6 < d < 4.1$ Å using a V3b-type Paris-Edinburgh press, with a 16:3:1 mixture of deuterated methanol, ethanol and water as a hydrostatic medium. The TiZr capsule gasket,[43] containing the sample, was also loaded with a small lead pellet to act as a pressure marker. Data were collected at ambient pressure and then at 0.40, 0.77, 1.03, 1.38, 2.30, 3.21, 4.31,

5.43, 6.65, 8.03, 8.82, 9.39 and 9.87 GPa. These pressures were calculated from the refined lead cell lattice parameter using a Birch-Murnaghan equation of state[44] with V_o = 30.3128 Å^3, K_o = 41.92 GPa, K' = 5.72. These parameters were derived by Fortes[45] as averages of the values determined in three earlier studies.[46-48] The standard deviations of the pressures obtained in this way are 0.01 – 0.03 GPa. The highest pressure attained was the limit of the experimental configuration employed on the instrument.

2.2.4 Structure refinements

Structure refinement was carried out in a three-stage procedure. In the first stage the X-ray and neutron data were combined in an 'X-N' refinement. The coordinates from these refinements were then used as the starting model for plane-wave DFT optimisation. In the final stage the DFT-optimised coordinates were used as restraints for a refinement against neutron powder data only. A justification for this rather elaborate procedure is given in the *Discussion* section.

2.2.5 Structure refinement stage 1: Initial refinement

Refinements of the compressed form of L-alanine were based on the co-ordinates determined at ambient conditions in the Cambridge Database entry LALNIN12.[23] The program used for refinement was TOPAS-Academic version 4.1.[49]

Up to 8.03 GPa refinements utilised both X-ray single crystal and neutron powder data simultaneously. In some refinements there was a difference between the pressures of the X-ray and neutron data sets of up to 0.4 GPa, but the assumption was made that the position and orientation of the molecule are the same. Above 8.03 GPa refinements were based only on neutron data.

Cell dimensions used for modelling the X-ray data were derived in the usual way from integration of the X-ray diffraction data and thereafter held fixed; those for modelling the neutron data were refined. The alanine molecule was represented using the Z-matrix formalism available in TOPAS, which enables refinements to be parameterised in terms of bond distances and angles rather than fractional atomic coordinates.

In the initial stages of refinement the primary intramolecular geometric parameters were held fixed, and only the positions and orientations of the molecules were allowed to vary. In the final stages all geometric parameters were allowed to refine in the constrained parameterisation described under 'Stage 3' below. A single parameter representing the difference between neutron and X-ray distances involving deuterium/hydrogen was also refined.

Displacement parameters obtained using X-ray and neutron data are known to differ.[50] Anisotropic displacement parameters (ADP's) for the non-H atoms and a common isotropic displacement parameter for the H-atoms were used to model the X-ray data. A common isotropic displacement parameter was used for the non-H atoms in modelling the neutron data; H-atom displacement parameters were set to 1.2 × this value. Also included in the powder-pattern modelling were structural data for Pb (the pressure marker) and Ni and WC (components of the Paris-Edinburgh cell anvils).

2.2.6 Structure refinement stage 2: Geometry optimisation using plane-wave DFT

DFT calculations were performed using the plane-wave pseudopotential method as implemented in the Castep code.[51] The PBE exchange-correlation functional[52] was used with Vanderbilt ultra-soft pseudopotentials[53] and a basis set cut-off energy of 600 eV. Brillouin zone integrations are performed on a symmetrized Monkhorst-Pack[54] **k**-point grid of dimensions 4 × 2 × 4. The starting point for geometry optimisation was the converged model from the experimental X-N refinements; the pressure points used were those from the neutron powder experiments. The unit cell and space group were held fixed, but all coordinates allowed to optimise. The total energy convergence tolerance was 10^{-5} eV/atom, with a maximum force tolerance of 0.03 eV $Å^{-1}$, a maximum displacement of 0.001 Å and a maximum stress tolerance of 0.05 GPa.

2.2.7 Structure refinement stage 3: Restrained refinements against neutron powder data

The final structural models for L-alanine-d_7 as a function of pressure were obtained by refinements using neutron powder data only with the fractional coordinates

restrained to those determined in the DFT optimisations from Stage 2. The restraints were more strongly weighted for datasets at 0.77 GPa, 4.31 GPa and 6.65 GPa to compensate for short neutron data collection times.

A conventional refinement would require 39 parameters to define the structure, position and orientation of the alanine molecule. Instead the Z-matrix model was retained. All NH distances were constrained to be equal (removing two parameters from the refinement). Similar constraints were applied to the CH distances and the CO distances (removing a total of 4 parameters). The HNC and HCC angles were constrained to be equal, and the HNCC and HCCN torsion angles involving the ammonium and methyl groups, and the torsions C3C2C1O1 and H4C2C1O1 were respectively constrained to be related by rotations of 120° (9 parameters saved); the carboxylate group was constrained to be planar (one parameter). These constraints reduced the number of geometric parameters required to 23.

Listings of selected crystal and refinement data are given in Table 2.1. The final fit for the structure at 9.87 GPa is shown in Figure 2.3. Cifs for all structures are available in the Supplementary Material.

2.2.8 PIXEL calculations

The final crystal structures obtained were used to calculate the molecular electron densities of the alanine molecules at ambient pressure and 9.87 GPa. Calculations were carried out with the program GAUSSIAN03[55] at the MP2 level of theory with the 6-31G** basis set. The electron density was used to calculate intermolecular interaction energies using the PIXEL method[56, 57] in the program package OPiX.[58] The output from these calculations yields a total lattice energy and a breakdown into its Coulombic (electrostatic), polarisation, dispersion and repulsion components.

2.2.9 Other programs used

Crystal structures were visualized using the programs MERCURY CSD 2.2,[59] DIAMOND;[60] movies were generated using CrystalMaker®.[61] Searches of the Cambridge Structural Database[20] utilized the program CONQUEST with database updates up to November 2008. Topological calculations were carried out using the program TOPOS 4.0.[62] The bulk modulus of L-alanine-d_7 was determined using the using the program EOSFIT.[63]

Table 2.1: Experimental details for selected data sets (others are available in the supplementary material). All data sets were collected at room temperature. 'R_{wp} No restraints' refers to a repeated refinement in which restraints were deleted.

Pressure/GPa	Ambient	0.77	2.30
Sample type and radiation used	Neutron powder	Neutron powder	Neutron powder
Chemical formula	$C_3D_7NO_2$	$C_3D_7NO_2$	$C_3D_7NO_2$
M_r	96.02	96.02	96.02
Cell setting, space group	Orthorhombic, *P*212121	Orthorhombic, *P*212121	Orthorhombic, *P*212121
a/Å	6.0186(6)	5.820(10)	5.6370(4)
b/Å	12.3298(11)	12.2494(19)	12.0464(7)
c/Å	5.7828(4)	5.7420(8)	5.6628(4)
V/Å^3	429.13(7)	409.39(11)	384.53(4)
Z	4	4	4
D_c/Mg m^{-3}	1.486	1.558	1.659
d_{max}, d_{min}/Å	4.1, 0.6	4.1, 0.6	4.1, 0.6
Pawley R_{wp}	2.864	5.816	1.875
R_{wp}	3.575	6.565	2.557
R_{wp} No restraints	3.514	6.405	2.442
S	1.146	1.115	1.324
Reflection/ profile data	2277	2277	2277

Table 2.1 continued

Pressure/GPa	4.31	8.03	9.87
Sample type and radiation used	Neutron powder	Neutron powder	Neutron powder
Chemical formula	$C_3D_7NO_2$	$C_3D_7NO_2$	$C_3D_7NO_2$
M_r	96.02	96.02	96.02
Cell setting, space group	Orthorhombic, *P*212121	Orthorhombic, *P*212121	Orthorhombic, *P*212121
a/Å	5.4850(5)	5.3105(3)	5.2459(4)
b/Å	11.7729(10)	11.4299(6)	11.3088(8)
c/Å	5.5875(5)	5.5015(3)	5.4696(4)
V/Å^3	360.80(5)	333.94(3)	324.48(4)
Z	4	4	4
D_c/Mg m^{-3}	1.768	1.910	1.966
d_{max}, d_{min}/Å	4.1, 0.6	4.1, 0.6	4.1, 0.6
Pawley R_{wp}	3.221	2.108	2.831
R_{wp}	3.885	2.737	3.444
R_{wp} *No restraints*	3.832	2.667	3.375
S	1.104	1.232	1.139
Reflection/ profile data	2277	2277	2277

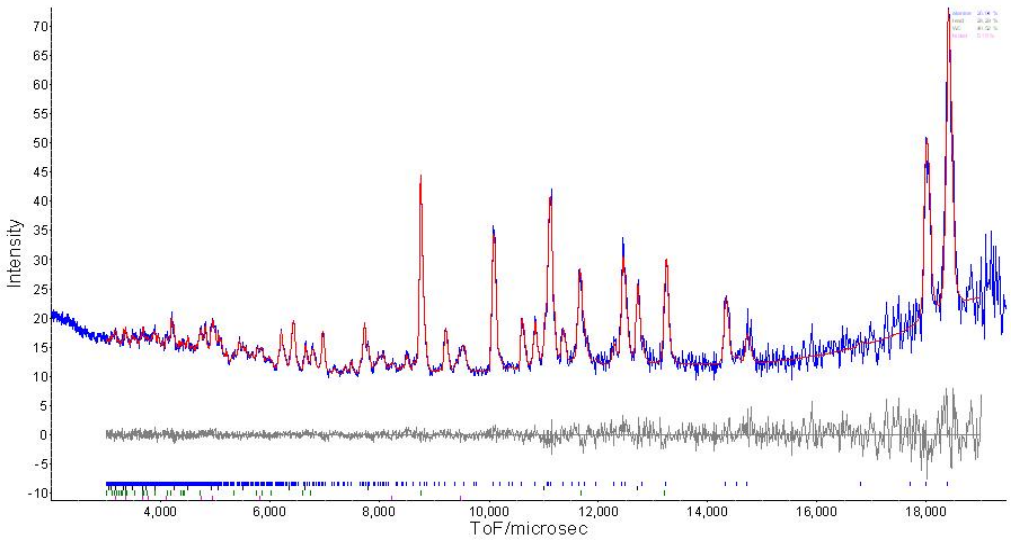

Figure 2.3 Final Rietveld fit for L-alanine at 9.87 GPa. Observed data are in blue, calculated in red, and the difference in grey. The minimum and maximum d-spacing are 0.6 and 4.1 Å respectively.

2.3 Results

2.3.1 The effect of pressure on the unit cell dimensions

The effect of pressure on the unit cell parameters of L-alanine-h_7 and $-d_7$ is shown in Figure 2.4. The cell dimensions of the H- and D- containing isotopologues follow the same trends. The cell axes and volume of the orthorhombic unit cell steadily decrease with each step in the pressure series, showing no abrupt discontinuities in trend, and no indication of any phase change. The bulk modulus (K_0), refined for a Birch-Murnaghan equation of state[44, 64] to third order using the neutron data is 13.4(7) GPa. The values of V_0 and K' refined to 430.4(11) Å^3 and 7.0(3), respectively. Corresponding data calculated for a Vinet equation of state[65, 66] were identical within error [V_0 = 430.6(11) Å^3, K = 13.3(6) GPa and K' = 7.1(2)].

The *a*, *b* and *c*-axes compress by 12.8%, 8.3% and 5.4%, respectively up to 9.87 GPa (using neutron data only). Rather unusually, the curve for the *b*-axis is initially slightly convex before coming concave beyond 2 GPa; the trends for a and *c* axes are convex throughout the range studied. The *a*-axis is longer than the *c*-axis at ambient pressure, but because it is more compressible, it becomes shorter above *ca.* 2 GPa. At this point the cell is *metrically* pseudo-tetragonal, though the structure is still orthorhombic and a compressed form of the ambient-pressure structure. In contrast to Freire and co-workers we see no evidence for an orthorhombic to tetragonal phase transition in the region of 2.2 GPa for alanine-h_7 or 1.5 GPa for alanine-d_7.[30, 31]

Additionally, no phase change was seen in L-alanine-d_7 above 9 GPa in contrast to the results reported in Ref. 33 which suggested a new high pressure polymorph exists (for L-alanine-h_7) at *ca.* 9 GPa.

2.3.2 The effect of pressure on the crystal structure

In general the intramolecular geometry (Table 2.2) of L-alanine does not change significantly as the effects of pressure are taken up in the 'softer' intermolecular geometry rather than in the covalent bonds. Exceptions to this are bond distances C1-C2 and N1-C2, which both decrease substantially (by 13 and 9σ, respectively) over the pressure range studied. While bond angles do not change, the

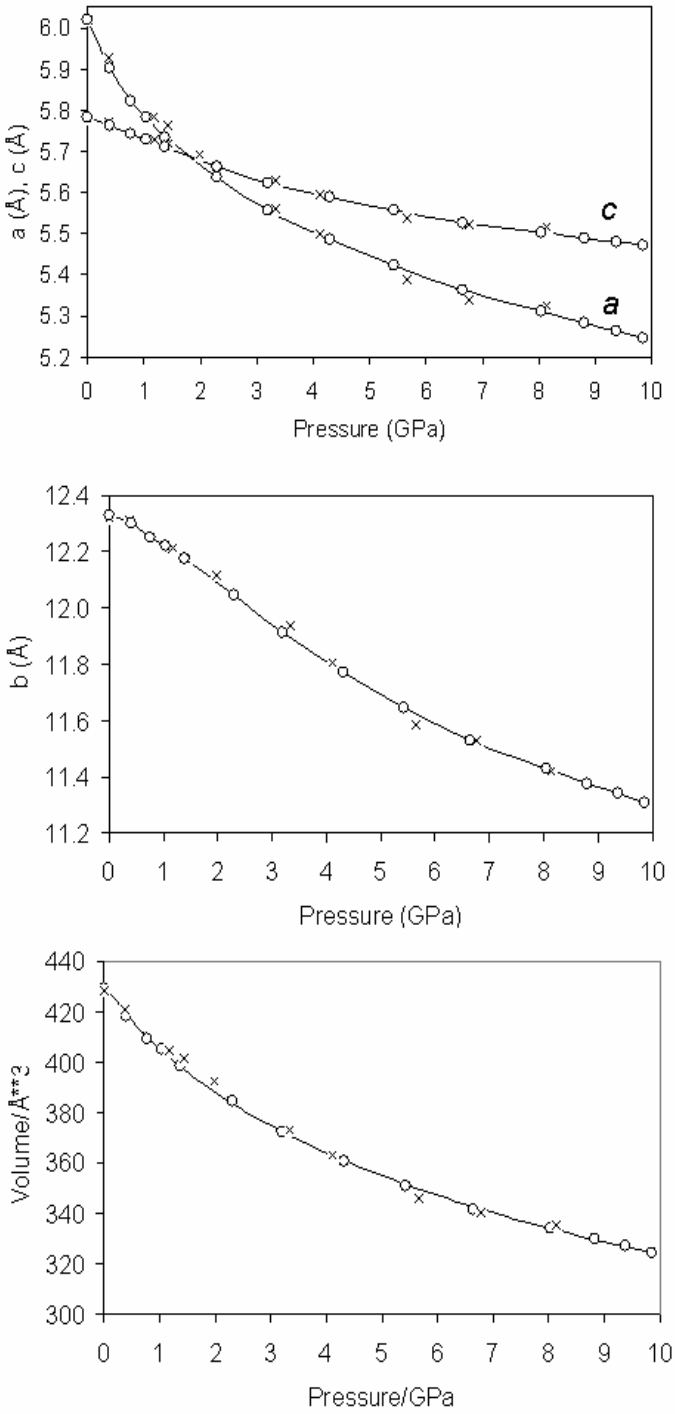

Figure 2.4 Variation of lattice parameters (*a, b* and *c*) and volume of alanine as a function of pressure as measured by single crystal X-ray on the h_7 isotopologue ('X') and neutron powder diffraction on the d_7 isotopologue (circles). The *a* and *c*-axes are plotted on the same graph (top) to show the cross-over at *ca* 2 GPa. In the bottom graph, showing volume, the trend-line represents the fitted third order Birch-Murnaghan equation of state.

changes in torsion angle are significant. The CO_2 torsion changes from -18.89(17)° to -13.99(12)° over the pressure series. The NH_3 torsion angle (Figure 2.5) remains constant up to 1.03 GPa, ranging between 58.2(7)° and 58.7(3)°. From 1.38 GPa it increases until *ca* 5 GPa, after which the trend flattens off. The standard uncertainties of the torsion angles in the range 0 – 0.77 GPa are relatively high because they were derived from rather short neutron data collections. The H1-N1-C2-C1 torsion angles derived from the DFT optimisations are also plotted in Figure 2.5. While there appears to be a large deviation between the red and blue curves in Figure 2.5 above 7 GPa, the distances between the DFT positions used for the restraints and the final refined positions are small: *e.g.* for the 8.82 GPa structure the largest difference is only 0.06 Å for the position of H1.

Table 2.2 Intramolecular bond distances, bond angles and torsion angles as a function of pressure

Pressure/GPa	Ambient	0.77	2.30
N-H/Å	1.044(6)	1.040(8)	1.043(4)
C-H/Å	1.097(5)	1.106(7)	1.095(3)
C1-C2/Å	1.531(3)	1.522(4)	1.514(2)
N1-C2/Å	1.486(4)	1.497(6)	1.479(3)
O1-C1/Å	1.254(7)	1.265(9)	1.255(5)
O2-C1/Å	1.254(7)	1.265(9)	1.255(5)
C2-C3/Å	1.534(5)	1.512(7)	1.544(3)
<N1-C2-C1/°	111.49(14)	111.66(19)	111.75(9)
<O1-C1-C2/°	117.9(4)	119.2(6)	117.7(3)
<O2-C1-C2/°	117.7(4)	116.5(6)	117.5(3)
<C3-C2-C1/°	111.08(15)	111.6(2)	111.53(10)
<H4-C2-C1/°	108.0(5)	106.8(6)	106.8(3)
<H-N-H/°	109.9(3)	108.3(4)	108.7(2)
<H-C-H/°	110.5(3)	110.1(4)	109.2(2)
τH1-N1-C2-C1/°	58.6(4)	58.5(5)	61.8(3)
τO2-C1-C2-N1/°	-18.89(17)	-18.8(2)	-16.85(11)
τC3-C2-C1-O1/°	103.67(18)	105.1(2)	107.28(12)
τH5-C3-C2-C1/°	55.9(3)	55.1(5)	53.8(2)

Table 2.2 continued

Pressure/GPa	4.31	8.03	9.87
N-H/Å	1.045(4)	1.037(3)	1.040(4)
C-H/Å	1.106(4)	1.100(3)	1.091(4)
C1-C2/Å	1.512(2)	1.4922(18)	1.481(2)
N1-C2/Å	1.468(3)	1.456(3)	1.439(3)
O1-C1/Å	1.266(5)	1.271(4)	1.273(5)
O2-C1/Å	1.266(5)	1.271(4)	1.273(5)
C2-C3/Å	1.504(4)	1.521(3)	1.527(4)
<N1-C2-C1/°	111.18(10)	111.71(8)	111.94(10)
<O1-C1-C2/°	118.4(3)	118.7(2)	119.5(3)
<O2-C1-C2/°	116.9(3)	116.8(3)	116.8(3)
<C3-C2-C1/°	112.49(10)	111.84(9)	111.13(11)
<H4-C2-C1/°	106.4(3)	105.3(3)	106.4(4)
<H-N-H/°	108.7(2)	108.37(18)	108.9(2)
<H-C-H/°	110.5(2)	109.49(18)	109.8(2)
τH1-N1-C2-C1/°	63.6(3)	63.9(2)	62.8(3)
τO2-C1-C2-N1/°	-16.48(11)	-14.25 (10)	-13.99(12)
τC3-C2-C1-O1/°	108.20(12)	109.09(11)	107.89(13)
τH5-C3-C2-C1/°	52.9(2)	52.15(18)	51.6(2)

It was clear from a difference map calculated after deletion of the ammonium H-atoms (H1-3) from the 9.87 GPa model that the ammonium group retains its integrity during compression. There is thus no suggestion of H-transfer to a neighbouring carboxylate. This conclusion is supported by the results of the periodic DFT optimisations and Freire's previously reported Raman data.[31] The pattern of H-bonding at 9.87 GPa is therefore much the same as at ambient pressure. The 'layer-forming' H-bond N1-H3···O2, shortens by 0.144(15) Å and the N1-H1···O1 H-bond, interlinking adjacent layers, contracts by 0.206(15) Å (Figure 2.6*ii*, Table 2.3). As the layers are compressed alternate C(5) chains slide in an anti-parallel fashion along the *c*-direction so as to avoid unfavourably repulsive interactions (Figure 2.6). At the same time the structure compresses along **b**. Both changes are very clearly demonstrated when the pressure series is viewed as a movie shot along the *a*-axis

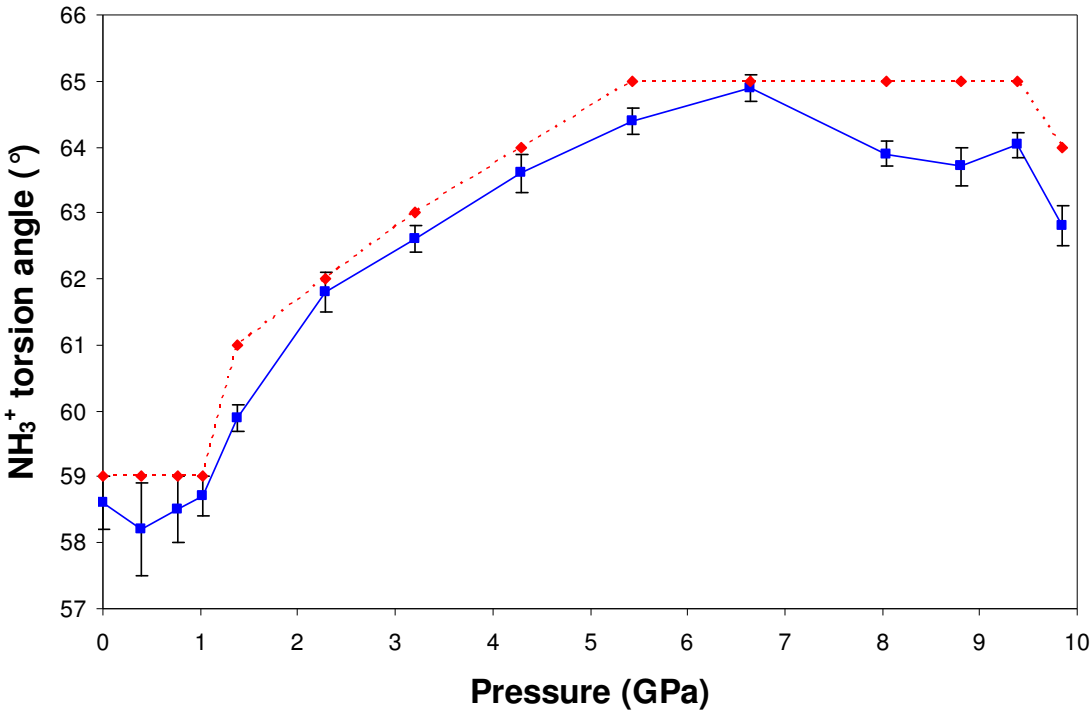

Figure 2.5 The NH_3 torsion angle (H1N1C2C1) plotted as a function of pressure. The DFT-optimised angles (fitted using the same parameterisation used for the refinement) are plotted in red and the experimental neutron data restrained by the calculated coordinates are shown in blue. The first change in trend is evident in the low pressure regime (~ 1 GPa) and a second change in trend is observed at ~ 5 GPa.

direction (see Supplementary Material). The effect of this is to cause the H-bond angle <N1-H3···O2 to change from 161.0(6)° to 141.5(4)°. A similar effect is seen in other amino acids such as L-serine, where a similar layer-sliding-plus-compression takes place after a phase transition.[13, 14]

The H-bond which forms the head to tail chains along **c** (N1-H2···O2) compresses by 0.051(16) Å. As this occurs the H-bonds formed by the N1-H2 (Figure 2.1*ii*), becomes more symmetrical or bifurcated. At ambient pressure N1-H2···O1 and N1-H2···O2 measure as 2.545(12) Å and 1.704(12) Å respectively and the O1···H2···O2 angle is 59.0(4)°. At 9.87 GPa, these distances have shortened to 2.232(9) Å and 1.653(10) Å and the angle is 68.8(4)°. Increased bifurcation of a chain-forming hydrogen bond with pressure is also seen in α-glycine at 6.2 GPa.[9]

Table 2.3 Hydrogen bonding parameters over a representative range of pressure between 0 and 9.87 GPa

Pressure/GPa	Ambient	0.77	2.30
N1-H1···O1^{i}/Å	1.819(12)	1.749(18)	1.764(9)
<N1-H1-O1^{i}/°	161.1(7)	161.0(9)	163.8(5)
N1-H2···O2^{ii}/Å	1.704(12)	1.677(17)	1.668(9)
<N1-H2-O2^{ii}/°	170.9(7)	172.9(9)	169.0(4)
N1-H2···O1^{ii}/Å	2.545(12)	2.523(16)	2.436(8)
<N1-H2-O1^{ii}/°	130.0(5)	126.7(7)	128.0(4)
N1-H3···O2^{iii}/Å	1.875(12)	1.839(18)	1.788(8)
<N1-H3-O2^{iii}/°	161.0(6)	159.9(9)	154.3(4)

Symmetry operators: i 3/2-x,-y,-1/2+z, ii x,y,-1+z, iii 1/2+x,1/2-y,1-z

Table 2.3 continued

Pressure/GPa	4.31	8.03	9.87
N1-H1···O1^{i}/Å	1.693(9)	1.640(7)	1.613(9)
<N1-H1-O1^{i}/°	165.3(5)	165.5(4)	165.3(5)
N1-H2···O2^{ii}/Å	1.651(9)	1.663(8)	1.653(10)
<N1-H2-O2^{ii}/°	165.5(4)	162.4(4)	161.2(5)
N1-H2···O1^{ii}/Å	2.362(8)	2.266(7)	2.232(9)
<N1-H2-O1^{ii}/°	127.6(4)	127.8(3)	127.9(4)
N1-H3···O2^{iii}/Å	1.763(9)	1.754(7)	1.731(9)
<N1-H3-O2^{iii}/°	150.2(4)	143.8(3)	141.5(4)

Symmetry operators: i 3/2-x,-y,-1/2+z, ii x,y,-1+z, iii 1/2+x,1/2-y,1-z

2.4 Discussion

2.4.1 Refinement strategy

A constant problem encountered in high-pressure single-crystal diffraction is shading of reciprocal space by the body of the pressure cell. Although the problem can be minimised by using short wavelength synchrotron radiation, data-set completeness of

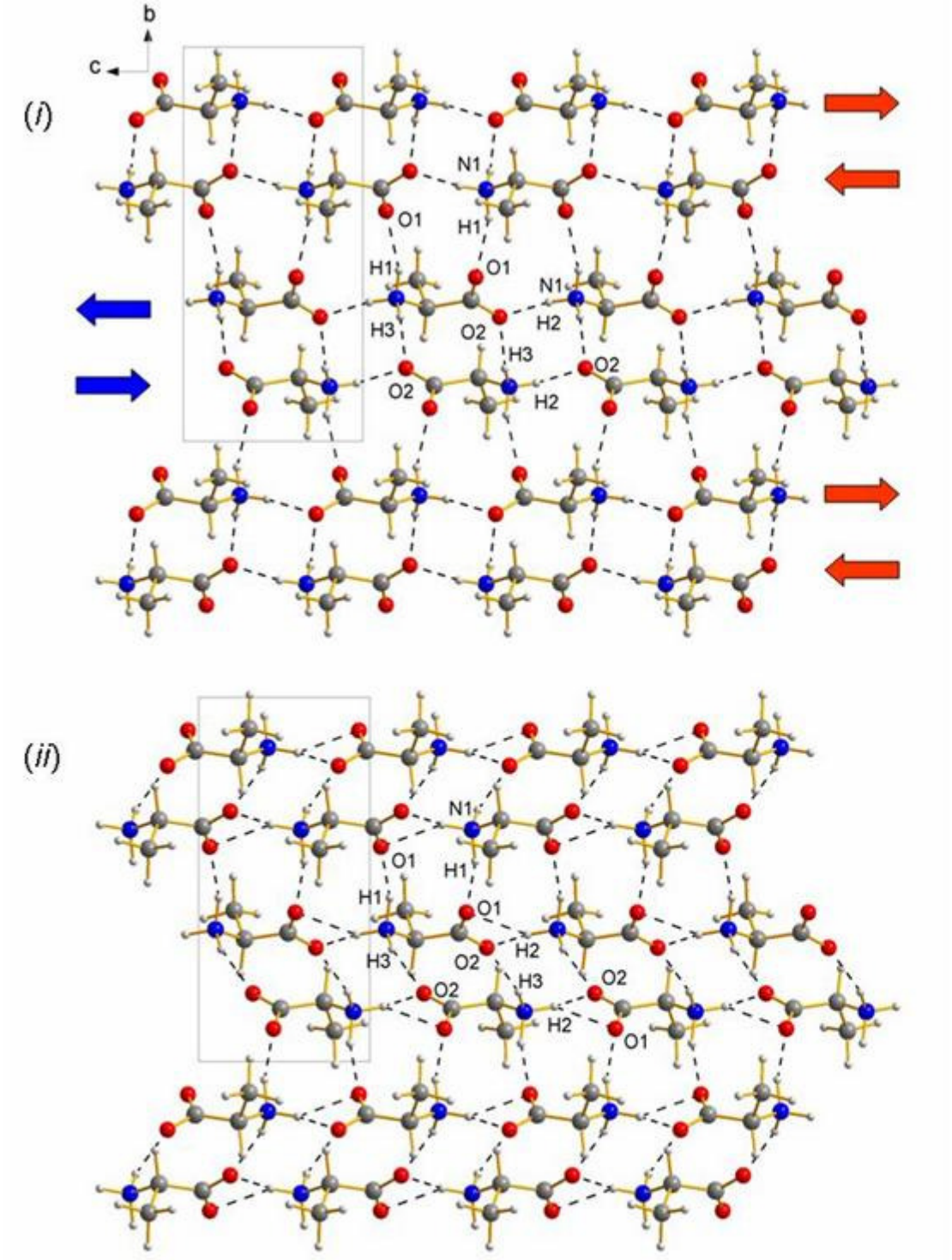

Figure 2.6 The crystal structure projected along the *a*-axis at (*i*) ambient pressure and (*ii*) 9.87 GPa. Each alternate layer is represented by either red or blue arrows and the arrow direction indicates chain movement upon application of pressure. The layers are deformed at higher pressure such that the molecules pack closer together through a deviation in linearity of the N1-H3···O2 bond. Both figures are on the same scale

40% or less is not uncommon, particularly in molecular compounds which tend to form crystals in the lowest symmetry crystal systems.

Low completeness affects all stages of structure analysis. With complete datasets the phase problem for small organic crystal structures can be solved routinely, but this is not the case at high pressure. Refinements suffer from low data-to-parameter ratios, and restraints and constraints have to be applied extensively. A particular problem in the context of the present study is that Fourier maps are distorted by missing zones of data, which makes H-atom location very uncertain.

In principle the problems of low completeness can be addressed by using powder diffraction, with neutron powder diffraction being particularly appropriate for problems involving the location of hydrogen. Although powder diffraction patterns are complete in the sense that no data are shaded, reflections are overlapped, and this too leads to loss of information, making use of restraints and constraints essential for structures of any complexity. A very attractive solution is to combine single crystal X-ray and neutron powder diffraction data, and refine crystal structures using both sets of data simultaneously in 'X-N refinements'. We have used this approach in studies of serine and serine hydrate at high pressure.[6, 7]

In practice certain assumptions are inevitably necessary. X-ray and neutron data sets are rarely at *exactly* the same pressure: they may differ by several kilobars, and it is necessary to assume that this difference in pressure is small enough not to affect the fractional coordinates of the atoms. Although it is usual to refine a parameter which takes into account the systematic difference between H positions derived from neutron and X-ray data, this 'one size fits all' approach is only partially successful, and fitting of the X-ray data is compromised. Finally, deuteration is essential for neutron powder diffraction so as to avoid the problems associated with incoherent scattering of H, and it is necessary to assume that deuteration does not affect the structure. In many cases this is reasonable, as the differences are likely to be small compared to the precision of the structure determination. In the present study this assumption is not reasonable, as the changes in the Raman spectra assigned to phase transitions occur at 2.2 GPa for alanine-h_7 but at 1.5 GPa for alanine-d_7.[30, 31, 67]

For this study on alanine we adopted a three-stage refinement strategy. The first stage was to carry out an X-N refinement, ignoring the problems described above. Independent refinements against only neutron or X-ray data showed that the geometry of the C_3NO_2 skeleton was the same at each pressure point within experimental error. Though the model does not accommodate any torsional or angular differences which might occur between parameters involving the H and D atoms, since the scattering of neutrons by D is so much more significant than scattering of X-rays by H, the positions for hydrogen were presumably mostly determined by the neutron data on the deuterated derivative.

The structures so obtained were then optimised using periodic DFT, holding the experimental cell dimensions and space group fixed, but allowing the fractional coordinates of all atoms to optimise. Periodic DFT calculations are now able to reproduce experimental structures with great accuracy; in fact, in some fields, for example solid state NMR, it is often found necessary to optimise an experimental crystal structure prior to calculation of NMR parameters in order to obtain a satisfactory match between observed and calculated spectra.[68-72] In a recent high-pressure study of salicylamide[73] the experimental atomic positions of the crystal structure were reproduced by DFT to within 0.06 Å, while the agreement with vibrational spectroscopic data was excellent.

When applied to molecular systems periodic DFT can suffer from the lack of proper treatment of dispersion interactions, and unit cell dimensions are often found to be too large in full optimisations, though this can be avoided by holding cell dimensions fixed at their experimental values. In the case of the present study on alanine, these are, of course, known with great accuracy, and the results of a DFT optimisation present a very attractive source of restraints. These are system-specific and avoid the need to make assumptions about typical distances and angles, which are particularly questionable at high pressure. They also enable the neutron powder data to be used on their own even for this (moderately) complex molecular system, avoiding the need to make assumptions about the behaviour of H- and D-isotopologues or the insensitivity of the structure to small changes in pressure, which were implicit in the X-N approach.

The third stage of refinement was therefore to use the neutron data alone, applying the DFT optimised coordinates as restraints, and controlling the data to parameter ratio further by incorporation of chemically reasonable constraints (local three-fold symmetry in the ammonium and methyl groups; planarity of the carboxylate). Restraints provide 'target values' for a refinement, and deviations which demanded by the experimental data can occur.

The extent to which the data fitting is affected by the restraints can be assessed simply by removing them and re-refining the structure. Values of R_{wp} from restrained and unrestrained refinements are listed in Table 2.1, and can be seen to be very similar to those from the restrained refinement, but the structural parameters from the unrestrained refinement are less precise (by a factor of between 2 and 6) than those from the restrained refinement. The value of R_{wp} can also be compared with that obtained in a structure-free Pawley refinement, which defines the lowest value of R_{wp} which can be expected on the basis of the phases included and the models for the background and peak-shape. These values are also listed in Table 2.1. The similarity of these three residuals in each case justifies the procedure used and demonstrates that the restraints are not unduly biasing data-fitting. Our experience in this and other systems suggests that use of incorrect restraints can lead to deviations of several percent in the values of R_{wp} for restrained and unrestrained refinements, as well as an obvious deterioration in the visual quality of data fitting.

The strategy outlined enables precise structural data to be extracted from the neutron diffraction data on alanine-d_7 without the need to make any assumptions about the effect of deuteration. The results can be correlated directly with those of Freire and co-workers on the Raman spectra of the same material.[31]

2.4.2 The bulk modulus of L-alanine

The bulk modulus of a material is the inverse of its volume compressibility, and is a measure of its resistance to compression: the higher the bulk modulus the harder the solid is to compress. Some representative values were listed by Slebodnick and co-workers, and form a useful scale: 6.6 GPa for $Ru_3(CO)_{12}$, 25 GPa NaCl, 37 GPa for quartz and 440 GPa for diamond.[74]

The following bulk moduli have been previously reported by us and others for amino acids: L-alanine [31.5(14) GPa],[33] L-α-glutamine [26.0(11) GPa],[75] serine monohydrate [18.9(3) GPa)][7] and L-cystine [29.1(4) GPa].[17] These values were mostly derived from single crystal diffraction studies, in which only a limited number of (pressure, cell volume) data points were available, and the low-pressure region often quite lightly sampled. Under these circumstances it is necessary to constrain the refinement of the bulk modulus, most commonly by assuming values of the first and second derivatives of the bulk modulus with pressure. A value of 4.0 for the former is often assumed.

The value of the bulk modulus of L-alanine-d_7 obtained here using a more extensive data set than available in other work was 13.4(7) GPa, a value considerably lower than those obtained previously. We were able to refine the value of $K' = (\partial K/\partial P)_T$, obtaining a value of 7.0(3). The zero-pressure volume, V_o refined to 430.4(11) Å^3, in good (i.e. within 3σ) agreement with the value of 429.13(7) Å^3 obtained directly from a Rietveld refinement of the structure against ambient-pressure diffraction data.

Similar classes of compound are normally found to have similar bulk moduli, and the relatively low value for the bulk modulus obtained in the present study suggests that other estimates may have been based on too low a value for K'. Alanine is more compressible at low pressures than implied by the choice of 4.0 for this quantity, and it seems reasonable to suggest that this comment would apply to other amino acids as well.

2.4.3 Preferred directions of compression

L-alanine is orthorhombic, and so the principal axes of the strain tensor coincide with the unit cell axes. The initial compressibilities of the axes are in the order $a > b > c$. The $C(5)$ chains formed by N1-H2···O2 H-bonds are built by lattice repeats along the *c*-axis, while the *b*-axis makes angles of 32.8(3) and 16.8(4)° with the N1-H3···O2 and N1-H1···O1 contacts, respectively at ambient pressure. The smallest angle made by the *a*-axis with any of the H-bonds is 57.5(3)° (N1-H3···O2), showing that the *a*-axis is least well aligned with any of the H-bonds in the system. H-bonds are relatively strong, directional interactions, and, though much depends on the shape of

the potential in each case, they are expected to be less compressible than other intermolecular interactions. The relatively high compressibility along the *a*-axis in L-alanine is consistent with this view. Equally, the axis along which H-bonded molecules are most closely aligned (*c*) in the head-to-tail C(5) chains is the least compressible direction.

PIXEL calculations indicate that at ambient pressure the energies of the H-bonds are: N1-H3···O2, -144.7 kJ mol^{-1}; N1-H2···O2, -117.9 kJ mol^{-1} and N1-H1···O1, -31.3 kJ mol^{-1}. The low energy of the last of these can be traced to the electrostatic term, which reflects the relatively close disposition of like-charged pairs of ammonium and carboxylate groups. There is little variation in the energy of the three H-bonds over the pressure series, with the greatest change seen for N1-H1···O1 H-bond which increases (i.e. becomes more positive) in energy by just 3 kJ mol^{-1} between 0 and 9.87 GPa. The energy of the N1-H2···O2 bond actually decreases by 0.6 kJ mol^{-1}.

The final pressure reached in this study was 9.87 GPa, and this is the highest pressure crystal structure of an amino acid yet described. The shortest H-bond at this pressure is N1-H1···O1, which reaches a value of 1.613(9) Å. This is based on neutron powder data only, and though the standard uncertainty is quite high, the value lies at the lower end of a histogram of ammonium-to-carboxylate H-bonds in amino acids harvested from the Cambridge Database. On the basis of the PIXEL energy calculations and comparison of intermolecular interaction distances with those in other systems, none of the H-bonds in L-alanine can be described as either abnormally short or as entering a repulsive region of its potential even at almost 10 GPa.

2.4.4 Topology of packing

In L-alanine at ambient pressure the molecular coordination number is 14. Voronoi-Dirichlet analysis, along the lines described by Blatov,[76, 77] reveals that the topology resembles a distorted body-centred cubic pattern, with a coordination sequence of 14-50-110 (that is, 14 molecules in the first coordination sphere, 50 in the second and so on). As pressure is increased the distortion gradually lessens, until, at the highest pressure reached, the topology is remarkably regular: Figure 2.7 compares the

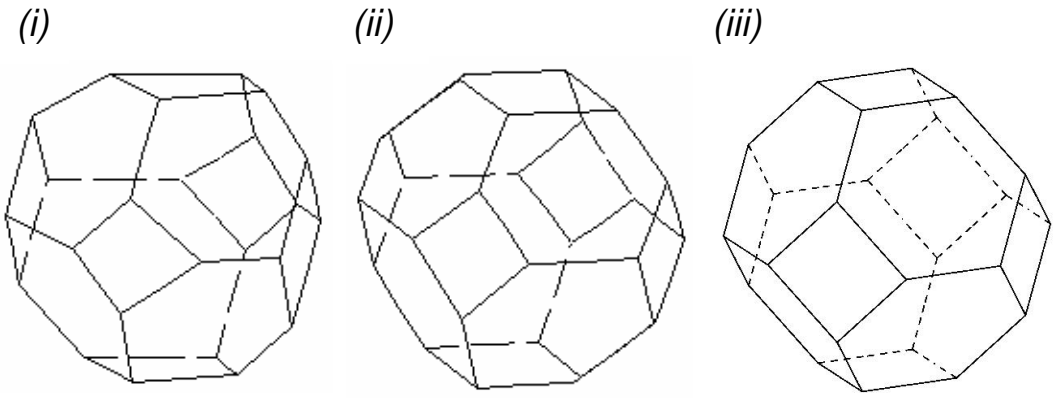

Figure 2.7 Voronoi-Dirichlet polyhedra representing packing topology in L-alanine at (*i*) ambient pressure and (*ii*) 9.87 GPa. The topology becomes more regular resembling that of the perfect BCC packing seen in tungsten (*iii*).

archetypal BCC topology of tungsten with L-alanine at 9.87 GPa. The similarity is striking.

At elevated pressures there is a thermodynamic need to fill space efficiently in order to minimise the pressure × volume contribution to free energy. The over-riding need to pack efficiently can lead to counter-intuitive results: in the phase transition from serine-II to serine-III at 8 GPa the H-bonds actually increase in length.[6, 14] In L-alanine it appears that efficient packing results in a particularly regular topology, normally seen for simple hard sphere structures. That this occurs for alanine and not other amino acids can perhaps be ascribed to its higher 'sphericity'. Blatov has shown that sphericity can be measured by the dimensionless second moment of inertia [designated G_3(mol)], which adopts a value of 0.0770 for a perfect sphere.[76, 78] The value for alanine at ambient pressure is 0.0807. By comparison values for glycine, serine and cysteine are 0.0811, 0.0822 and 0.0813, respectively. At the highest reported pressure of 9.87 GPa, the G_3 value for L-alanine is 0.0798.

2.4.5 Phase stability of L-alanine-d_7 to 10 GPa

Although diffraction methods form the best means for deriving precise geometric and structural data on the effect of pressure on crystalline materials, vibrational

spectroscopy has also been used to detect phase transitions. Dramatic changes in IR or Raman spectra have been shown to occur in some compounds, indicating that some substantial molecular rearrangement has occurred. For example, changes in all regions of the Raman spectra of $Mn_2(CO)_{10}$ at 0.5 GPa and in $Re_2(CO)_{10}$ at 0.8 GPa have been interpreted in terms of a change from a staggered to eclipsed conformation about the metal-metal bond.[79] Amongst the amino acids, the phase transitions in cysteine, serine and β-glycine have been observed in Raman spectra.[11, 15, 16]

In other cases the changes in the vibrational spectra are more subtle. A parameter typically extracted in high-pressure vibrational work is the gradient of a frequency *versus* pressure curve ($d\nu/dP$). A large value of this parameter for a particular mode implies that that the geometry of the moiety involved suffers a significant distortion with pressure, while discontinuities in the slopes of frequency versus pressure plots are taken to imply phase transitions. The relative intensities of Raman bands can also change with pressure, and discontinuities in intensity trends have been interpreted in terms of phase transitions.

The effect of pressure on L-alanine-h_7 and L-alanine-d_7 has been extensively studied by Freire and co-workers using Raman spectroscopy. A phase transition at 2.2 GPa was postulated for L-alanine-h_7 on the basis of a reversal in the trend in the relative intensities of low frequency librational bands and the appearance of a new band at 122 cm^{-1}.[30] This was supported by a change in the value of $d\nu/dP$ for other low-frequency bands.

Raman studies on L-alanine-d_7 indicated that the crystal went through the same transition as the h_7 isotopologue at *ca.* 1.5 GPa (not 2.2 GPa) as a consequence of deuteration.[31] This conclusion was based on the splitting of $\nu_{asym}(CD_3)$ and $\delta_{asym}(ND_3^+)$ at 2250 cm^{-1} and 1200 cm^{-1}, respectively, and the appearance of a new band at *ca.* 220 cm^{-1}. It was also suggested, also on the basis of trends in $d\nu/dP$, that a conformational change of the ND_3^+ group occurs at 4.4 GPa.

The presence of the phase transition in L-alanine-h_7 was supported by energy dispersive powder diffraction data.[32, 33] Though barely visible in the raw data, profile analysis suggested that 110/011 and 120/021 doublets in the low-pressure patterns merge into single peaks at 2.2 GPa, suggesting that the sample undergoes a structural

phase transformation from orthorhombic to tetragonal symmetry. The sample was said to remain in this phase up to 9 GPa.

We find no evidence for a phase transition around 2.2 GPa or 1.5 GPa in either L-alanine-h_7 or -d_7. For both L-alanine-h_7 and –d_7 the unit cell became *metrically* tetragonal at around 2 GPa, but the structure is a compressed form of the orthorhombic starting phase. The change in metric symmetry is the result of one cell dimension (*a*) being more compressible than another (*c*) as the result of the different distribution of H-bonds along these directions (see above). This partially explains the energy dispersive X-ray results, though we find that the trend continues as pressure increases, so that the orthorhombic metric symmetry is unambiguously re-established by 3 GPa.

In their first paper on L-alanine, Freire and co-workers mention the possibility that their spectroscopic results could be due to conformational changes, though they rejected this explanation in favour of their phase transition hypothesis.[30] Our data suggest that their first explanation is the correct one. Figure 2.5 shows the change in $\tau(NH_3^+)$ with pressure. Between 0.40 GPa and 1.03 GPa the torsion angle is relatively unchanged, but then begins to increase between 1.4 and 5.43 GPa, at which point it levels-off. The pressures at which these changes occur match Freire's observations on L-alanine-d_7 rather well, and suggest that the changes observed in the Raman spectra are probably associated with the on-set of changes in the torsion angle of the ammonium group. The change in $d\nu/dP$ seen in Raman spectra at 4.4 GPa may correspond to the 'levelling off' of the curve shown in Figure 2.5 which occurs at a similar pressure.

Freire and co-workers have shown that the NH_3^+ torsional vibrational mode is unusual in having a negative $d\nu/dP$ (-2 $cm^{-1}GPa^{-1}$), pointing to a weakening of the force constant at higher pressures.[67] They interpreted this as implying that the N-H···O bonds become less linear with pressure. Our own results support this explanation: the N1-H3···O2 bond angle decreases from 161.0(6)° to 141.5(4)° due to sliding between chains of molecules within each layer (see Figure 2.6 and the movie available in the supplementary material).

A second phase transition has been suggested on the basis of rather noisy energy dispersive X-ray powder data on L-alanine-h_7 to occur above 9 GPa [see

Figure 2c in [33]]. The diffraction data were indexed on a monoclinic unit cell with dimensions a = 10.159(18), b = 4.757(12), c = 7.282(13) Å, and β = 100.67(15)°. We find no evidence for this transition in our neutron powder data, though these were collected on a deuterated sample. If the conclusions based on the energy dispersive data are correct, then the effect seen here is an unusual example of isotopic polymorphism, also seen recently in pyridine[80] and in 4-methylpyridine pentachlorophenol.[81-83]

2.5 Conclusions

The effect of pressure on L-alanine has been studied in a joint X-ray and neutron diffraction study on the isotopically normal and perdeuterated derivatives. The bulk modulus was found to be 13.6(7) GPa, rather lower than values given elsewhere for other amino acids. It is likely that the difference is due to the use of too small a value of the pressure derivative $(\partial K/\partial P)_T$ in previous work.

No evidence was found for an orthorhombic to tetragonal phase transition at 1.5 GPa or 2.2 GPa, as had been suggested by other authors on the basis of Raman and energy dispersive X-ray powder diffraction. The unit cell is, however, approximately metrically tetragonal between 2 and 3 GPa. A second phase transition above 9 GPa suggested by the energy dispersive study on L-alanine-h_7 was not observed in the perdeuterated derivative. Changes in vibrational spectra which had previously been thought to be a consequence of a phase transition at *ca* 2 GPa are probably the result of changes in conformation and H-bonding at the ammonium group.

By 9.87 GPa N-H···O H-bond distances span the range 1.613(9) to 1.731(9) Å, and the crystal structure adopts what, for a molecular structure, is an unusually regular BCC topology. The highest pressure attained in the present work was 9.87 GPa and this is the highest pressure at which three dimensional structural data have been obtained for an amino acid.

2.6 References

1. S. A. Moggach, S. Parsons and P. A. Wood, *Crystallography Reviews*, 2008, **14**, 143-184.
2. S. A. Moggach and S. Parsons, *Spectroscopic Properties of Inorganic Organometallic Compounds*, 2009, **40**, 324-354.
3. F. P. A. Fabbiani and C. R. Pulham, *Chemical Society Reviews*, 2006, **35**, 932-942.
4. E. V. Boldyreva, *Acta Crystallographica, Section A: Foundations of Crystallography*, 2008, **A64**, 218-231.
5. A. Katrusiak, *Acta Crystallographica, Section A: Foundations of Crystallography*, 2008, **A64**, 135-148.
6. P. A. Wood, D. Francis, W. G. Marshall, S. A. Moggach, S. Parsons, E. Pidcock and A. L. Rohl, *CrystEngComm*, 2008, **10**, 1154-1166.
7. R. D. L. Johnstone, D. Francis, A. R. Lennie, W. G. Marshall, S. A. Moggach, S. Parsons, E. Pidcock and J. E. Warren, *CrystEngComm*, 2008, **10**, 1758-1769.
8. P. A. Wood, R. S. Forgan, D. Henderson, S. Parsons, E. Pidcock, P. A. Tasker and J. E. Warren, *Acta Crystallographica, Section B: Structural Science*, 2006, **B62**, 1099-1111.
9. A. Dawson, D. R. Allan, S. A. Belmonte, S. J. Clark, W. I. F. David, P. A. McGregor, S. Parsons, C. R. Pulham and L. Sawyer, *Crystal Growth & Design*, 2005, **5**, 1415-1427.
10. S. V. Goryainov, E. V. Boldyreva and E. N. Kolesnik, *Chemical Physics Letters*, 2006, **419**, 496-500.
11. S. V. Goryainov, E. N. Kolesnik and E. V. Boldyreva, *Physica B: Condensed Matter* 2005, **357**, 340-347.
12. E. V. Boldyreva, S. N. Ivashevskaya, H. Sowa, H. Ahsbahs and H.-P. Weber, *Zeitschrift für Kristallographie*, 2005, **220**, 50-57.
13. S. A. Moggach, D. R. Allan, C. A. Morrison, S. Parsons and L. Sawyer, *Acta Crystallographica, Section B: Structural Science*, 2005, **61**, 58-68.

14. S. A. Moggach, W. G. Marshall and S. Parsons, *Acta Crystallographica, Section B: Structural Science*, 2006, **B62**, 815-825.

15. E. V. Boldyreva, H. Sowa, Y. V. Seryotkin, T. N. Drebushchak, H. Ahsbahs, V. Chernyshev and V. Dmitriev, *Chemical Physics Letters*, 2006, **429**, 474-478.

16. S. A. Moggach, D. R. Allan, S. J. Clark, M. J. Gutmann, S. Parsons, C. R. Pulham and L. Sawyer, *Acta Crystallographica, Section B: Structural Science*, 2006, **B62**, 296-309.

17. S. A. Moggach, D. R. Allan, S. Parsons, L. Sawyer and J. E. Warren, *Journal of Synchrotron Radiation*, 2005, **12**, 598-607.

18. M. Yamashita, S. Inomata, K. Ishikawa, T. Kashiwagi, H. Matsuo, S. Sawamura and M. Kato, *Acta Crystallographica, Section E: Structure Reports Online*, 2007, **E63**, o2762-o2764.

19. C. Murli, S. M. Sharma, S. Karmakar and S. K. Sikka, *Physica B: Condensed Matter (Amsterdam, Netherlands)*, 2003, **339**, 23-30.

20. F. H. Allen, *Acta Crystallographica, Section B*, 2002, **58**, 380-388.

21. H. J. Simpson, Jr. and R. E. Marsh, *Acta Crystallographica*, 1966, **20**, 550-555.

22. J. D. Dunitz and R. R. Ryan, *Acta Crystallographica*, 1966, **21**, 617-618.

23. M. S. Lehmann, T. F. Koetzle and W. C. Hamilton, *Journal of the American Chemical Society*, 1972, **94**, 2657-2660.

24. R. Destro, R. E. Marsh and R. Bianchi, *Journal of Physical Chemistry A*, 1988, **92**, 966-973.

25. W. Q. Wang, Y. Gong, Z. Liang, F. L. Sun, D. X. Shi, H. J. Gao, X. Lin, P. Jiang and Z. M. Wang, *Surface Science*, 2002, **512**, L379-L384.

26. R. Sullivan, M. Pyda, J. Pak, B. Wunderlich, J. R. Thompson, R. Pagni, H. Pan, C. Barnes, P. Schwerdtfeger and R. Compton, *Journal of Physical Chemistry A*, 2003, **107**, 6674-6680.

27. C. C. Wilson, D. Myles, M. Ghosh, L. N. Johnson and W. Wang, *New Journal of Chemistry*, 2005, **29**, 1318-1322.

28. W. Wang, F. Yi, Y. Ni, Z. Zhao, X. Jin and Y. Tang, *Journal of Biological Physics*, 2000, **26**, 51-65.

29. J. Bernstein, R. E. Davis, L. Shimoni and N.-L. Chang, *Angewandte Chemie International Edition*, 1995, **34**, 1555-1573.

30. A. M. R. Teixeira, P. T. C. Freire, A. J. D. Moreno, J. M. Sasaki, A. P. Ayala, J. Mendes Filho and F. E. A. Melo, *Solid State Communications*, 2000, **116**, 405-409.

31. R. O. Gonçalves, P. T. C. Freire, H. N. Bordallo, J. A. Lima Jr, F. E. A. Melo, J. Mendes Filho, D. N. Argyriou and R. J. C. Lima, *Journal of Raman Spectroscopy* 2009, **40**, In press. DOI 10.1002/jrs.2209.

32. J. S. Olsen, L. Gerward, A. G. Souza Filho, P. T. C. Freire, J. Filho and F. E. A. Mendes Melo, *High Pressure Research*, 2006, **26**, 433-437.

33. J. S. Olsen, L. Gerward, P. T. C. Freire, J. Mendes Filho, F. E. A. Melo and A. G. Souza Filho, *Journal of Physics and Chemistry of Solids*, 2008, **69**, 1641-1645.

34. L. Merrill and W. A. Bassett, *Review of Scientific Instruments*, 1974, **45**, 290-294.

35. S. A. Moggach, D. R. Allan, S. Parsons and J. E. Warren, *Journal of Applied Crystallography*, 2008, **41**, 249-251

36. G. J. Piermarini, S. Block, J. D. Barnett and R. A. Forman, *Journal of Applied Physics*, 1975, **46**, 2774-2780.

37. A. Dawson, D. R. Allan, S. Parsons and M. Ruf, *Journal of Applied Crystallography*, 2004, **37**, 410-416.

38. Bruker-Nonius, *SAINT version 7, Program for integration of area detector data*, (2006).

39. G. M. Sheldrick, *SADABS Version 2008-1*, (2008) University of Göttingen, Göttingen, Germany.

40. R. H. Blessing, *Journal of Applied Crystallography*, 1997, **30**, 421-426.

41. ISIS, *ISIS 96 - ISIS Facility Annual Report 1995-96, Rutherford Appleton Laboratory*, 1996, **RAL-TR-96-050**, 61-62.

42. ISIS, *ISIS 97 - ISIS Facility Annual Report 1996-97, Rutherford Appleton Laboratory*, 1997, **RAL-TR-97-050**, 28-29.

43. W. G. Marshall and D. J. Francis, *Journal of Applied Crystallography*, 2002, **35**, 122-125.

44. F. Birch, *Physical Review*, 1947, **71**, 809-824.

45. A. D. Fortes, University of London, 2004.

46. A. Z. Kuznetsov, V. Dmitriev, L. Dubrovinsky, V. Prakapenka and H. P. Weber, *Solid State Communications*, 2002, **122**.

47. R. A. Miller and D. E. Schuele, *Journal of Physics and Chemistry of Solids*, 1969, **30**, 589-600.

48. D. L. Waldorf and G. A. Alers, *Journal of Applied Physics*, 1962, **33**, 3266-3269.

49. A. Coelho, *TOPAS-Academic: General Profile and Structure Analysis Software for Powder Diffraction Data. Version 4.1*, (2007), Brisbane, Australia.

50. R. H. Blessing, *Acta Crystallographica, Section B: Structural Science*, 1995, **B51**, 816-823.

51. S. J. Clark, M. D. Segall, C. J. Pickard, P. J. Hasnip, M. J. Probert, K. Refson and M. C. Payne, *Zeitschrift für Kristallographie.* , 2005, **220**, 567-570.

52. J. P. Perdew, K. Burke and M. Ernzerhof, *Physical Review Letters*, 1996, **77**, 3865.

53. D. Vanderbilt, *Physical Review B* 1990, **41**, 7892-7895.

54. H. J. Monkhorst and J. D. Pack, *Physical Review B*, 1976, **13**, 5188.

55. M. J. Frisch, G. W. Trucks, H. B. Schlegel, G. E. Scuseria, M. A. Robb, J. R. Cheeseman, J. A. Montgomery Jr., T. Vreven, K. N. Kudin, J. C. Burant, J. M. Millam, S. S. Iyengar, J. Tomasi, V. Barone, B. Mennucci, M. Cossi, G. Scalmani, N. Rega, G. A. Petersson, H. Nakatsuji, M. Hada, M. Ehara, K. Toyota, R. Fukuda, J. Hasegawa, M. Ishida, T. Nakajima, Y. Honda, O. Kitao, H. Nakai, M. Klene, X. Li, J. E. Knox, H. P. Hratchian, J. B. Cross, V. Bakken, C. Adamo, J. Jaramillo, R. Gomperts, R. E. Stratmann, O. Yazyev, A. J. Austin, R. Cammi, C. Pomelli, J. W. Ochterski, P. Y. Ayala, K. Morokuma, G. A. Voth, P. Salvador, J. J. Dannenberg, V. G. Zakrzewski, S. Dapprich, A. D. Daniels, M. C. Strain, O. Farkas, D. K. Malick, A. D. Rabuck, K. Raghavachari, J. B. Foresman, J. V. Ortiz, Q. Cui, A. G. Baboul, S. Clifford, J. Cioslowski, B. B. Stefanov, G. Liu, A. Liashenko, P. Piskorz, I. Komaromi, R. L. Martin, D. J. Fox, T. Keith, M. A. Al-Laham, C. Y. Peng,

A. Nanayakkara, M. Challacombe, P. M. W. Gill, B. Johnson, W. Chen, M. W. Wong, C. Gonzalez and J. A. Pople, *Gaussian 03, Revision E.01*, (2003) Gaussian, Inc., .

56. A. Gavezzotti, *Zeitschrift für Kristallographie*, 2005, **220**, 499-510.
57. A. Gavezzotti, *Molecular Aggregation: Structure Analysis and Molecular Simulation of Crystals and Liquids*, Oxford University Press, Oxford, UK, 2007.
58. A. Gavezzotti, *OPiX: A computer program package for the calculation of intermolecular interactions and crystal energies.*, (2003), University of Milan, Italy.
59. C. F. Macrae, I. J. Bruno, J. A. Chisholm, P. R. Edgington, P. McCabe, E. Pidcock, L. Rodriguez-Monge, R. Taylor, J. van de Streek and P. A. Wood, *Journal of Applied Crystallography*, 2008, **41**, 466-470
60. K. Brandenburg and H. Putz, *DIAMOND, version 3.2, Visual crystal structure information system*, (2005) Crystal Impact, Bonn, Germany.
61. CrystalMaker, *A crystal and molecular structures program for MAC and Windows.*, (2009), Oxford, UK.
62. V. A. Blatov, A. P. Shevchenko and V. N. Serezhkin, *Journal of Applied Crystallography*, 2000, **33**, 1193.
63. R. J. Angel, *EOSFIT version 5.2*, (2002) Virginia Tech, Blackburg, VA, USA.
64. R. J. Angel, *Reviews in Mineralogy and Geochemistry*, 2002, **41**, 35-59.
65. P. Vinet, J. H. Rose, J. Ferrante and J. R. Smith, *Journal of Physics: Condensed Matter*, 1989, **1**, 1941-1963.
66. P. Vinet, J. R. Smith, J. Ferrante and J. H. Rose, *Physical Review B: Condensed Matter*, 1987, **35**, 1945-1953.
67. P. T. C. Freire, F. E. A. Melo, J. Mendes Filho, R. J. C. Lima and A. M. R. Teixeira, *Vibrational Spectroscopy*, 2007, **45**, 99-102.
68. S. E. Ashbrook, M. Cutajar, J. M. Griffin, Z. A. D. Lethbridge, R. I. Walton and S. Wimperis, *Journal of Physical Chemistry C* 2009, **113**, 10780-10789.
69. S. E. Ashbrook, M. Cutajar, C. J. Pickard, R. I. Walton and S. Wimperis, *Physical Chemistry Chemical Physics*, 2008, **10**, 5754-5764.

70. D. L. Bryce, E. B. Bultz and D. Aebi, *Journal of the American Chemical Society*, 2008, **130**, 9282-9292.

71. N. Mifsud, B. Elena, C. J. Pickard, A. Lesage and L. Emsley, *Physical Chemistry Chemical Physics*, 2006, **8**, 3418-3422.

72. C. M. Widdifield and D. L. Bryce, *Physical Chemistry Chemical Physics*, 2009, **11**, 7120-7122.

73. R. D. L. Johnstone, A. R. Lennie, S. F. Parker, S. Parsons, E. Pidcock, P. R. Richardson, J. E. Warren and P. A. Wood, *CrystEngComm*, 2010, **12**, 1065-1078

74. C. Slebodnick, J. Zhao, R. Angel, B. E. Hanson, Y. Song, Z. Liu and R. J. Hemley, *Inorganic Chemistry*, 2004, **43**, 5245-5252.

75. P. Lozano-Casal, D. R. Allan and S. Parsons, *Acta Crystallographica, Section B: Structural Science*, 2008, **64**, 466-475.

76. E. V. Peresypkina and V. A. Blatov, *Acta Crystallographica, Section B*, 2000, **56**, 501-511.

77. E. V. Peresypkina and V. A. Blatov, *Acta Crystallographica, Section B*, 2000, **56**, 1035-1045.

78. E. V. Peresypkina and V. A. Blatov, *Journal of Molecular Structure: THEOCHEM*, 1999, **489**, 225-236.

79. D. M. Adams, P. D. Hatton and A. C. Shaw, *Journal of Physics: Condensed Matter*, 1991, **3**, 6145-6158.

80. S. Crawford, M. T. Kirchner, D. Blaeser, R. Boese, W. I. F. David, A. Dawson, A. Gehrke, R. M. Ibberson, W. G. Marshall, S. Parsons and O. Yamamuro, *Angewandte Chemie, International Edition*, 2009, **48**, 755-757.

81. Z. Malarski, I. Majerz and T. Lis, *Journal of Molecular Structure*, 1987, **158**, 369-377.

82. Z. Malarski, I. Majerz and T. Lis, *Journal of Molecular Structure*, 1996, **380**, 249-256.

83. J. Zhou, Y.-S. Kye and G. S. Harbison, *Journal of the American Chemical Society*, 2004, **126**, 8392-8393.

Chapter 3

Alanine at 13.6 GPa and its Pressure-Induced Amorphisation at 15 GPa*

*Nicholas P. Funnell, William G. Marshall and Simon Parsons, *CrystEngComm*, (2011), 13(19), 5841-5848

3.1 Introduction

The crystal structures of amino acids at high pressure have been systematically investigated by several groups. They are attractive systems to study crystallographically as, though they have relatively simple structures, they possess several types of intermolecular interaction including hydrogen bonding, Coulombic and dispersion attractions. The Coulombic interactions, which are of particular importance at long range, occur by virtue of the fact that the amino acids crystallise as zwitterions.

Summaries of work done on amino acids at high pressure are available in a number of review articles.[1-4] Some amino acids undergo pressure-induced phase transformations. The β-polymorph of glycine transforms to a δ-phase[5] (designated β' in refs 6-8) at 0.8 GPa. The γ-polymorph transforms sluggishly to a different high-pressure phase, designated ε by us and δ by Boldyreva, at a pressure and rate which depends on the sample; the transformation is usually complete by about 4 GPa. On decompression the ε phase transforms back to the γ phase via an intermediate ζ phase not seen during compression.[6] Other transitions have been observed in L-serine,[7-12] L-cysteine,[13] DL-cysteine,[14] serine hydrate[15] and the tripeptide glutathione.[16]

By contrast to the other polymorphs of glycine, the α-phase does not undergo any transitions at all, even, according to Raman spectra, up to 20 GPa.[17] Alanine (Figure 3.1),[18, 19] aspartic acid,[20] glutamine,[21] threonine,[22] glycyl-glycine,[23] alanyl-valine,[24] cystine,[25] asparagine monohydrate[20] and DL-serine[26] are also examples of amino acids and short peptides which have so far resisted attempts to induce a phase transition by applying pressure. The highest pressure crystallographic data are available for alanine. We have described a joint single-crystal X-ray and neutron powder diffraction study of alanine up to 9.85 GPa;[18] Boldyreva recently reached an even higher pressure, 12.3 GPa, in an X-ray powder diffraction study.[19] Previous Raman and dispersive X-ray powder diffraction work had suggested that transitions occurred at 2 and 9 GPa,[27-32] but neither was observed in Boldyreva's or our own studies.

Though structures like α-glycine and alanine thus appear to be very robust towards compression, surely *something* must happen to them if pressure continues to

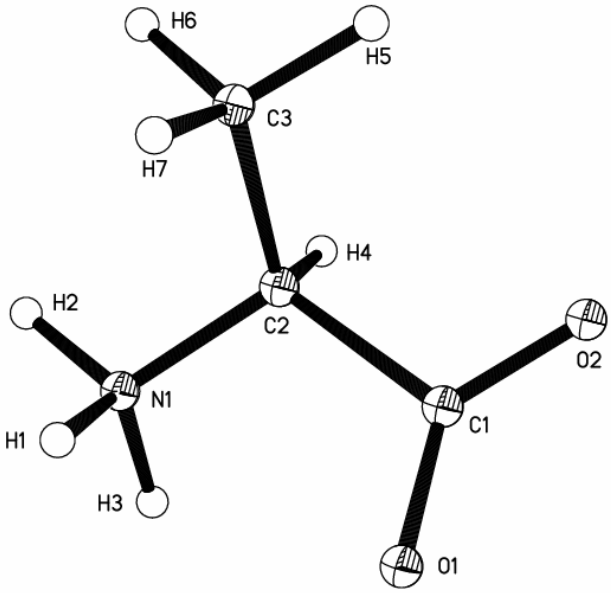

Figure 3.1 Molecular structure diagram of L-alanine showing the numbering scheme used.

be increased. In this paper we describe a neutron powder diffraction study of alanine up to 15 GPa, the highest pressure for which diffraction data have been collected on an amino acid, or indeed, any organic system, other than benzene.[33]

3.2 Experimental

3.2.1 Sample preparation

The neutron powder diffraction measurements were carried out with L-alanine-d_7 obtained from CDN isotopes and was used as supplied.

3.2.2 High-pressure neutron powder diffraction

Powdered L-alanine-d_7 was loaded into a double toroid TiZr capsule gasket mixed in a 5:4 ratio by mass with MgO, which was used as a pressure marker.[36] A 4:1 mixture of deuterated methanol and ethanol was used as a hydrostatic medium. Neutron data were collected using the time-of-flight technique on the PEARL instrument at ISIS.[37, 38] Data sets were collected between ambient pressure and 15.46 GPa in the range $0.6 < d < 4.1$ Å using a V4b-type Paris-Edinburgh press equipped with sintered

diamond double toroid anvils.[39, 40] The temperature of the press was varied by means of resistive band heaters attached to the breech and the cylinder housing.

Data were collected at ambient pressure and temperature and then at 3.91, 7.61 and 8.72 GPa. Above 9 GPa it was necessary to warm the sample in order to maintain hydrostatic conditions (see below),[41] and further data were collected at the following pressure/temperature points: 9.96 GPa/32°C, 11.74 GPa/42°C, 13.15 GPa/67°C, 13.60 GPa/67°C and 15.46 GPa/80°C. After collecting data at 15.46 GPa the pressure and temperature were decreased to 1.59 GPa and 27°C and another pattern was collected.

A powder diffraction profile suitable for refinement was obtained after focusing the 1080 individual detector element spectra of the $2\theta=90^{o}$ bank, normalisation of the summed pattern with respect to the incident beam monitor and the scattering from a standard vanadium sample and, finally, a correction for the wavelength and scattering-angle dependence of the neutron attenuation by the anvil and gasket materials (Figure 3.2). Only the central 50% of the detector elements in the 90° bank were used as an intense diamond signal dominated the powder pattern when all the elements were used. This intense Bragg peak overlapped with MgO reflections, making pressure calculation less reliable.

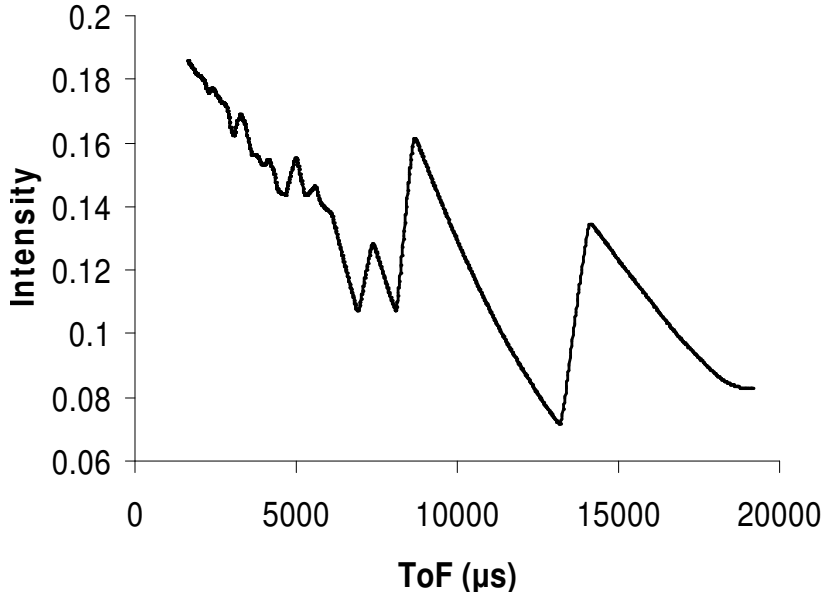

Figure 3.2. Plot of the function used to correct for incident and scattered neutron beam attenuation by the sintered-diamond double-toroid anvil materials.

The pressures quoted were calculated from the refined MgO cell parameter using a Birch-Murnaghan equation of state with V_0 = 74.76856 Å^3, K_0 = 160 GPa and K' = 4.2.[42]

3.4.3 Structure refinement

Starting values for the unit cell dimensions and fractional coordinates were taken from Ref 20.

The Pawley method was used to extract unit cell dimensions from the data sets at 0, 3.91, 7.61, 8.72 and 9.96 GPa (TOPAS Academic).[43] Structures in this range have been previously reported,[20] and these data were not analysed further.

Rietveld refinements of L-alanine at 11.74 and 13.60 GPa were based on the Z-matrix formalism in TOPAS. This allows the refinement to be parameterised in terms of bond distances and angles rather than fractional atomic coordinates. The model used is described in detail in our previous paper.[20] As we also described previously, the fractional coordinates of the refinement model were restrained to values obtained from periodic density functional theory (DFT) calculations (see below). Common isotropic thermal parameters were used for non-H and H atoms. The line shape function consisted of two back-to-back exponentials convoluted with a pseudo-voigt. Peaks from the diamond and MgO were modelled with the Pawley method.

The final fits to the data are shown in Figure 3.3; refinement data are given in Table 3.1. CIFs for both of these structures are available in the ESI.

3.4.4 Periodic DFT calculations

The restraints referred to in the previous section were obtained by optimising the structures of L-alanine at 11.74 and 13.60 GPa using periodic DFT calculations performed using the plane-wave pseudopotential method as implemented in CASTEP.[44] The PBE exchange-correlation functional was used[45] with Vanderbilt ultra-soft pseudopotentials[46] and a basis set cut-off energy of 600 eV. A correction for dispersion effects[47] was found to make little difference to the results, and was therefore not applied. Brillouin zone integrations were performed on a symmetrized Monkhorst-Pack[48] *k*-point grid of dimensions $4 \times 2 \times 4$. The total energy

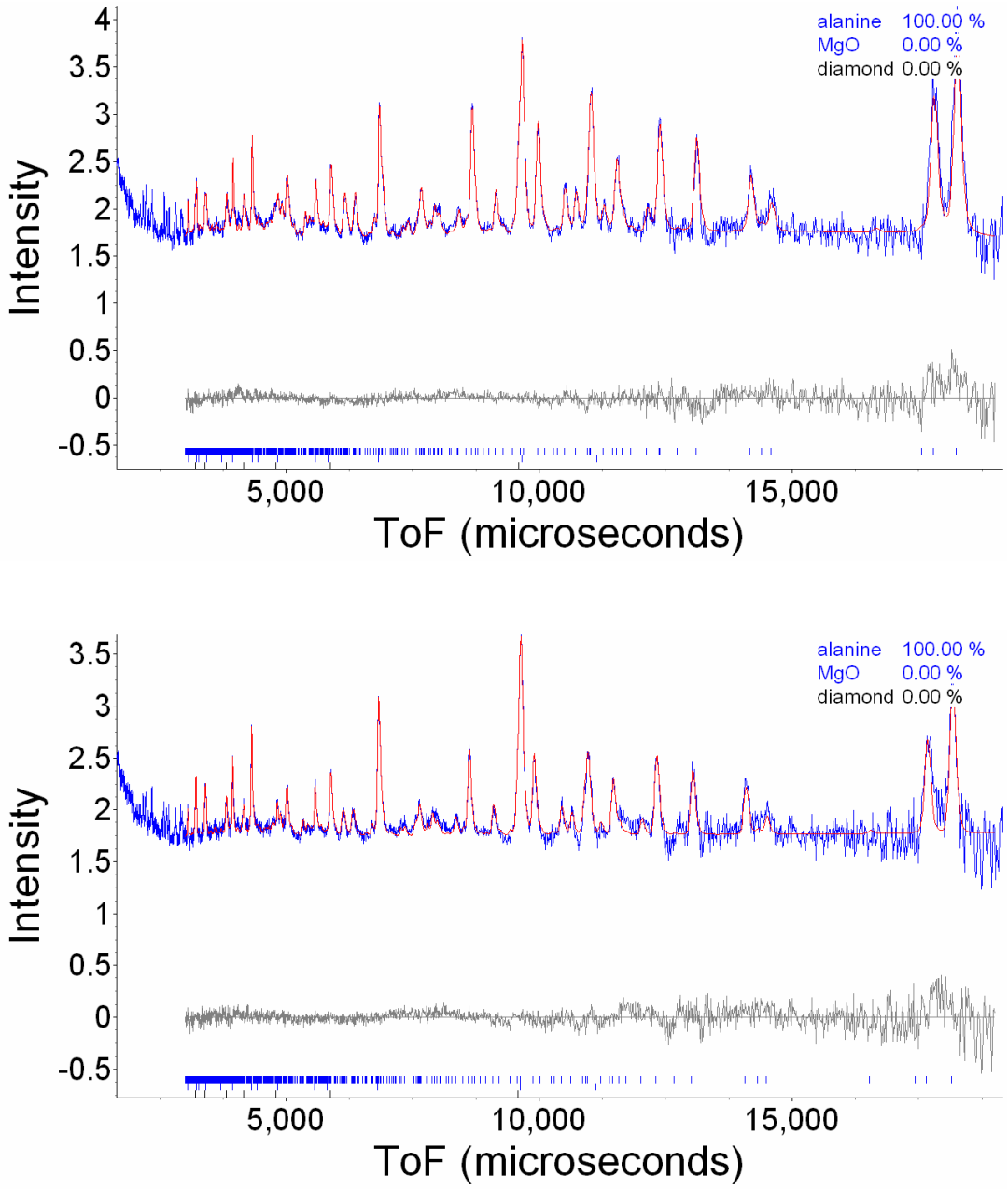

Figure 3.3 Rietveld fits to the powder pattern data at 11.74 GPa (top) and 13.60 GPa (bottom). The minimum and maximum d-spacing used for both sets of data are 0.6 and 4.1 Å respectively

Table 3.1. Crystal refinement data for the structures at 11.74 and 13.60 GPa

Pressure / GPa, temperature / K	11.74, 315	13.60, 340
Formula	$C_3D_7NO_2$	$C_3D_7NO_2$
M_r / g mol^{-1}	96.02	96.02
Crystal system, space group	Orthorhombic, $P2_12_12_1$	Orthorhombic, $P2_12_12_1$
a-axis / Å	5.1829(5)	5.1362(7)
b-axis / Å	11.1940(12)	11.1258(19)
c-axis / Å	5.4388(5)	5.4146(8)
V / Å^3	315.54(6)	309.41(8)
Z	4	4
D_c / Mg m^{-3}	2.021	2.061
d_{max}, d_{min} / Å	0.6, 4.1	0.6, 4.1
Pawley R_{wp}	3.496	4.027
R_{wp}	4.672	4.922
S	1.320	1.266
Reflection / profile data	2442	2442

convergence tolerance was 10^{-5} eV per atom, with a maximum force tolerance of 0.03 eV Å^{-3}, a maximum displacement of 0.001 Å and a maximum stress tolerance of 0.05 GPa. The fractional coordinates of all atoms were allowed to optimise while holding the unit cell dimensions fixed to values obtained from Pawley fits to the experimental neutron diffraction data. These conditions are the same as those used in our previous work on alanine. The starting coordinates were obtained from a refined structure at 9.86 GPa also taken from our previous study.

3.4.5 PIXEL calculations

Electron densities were calculated for the structures at 11.74 and 13.60 GPa using the program GAUSSIAN03[49] at the MP2 level of theory with the 6-31G** basis set. The density information was then used in the PIXEL[50-52] method to calculate the principal intermolecular contact energies in alanine. The calculations are based on a cluster of molecules which is built up around a central reference molecule. The interaction energy between the reference molecule and each molecule within the cluster is

calculated as the sum of four terms which account for the Coulombic, polarisation, dispersion and repulsion contributions. The sum of these energies is an estimate of the lattice energy. In the present calculations the radius of the cluster was 12 Å as we were interested only in interaction energies in the immediate environment of the reference molecule; a full lattice energy calculation would have required a substantially larger radius than this. Further details on PIXEL calculations are available in Gavezzotti's papers.

3.4.6 Other programs used

Crystal structures were visualised and contact-surface voids were calculated using MERCURY CSD 2.3[53] with a probe radius of 0.2 Å and an approximate grid spacing of 0.1 Å. Cambridge Structural Database[54] searches were carried out using the program CONQUEST[55] with database updates up to November 2010. The bulk modulus was calculated using the program EOSFIT.[56] Hirshfeld fingerprint plots were calculated with CrystalExplorer 2.1.[57] Geometrical calculations were carried out with PLATON.[58]

3.5 Results

3.5.1 The effect of pressure on L-alanine-d_7

The crystal structure of alanine consists of corrugated layers in which molecules are connected by N-H···O H-bonds between ammonium and carboxylate groups; the layers are connected by more N-H···O H-bonds into a three-dimensional network. A more detailed description has been given elsewhere.[20, 59-61]

On increasing pressure to 13.60 GPa, the structure of L-alanine-d_7 remained in a compressed form of the ambient phase (Figure 3.4). The *a, b* and *c*-axes compressed by 14.66 %, 9.77 % and 6.37 %, respectively. The molecular volume (= unit cell volume/number of molecules per cell) decreased by 27.90% over this range. Plots of the cell axes and volume as a function of pressure are shown in Figure 3.5. No abrupt discontinuities in trend were seen even though the temperature of the sample was raised above room temperature for the highest pressure points. The shape of the curve for the *b*-axis at low pressure is different from those of the *a* and *c*-axes, being slightly convex. This is due to a change in mode of compression along

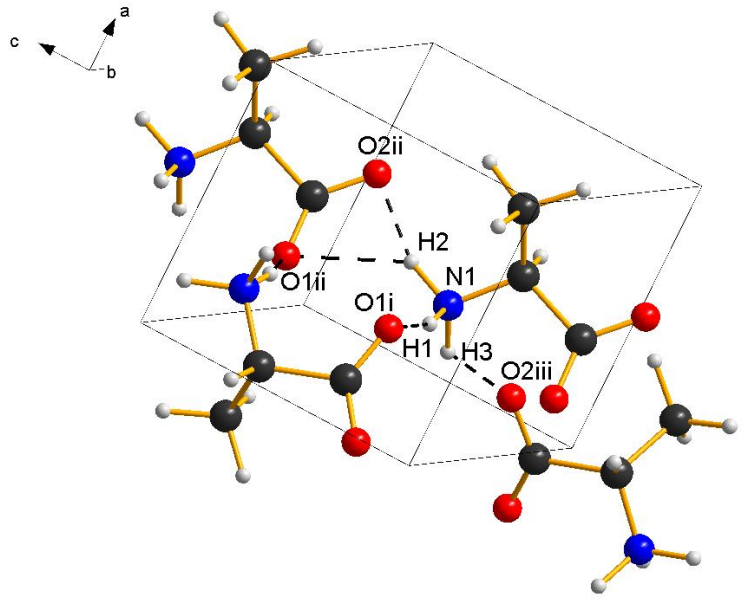

Figure 3.4 The crystal structure of L-alanine at 13.60 GPa. The crystal packing is simply a more compressed version of the ambient form. *Symmetry operators*: *i 3/2-x,-y,-1/2+z. ii x,y,-1+z. iii 1/2+x,1/2-y,-1-z*

this direction as pressure is increased. Initially the response to pressure is reorientation of the ammonium group; above 0.76 GPa the layers start to slide over each other.

Using the pressure vs volume data derived from previous neutron diffraction experiments in combination with those obtained in this study, the bulk modulus of L-alanine has been re-calculated. The bulk modulus (K_0), refined using a 3rd order Birch-Murnaghan equation of state,[62, 63] is 13.1(6) GPa. The values of V_0 and K' refined to 431.1(11) Å^3 and 7.1(3) respectively. These data are in good agreement with those obtained in our previous study of L-alanine to 10 GPa (K_0 = 13.4(7) GPa, V_0 = 429.13(7) Å^3, K' = 7.0(3)).

On increasing pressure to 15.46 GPa the material became amorphous, the powder pattern showing only the Bragg peaks corresponding to diamond and MgO. When the pressure was decreased to 1.59 GPa, the L-alanine reflections reappeared. Powder patterns for selected pressures in the sequence 0 → 15.46 → 1.59 GPa are shown in Figure 3.6.

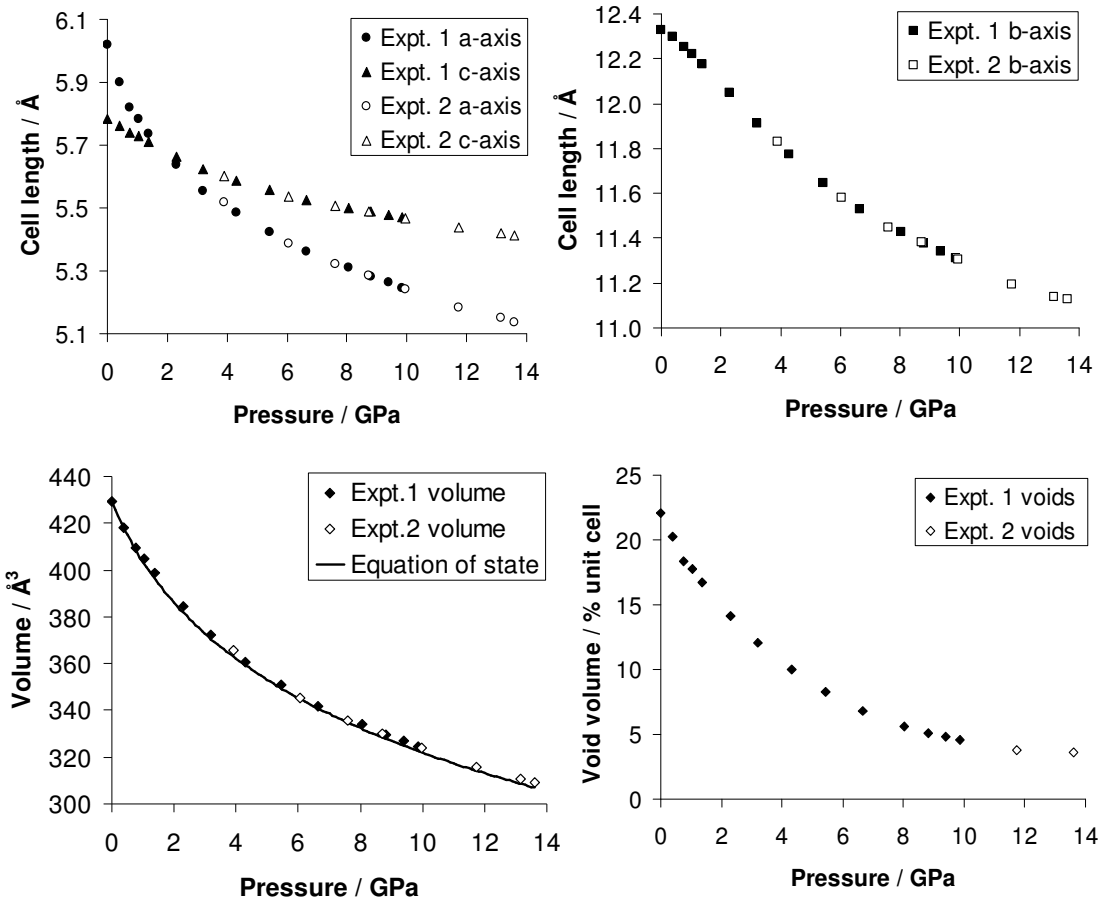

Figure 3.5. Plots of the unit cell axes and volume as a function of pressure. *a*- and *c*-axes are shown in the upper left plot, *b*-axes in the upper right, molecular volume in the lower left and void volume in the lower right. Data from our previous study (Expt. 1) and from this investigation (Expt. 2) are plotted in filled and open symbols respectively. A third-order Birch-Murnaghan equation of state is displayed on the volume plot. The standard deviations are within the size of the data points.

3.5.2 The effect of pressure on hydrogen bonding

Under ambient conditions, three hydrogen bonds form between the ammonium group and oxygen atoms of 3 neighbouring carboxylate groups. At ambient pressure the H-bonds, N1-H1···O1, N1-H2···O2 and N1-H3···O2, measure 1.861(6), 1.767(6) and 1.820(8) Å, respectively (obtained from Cambridge Structural Database; Refcode LALNIN12).[60] At 13.60 GPa corresponding data are 1.69(2), 1.754(3) and 1.763(2) Å. Details on hydrogen bond lengths and angles at ambient pressure, 11.74 and

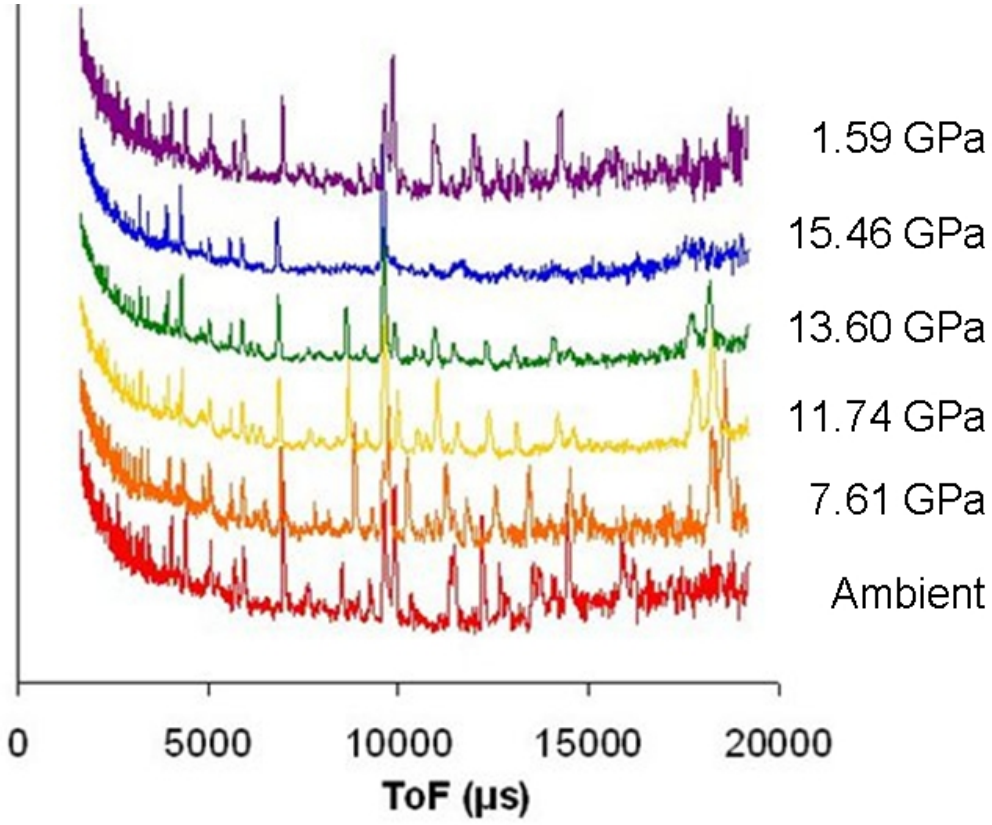

Figure 3.6 L-alanine powder patterns at selected pressures. At 15.46 GPa, the sample becomes amorphous; the only remaining Bragg peaks are from the MgO and diamond. Upon subsequent decompression to 1.59 GPa, the L-alanine reflections return. The pattern at 15.46 GPa was not corrected for attenuation by the diamond anvils as Rietveld refinement was not possible. For ease of comparison, the uncorrected patterns are shown for the other pressures.

13.60 GPa are given in Table 3.2. A short C3-H5···O1 distance measuring 2.02 Å is present at 13.6 GPa.

3.6 Discussion

3.6.1 Maintaining hydrostatic conditions with MeOH:EtOH above 10 GPa

In practice it is rare when studying organic and metal-organic systems to exceed a pressure of 10 GPa. Usually this is because the samples become amorphous or otherwise degrade at a lower pressure. A further reason is that the hydrostatic media most commonly and conveniently used become non-hydrostatic at higher pressures.

Table 3.2. Hydrogen bond parameters at ambient pressure (LALNIN12), 11.74 and 13.60 GPa[a]. The values given for the ambient structure (LALNIN12) have been obtained from ref [60] where details of the N1-H2···O1 parameters are not provided. The values used here have been calculated from a Crystallographic Information File of LALNIN12 using PLATON.

Pressure/GPa	Ambient	11.74	13.60
N1-H1···O1^{i}/Å	1.861(3)	1.606(14)	1.69(2)
<N1-H1-O1^{i}/°	160.9(2)	163.8(8)	160.8(14)
N1-H2···O2^{ii}/Å	1.780(2)	1.720(16)	1.754(3)
<N1-H2-O2^{ii}/°	168.1(2)	160.7(8)	159.8(13)
N1-H3···O2^{iii}/Å	1.828(3)	1.763(14)	1.763(2)
<N1-H3-O2^{iii}/°	163.7(2)	138.7(7)	136.3(12)
N1-H2···O1^{ii}/Å	2.52	2.221(14)	2.19(2)
<N1-H2-O1^{ii}/°	133	129.3(7)	131.4(11)

[a] *Symmetry operators: i 3/2-x,-y,-1/2+z. ii x,y,-1+z. iii 1/2+x,1/2-y,-1-z*

For example, a 4:1 mixture of methanol-ethanol, which remains hydrostatic to 10.5 GPa as determined by the ruby fluorescence method.[64]

That the present experiments could have been carried out at all is owed to Klotz *et al.*,[41] who have developed a method to reach hydrostatic pressures of *ca.* 17 GPa using methanol-ethanol as a pressure-transmitting medium. Heating the cell by *ca.* 11 K per 1 GPa pressure increment prevents the methanol-ethanol from pressure-freezing; maintaining the hydrostatic nature of the medium at elevated pressures. These conditions can be achieved on the PEARL instrument at ISIS using a Paris-Edinburgh cell with band heaters.

3.6.2 Phase behaviour and compression of intermolecular contacts in L-alanine

Our data show that no solid-solid phase transformations occur up to 13.60 GPa. It has already been established that a proposed orthorhombic-to-tetragonal transition at *ca.* 2.2 GPa[30-33] is due to the *a* and *c*-axes becoming metrically equal, arising from a difference in their relative compressibilities.[20, 21] A transition to a monoclinic phase

at *ca.* 9 GPa has been suggested on the basis of energy dispersive powder X-ray data.[31, 33] However, we find no evidence for this form of L-alanine either, in agreement with results published by Tumanov *et al.*[21]

At the highest pressure in this study (13.60 GPa for the crystalline phase), the shortest H-bond is 1.69(2) Å. A histogram of N-H···O contacts within the category 'amino acids, peptides and complexes' in the Cambridge Structural Database is shown in Figure 3.7. Although an N-H···O contact of 1.69(2) Å lies at the lower end of this histogram, it cannot be considered as being abnormally short, as there are 61 structures with N-H···O contact distances of 1.6-1.7 Å and 16 with 1.5-1.6 Å.

The compression of the H-bonds was quantified energetically with PIXEL calculations which compute intermolecular energies in the solid state.[51, 52, 65] The strongest intermolecular interactions at ambient pressure are the hydrogen bonds N1-H3···O2, N1-H2···O2 and N1-H1···O1 which have total intermolecular energies of -148.4, -122.7 and -29.8 kJ mol^{-1} respectively, at ambient conditions. These change by +25.3, +12.9 and -2.1 kJ mol^{-1} over the course of compression to 13.60 GPa. The differences can be traced to a net increase in repulsive energy (which increases by +105.9, +77.5 and +58.7 kJ mol^{-1} respectively). The repulsion is largely balanced by the increasingly negative sum of the remaining attractive components, in particular

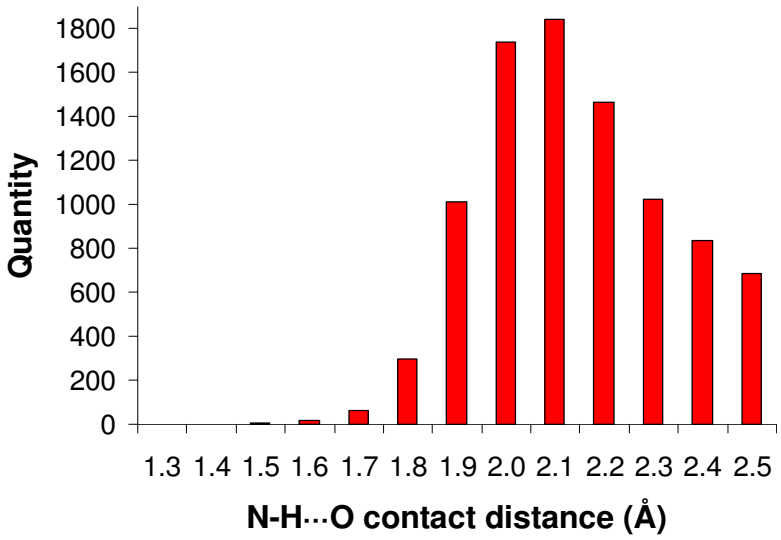

Figure 3.7 Distribution of N-H···O contact distances for 'amino acids, peptides and complexes' in the Cambridge Structural Database.

the Coulombic interactions. Tables containing complete details of PIXEL energies for each hydrogen bond at pressure points between ambient pressure and 13.60 GPa can be found in the ESI.

Analysis of H···H contacts reveals that these are not unusually short either. Hirshfeld fingerprint plots[66] for L-alanine at ambient pressure (LALNIN12)[60] and 13.60 GPa are shown in Figure 3.8. The diffuse regions of points at long values of d_e/d_i in the ambient-pressure plot are a consequence of voids in the structure, and these are much reduced at high pressure, as expected. The outer 'spikes' of the plot are typical of N-H···O interactions, and the regions of the fingerprint that lie on the diagonal correspond to H···H contacts. These naturally become shorter on compression. At 13.60 GPa, there are two H···H contacts that are shorter than the sum of their van der Waals radii, measuring 2.03(2) and 2.10(3) Å. However, shorter H···H contacts have been seen in other amino acids such as L-serine II at 5.2 GPa[10, 11] (shortest H···H contact distance, 1.91 Å), and none approach 1.7 Å, a practical limit identified by Wood *et al.*[67] in organic crystal structures under pressures of up to 10 GPa.

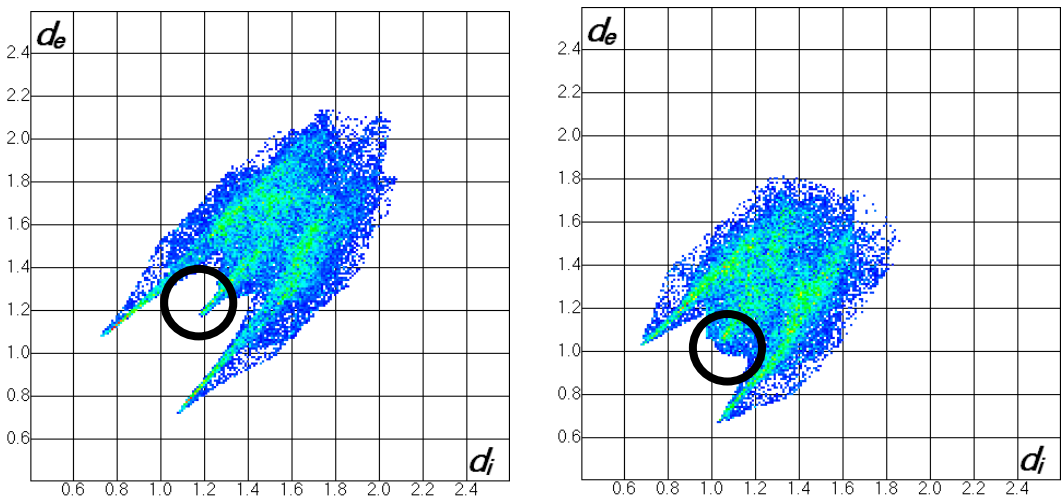

Figure 3.8 Hirshfeld fingerprint plot of L-alanine at ambient pressure (left) and 13.60 GPa (right). The circled regions indicate the shortest H···H contacts

3.6.3 Pressure-induced amorphisation

Above 15 GPa and 80°C, the sample transformed to an amorphous phase. Decompression of the sample at room temperature reveals that the transition is reversible. At 1.59 GPa / 27 °C, the crystalline phase was re-established and could be indexed on an orthorhombic cell (a = 5.721(3) Å, b = 12.155(3) Å, c = 5.695(2) Å).

Pressure-induced amorphisation is a widely-studied phenomenon in ice and in minerals and other extended solids.[68] Since it is generally associated with volume collapse it is currently of interest in the field of porous solids such as zeolites[69, 70] and metal-organic frameworks.[71] It has hardly been investigated in any detail at all in organic molecular systems. One notable exception is benzene, which transforms to amorphous hydrogenated carbon;[72] the transition pressure for this reaction depends on temperature, but, for example, occurs at 33 GPa and 423 K. The mechanism of the transition has been modelled using molecular dynamics, revealing the importance of short intermolecular distances which occur as molecules vibrate.

The paucity of data on pressure-amorphised molecular materials in part just reflects the generally more extensive high-pressure work that has been carried out on non-molecular solids. It also reflects the difficulty of extracting structural information on amorphous molecular solids. Vibrational spectra which have provided valuable insights into other amorphous systems tend to be very broad and featureless in amorphised organics. In this context, recent advances in total scattering methods, which are beginning to be applied to framework materials,[69] should enable a much more detailed picture of pressure-amorphised molecular solids to be obtained.

PIXEL and Hirshfeld surface analysis suggests that the amorphisation is not driven by relief of destabilising contacts, implying that the process is driven by minimisation of the pressure x volume contribution to the free energy. In molecular organic materials, the effects of pressure are usually taken up by voids in the structure as these require significantly less energy to compress than covalent bonds. Calculation of the contact-surface void space[53] using Mercury CSD shows that under ambient conditions the voids comprise 22.1% of the unit cell volume. At 13.60 GPa, the voids occupy only 3.6 %, corresponding to 11.11 $Å^3$ of the total cell volume at this pressure. A plot of the total void volume, expressed as a percentage of the unit

cell volume, as a function of pressure is shown in Figure 3.5. The data trend suggests that reduction in volume of interstitial voids occurs until *ca.* 14 GPa where it levels off. Beyond this point it appears that the structure of the crystalline phase can not sustain further volume decrease. The only way for the alanine molecules to access the remaining void space is to transform to a different phase, in this case by disrupting the long-range order of the structure and collapsing the volume.

3.6.4 The effect of pressure on N-H and C-O bond distances

In their recent work on alanine Tumanov *et al.*[21] noted that the C-O bond lengths are different at ambient pressure, but become more similar as pressure increases. This observation was based on single-crystal X-ray diffraction data, and though no two pairs of C-O distances ever differ to a level of statistical significance (i.e. by more that 3σ), there is a discernable trend in the data depicted in Figure. 4a of Tumanov et al.'s paper, reproduced here in Figure 3.9. The suggested change is also consistent with shifts in the C-O stretching frequencies measured by Raman spectroscopy.

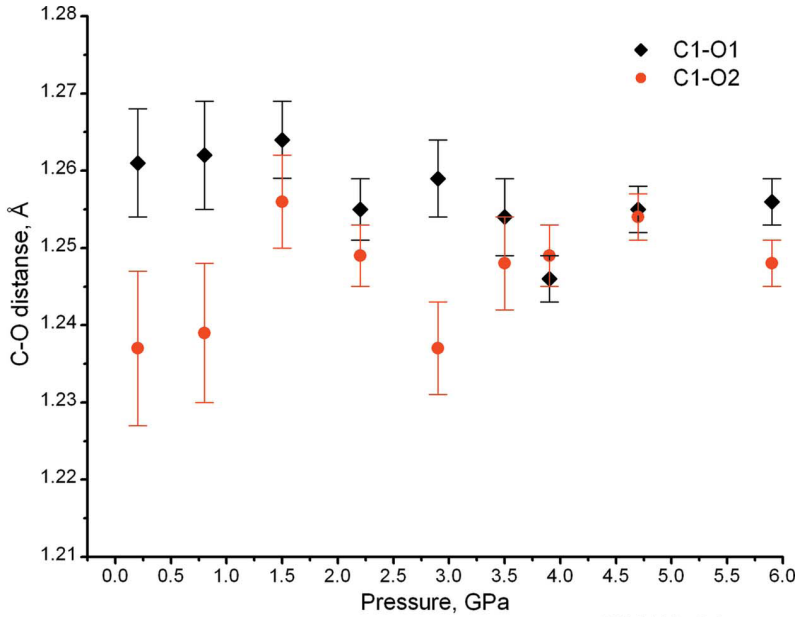

Figure 3.9 Variation in C-O bond distances reported by Tumanov *et al* [21]

In the case of the weakest H-bond, N1-H1···O1, which is formed approximately perpendicular to the CO_2 plane, the C1-O1 distance increases in length as the H-bond distance decreases.[1] This, along with an increase in the N-H bond length, is what would normally be expected. By contrast, the C1-O2 bond, which forms the two strongest H-bonds involving H2 and H3, decreases in length. This unusual effect was interpreted[21] in terms of changes in position of the H-atom with pressure. The decrease in the C1-O2 distance was associated with a shortening of the N-H bond because of the zwitterionic character of alanine in the solid state. Tumanov et al. explained this idea by reference to the limit of dissociation, which would cause the ammonium to become deprotonated, and the carboxylate oxygen to become protonated with an increase in C-O distance: hence a long C-O bond is associated with a long N-H bond and vice versa.

The changes in N-H and C-O distance would not be observed in the structures reported here or in ref. [20] as average values for these parameters were refined; the changes are anyway too small to be seen in structures derived from medium-resolution neutron powder data. However we do see in the DFT optimisations small, but consistent bond length changes with similar trends to those suggested by Tumanov et al. Table 3.3 shows that C1-O1 and N1-H1 increase in length, while C1-O2 and N1-H2/3 decrease. The lengths of the optimised C-O distances are *ca* 0.02 Å longer than those seen experimentally. One source for this difference may be underestimation of X-ray distances because of thermal motion or asymmetry of electron density. A more important source is probably inaccuracy in the level of theory used: Koch and Holthausen[73] report that overestimation of C-C and C-O multiple bond distances by up to 0.02 Å is typical in DFT calculations. Tumanov *et al.*'s data suggest that both C-O distances change by about 0.01 Å; the theoretical values for C1-O1 and C1-O2 are 0.002 and -0.009 Å, respectively. The changes in the DFT N1-H1,2,3 distances were 0.003, -0.007 and -0.013 Å, respectively.

A very high level of precision indeed would be needed to observe changes of the magnitudes reported above with crystallographic methods, though vibrational

[1] Note that the atomic numbering used in Tamenov *et al*'s paper has been changed to be consistent with the one used in this paper. Our O1 and O2 correspond to Tumenov et al.'s O2 and O1, respectively. Other non-H atoms are labelled equivalently. For H-atoms our H1-H7 correspond to Tumenov's H13, H12, H11, H21, H33, H31 and H32.

Table 3.3. Selected bond distances derived from geometry optimised structures.

Pressure/GPa	*d* C1-O1/Å	*d* C1-O2/Å	*d* N1-H1/Å	*d* N1-H2/Å	*d* N1-H3/Å
Ambient	1.2622	1.2821	1.0494	1.0696	1.0524
0.40	1.2619	1.2817	1.0490	1.0688	1.0524
0.76	1.2616	1.2813	1.0495	1.0699	1.0519
1.03	1.2620	1.2810	1.0492	1.0699	1.0506
1.38	1.2621	1.2800	1.0498	1.0681	1.0492
2.29	1.2627	1.2788	1.0501	1.0681	1.0475
3.20	1.2634	1.2772	1.0511	1.0667	1.0443
4.30	1.2639	1.2756	1.0513	1.0650	1.0427
5.43	1.2640	1.2740	1.0518	1.0634	1.0408
6.65	1.2639	1.2733	1.0528	1.0627	1.0397
Total change	0.0017	-0.0088	0.0034	-0.0069	-0.0127

spectroscopy is sensitive enough to detect them. Similar comments could be made in other areas of chemistry. In metal carbonyl chemistry, for example, the infra-red C-O stretching frequency is a more sensitive probe of electronic effects such as π-bonding than C-O distance.

3.7 Conclusions

The structure of L-alanine-d_7 has been studied by neutron diffraction up to 15.46 GPa, currently the highest pressure for which 3-D structural data have been obtained for an amino acid. The material transforms reversibly to an amorphous phase at *ca.* 15 GPa due to volume collapse of the structure and it is currently the only amino acid known to undergo a transition of this type. As pressure is increased towards the amorphisation point the sample becomes an increasingly compressed version of the ambient phase. There is no sign of any other phase transition over this pressure regime, although the cell is metrically tetragonal at 2.2 GPa. On decompression to 1.59 GPa after amorphisation, the sample was found to have recrystallised with the same crystal packing as the ambient phase.

The H-bond lengths range between 1.69(2) and 2.19(2) Å at the highest pressure for which data were refined using the Rietveld method, but cannot be considered as being extraordinarily short in the context of similar interactions in the Cambridge Structural Database. Void-volume calculations suggest that collapse of the structure is induced by exhaustion of the capacity for further compression of the crystalline phase at *ca.*14 GPa. Support for anomalous bond distance changes within N-H···O H-bonds identified in an earlier study was seen in the results of periodic DFT optimisations, the results of which had also been used as a source of restraints in the Rietveld refinements.

3.8 References

1. S. A. Moggach, S. Parsons and P. A. Wood, *Crystallography Reviews*, 2008, **14**, 143-184.
2. E. V. Boldyreva, *Acta Crystallographica, Section A: Foundations of Crystallography*, 2008, **A64**, 218-231.
3. E. V. Boldyreva, H. Sowa, H. Ahsbahs, S. V. Goryainov, V. V. Chernyshev, V. P. Dmitriev, Y. V. Seryotkin, E. N. Kolesnik, T. P. Shakhtshneider, S. N. Ivashevskaya and T. N. Drebushchak, *Journal of Physics: Conference Series*, 2008, **121**, 022023.
4. E. V. Boldyreva, *Phase Transitions*, 2009, **82**, 303-321.
5. A. Dawson, D. R. Allan, S. A. Belmonte, S. J. Clark, W. I. F. David, P. A. McGregor, S. Parsons, C. R. Pulham and L. Sawyer, *Crystal Growth & Design*, 2005, **5**, 1415-1427.
6. E. V. Boldyreva, S. N. Ivashevskaya, H. Sowa, H. Ahsbahs and H.-P. Weber, *Zeitschrift fuer Kristallographie*, 2005, **220**, 50-57.
7. S. V. Goryainov, E. V. Boldyreva and E. N. Kolesnik, *Chemical Physics Letters*, 2006, **419**, 496-500.
8. S. V. Goryainov, E. N. Kolesnik and E. V. Boldyreva, *Physica B: Condensed Matter*, 2005, **357**, 340-347.
9. S. A. Moggach, D. R. Allan, C. A. Morrison, S. Parsons and L. Sawyer, *Acta Crystallographica, Section B: Structural Science*, 2005, **61**, 58-68.

10. S. A. Moggach, W. G. Marshall and S. Parsons, *Acta Crystallographica, Section B: Structural Science*, 2006, **B62**, 815-825.
11. P. A. Wood, D. Francis, W. G. Marshall, S. A. Moggach, S. Parsons, E. Pidcock and A. L. Rohl, *CrystEngComm*, 2008, **10**, 1154-1166.
12. E. V. Boldyreva, H. Sowa, Y. V. Seryotkin, T. N. Drebushchak, H. Ahsbahs, V. Chernyshev and V. Dmitriev, *Chemical Physics Letters*, 2006, **429**, 474-478.
13. T. N. Drebushchak, H. Sowa, Y. V. Seryotkin, E. V. Boldyreva and H. Ahsbahs, *Acta Crystallographica, Section E: Structure Reports Online*, 2006, **E62**, o4052-o4054.
14. E. N. Kolesnik, S. V. Goryainov and E. V. Boldyreva, *Doklady Physical Chemistry*, 2005, **404**, 169-172.
15. S. A. Moggach, D. R. Allan, S. J. Clark, M. J. Gutmann, S. Parsons, C. R. Pulham and L. Sawyer, *Acta Crystallographica, Section B: Structural Science*, 2006, **B62**, 296-309.
16. V. S. Minkov, N. A. Tumanov, R. Q. Cabrera and E. V. Boldyreva, *CrystEngComm*, 2010, **12**, 2551-2560.
17. R. D. L. Johnstone, D. Francis, A. R. Lennie, W. G. Marshall, S. A. Moggach, S. Parsons, E. Pidcock and J. E. Warren, *CrystEngComm*, 2008, **10**, 1758-1769.
18. S. A. Moggach, A. R. Lennie, C. A. Morrison, P. Richardson, F. A. Stefanowicz and J. E. Warren, *CrystEngComm*, 2010, **12**, 2587-2595.
19. C. Murli, M. Surinder, S. Karmaker and S. K. Sikka, *Physica B*, 2003, **339**, 23-30.
20. N. P. Funnell, A. Dawson, D. Francis, A. R. Lennie, W. G. Marshall, S. A. Moggach, J. E. Warren and S. Parsons, *CrystEngComm*, 2010, **12**, 2573-2583.
21. N. A. Tumanov, E. V. Boldyreva, B. A. Kolesov, A. V. Kurnosov and R. Quesada Cabrera, *Acta Crystallographica, Section B: Structural Science*, 2010, **B66**, 458-471.
22. P. Lozano-Casal, *PhD Thesis, The University of Edinburgh*, 2006.

23. P. Lozano-Casal, D. R. Allan and S. Parsons, *Acta Crystallographica, Section B: Structural Science*, 2008, **64**, 466-475.

24. S. Patterson, *MSc Dissertation, University of Edinburgh*, 2010.

25. S. A. Moggach, D. R. Allan, S. Parsons and L. Sawyer, *Acta Crystallographica, Section B: Structural Science*, 2006, **B62**, 310-320.

26. S. A. Moggach, C. H. Gorbitz and J. E. Warren, *CrystEngComm*, 2010, **12**, 2322-2324.

27. S. A. Moggach, D. R. Allan, S. Parsons, L. Sawyer and J. E. Warren, *Journal of Synchrotron Radiation*, 2005, **12**, 598-607.

28. E. V. Boldyreva, E. N. Kolesnik, T. N. Drebushchak, H. Sowa, H. Ahsbahs and Y. V. Seryotkin, *Zeitschrift für Kristallographie*, 2006, **221**, 150-161.

29. P. T. C. Freire, F. E. A. Melo, J. Mendes Filho, R. J. C. Lima and A. M. R. Teixeira, *Vibrational Spectroscopy*, 2007, **45**, 99-102.

30. J. M. De Souza, P. T. C. Freire, H. N. Bordallo and D. N. Argyriou, *Journal of Physical Chemistry B*, 2007, **111**, 5034-5039.

31. J. S. Olsen, L. Gerward, A. G. Souza Filho, P. T. C. Freire, J. Filho and F. E. A. Mendes Melo, *High Pressure Research*, 2006, **26**, 433-437.

32. A. M. R. Teixeira, P. T. C. Freire, A. J. D. Moreno, J. M. Sasaki, A. P. Ayala, J. Mendes Filho and F. E. A. Melo, *Solid State Communications*, 2000, **116**, 405-409.

33. J. S. Olsen, L. Gerward, P. T. C. Freire, J. Mendes Filho, F. E. A. Melo and A. G. Souza Filho, *Journal of Physics and Chemistry of Solids*, 2008, **69**, 1641-1645.

34. R. O. Goncalves, P. T. C. Freire, H. N. Bordallo, J. A. Lima, Jr., F. E. A. Melo, J. Mendes Filho, D. N. Argyriou and R. J. C. Lima, *Journal of Raman Specroscopy*, 2009, **40**, 958-963.

35. L. Ciabini, F. A. Gorelli, M. Santoro, R. Bini, V. Schettino and M. Mezouar, *Physical Reviews B: Condensed Matter and Material Physics*, 2005, **72**, 094108/094101-094108/094107.

36. W. G. Marshall and D. J. Francis, *Journal of Applied Crystallography*, 2002, **35**, 122-125.

37. ISIS, *ISIS 96 - ISIS Facility Annual Report 1995-96, Rutherford Appleton Laboratory*, 1996, **RAL-TR-96-050**, 61-62.

38. ISIS, *ISIS 97 - ISIS Facility Annual Report 1996-97, Rutherford Appleton Laboratory*, 1997, **RAL-TR-97-050**, 28-29.

39. J. M. Besson and R. J. Nelmes, *Physica B: Condensed Matter*, 1995, **213&214**, 31-36.

40. J. M. Besson, R. J. Nelmes, G. Halem, J. S. Loveday, G. Weill and S. Hull, *Physica B: Condensed Matter*, 1992, **180-181**, 907-910.

41. S. Klotz, L. Paumier, G. Le Marchand and P. Munsch, *High Pressure Research*, 2009, **29**, 649-652.

42. D. Martinez-Garcia, Y. L. Godec, M. Mezouar, G. Syfosse, J. P. Itíe and J. M. Besson, *High Pressure Research*, 2000, **18**, 339-344.

43. A. Coelho, *TOPAS-Academic: General Profile and Structure Analysis Software for Powder Diffraction Data. Version 4.1*, (2007), Brisbane, Australia.

44. S. J. Clark, M. D. Segall, C. J. Pickard, P. J. Hasnip, M. J. Probert, K. Refson and M. C. Payne, *Zeitschrift für Kristallographie*, 2005, **220**, 567-570.

45. J. P. Perdew, K. Burke and M. Ernzerhof, *Physical Review Letters*, 1996, **77**, 3865.

46. D. Vanderbilt, *Physical Review B*, 1990, **41**, 7892-7895.

47. S. Grimme, *Journal of Computational Chemistry*, 2006, **27**, 1787-1799.

48. H. J. Monkhorst and J. D. Pack, *Physical Review B*, 1976, **13**, 5188.

49. M. J. Frisch, G. W. Trucks, H. B. Schlegel, G. E. Scuseria, M. A. Robb, J. R. Cheeseman, J. A. Montgomery Jr., T. Vreven, K. N. Kudin, J. C. Burant, J. M. Millam, S. S. Iyengar, J. Tomasi, V. Barone, B. Mennucci, M. Cossi, G. Scalmani, N. Rega, G. A. Petersson, H. Nakatsuji, M. Hada, M. Ehara, K. Toyota, R. Fukuda, J. Hasegawa, M. Ishida, T. Nakajima, Y. Honda, O. Kitao, H. Nakai, M. Klene, X. Li, J. E. Knox, H. P. Hratchian, J. B. Cross, V. Bakken, C. Adamo, J. Jaramillo, R. Gomperts, R. E. Stratmann, O. Yazyev, A. J. Austin, R. Cammi, C. Pomelli, J. W. Ochterski, P. Y. Ayala, K. Morokuma, G. A. Voth, P. Salvador, J. J. Dannenberg, V. G. Zakrzewski, S. Dapprich, A. D. Daniels, M. C. Strain, O. Farkas, D. K. Malick, A. D.

Rabuck, K. Raghavachari, J. B. Foresman, J. V. Ortiz, Q. Cui, A. G. Baboul, S. Clifford, J. Cioslowski, B. B. Stefanov, G. Liu, A. Liashenko, P. Piskorz, I. Komaromi, R. L. Martin, D. J. Fox, T. Keith, M. A. Al-Laham, C. Y. Peng, A. Nanayakkara, M. Challacombe, P. M. W. Gill, B. Johnson, W. Chen, M. W. Wong, C. Gonzalez and J. A. Pople, *Gaussian 03, Revision E.01*, (2003) Gaussian, Inc., .

50. A. Gavezzotti, *OPiX: A computer program package for the calculation of intermolecular interactions and crystal energies.*, (2003), University of Milan, Italy.
51. A. Gavezzotti, *Zeitschrift für Kristallographie.*, 2005, **220**, 499-510.
52. A. Gavezzotti, *Molecular Aggregation: Structure Analysis and Molecular Simulation of Crystals and Liquids*, Oxford University Press, Oxford, UK, 2007.
53. C. F. Macrae, I. J. Bruno, J. A. Chisholm, P. R. Edgington, P. McCabe, E. Pidcock, L. Rodriguez-Monge, R. Taylor, J. van de Streek and P. A. Wood, *Journal of Applied Crystallography*, 2008, **41**, 466-470
54. F. H. Allen, *Acta Crystallographica, Section B*, 2002, **58**, 380-388.
55. I. J. Bruno, J. C. Cole, P. R. Edgington, M. Kessler, C. F. Macrae, P. McCabe, J. Pearson and R. Taylor, *Acta Crystallographica, Section B: Structural Science*, 2002, **B58**, 389-397.
56. R. J. Angel, *EOSFIT version 5.2*, (2002) Virginia Tech, Blackburg, VA, USA.
57. S. K. Wolff, D. J. Grimwood, J. J. McKinnon, D. Jayatilaka and M. A. Spackman, 2007.
58. A. L. Spek, *Journal of Applied Crystallography*, 2003, **36**, 7-13.
59. J. D. Dunitz and R. R. Ryan, *Acta Crystallographica*, 1966, **21**, 617-618.
60. M. S. Lehmann, T. F. Koetzle and W. C. Hamilton, *Journal of the American Chemical Society*, 1972, **94**, 2657-2660.
61. R. Destro, R. E. Marsh and R. Bianchi, *Journal of Physical Chemistry A*, 1988, **92**, 966-973.
62. R. J. Angel, *Reviews in Mineralogy and Geochemistry*, 2002, **41**, 35-59.
63. F. Birch, *Journal of Geophysical Research, B* 1986, **91**, 4949-4954.

64. S. Klotz, J. C. Chervin, P. Munsch and G. Le Marchand, *Journal of Physics D: Applied Physics*, 2009, **42**, 075413/075411-075413/075417.

65. J. D. Dunitz and A. Gavezzotti, *Angewandte Chemie, International Edition*, 2005, **44**, 1766-1787.

66. J. J. McKinnon, M. A. Spackman and A. S. Mitchell, *Acta Crystallographica, Section B*, 2004, **60**, 627-668.

67. P. A. Wood, J. J. McKinnon, S. Parsons, E. Pidcock and M. A. Spackman, *CrystEngComm*, 2008, **10**, 368-376.

68. M. C. Wilding, M. Wilson and P. F. McMillan, *Chemical Society Reviews*, 2006, **35**, 964-986.

69. K. W. Chapman, P. J. Chupas, G. J. Halder, J. A. Hriljac, C. Kurtz, B. K. Greve, C. J. Ruschman and A. P. Wilkinson, *Journal of Applied Crystallography*, 2010, **43**, 297-307.

70. J. E. Readman, P. M. Forster, K. W. Chapman, P. J. Chupas, J. B. Parise and J. A. Hriljac, *Chemical Communications*, 2009, 3383-3385.

71. K. W. Chapman, G. J. Halder and P. J. Chupas, *Journal of the American Chemical Society*, 2009, **131**, 17546-17547.

72. L. Ciabini, M. Santoro, F. A. Gorelli, R. Bini, V. Schettino and S. Raugei, *Naure Materials*, 2007, **6**, 39-43.

73. W. Koch and M. C. Holthausen, *A Chemist's Guide to Density Functional Theory*, Wiley-VCH, Weinheim, Germany, 2000.

Chapter 4

Using Pressure to Direct Polymorph Formation: Overcoming Isotopic Polymorphism in the 4-Methylpyridine – Pentachorophenol Co-Crystal*

*Nicholas P. Funnell, David R. Allan, Andrew G. P. Maloney and Simon Parsons, *in preparation*

4.1 Introduction

New crystalline polymorphs are most commonly accessed by application of temperature or variation of crystallisation conditions. Much more unusual is the formation of different phases for isotopologues, so called *isotopic polymorphism*. So far the only isotope variation to have been studied is deuteration, and observation of this rare phenomenon has mostly been limited to inorganic crystals. Examples recently listed by Harbison include ammonium dihydrogen phosphate, ammonium dehydrate arsenate, sodium trihydrogen selenite and chromium hydroxide oxide.[1-3] In the organic solid state it occurs in pyridine and co-crystals of 4-methylpyridine pentachlorophenol (MP-PCP).

Isotopic polymorphism in the last of these compounds was first reported by Majerz *et al* through non-identical IR and UV spectra for the two isotopologues.[4] X-ray crystal structures show that isotopically normal MP and PCP co-crystallise in the triclinic space group *P*-1 (CSD refcode: GADGUN), hereafter referred to as phase T-H.[5] When the phenolic oxygen is deuterated, the co-crystal adopts the monoclinic space group *Cc* (CSD refcode: GADGUN01), phase M-D. A summary of the phase nomenclature used in this study is given in Table 4.1; the structure and numbering scheme of MP-PCP are given in Scheme 4.1 and unit cell packing diagrams of the two forms are shown in Figure 4.1.

In both forms a hydrogen bond exists between the O donor and the N acceptor of the PCP and MP components. The H-bond is stronger in T-H; H···N = 1.47(6) Å in T-H and 1.85(5) Å in M-D, both measured by X-ray diffraction under ambient conditions. The shorter of these bonds is a low-barrier hydrogen bond, where the proton is approximately centred between the N and O atoms.[6]

Table 4.1 Polymorph naming scheme. 'T' and 'M' refer to triclinic and monoclinic respectively and 'H' and 'D' represent hydrogen and deuterium substitution at the phenolic oxygen. The names in bold indicate crystal structures that have been determined previously.

Isotope	Space group	
	P-1	*Cc*
MP-PCP-h_1	**T-H**	M-H
MP-PCP-d_1	T-D	**M-D**

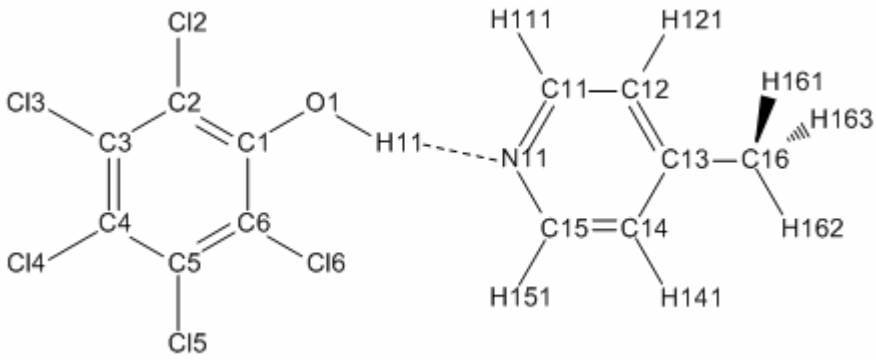

Scheme 4.1. Chemical structure diagram depicting the numbering scheme used

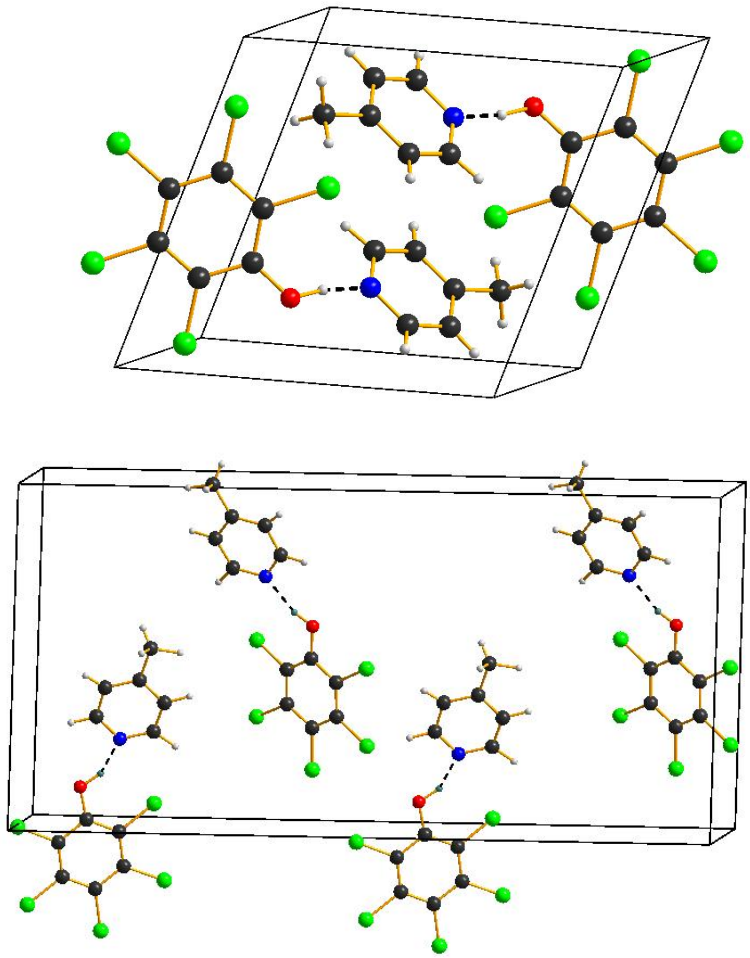

Figure 4.1 Crystal packing of one unit cell for the T-H (top) and M-D (bottom) polymorphs

A variable-temperature neutron diffraction study on T-H showed that the proton migrates from the O towards the N on cooling, and is situated closer to the N than the O at temperatures lower than 80 K.[7] Evidence from X-ray studies on M-D indicate that this behaviour is not observed – the oxygen is unambiguously the H-bond donor, though the lowest temperature to have been applied is 80 K.[8] Details of hydrogen bonding parameters for several recorded structures in the CSD and for the structures obtained in this study are given in Table 4.2.

^{1}H MAS NMR investigations have shown that the polymorphism is driven exclusively by the proton at the phenolic position - if all the ^{1}H atoms in the structure are substituted with the exception of the phenolic site, the result is still the *P*-1 polymorph.[9] In the same study, attempts were made to encourage crystallisation of M-H and T-D by seeding the solutions with crystalline samples of the other phase. This was reported as being largely unsuccessful; only a small quantity of the monoclinic form was grown using deuterium-free solutions and no triclinic crystals were observed at all for the partially-deuterated samples. Neither could the polymorph be influenced by repeated melting/freezing of the crystal samples.

Table 4.2 Hydrogen bond lengths from all existing MP-PCP structures in the CSD and also for the structures reported in this experiment (designated N/A in the CSD Refcode column). Estimated standard deviations are given in parentheses where possible.

CSD Refcode	Phase	Temperature / K, Pressure / GPa	O-H/D / Å	N-H/D / Å	O···N / Å
GADGUN	T-H	295(1), ambient	1.09(6)	1.47(6)	2.552(6)
GADGUN02		80(2), ambient	1.22(4)	1.29(4)	2.515(4)
N/A		ambient, 4.59	0.826	1.729(5)	2.516(5)
GADGUN01	M-D	299(2), ambient	0.94(5)	1.85(5)	2.638(3)
GADGUN06	M-D	80(2), ambient	1.04(8)	1.73(8)	2.628(6)
N/A	M-H	ambient, 0.41	0.826	1.848(14)	2.614(14)
N/A		150, ambient	0.825	1.894(6)	2.623(6)
GADGUN05	T-H	200(<1), ambient	1.228(11)	1.306(11)	2.525(4)
GADGUN04		150(<1), ambient	1.229(11)	1.300(11)	2.519(4)
GADGUN03		125(<1), ambient	1.241(10)	1.288(10)	2.519(4)
RAKQOJ01		100(<1), ambient	1.258(8)	1.265(8)	2.513(3)
RAKQOJ		80(<1), ambient	1.266(8)	1.255(8)	2.513(3)
RAKQAV02		60(<1), ambient	1.275(10)	1.249(10)	2.515(4)
RAKQAV01		45(<1), ambient	1.279(8)	1.242(8)	2.513(3)
RAKQAV		20(<1), ambient	1.309(7)	1.206(6)	2.506(2)

In order to understand the origin of this polymorphism inelastic neutron scattering, and solid state ^{1}H and ^{2}H NMR techniques have been employed to monitor the vibrational characteristics of the H-bond.[10] From these data, Harbison has proposed models for the energy potentials of each polymorph (Figure 4.2 - reproduced from Ref 10). In the triclinic case the potential is a symmetric double well where the zero point energies (ZPEs) for the ^{1}H and ^{2}H hydrogen bonds lie very close to one another. Either energy well can be occupied depending only on whether the proton is located closer towards the phenolic oxygen or the pyridine nitrogen. The potential for the monoclinic form is a single asymmetric energy well where the energy separation between ZPEs is greater, such that they 'straddle' the ZPEs of the triclinic alternative. This theory concisely explains the stabilities exhibited by the T-H and M-D polymorphs. Dove states that a low-symmetry polymorph will usually be more stable at low temperature and high pressure conditions than its corresponding high-symmetry form.[11] This can be understood through the Gibbs free energy equation, $G = U + PV - TS$, where the symbols have their usual thermodynamic meanings. Low-symmetry solid phases tend to be denser than their high-symmetry

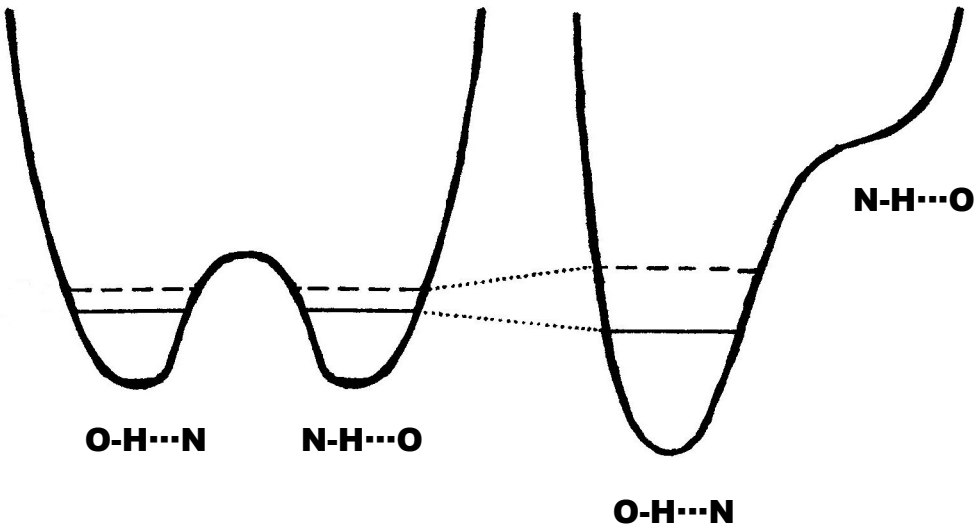

Figure 4.2. Cartoon showing zero point energies of the phenolic hydrogen and deuterium represented by dashed and solid lines respectively. The triclinic potential is shown on the left and the monoclinic on the right. The figure is reproduced from ref 10.

forms which leads to more favourable values of *U* and *PV*. The lower density of the high-symmetry polymorphs means they usually possess lower phonon frequencies and thus have higher entropy. At low temperature, the *TS* contribution to *G* is diminished but increasing temperature can make the high-symmetry form competitive through *TS*.

This is not always the case for organic molecular systems though. A new polymorph of salicylamide, with higher symmetry than its ambient phase, was grown through in-situ crystallisation at high pressure.[12] This form was found to possess a lower cohesive energy than its ambient phase, in contrast to the general view presented by Dove, but this was compensated for by the *TS* term. The stabilising influence of the *TS* term was attributed to elongation of the H-bonds with respect to the ambient phase, which resulted in lower phonon frequencies and thus higher entropy. This case study demonstrates the importance of considering the effects of entropy in molecular systems, where shortening of intermolecular interactions as a result of minimising *PV* can actually be energetically destabilising in terms of *U*.

The aim of this investigation is to obtain the MP-PCP polymorphs that have yet to be reliably observed – the M-H and T-D forms. The volumes occupied by one formula unit in T-H and M-D at RT are 363.0 and 355.7 $Å^3$, respectively. At elevated pressure the need to minimise the *PV* contribution to the Gibbs free energy means that lower volume polymorphs can become thermodynamically favoured, even at the expense of forming less favourable intermolecular interactions. We report how the M-H polymorph can be obtained through the application of pressure to isotopically normal MP-PCP. Furthermore statistical thermodynamic calculations, accounting for the effects of temperature, have been performed which show how the *TS* term affects relative polymorph stability. From these, the experimental conditions for growth of the T-D phase have been identified.

4.2 Experimental

4.2.1 Direct compression of a T-H single-crystal sample

Materials were obtained from Sigma-Aldrich and used as received. Methylpyridine (0.18 mL, 1.85 mmol) and pentachlorophenol (0.495 g 1.859 mmol) were mixed in a

1:1 molar ratio and refluxed in carbon tetrachloride for 20 minutes. Crystals were grown by slow evaporation of the resulting solution.

A single crystal was loaded in a Merrill-Bassett diamond anvil cell (DAC) with an opening angle of 80°, equipped with Boehler-Almax brilliant-cut diamonds with 600 μm culets, a tungsten gasket and tungsten carbide backing plates.[13, 14] A small ruby chip was included as a pressure calibrant, using the ruby fluorescence method to measure the pressure and a 1:1 mixture of pentane:isotpentane was loaded as a hydrostatic pressure-transmitting medium.[15] Diffraction data were then collected at the pressures 0.207, 0.568 1.469, 2.862, 3.753, 4.56, 4.57 and 4.59 GPa.

4.2.2 In situ crystal growth of M-H at high pressure

A solution was prepared by dissolving a 1:1 molar ratio of 4-methylpyridine (0.23 mL, 2.36 mmol) and pentachlorophenol (0.6400 g, 2.403 mmol) in a minimum volume of acetonitrile. The solution was loaded into a DAC with an opening angle of 60°, equipped with Boehler-Almax brilliant-cut diamonds with 600 μm culets, a tungsten gasket and tungsten carbide backing plates. A small ruby chip was included to measure the pressure. Crystallisation was induced by increasing pressure to 0.5 GPa. The crystallites formed were re-dissolved with a hot-air gun until very few seeds remained. These were allowed to grow as the cell cooled back to R.T. Diffraction data were then collected. The average pressure in the cell during the data collection was measured to be 0.4 GPa, having reduced slightly from its initial set point prior to crystal growth. The acetonitrile solvent also crystallised at this pressure and the structural details of this are available in the supplementary information.

4.2.3 High pressure data collection and processing

Diffraction data for the direct compression of T-H were collected using a Rigaku Saturn 724 CCD detector with silicon-monochromated synchrotron radiation on I19 at the Diamond Light Source (λ = 0.6889 Å). Crystal and refinement statistics for all structures are listed in Table 4.3. Frames were recorded with 1s exposures with a scan width of 1° scanning about the φ and ω circles. The images were converted from Rigaku to Bruker format using the programme ECLIPSE.[16] Data were integrated using dynamic masking of the regions of the detector shaded by the

Table 4.3 Crystal refinement data for phase M-H at 0.41 GPa and the recovered crystal at 150 K. Three values are given for the R_{int} of the structure at 0.41 GPa; one for each crystal domain that was found, which were merged at the later stages of processing

Pressure / GPa, temperature / K	**4.59, 298**	**0.41, 298**	**0, 150**
M_r	359.47	359.47	359.47
Space group	*P*-1	*Cc*	*Cc*
a-axis / Å	7.0422(8)	3.8385(6)	3.8618(2)
b-axis / Å	8.051(5)	27.440(3)	27.5870(14)
c-axis / Å	12.095(3)	13.124(5)	13.1964(5)
α / °	101.44(4)	90	90
β / °	114.252(14)	101.41(2)	101.253(4)
γ / °	101.16(2)	90	90
Volume / Å^3	570.6(4)	1355.0(6)	1378.86(11)
Z	2	4	4
Density / Mg m^{-3}	2.092	1.762	1.731
Crystal form, colour	Colourless block	Colourless rod	Colourless block
Crystal size / mm	*ca.* 0.1 × 0.2 × 0.2	*ca.* 0.05 × 0.05 x 0.2	0.168 x 0.069 x 0.045
T_{min}	0.75	0.83	0.50
T_{max}	0.90	0.98	0.65
μ / mm^{-1}	1.054	0.0371	0.950
No. of measured, independent and observed [$I > 2.0\sigma(I)$] reflections	1837, 516, 466	7511, 1086, 801	4092, 2125, 1982
R_{int}	0.0422	0.0563, 0.0757, 0.0806	0.060
$R[F^2 > 2.0\sigma(F^2)]$	0.0376	0.0491	0.0486
$wR(F^2)$	0.0381	0.1460	0.1262
Goodness of fit	1.0266	0.9169	1.0266
No. of parameters	102	102	173
Weighting scheme	w'=1/ $\sigma^2(F_o)$ w''=[1-($\Delta(F)$/6 x $\Delta(F_c)$)^2]^2	w=w' x [1-($\Delta(F)$/6 x $\Delta(F_c)$)^2]^2	w = 1/[$\sigma^2(F_o^2)$ + $(0.092P)^2$ + 0.730P x Sinθ
$(\Delta/\sigma)_{max}$	0.0001943	0.0001025	0.0003985
$\Delta\rho_{max}$, $\Delta\rho_{min}$ / eÅ^{-3}	0.45, -0.46	0.55, -0.49	0.68, -0.39
Completeness, resolution / Å	22%, 0.80	63%, 0.92	99%, 0.81

pressure cell and the regions of high intensity attributed to the tungsten gasket, with the programme SAINT.[17] Absorption corrections were carried out with the program SADABS.[18]

Diffraction data for the M-H sample were also collected on I19 at the Diamond Light Source (λ = 0.5159 Å). Frames were recorded with 1s exposures, with a width of 0.5° scanning about the omega circle. The images were converted from Rigaku to Bruker format using the programme ECLIPSE. Four domains of phase M-H were identified and each of these was integrated separately. Data were integrated in the same way as described above. One of the domains produced relatively poor integration statistics and was discarded. The reflection data of the three remaining domains were combined in SORTAV in order to increase the completeness of the data (63% to 0.92 Å).[19] Absorption corrections were carried out with the program SADABS.

Structure refinements against F^2 were carried out in Crystals using the starting coordinates for T-H (GADGUN) and M-D (GADGUN01) determined at ambient pressure.[20] Due to the low completeness of the datasets all primary bond distances and angles were restrained to the values of the starting model. Only the chlorine atoms were allowed to refine anisotropically in order to reduce the number of parameters. Hydrogen atoms could not be located in a difference map for the T-H structures and were all placed geometrically. All H atoms for the M-D structure were placed geometrically except for the methyl hydrogens, which were located in a difference map. The phenolic H atom could not be located from the diffraction data and has been included in the same position as observed in the ambient-pressure structure. All the H atom positions were regularised and were subsequently constrained to ride on their host atoms.

4.2.4 Recovery of M-H at ambient pressure

Crystals of M-H were grown at high pressure as described above in Section 4.2.2 and then recovered from the cell. As the cell was opened, pressure decreased, increasing the solubility of the crystal in the acetonitrile solvent. This made rapid recovery of the crystal essential – cooling the DAC with dry ice facilitated this procedure. Some dissolution of the sample was unavoidable, though, and the crystallite obtained (0.05 x 0.07 x 0.17 mm) was significantly smaller than that first grown.

Diffraction data for the recovered crystal were collected on an Agilent Technologies SuperNova with an Atlas detector at 150 K using CuK_α radiation. Low

angle reflections were collected with 3 s exposures and high angle reflections, 30 s, scanning about the ω circle with frame widths of 1°. Data were integrated and corrected for absorption using CrysAlisPro.[21] Data were merged in SORTAV. Structure refinements against F^2 were carried out in Crystals. All atoms were located in a difference map and all non-H atoms were refined anisotropically. The geometries of the H-atoms were regularised with restraints and were subsequently constrained to ride on their host atoms.

4.2.5 Growth and unit cell determination of T-D

MP-PCP-d_1 was synthesised by stirring pentachlorophenol (0.5006 g, 1.880 mmol) in methanol-d_1 under nitrogen for 3 hours.[22] Methyl-pyridine (*ca.* 0.2 mL, 2.055 mmol) was added in a 1:1 molar ratio and the resulting compound was dissolved in a minimum volume of dry acetonitrile. The sample was cooled to 243 K to encourage crystallisation. Growth of rod-like and plate-like crystals was observed; morphologies which are characteristic of the monoclinic and triclinic phases respectively. Diffraction data were collected on a single plate-like crystal using a three-circle Bruker APEX II diffractometer. The unit cell, determined by APEX II, was found to be *a*=7.48(2), *b*=9.11(3), *c*=13.59(4) Å, α=99.82(4), β=118.07(3) and γ=103.68(3)°. Poor diffraction quality of the crystal prevented full structural determination.

4.2.6 Vibrational frequency calculations

DFT calculations were performed using the DMOL^3 package implemented in the Accelrys Materials Studio software.[23] The PBE exchange-correlation functional was used with the Grimme dispersion correction.[24, 25] A numerical basis set (DNP 3.5) was used and Brillouin zone integrations were performed on a *k*-point grid with a spacing of 0.07 $Å^{-1}$.[26] The total energy convergence was 0.00001 eV and the maximum displacement allowed was 0.005 Å.

The starting coordinates for the calculations were taken from GADGUN04 for the T-H polymorph and the refined structure of the crystal recovered from pressure for the M-H phase. The cell dimensions were initially held fixed whilst the atomic coordinates were allowed to refine. The structures were allowed to relax in

*P*1 prior to the frequency calculations. A second set of frequency calculations were carried out with the cell dimensions being allowed to optimise. The frequencies for T-D and M-D were obtained by repeating the final frequency calculations for fixed and refined-cell optimisations, but substituting H with D. For simplicity only the results from the optimisations using fixed cell dimensions are reported here as similar results are obtained when the cell dimensions are allowed to optimise.

4.3 Results and Discussion

4.3.1 Compression study of T-H to 4.59 GPa

Given the more efficient packing in M-D, it was initially thought possible that pressure would cause an undeuterated triclinic crystal to transform to the monoclinic form, thus obtaining M-H. However, when T-H was studied by single crystal diffraction up to 4.59 GPa the crystal remained in a compressed form of the triclinic phase. Increasing the pressure above 4.59 GPa led to collapse of the crystal.

The cell dimensions of the structure measured at the highest pressure of 4.59 GPa are *a*=7.0422(8), *b*=8.051(5), *c*=12.095(3) Å, α=101.44(4), β=114.252(14) and γ=104.216(2)°. These lattice parameters are significantly smaller than those observed at ambient conditions (GADGUN) where the cell lengths are *a*=7.408(6), *b*=8.934(7) and *c*=13.653(9) Å. The cell compressibility is of the order *c* (11.4%) > *b* (9.9%) > *a* (4.9%). Details of the crystal structure refinement at 4.59 GPa are given in Table 4.3 and a CIF is supplied in the supplementary information.

4.3.2 Reproducible in-situ growth of M-H crystals at high pressure

Transitions between crystalline polymorphs can often demand substantial reorganisation of the molecules, and a disadvantage of taking a crystal grown at ambient conditions and then applying pressure to it is that if the energy barrier for reorganisation is too high a phase can become kinetically trapped. One way to circumvent this problem is to grow a crystal *in situ* at high pressure from either liquid or solution so that the sample never has to pass through an unfavourable 'state of reorganisation'.

The high-pressure and low-temperature diffraction showed that the denser, M-H polymorph can be grown reproducibly from MeCN solution at 0.5 GPa. Exhaustive indexing of the diffraction pattern revealed 4 domains of phase M-H and 1 domain of acetonitrile. Previously the M-H phase has only ever been observed in very small quantities when seeding the liquid protonated compound with M-D crystals. The exclusive formation of M-H here reflects the need to pack efficiently at elevated pressure.

It was possible to recover small crystals of M-H from the DAC to ambient conditions as they did not revert to the triclinic polymorph. On a second sample, complete diffraction data were collected on an Agilent Technologies SuperNova at 150 K. Images of the crystals in the DAC sample chamber and the recovered crystal mounted on a goniometer head are shown in Figure 4.3.

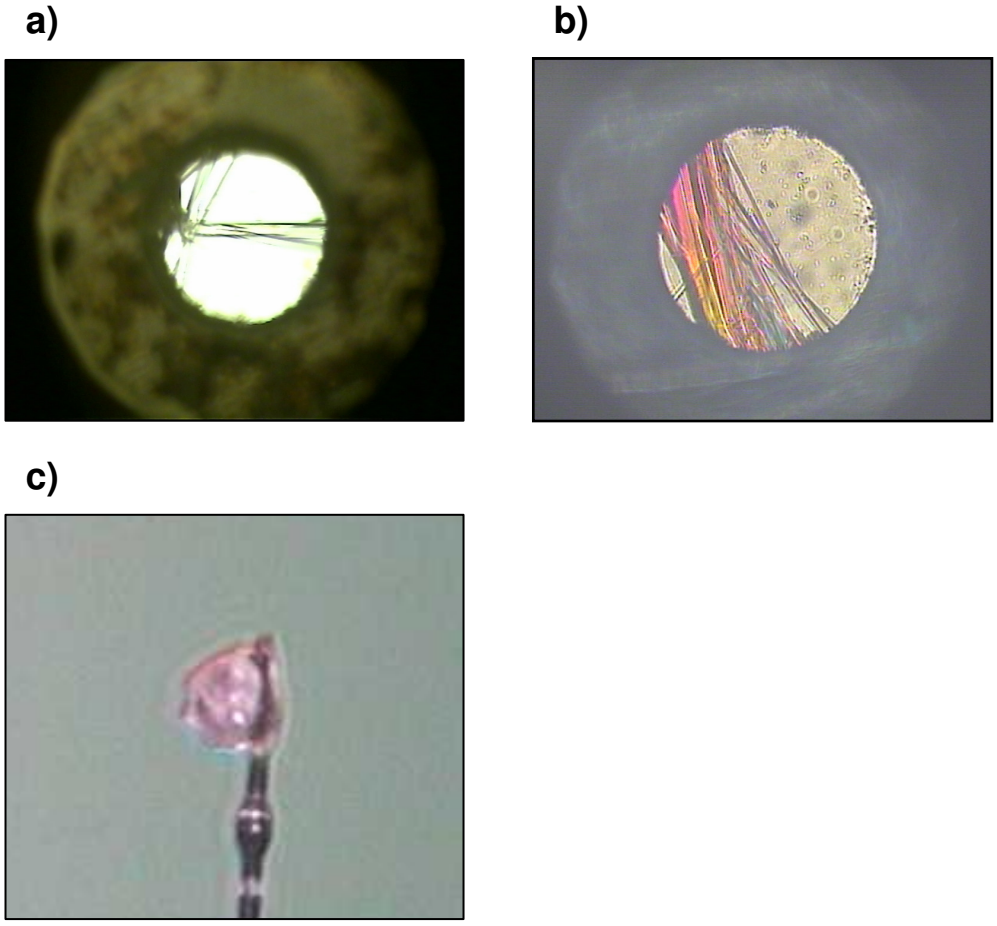

Figure 4.3. Images showing, **a)** M-H crystals grown at pressure in the cell chamber, **b)** the crystals grown at pressure from which the recovered crystal was obtained (the colouration is due to a polariser), and **c)** the recovered crystal (0.05 × 0.07 × 0.17 mm) mounted on a glass wool fibre

4.3.3 The effect of pressure and temperature on the cell dimensions and molecular geometry

The crystal structure of phase M-H is shown in Figure 4.4. The cell dimensions obtained at 0.41 GPa are *a*=3.8385(6), *b*=27.440(3), *c*=13.124(5) Å and β=101.41(2)°. These values are significantly different from those observed at ambient conditions (*c.f.* GADGUN01: *a*=3.942(3), *b*=27.73(3), *c*=13.297(9) Å, β=101.81(6) where the order of axis compressibility, observed up to 0.41 GPa is *a* (2.63%) > *c* (1.30%) > *b* (1.05%).

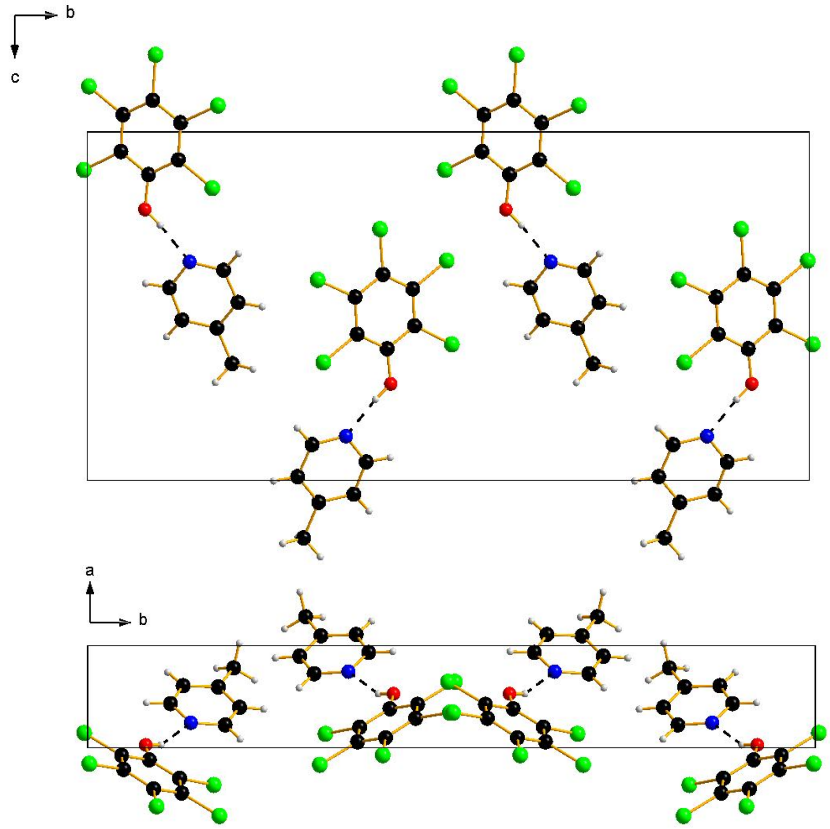

Figure 4.4. Unit cell packing diagram of phase M-H viewed along **a** (top) and **c** (bottom). Hydrogen bonds are represented by black dotted lines. Each MP-PCP pair is related to another by glide planes along **c**.

The unit cell of the crystal recovered from pressure, at 150 K, has the dimensions *a*=3.8618(2), *b*=27.587(14), *c*=13.1964(5) Å and β=101.56(4)°. These are, again, significantly shorter than those of GADGUN01. The *a*-axis in particular is rather susceptible to the effects of temperature, decreasing by 2.03%. This is consistent with the cell dimensions reported by Malarski *et al* for M-D at 80 K

(GADGUN06): *a*=3.826(2), *b*=27.54(2), *c*=13.209(12) Å and β=101.38(9)°, showing that the *a*-axis has decreased by 2.94%.[8] It may be significant that the M-D structure disorders at 80 K over two sites which may also influence the magnitude of the cell axes. An X-ray diffraction experiment at 80 K shows that the M-H polymorph also exhibits this behaviour, along with a 2.87% reduction in the *a*-axis, with respect to GADGUN01. An assessment of other published and unpublished data on the effects of temperature on small organic compounds, notably the amino acids L-alanine, L-tyrosine, L-α-glycine and L-β-glycine, shows that the maximum change in any cell axis tends not to exceed 1% when cooled to 150 K.[27] The larger difference seen here suggests the presence of weaker intermolecular interactions along **a**, which are discussed below.

The only significant difference between the intramolecular parameters in the M-H structures at 0.41 GPa and 150 K, and M-D (GADGUN01) is the orientation of the methyl group. In both of our structures, the methyl hydrogen atoms were located in a difference map and their geometries were then regularised to C_{3v} symmetry. In both GADGUN01 and the structure at 150 K, one of the hydrogen atoms in the methyl group is located approximately in the plane of the aromatic ring. In the high-pressure structure, none of the hydrogen atoms are aligned with the aromatic ring plane. The root mean square deviation (RMSD) was calculated in Mercury CSD between the structures which confirmed a high level of similarity; the maximum RMSD value calculated was 0.0333 Å for the structures at 0.41 GPa and GADGUN01.[28] A diagram of the M-H models at 150 K and 0.41 GPa, overlaid with that of ambient M-D (GADGUN01) is shown in Figure 4.5.

The phenolic proton for the M-H sample at 0.41 GPa could not be located in a Fourier difference map so it was placed geometrically and was subsequently constrained to ride on the oxygen donor atom for the later stages of refinement. Based on the O(1)···N(11) distance, owing to the uncertainty in the position of the phenolic proton, the hydrogen bond measures 2.61(1) Å. This is not a significant change from the O···N distance seen in GADGUN01 at ambient pressure – 2.638(3) Å. This strong interaction lies approximately in the *bc* plane and is not well-aligned with the *a*-axis, hence **a** is the most compressible direction. The aromatic rings stack face-to-face along this axis meaning there must be an increase in π-π interactions

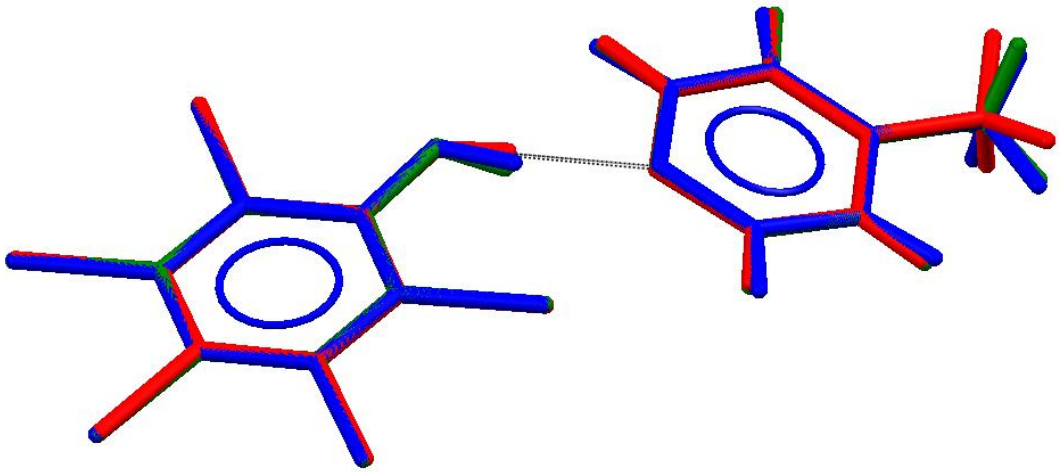

Figure 4.5. A diagram of the M-H models at 0.41 GPa and 150 K overlaid with the ambient M-D structure (refcode: GADGUN01) shown in red, green and blue respectively. Black dotted lines represent the hydrogen bonds.

along this direction as pressure is applied. At ambient pressure the centroid-centroid distance between aromatic rings is 3.942(6) Å and at 0.41 GPa, it has decreased to 3.84(2) Å. This change can largely be attributed to a decrease in the π-π stacking distance, as opposed to the π-π offset which decreases by a relatively small amount (*ca.* 0.05 Å). Space-filling diagrams show large interstitial voids are present and it is these that take up the effects of pressure.

4.3.4 Relative polymorph stabilities

The H-bond zero-point energy models for the four possible structures (T-H, T-D, M-H and M-D), described by Harbison, and described in the *Introduction*, provide a possible theoretical explanation for the observed effect of isotopic substitution, but they have yet to be quantified. We have attempted to calculate the relative stabilities of each polymorph using periodic DFT. In addition to the ZPE terms, the internal energies (U_0), vibrational enthalpies (E_{vib}) and temperature × entropy (TS) terms have also been included in the calculation to build a more complete representation of the thermodynamic properties. By including these extra terms, the effect of temperature can be modelled, albeit within a harmonic approximation.

Single-crystal neutron diffraction data collected on T-H indicate that at 20 K the H-atom involved in the short H-bonding interaction is located nearer to the N than to the O (Table 4.2). The DFT-optimised T-H structure, which omits thermal effects and is effectively at 0 K, also shows the H to be closer to the nitrogen atom. More generally the level of agreement between the observed and optimised crystal structures of T-H and M-D is excellent, with respective RMS deviations of 0.081 and 0.072 calculated for a cluster of 15 molecules, as described by Macrae *et al* and Chisholm and Motherwell.[28, 29] Selected parameters derived from the optimisation are listed in Table 4.4.

Phonon frequencies calculated for T-H, T-D, M-H and M-D were used to evaluate zero point energies and thermal corrections to enthalpy and the entropy at temperatures between 300 and 700 K. The procedure used followed that described by Hudson and Johnstone *et al.*[12, 30] These calculations enable free energies of the polymorphs to be compared as a function of temperature. These data are plotted in Figure 4.6, in which energies are quoted relative to that of the T-H polymorph.

Table 4.4 Unit cell dimensions, H-bond distances and ZPEs for the optimised triclinic and monoclinic structures. The deuterated analogues have the same unit cell as the hydrogen-containing structures. The H-bond distances are the same for H and D versions of each polymorph under the same optimisation conditions. Estimated standard deviations are given in parentheses where possible

Phase	T-H	M-H	T-D	M-D
a-axis / Å	7.296	3.8618	7.296	3.8618
b-axis / Å	8.884	27.5870	8.884	27.5870
c-axis / Å	13.313	13.313	13.313	13.313
α / °	99.99	90	99.99	90
β / °	117.91	101.253	117.91	101.253
γ / °	103.94	90	103.94	90
ZPE / kJmol^{-1}	457.19	450.20	449.39	442.32
O-H/D / Å	1.458	1.041	1.458	1.041
N-H/D / Å	1.110	1.640	1.110	1.640

The plot shows that the hierarchy of stability proposed by Harbison (i.e. M-D > T-D > T-H > M-H) occurs in a relatively narrow range of temperature, 390-400 K (Figure 4.7). Below *ca.* 390 K the order of stability is T-D > M-D > TH > M-H and above *ca.* 400 K it is M-D > T-D > M-H > T-H. Harbison's stability series is shifted to lower temperature (360-370 K) when data were calculated using optimised cell

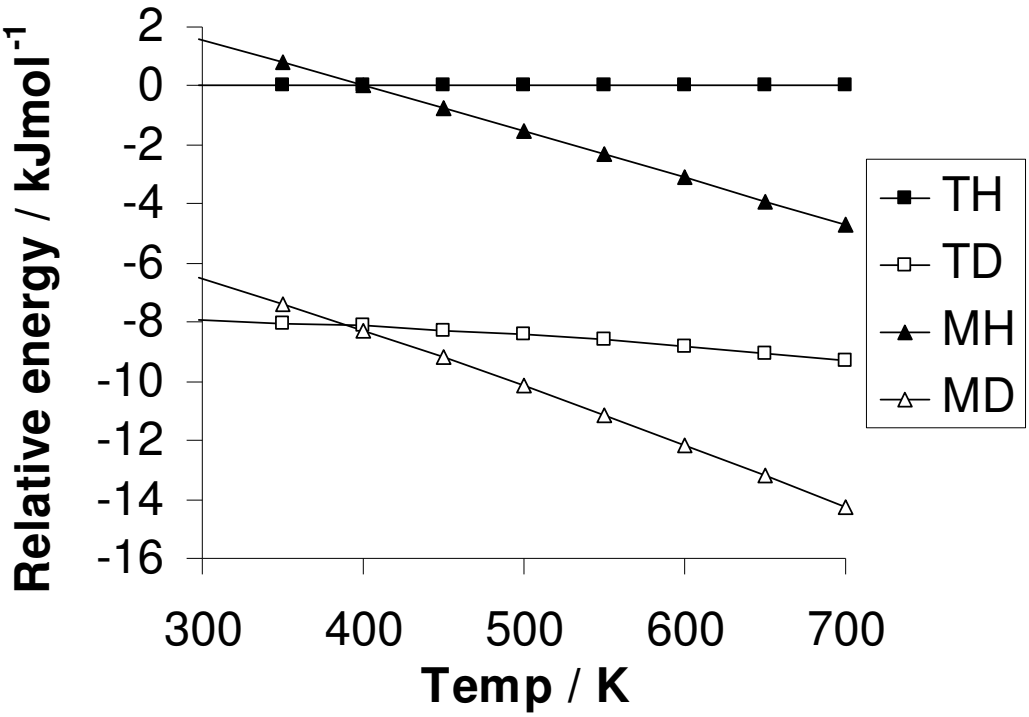

Figure 4.6. Calculated polymorph stabilities, relative to T-H, between 300 and 700 K.

dimensions. The change in the order of stability with temperature occurs because the gradients associated with the monoclinic and triclinic forms are very different.

Harbison's stability series was derived from results of polymorphism studies conducted at room temperature. The proposed stability order M-D > T-D > T-H > M-H would also apply under the same conditions, whereas the calculations indicate that it holds at *ca* 400 K. The difference is likely to be a consequence of the approximations made in calculating the frequencies, most notably the assumption of harmonic behaviour, but possibly also the neglect of phonon dispersion.

Within the harmonic approximation the difference in the energy gradients of each polymorph as a function of temperature can only be due to either the E_{vib} or TS terms as they exhibit temperature dependence. The largest contribution to these terms comes from low-frequency vibrations. Table 4.5 shows the calculated E_{vib} and TS terms at 298.15 and 700 K corresponding to the regions 0-250, 250-500 and >500 cm^{-1} for each polymorph. The Table shows that although the E_{vib} term certainly becomes more influential as temperature is increased, the TS term is mostly responsible for determining the gradients of the free energy versus temperature plots.

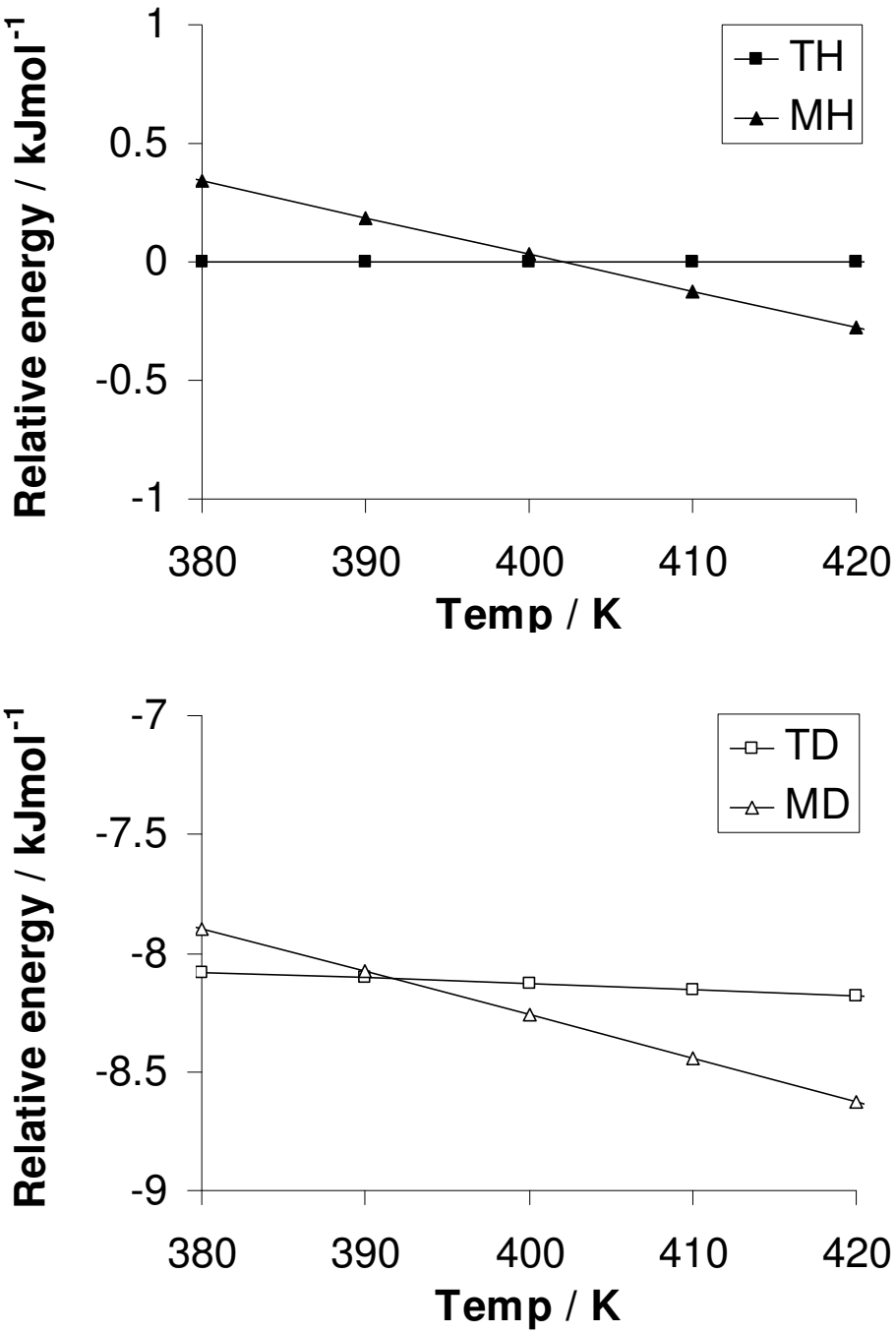

Figure 4.7. Enhanced region of Figure 4.5 (380-420 K) showing the T-H / M-H polymorphs (top) and T-D / M-D polymorphs (bottom)

Table 4.5. E_{vib} and *TS* terms for each polymorph at 298.15 and 700 K, showing the contributions from the frequency regions 0-250, 250-500 and >500 cm^{-1}. Energies are given in units of kJ mol^{-1}.

Polymorph		0-250 cm^{-1}		250-500 cm^{-1}		>500 cm^{-1}	
		298.15 K	700 K	298.15 K	700 K	298.15 K	700 K
T-H	E_{vib}	36.67	104.00	8.80	38.54	5.19	69.3
	TS	81.19	290.45	13.34	74.89	6.63	103.74
M-H	E_{vib}	36.03	100.23	9.75	41.30	5.52	71.44
	TS	83.57	291.41	15.01	81.52	7.06	107.4
T-D	E_{vib}	36.70	104.03	8.81	38.56	5.42	71.33
	TS	81.28	290.66	13.36	74.94	6.93	107.05
M-D	E_{vib}	36.68	102.46	9.45	40.82	5.53	71.66
	TS	84.70	296.41	14.42	79.84	7.06	107.72

The low-frequency vibrations at 0-250 cm^{-1} are evidently the main contributors to these terms, as would be expected.

4.3.5 Experimental conditions for growth of T-D

A consequence of the calculated free energy trends illustrated in Figure 4.6 is that the T-D polymorph evidently becomes competitive as temperature is lowered. In order to test this prediction crystallisation of MP-PCP-d_1 was carried out at 243 K. This resulted in the formation of two different types of crystal – a large quantity of rods and a smaller number of plates. The rod-like morphology is characteristic of the known M-D form. The plate-shaped crystals were identified as the sought-after T-D form on the basis of their unit cell dimensions at 150 K [*a*=7.48(2), *b*=9.11(3), *c*=13.59(4) Å, α=99.82(4), β=118.07(3) and γ=103.68(3)°], based on 69 data in the range $9.21 < 2\theta < 43.38$.

4.4 Conclusions

We have demonstrated that it is possible to crystallise isotopically normal MP-PCP from pressure in the unit cell of its deuterated analogue. That the crystal is stable, but not obtainable, at ambient conditions illustrates the potential for high pressure in crystal engineering. In the context of some other studies on molecular systems, the pressure required to grow this alternate form of MP-PCP is rather modest. At 0.41 GPa, the energetic advantage to pack with *Cc* symmetry in preference to *P*-1 is 2.17

kJ mol^{-1} which, evidently, is sufficient to drive the transformation. Therefore the proposed theory that the zero point energies (or free energies in our modelling) of the phenolic ^{1}H / ^{2}H in the triclinic and monoclinic forms are very similar appears to be correct based on the new polymorph obtained in this study.

The order of polymorph stabilities predicted by Harbison has been reproduced by periodic DFT and statistical thermodynamics calculations, albeit over a narrow temperature range at approximately 100 K higher than observed experimentally. However, the calculated relationship between polymorph stability and temperature revealed the low-temperature conditions at which the T-D polymorph is favoured. Unit cell determination of MP-PCP-d_1 grown at 243 K showed that the T-D phase had been grown. Unlike the M-H phase which has been seen in very small quantities before, the T-D phase, to the best of the author's knowledge, has never been experimentally observed before.

4.5 References

1. A. A. Khan and W. H. Baur, Acta Crystallographica, *Section B: Structural Crystallography and Crystal Chemistry*, 1973, **29**, 2721-2726.
2. S. F. Kaplan, M. I. Kay and B. Morosin, *Ferroelectrics*, 1970, **1**, 31-36.
3. T. Fujihara, M. Ichikawa, T. Gustafsson, I. Olovsson and T. Tsuchida, *Ferroelectrics*, 2001, **259**, 133-138.
4. I. Majerz, Z. Malarski and T. Lis, *Journal of Molecular Structure*, 1990, **240**, 47-58.
5. Z. Malarski, I. Majerz and T. Lis, *Journal of Molecular Structure*, 1987, **158**, 369-377.
6. T. Steiner, C. C. Wilson and I. Majerz, *Chemical Communications* (Cambridge), 2000, 1231-1232.
7. T. Steiner, I. Majerz and C. C. Wilson, *Angewandte Chemie, International Edition*, 2001, **40**, 2651-2654.
8. Z. Malarski, I. Majerz and T. Lis, *Journal of Molecular Structure*, 1996, **380**, 249-256.

9. J. Zhou, Y.-S. Kye and G. S. Harbison, *Journal of the American Chemical Society*, 2004, **126**, 8392-8393.
10. J. Zhou, Y.-S. Kye, A. I. Kolesnikov and G. S. Harbison, *Isotopes in Environmental and Health Studies*, 2006, **42**, 271-277.
11. M. T. Dove, *Structure and Dynamics: An Atomic View of Materials*, 2003.
12. R. D. L. Johnstone, A. R. Lennie, S. F. Parker, S. Parsons, E. Pidcock, P. R. Richardson, J. E. Warren and P. A. Wood, *CrystEngComm*, 2010, **12**, 1065-1078.
13. L. Merrill and W. A. Bassett, *Reviews of Scientific Instruments*, 1974, **45**, 290-294.
14. S. A. Moggach, D. R. Allan, S. Parsons and J. E. Warren, *Journal of Applied Crystallography*, 2008, **41**, 249-251.
15. G. J. Piermarini, S. Block, J. D. Barnett and R. A. Forman, *Journal of Applied Physics*, 1975, **46**, 2774-2780.
16. S. Parsons, *ECLIPSE*, The University of Edinburgh, Edinburgh, UK, 2009.
17. Bruker-Nonius, *SAINT* version 7, Program for integration of area detector data, 2006.
18. G. M. Sheldrick, University of Göttingen, Göttingen, Germany., 2008.
19. R. H. Blessing, *Journal of Applied Crystallography*, 1997, **30**, 421-426.
20. P. W. Betteridge, J. R. Carruthers, R. I. Cooper, K. Prout and D. J. Watkin, *Journal of Applied Crystallography*, 2003, **36**, 1487.
21. Agilent, *Crysalis PRO*, Agilent Technologies, Yarnton, England, 2010.
22. A. Pawlukojc, I. Natkaniec, I. Majerz and L. Sobczyk, *Spectrochimica Acta, Part A: Molecular and Biomolecular Spectroscopy*, 2001, **57A**, 2775-2779.
23. B. Delley, *Journal of Chemical Physics*, 1990, **92**, 508-517.
24. J. P. Perdew, K. Burke and M. Ernzerhof, *Physical Review Letters*, 1996, **77**, 3865-3868.
25. S. Grimme, *Journal of Computational Chemistry*, 2006, **27**, 1787-1799.
26. H. J. Monkhorst and J. D. Pack, *Physical Reviews B: Solid State*, 1976, **13**, 5188.
27. E. V. Boldyreva, T. N. Drebushchak and E. S. Shutova, *Zeitschrift für Kristallographie*, 2003, **218**, 366-376.

28. C. F. Macrae, I. J. Bruno, J. A. Chisholm, P. R. Edgington, P. McCabe, E. Pidcock, L. Rodriguez-Monge, R. Taylor, J. van de Streek and P. A. Wood, *Journal of Applied Crystallography*, 2008, **41**, 466-470.

29. J. A. Chisholm and S. Motherwell, *Journal of Applied Crystallography*, 2005, **38**, 228-231.

30. S. A. Rivera, D. G. Allis and B. S. Hudson, *Crystal Growth & Design*, 2008, **8**, 3905-3907.

Chapter 5

The Phase Behaviour of Aniline at High Pressure and Low Temperature*

*Nicholas P. Funnell, William G. Marshall and Simon Parsons, *in preparation*

5.1 Introduction

In the organic solid state, crystal packing is frequently determined by hydrogen bonding if the necessary donor and acceptor groups are present. Studies of organic compounds at high pressure, such as the amino acids, have shown that hydrogen bonds are generally quite responsive to compression as these are weaker than covalent bonds. For example, in L-alanine an intermolecular H-bond was seen to compress from 1.861(3) Å to 1.69(2) Å when 13.6 GPa of pressure was applied.[1]

It has also been seen that H-bonds can become less stabilising at high pressure if they are forced towards a repulsive region of their potential.[2, 3] Alleviation of this repulsion can potentially be achieved through reformation of the H-bonding network, sometimes even resulting in longer H-bonds.[4] The idea that H-bonding can be tuned with pressure, such that it is no longer the most influential intermolecular interaction in directing crystal packing, i.e. the most stabilising interaction, can be tested by investigating systems with weak H-bonds, such as those where the H-bond acceptor and donor atoms are nitrogen. A systematic study on intermolecular interaction energies showed that N-H···N bond strength typically ranges between 20 and 40 kJ mol^{-1}, where the equilibrium H···N distance is between 1.9 and 2.1 Å.[5] The amines, which form N-H···N bonds are ideal systems to explore the extent of stabilisation shown by these weak interactions. The effects of pressure on the crystal structure of aniline (amino-benzene) are reported.

Two disadvantages associated with directly compressing a solid sample are that the material can become kinetically trapped if there is a prohibitively high energy barrier to transformation. The second is that some materials simply do not exist as solids at ambient temperature. Crystallisation of a pure liquid or solution in-situ at high pressure enables growth of a single-crystal or powder which bypasses any potential kinetic energy barriers. Successful experiments involving *in-situ* pressure-induced crystallisation have been reported for pure liquids including pyridine, nitric acid and 1,2,3-trichloropropane and solutions which include leucine, sulphuric acid monohydrate and hydrates of sodium sulphate.[6-11]

Aniline is a small organic molecule, consisting of an amino-substituted benzene ring, which exists as a liquid under ambient conditions. It is a widely-used industrial chemical, where its major role is as a synthetic precursor for various compounds including polyurethane, paracetamol and indigo dye. Previous structural studies of aniline mostly comprise of experimental and computational determination of vibrational spectra, although the thermodynamic properties of aniline have also been explored by Takagi, measuring the ultrasonic velocity as a function of pressure and temperature.[12-14] The freezing pressure at ambient temperature is reported in the same investigation as being *ca.* 0.19 GPa.

One crystal structure of aniline has been deposited in the Cambridge Structural Database (CSD, Refcode: BAZGOY), submitted by Fukuyo *et al.*[15] The crystal was reported to grow at 252 K, crystallising in the monoclinic space group $P2_1/c$ with the cell dimensions a=21.822(8) Å, b=5.867(4) Å, c=8.386(6) Å, β=101.01(5)° and Z=8 (hereafter referred to as phase I). The crystal structure of a denser phase of aniline with orthorhombic symmetry, grown at high pressure (hereafter phase II) has been previously solved in $Pbn2_1$ (a non-standard setting of $Pna2_1$) by direct methods, described in unpublished work by Dawson and Parsons, 2000. This report describes our investigation into: 1) the effect of high pressure on the phase II structure of aniline and determination of its bulk modulus at ambient temperature, 2) the effect of subsequent decompression on the sample and whether the crystal packing proceeds via the less dense monoclinic phase before the melting transition, and 3) the effect of pressure on intermolecular interaction energies. Furthermore, we report our own low-temperature crystal growth of phase I.

5.2 Experimental

5.2.1 Sample preparation

High-pressure and low-temperature, single-crystal X-ray diffraction measurements were carried out using aniline-h_7, obtained from Sigma-Aldrich. Neutron powder diffraction measurements were carried out using aniline-d_7, obtained from CDN isotopes. Both samples were used as supplied.

5.2.2 High-pressure single-crystal X-ray diffraction data collection

Aniline-h_7 was loaded into a Merrill-Bassett diamond anvil cell (opening angle 80°), equipped with Boehler-Almax brilliant-cut diamonds with 600 μm cutlets, a tungsten gasket and tungsten carbide backing plates.[16, 17] A ruby chip was also loaded in the sample chamber so the internal pressure could be measured using the ruby fluorescence method.[18] Pressure was increased to 0.8 GPa, where crystallisation of the sample occurred. The resulting crystallites were melted back until only one remained, which was allowed to grow slowly, eventually filling the sample chamber (*ca.* 0.3 x 0.3 x 0.05 mm). Images of the crystal growth starting from a single crystallite are shown in Figure 5.1. X-ray diffraction data were collected on an Agilent Technologies SuperNova, equipped with an Atlas detector. All data collections were performed with Mo radiation, scanning about the omega circle at room temperature. Data were integrated, corrected for absorption and merged using CrysAlisPro.[19] Data collections were carried out at an initial pressure of 0.8 GPa and then at the pressures, 0.71, 0.50 and 0.27 GPa.

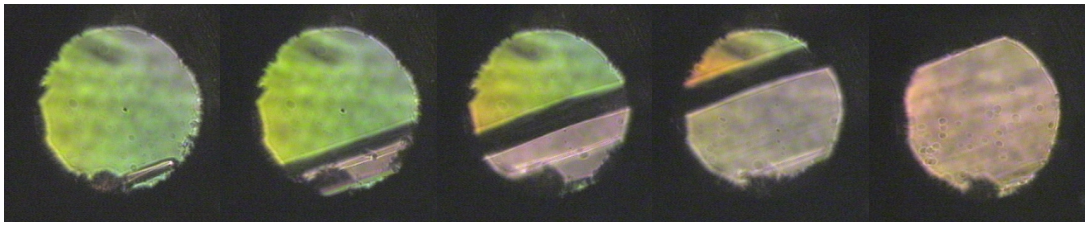

Figure 5.1. Progressive pressure-induced growth of the aniline single-crystal at 0.8 GPa. The view shown is looking directly into the diamond anvil cell sample chamber under magnification. The apparent colouration of the crystal and hydrostatic media are due to the use of a polariser.

5.2.3 High-pressure neutron powder diffraction data collection

Aniline-d_7 was mixed with a 4:1 methanol-ethanol hydrostatic medium in a 4:1 ratio and loaded into a TiZr sample gasket.[20] A CaF_2 pressure marker and SiO_2 wool, which provided multiple nucleation sites, were also included.[21]

Neutron powder data were collected using the time-of-flight technique with the PEARL beamline high-pressure diffractometer (HiPr) at the ISIS spallation source.[22, 23] Data sets between ambient pressure and 7.37 GPa were collected at approximate intervals of 0.3 GPa in the range $0.6 < d < 4.1$ Å using a V3-type Paris-

Edinburgh press equipped with zirconium-toughened alumina anvils. The sample was then decompressed and data were collected at 3.95, 2.34, 1.39, 1.11, 0.95, 0.60 and 0.33 GPa. The sample melted on further decompression and was re-crystallised by increasing pressure to 0.65 GPa. At this point phase I was present and further compression data were then collected at 0.57, 0.84 and 1.04 GPa. These pressures were calculated from the refined CaF_2 lattice parameter using a Birch-Murnaghan equation of state with V_0 =163.293 Å^3, K_0 = 81.0 GPa and K' = 5.22.[24] The value used for V_0 was 163.293470 Å^3 obtained at 0 GPa.

5.2.4 Structure refinement of the high-pressure data

Structure refinements were carried out using the program TOPAS Academic.[25] The initial coordinates of the model were derived from plane-wave density functional theory (DFT) geometry optimisations of the previously-determined high-pressure phase of aniline, using the CASTEP package.[26] Details of the computational parameters used are given below. Crystal structure refinement data for the structures at 0.74 and 7.37 GPa are available in Table 5.1.

Table 5.1. Powder refinement data for the phase II structures at 0.74 and 7.37 GPa

Pressure / GPa	**0.74**	**7.37**
Sample and radiation type	Neutron powder	Neutron powder
Chemical formula	C_6D_7N	C_6D_7N
M_r / g mol^{-1}	100.17	100.17
Cell setting, space group	Orthorhombic, *Pna*2$_1$	Orthorhombic, *Pna*2$_1$
a / Å	8.2044(7)	7.5203(9)
b / Å	5.7091(7)	5.2718(10)
c / Å	21.012(3)	19.579(3)
V / Å^3	984.2(2)	776.2(2)
Z	8	8
D_c / Mg m^{-3}	1.352	1.714
d_{max}, d_{min} / Å	0.6, 4.1	0.6, 4.1
Pawley R_{wp}	2.924	3.205
R_{wp}	4.012	4.714
S	0.888	0.854
Reflection / profile data	2598	2598

The Pawley method was used to obtain unit cell dimensions for all pressure points listed above. A single joint-Rietveld refinement was performed on all the phase II neutron powder data between ambient pressure and 7.37 GPa, and the high-pressure X-ray single crystal data at 0.8 and 0.71 GPa. A Z-matrix formalism was used for each dataset, where the molecule is described in terms of bond distances and angles rather than fractional coordinates. An orthorhombic starting model for the neutron powder data was derived from a DFT optimisation of the monoclinic structure BAZGOY. The numbering scheme for the asymmetric unit of aniline used is shown in Scheme 5.1.

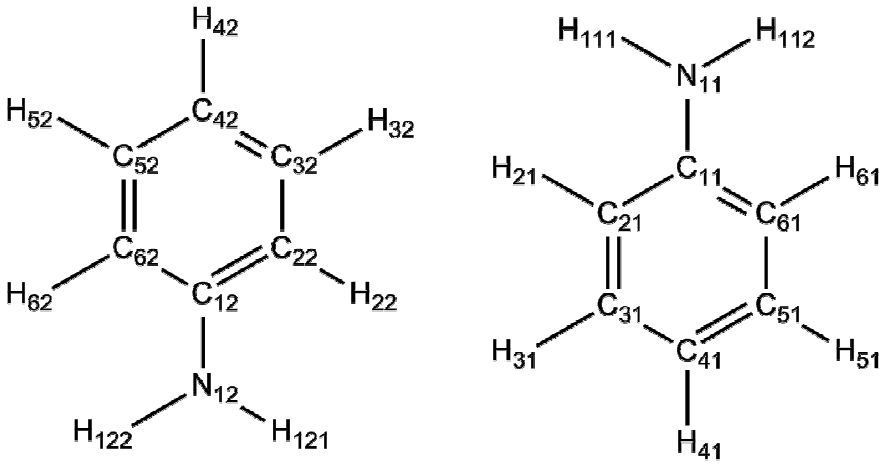

Scheme 5.1. Molecular structure of aniline and the numbering scheme used.

The C-C bond lengths and associated angles and the C-N bonds were each modelled by a single global parameter that was refined against all data. Similar parameters were used for the C-H and N-H distances and H-C-C angles but these were held fixed to average values derived from DFT optimisations and single-crystal experiments.

The four H-N-C-C dihedral angles (per asymmetric unit) were restrained to have a quadratic relationship with pressure where the three constants associated with each equation were held fixed to the same values across all datasets. The values used for these equations were derived from trends observed in DFT optimisations.

The N atom was permitted to deviate from the plane of the aromatic ring, by allowing refinement of global parameters corresponding to the C61-C11-N11-C21 and C62-C12-N12-C22 torsion angles although these were constrained to show a linear dependence on pressure. The initial constant terms were set to -174 and 174°, found from single-crystal diffraction and the gradients were set to 0.0594 and -0.1428 respectively, observed in DFT optimisations. Both the constants and gradients were refined against all data. A single parameter was refined for the H-N-C angles within each dataset, which was restrained against the average value observed in the DFT optimisations at the relevant pressure.

Also included in the powder pattern modelling were structural data for CaF_2 (the pressure marker) and Al_2O_3 and ZrO_2 (components of the Paris-Edinburgh cell anvils). In several datasets the refinement of the ZrO_2 line shape was unstable and so a single line shape parameter was refined for all data.

The phase I compression data were processed in a separate joint refinement. Here, the H-N-C-C dihedral angles and H-N-C angles were refined in each individual dataset but were restrained against the values seen in the DFT optimisations. A single global parameter was refined for each angle and torsion associated with the C-N deformation. Similarly to the phase II data, a single parameter for the ZrO_2 line shape was refined for all data.

5.2.5 Low-temperature single-crystal growth, X-ray diffraction data collection and refinement

Aniline-h_7 was sealed in a glass capillary with an inner diameter of *ca.* 0.12 mm and was mounted on a Bruker three-circle Apex II diffractometer equipped with an Oxford Cryosystems low temperature device. The sample was cooled to 257 K; 10 degrees below the melting point and flash-frozen with liquid nitrogen to yield a polycrystalline mass. An OHCD Laser Assisted Crystal Growth Device was then used to obtain a single crystal, using Boese's zone-melting method.[27]

Data collections were carried out at 150 and 100 K using Mo radiation. The data were integrated in SAINT and corrected for absorption by SADABS.[28, 29] The structure was solved using SIR92.[30] Refinements were performed against F^2 in CRYSTALS.[31]

5.2.6 DFT calculations

Geometry optimisations were performed by plane wave Density Functional Theory (DFT) using the CASTEP code. The PBE exchange-correlation functional was used with soft pseudopotentials generated by the program.[32] A plane-wave basis set with E_{max} = 600 eV was used and Brillouin zone integrations were performed by Monkhorst-Pack k-point sampling at intervals of 0.1 $Å^{-1}$.[33] The effects of dispersion were corrected for using the G06 semi-empirical dispersion correction scheme.[34] The unit cell dimensions were held fixed at the experimentally observed values. The total energy convergence was 10^{-8} eV per atom, the maximum force tolerance was 0.005 eV $Å^{-1}$ and the maximum stress tolerance was 0.005 GPa. The initial Rietveld refinements of the neutron powder data were used to provide starting coordinates for optimisations of both the monoclinic and orthorhombic forms of aniline.

5.2.7 Frequency Calculations

Geometry optimisation and frequency calculations on the experimentally determined structures were performed using plane-wave DFT using DMOL, implemented in Accelry Materials Studio.[35] The BLYP exchange-correlation functional was used.[36, 37] The DNP basis set was used and Brillouin zone integrations were performed by Monkhorst-Pack k-point sampling at intervals of 0.07 $Å^{-1}$. The total energy convergence was 10^{-5} Ha per atom, the maximum force tolerance was 0.002 Ha $Å^{-1}$ and the maximum displacement was 0.005 Å. The calculated frequencies for phase I aniline show rather good agreement with frequencies determined by inelastic neutron scattering (INS) data on the same phase, collected by Herzog-Cance *et al*, demonstrating the reliability of the calculations.[38] An overlay of the calculated and experimental spectra is shown in Figure 5.2.

5.2.8 PIXEL calculations

The final neutron powder crystal structures were used to calculate the molecular electron densities of phase II at 0.74 and 7.37 GPa. Calculations were carried out with the program GAUSSIAN09 at the MP2 level of theory with the 6-31G** basis

set.[39] The electron density was used with the program OPiX to calculate the intermolecular interaction energies.[40]

5.2.9 Other programs used

Structures were visualised using Mercury CSD 2.3.[41] Images of the diamond anvil cell sample chamber were recorded using IC capture. The bulk modulus was calculated using EOSFIT.[42]

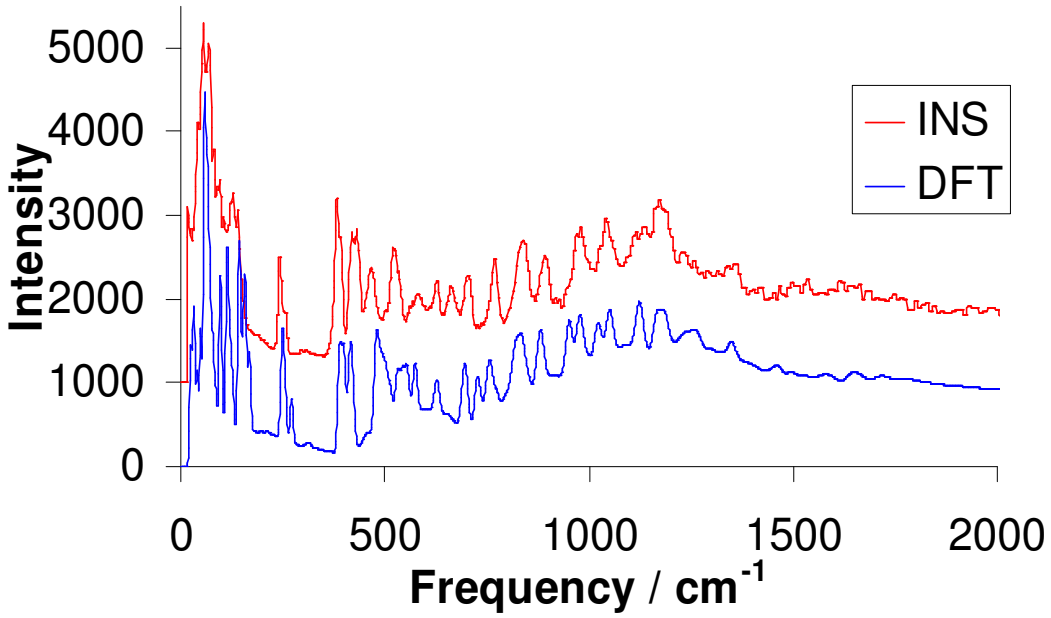

Figure 5.2. Overlay of the experimentally determined INS spectra for phase I aniline with the spectra calculated by DFT

5.3 Results

5.3.1 Crystal packing of phase I and II and their structural relationship

The molecules are approximately planar except for the hydrogen atoms on the amino group, which are displaced to one side of the aromatic plane and the C-N bond which is displaced from the plane of the aromatic ring. This geometry is predicted by plane-wave DFT and has been seen experimentally via spectroscopy and diffraction studies (by Fukuyo *et al* and our own structure determinations reported here). The neutron powder data are not sensitive enough to allow unrestrained refinement of the C-N deformation. However, a marked improvement was seen in the R-factor of the single

crystal data when the C61-C11-N11-C21 and C62-C12-N12-C22 torsion angles were allowed to refine from values previously fixed at 180°. The effect of refinement caused the N atom to move out of the mean plane by 0.114 and 0.125 Å in the two molecules.

Figure 5.3 shows the crystal packing of phases I and II, at 150 K and 0.8 GPa respectively, projected along the *b*-axis. In phase II, the aniline molecules are arranged in layers in the *ab* face, stacking along the *c*-axis. Within each layer the aniline molecules are arranged in two distinct orientations with respect to the *b*-axis. Molecules of alternate orientation are held together by N-H···π-face interactions (N11-H111 and N12-H121). Each molecule is related to neighbouring molecules along *a* by *a*-glides perpendicular to *b*. Adjacent layers of molecules are not symmetry related (molecules are coloured by symmetry-equivalence in Figure 5.3). Each layer forms hydrogen bonds to one of the neighbouring layers (N11-H112···N12 and N12-H122···N11) and interacts via dispersive forces with the other layer.

The crystal packing of phase I is deceptively similar to that of phase II. Here, the layers of aniline molecules are not stacked alternately by symmetry equivalence. The presence of inversion centres results in crystallographically-equivalent layers being arranged in pairs along the *c*-axis instead. This means that the two structures are non-superimposable despite the apparent similarity. Four layers of each structure can be overlaid successfully – indicated by brackets in Figure 5.3 - but the next four in either direction along the *c*-axis cannot as the molecules in these layers are mirror images of each other. Figure 5.4 shows this feature in more detail.

5.3.2 The effect of pressure on the unit cell dimensions: neutron powder diffraction

The liquid aniline sample crystallised between ambient pressure and 0.714 GPa in $Pna2_1$ with cell dimensions *a*=8.2044(7) Å, *b*=5.7090(7) Å and *c*=21.012(3) Å. Pressure was then increased by raising the applied load in increments of three tonnes until a final pressure of 7.37 GPa was attained where the cell dimensions measured *a*=7.5203(10) Å, *b*=5.2718(10) Å and *c*=19.579(3) Å, indicating that the *a*, *b* and *c*-axes compress by 8.34, 7.66 and 6.84% respectively. The volume was found to compress by 21.13%. The crystal structure of aniline at this pressure is shown in

Figure 5.5. The corresponding powder diffraction patterns for these pressure points and the Rietveld fit to the data are shown in Figure 5.6.

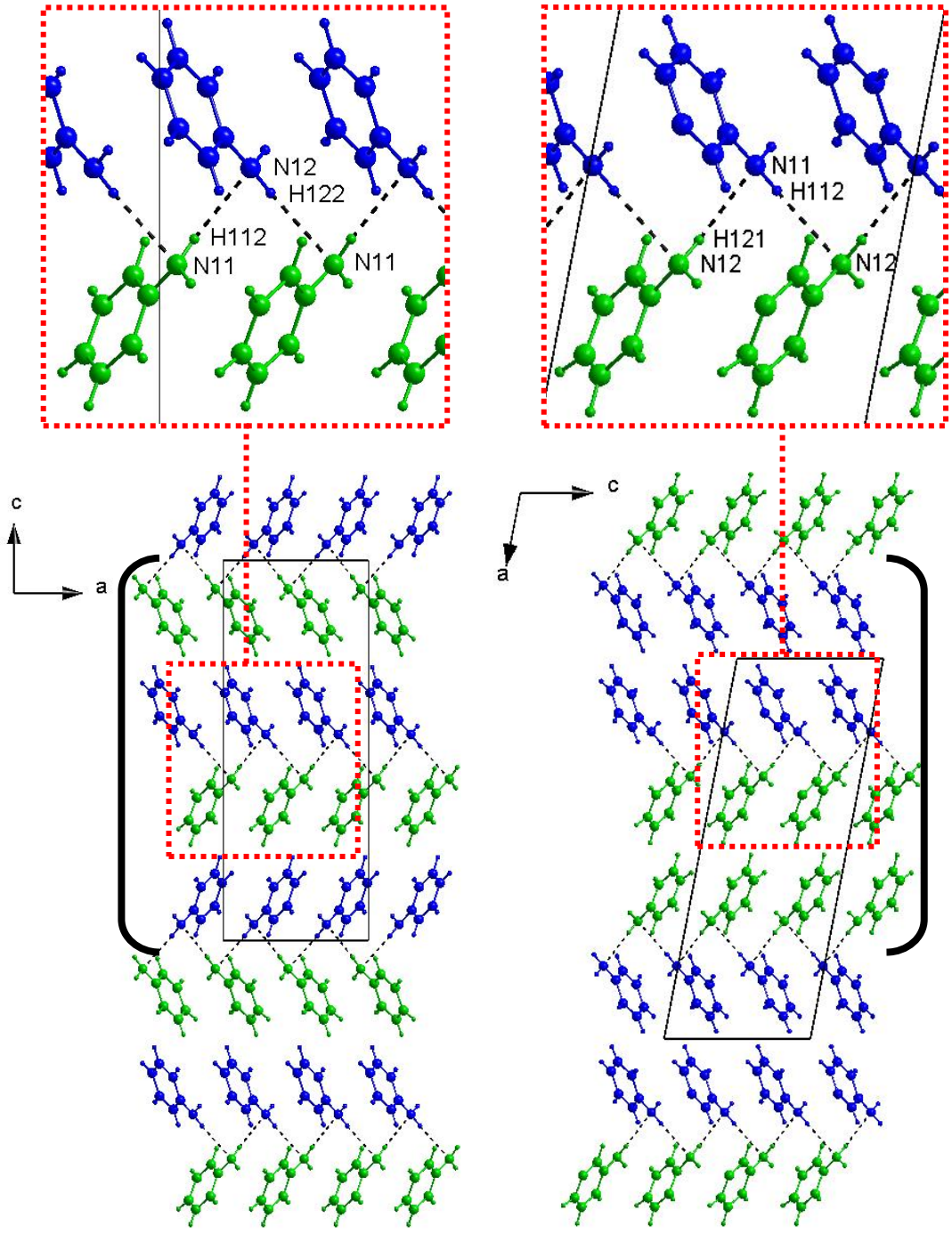

Figure 5.3. Crystal structures of phase II at 0.8 GPa (left) and phase I at 150 K (right) projected along the *b*-axis. Molecules are coloured by symmetry equivalence. The brackets indicate the layers of phase I and II that are superimposable. The next four layers in either direction along **c** are non-superimposable. Hydrogen bonds are represented by black dotted lines.

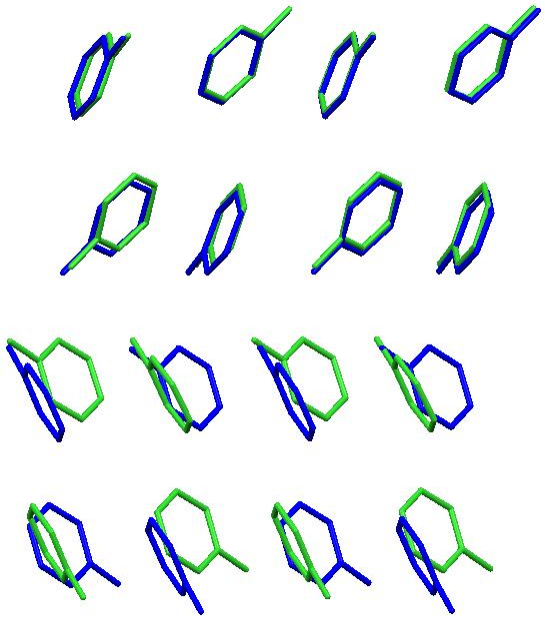

Figure 5.4. Overlay of phase I (blue) with phase II (green). Hydrogen atoms have been removed for clarity. The top two layers show overlapping molecules and the lower two show molecules that are related by a mirror located approximately in the plane of the page.

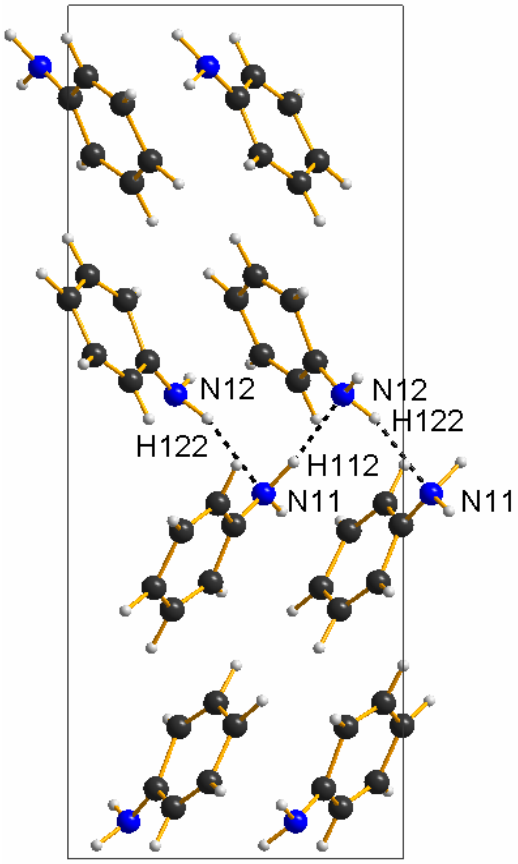

Figure 5.5. The unit cell of phase II at 7.37 GPa. Hydrogen bonds are represented by black dotted lines

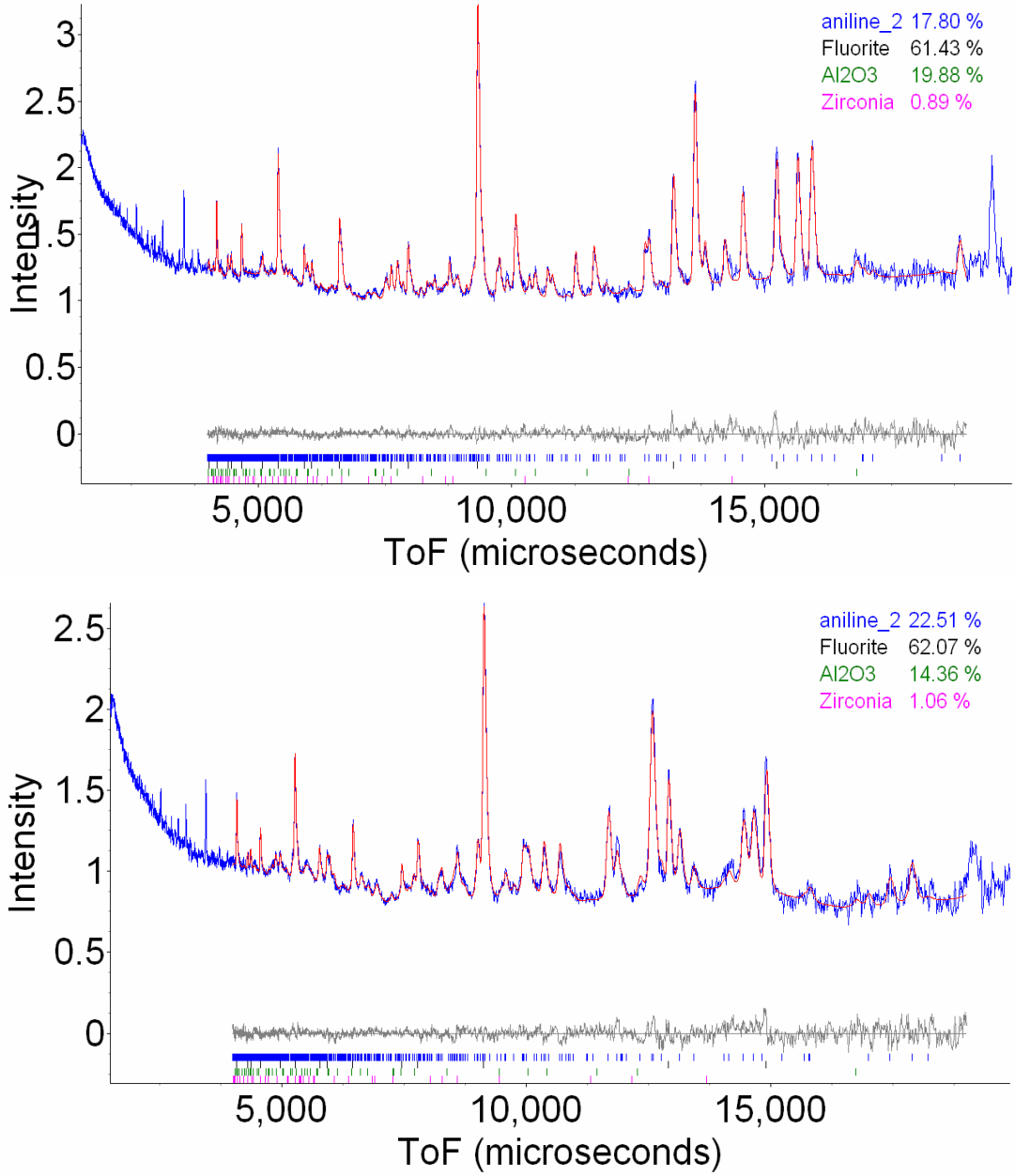

Figure 5.6. Powder diffraction patterns and the Rietveld fit to the data at 0.74 GPa (top) and 7.37 GPa (bottom). The minimum and maximum d-spacing used for both datasets are 0.6 and 4.1 respectively

The pressure was then released to 3.95 GPa, where the powder pattern showed no change in phase. Additional short datasets (of sufficient quality to identify the crystal phase) were collected between this pressure and *ca.* 0.3 GPa. The cell dimensions on decompression followed the same trend, as they did on compression, showing little evidence of hysteresis. Plots of the cell axes as a function of compression and decompression are shown in Figure 5.7. At 0.33 GPa, the diffraction pattern could be indexed as a mixture of phases I and II.

Further decompression induced melting in the sample, at which point pressure was reapplied to 0.648 GPa. The pattern obtained at this pressure was solely that of phase I, with cell dimensions a=21.460(7) Å, b=5.7329(5) Å, c=8.2274(5) Å and β=100.962(9)°. Data were then collected at 0.84 and 1.06 GPa, where the sample simply became a more compressed version of the monoclinic form.

5.3.3 The effect of pressure on the unit cell dimensions: single-crystal X-ray diffraction

When grown at 0.8 GPa, aniline crystallised in the orthorhombic space group $Pna2_1$, with unit cell dimensions a=8.1757(14) Å, b=5.6902(3) Å and c=20.9980(9) Å. As pressure was decreased to 0.71 and then 0.50 GPa the crystal became a less compressed version of the structure at 0.8 GPa (a=8.205(9) Å, b=5.7371(14) Å and c=21.022(6) Å). The crystal cracked as the pressure was reduced. 0.27 GPa was the lowest pressure at which data could be collected however the diffraction pattern was of poor quality and could not be indexed. Images of the single crystal at various pressures are shown in Figure 5.8.

5.3.4 The effect of temperature on the cell dimensions of monoclinic aniline

Following crystallisation at 257 K, the aniline sample was cooled to 150 K where the cell dimensions were recorded as being a=21.6354(8) Å, b=5.8253(2) Å, c=8.33002(3) Å and β=101.069(3)°. When cooled to 100 K, the cell dimensions were a=21.5674(8) Å, b=5.8052(2) Å, c=8.2949(3) Å and β=101.043(2)°.

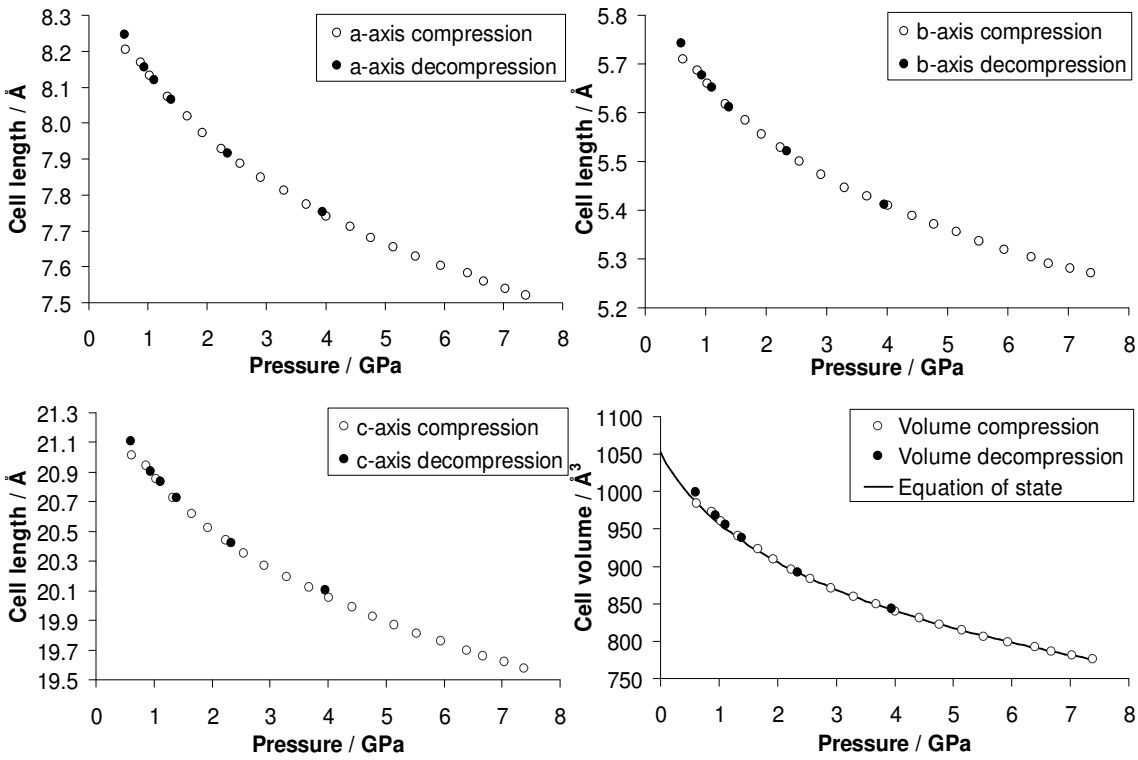

Figure 5.7. The cell dimensions and volume plotted as a function of pressure. A 3rd-order Birch-Murnaghan equation of state, derived from the data collected on compression is fitted to the cell volume plot. The standard deviations on the measurements are within the size of the data points.

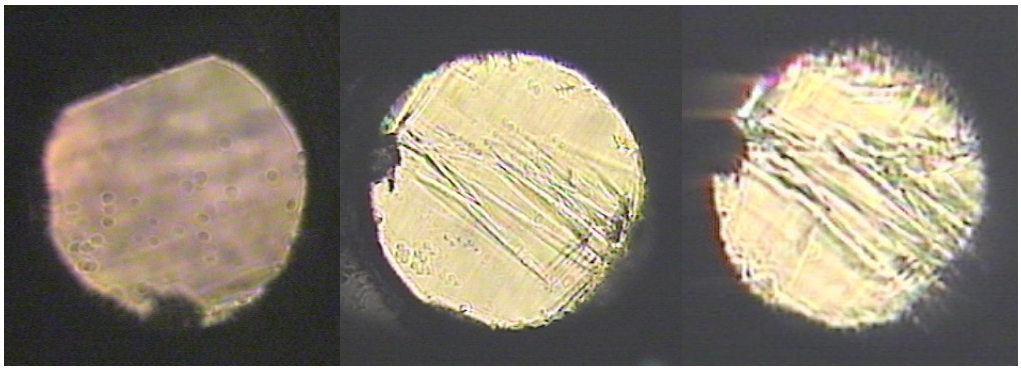

Figure 5.8. Images of the crystal in the sample chamber at 0.8 GPa (left), 0.50 GPa (centre) and 0.27 GPa (right). The crystal surface becomes increasingly cracked as pressure is decreased. The dark object at the edge of the cell chamber is the ruby chip

5.3.5 Structural comparison of low-temperature and high-pressure phase I

The phase I structure collected at 100 K shows a high degree of similarity with the geometry optimised phase I structure collected at 0.84 GPa. The optimisation was

performed due to a relatively poor signal-to-noise ratio in the powder pattern. The cell dimensions are similar – the greatest difference is seen in the *a*-axis, which is shorter in the high-pressure structure by 0.21 Å. The hydrogen bonds (based on the N···N distances due to the uncertainty of H location by X-rays) are longer in the low temperature data, measuring 3.323 and 3.173 Å, *c.f.* 3.302 and 3.126 Å at high pressure. The deformation of the N atom from the mean aromatic plane is marginally greater for the optimised high-pressure structure than the low-temperature form. The distances of the N atoms from the mean planes are 0.107 and 0.108 Å for the 100 K structure and 0.107 and 0.116 Å in the high-pressure form.

5.4 Discussion

5.4.1 Treatment of specific intramolecular parameters

The powder data used in this experiment are medium-resolution and consequently there was a need to constrain the majority of the molecular geometry of the aniline model. A greater degree of freedom was permitted for refinement of the NH_2 group and the C-N bond. The sources of the restraints used in the Rietveld refinement are the single-crystal refinements at high pressure and the calculated geometry of molecules optimised by plane-wave DFT. The DFT optimisations were carried out with fixed unit cell axes, starting from experimental coordinates derived from the preliminary, unrestrained, neutron powder refinements. DFT-derived restraints have been used previously to assist high-pressure powder refinement and a justification of treating data in this way is given in these investigations.[43]

It is well established that the C-N bond deviates from the mean plane of the aromatic ring. The single-crystal data at 8 kbar reported here show this to be 5.5 and 6.1° for the two molecules in the asymmetric unit. The DFT optimisations for each pressure point show that the extent of deformation varies linearly as a function of pressure, increasing by *ca.* 0.64 and 0.91° over the course of compression to 7.37 GPa. However, the absolute values of the angles are underestimated at low pressure by 2.6 and 2.46° respectively. Therefore the angles observed in the single crystal data at 8 kbar (-174 and 174°) were used as starting values for the intercepts in the linear relationships describing the C-N deformation. The value of τC61-C11-N11-C21

refined to -174.47(11)° at 0.74 GPa and -177.2(5)° at 7.37 GPa, becoming more planar with pressure. τC62-C12-N12-C22 appeared to become marginally less planar between 0.74 and 7.37 GPa, refining to 173.94(12) and 173.4(6) GPa respectively although this is not a significant change. A combination of the C-N deformation and the τH-N-C-C angle change (treated with a quadratic restraint to pressure) prevents short H···H contacts from occurring in the crystal structure between the H112 and H51 atoms. The energy contributions of this specific dimer interaction are discussed in more detail below.

5.4.2 Bulk modulus of phase II

The bulk modulus (K_o) of phase II was found to be 6.980(19) GPa, derived from a third-order Birch-Murnaghan equation of state, fitted to the powder diffraction compression data.[44] The values of K' and V_0 refined to 9.16(4) and 1052.5(3) Å^3 respectively. Owing to the lack of structural data at ambient pressure, a value for V_0 was extrapolated from a third-order polynomial fit to datasets below 3.678 GPa where it was found to be 1052.4 Å^3. The bulk modulus indicates that aniline is rather compressible, most likely a reflection of the relatively weak intermolecular interactions - *c.f.* the bulk modulus of L-alanine, 13.1(6) GPa; a system which possesses strong intermolecular interactions but is still considered to be rather compressible.[1]

5.4.3 Preferred directions of compression

The principal axes of the orthorhombic unit cell coincide with those of the strain tensor. The compressibility of the cell axes is of the order $a > b > c$, although there is only a small difference between the three; a is only 1.5% more compressible than c. This near-isotropic compression of the cell is likely to be a result of all significant intermolecular interactions being aligned approximately between all three cell axes. Only the hydrogen bonds appear to be poorly aligned with the b-axis, lying approximately in the ac plane.

5.4.4 Evaluation of specific dimer energies in phase II

The PIXEL method, developed by Gavezotti, enables computational determination of both lattice and dimer energies by considering whole molecule-molecule interactions rather than atom-atom interactions.[45] The energies can be broken down into individual, chemically meaningful, contributions from Coulombic, polarisation, dispersive and repulsive forces. The specific dimers described here have been given the labels 'AA', 'AB' or 'BB' depending on whether they are symmetry-related or not, i.e. 'AB' refers to a dimer consisting of symmetry-independent molecules. Each dimer interaction is numbered and illustrated in Figure 5.9.

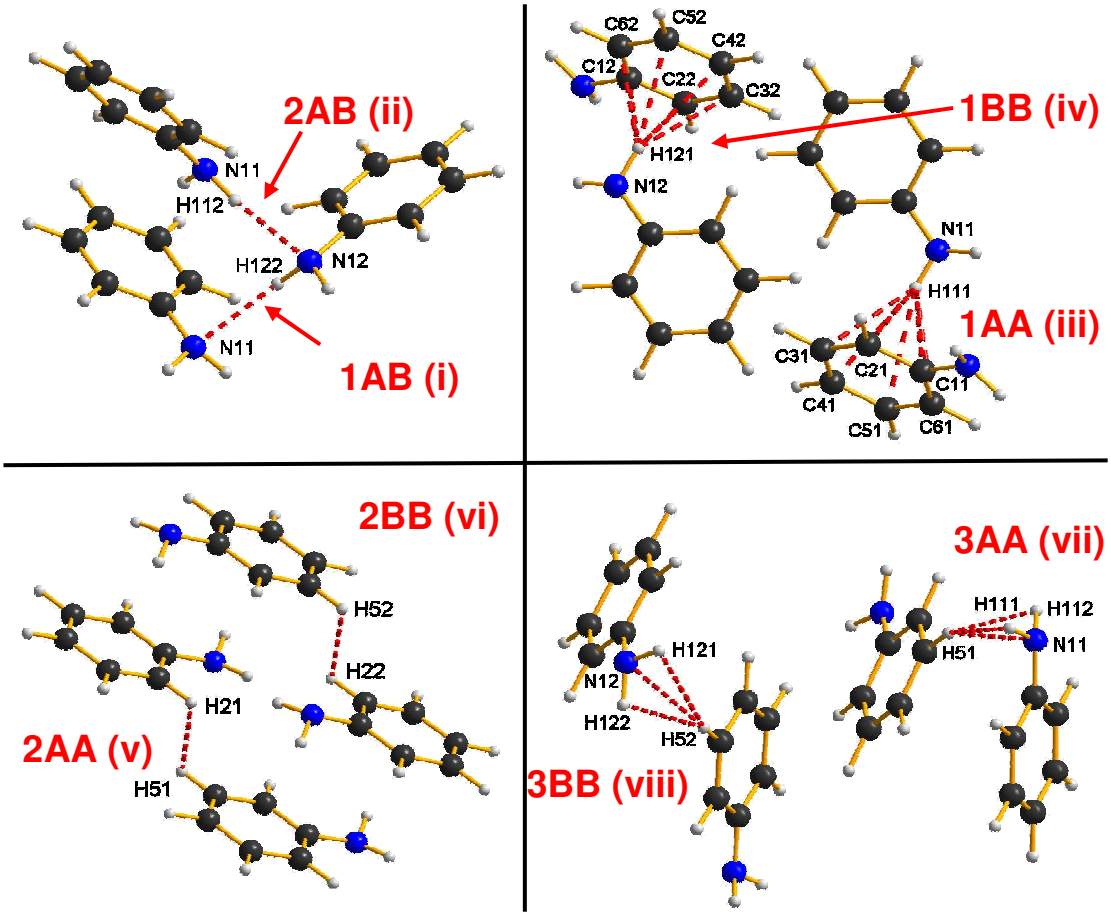

Figure 5.9. Significant intermolecular interactions identified by PIXEL. Red dotted lines indicate the primary region of the interaction. Roman numerals corresponding to symmetry operators are given in parentheses. Symmetry operators: (i) 1-x, 1-y, 1/2+z. (ii) 1/2-x, -1/2+y, 1/2+z. (iii) -1/2+x, 1/2-y, z. (iv) -1/2+x, 3/2-y, z. (v and vi) x, 1-y, z. (vii) -1/2+x, 3/2-y, z. (viii) -1/2+x, 1/2-y, z.

PIXEL shows that despite both the aniline molecules in the asymmetric unit appearing to possess relatively similar environments, they exhibit different responses to compression. PIXEL lattice energies and specific dimer energies for the interactions discussed below, at 0.74 and 7.37 GPa are given in Table 5.2.

Table 5.2. PIXEL specific dimer energies and lattice energies at 0.74 GPa and 7.38 GPa, given in units of kJ mol^{-1}. Each total energy is broken down into its separate Coulombic, polarization, dispersive and repulsive components.

Pressure / GPa	0.74 GPa				
	Coul	**Pol**	**Disp**	**Rep**	**Tot**
1AB	-12.1	-7.3	-17.3	22.5	-14.2
2AB	-21.4	-9.6	-12.9	32.4	-11.6
1AA	11.7	-4.8	-17.1	13.9	-19.8
1BB	-11.5	-4.6	-16.6	13.0	-19.7
2AA	-7.4	-2.7	-14.1	11.7	-12.5
2BB	-9.0	-3.6	-16.0	15.6	-13.0
3AA	-5.0	-3.8	-18.9	20.2	-7.6
3BB	-1.2	-2.0	-14.2	9.2	-8.2
Lattice energy	-94.2	-42.5	-175.2	165.3	-146.6

Pressure / GPa	7.37 GPa				
	Coul	**Pol**	**Disp**	**Rep**	**Tot**
1AB	-26.0	-15.0	-25.0	54.4	-11.7
2AB	-39.4	-23.0	-18.8	82.6	1.5
1AA	-32.0	-18.6	-34.1	73.4	-11.4
1BB	-24.5	-12.0	-28.4	47.7	-17.2
2AA	-19.9	-9.3	-25.4	45.9	-8.8
2BB	-38.9	-29.8	-40.8	121.3	11.7
3AA	-36.8	-25.6	-39.1	121.4	19.9
3BB	-6.2	-7.3	-23.7	37.2	0
Lattice energy	-274.0	-163.5	-325.7	714.5	-48.7

At 0.74 GPa, the strongest attractive interactions are 1AA and 1BB – where H111 and H121 are oriented towards the aromatic ring of a neighbouring symmetry-related molecule. PIXEL calculates these energies as -19.8 and -19.7 kJ mol^{-1} respectively.

Compression to 7.37 GPa causes the energies of 1AA and 1BB to increase to -11.4 and -17.2 kJ mol^{-1} respectively.

The second strongest interactions are the hydrogen bonds, N12-H122···N11 (1AB) and N11-H112···N12 (2AB) which have respective energies of -14.2 and -11.6 kJ mol^{-1}. The H···N distances are 2.485(2) and 2.305(2) Å respectively. Over the course of compression, 1AB decreases to 2.229(17) Å giving a final total energy of -11.7 kJ mol^{-1}. The total energy of 2AB increases by a much larger amount, such that it becomes destabilising (1.5 kJ mol^{-1}) at the highest pressure attained where the N12···H112 distance measures 1.913(2) Å. This large energy increase, mainly due to the repulsive term which increases by 50.2 kJ mol^{-1}, actually renders the H-bond one of the weaker attractive interactions at high pressure; 1AA, 2AA, 1AB, 1BB, and 3BB are all more stabilising at 7.37 GPa. The increased repulsive contribution is likely to be due to the decreasing H-bond length but it is not abnormally short in the context of N-H···N contacts in the CSD which show a minimum distance of *ca.* 1.84 Å.

2AA and 2BB are formed between molecules related by unit cell translations along *b*. Both interactions are initially stabilising at 0.74 GPa, measuring -12.5 and -13 kJ mol^{-1} for 2AA and 2BB respectively. Whereas the energy of 2AA increases by only 3.7 kJ mol^{-1} at high pressure, 2BB increases by 24.7 kJ mol^{-1} making the overall energy of 2BB repulsive, measuring +11.7 kJ mol^{-1}. The development of close contacts between aromatic H-atoms (the shortest of which at 7.37 GPa is 2.16(5) Å) is the most likely explanation for this observation.

The remaining notable interactions, 3AA and 3BB are mostly comprised of dispersive contributions originating from the close proximity of the NH_2 group to H-atoms of a nearby aromatic ring. The 3BB interaction energy increases by a moderate amount, measuring -8.2 kJ mol^{-1} at 0.74 GPa and 0 kJ mol^{-1} at 7.37 GPa. The effect of pressure on the 3AA interaction is more significant, changing from -7.6 kJ mol^{-1} to 19.9 kJ mol^{-1}; the largest change observed for any of the dimer interactions.

Whilst the Coulombic, polarisation and dispersive contributions to this interaction decrease in energy by 31.8, 21.8 and 20.2 kJ mol^{-1} respectively, it is an increase of 101.2 kJ mol^{-1} in repulsive energy, which is ultimately responsible for the total energy increase. This can be attributed to the short contacts H51···H112 (1.71(3)

Å) and H52···H122 (2.22(4) Å) at 7.37 GPa, highlighted in Figure 5.9. The former of these approaches an H···H contact lower-limit of 1.7 Å identified by Wood *et al* for organic crystal structures up to 10 GPa, hence the large increase in repulsive energy.[46]

The fact that the 1AA and 1BB interactions are the strongest present in the crystal structure, even at the lowest pressure studied, show that the N-H···N hydrogen bonds are not the most influential interactions in the context of directing crystal packing. This has been seen before in a systematic assessment of the dimer energies in the crystal structures of the primary amines. The idea proposed in the *Introduction* that H-bonds can become destabilising with pressure has clearly been demonstrated here. Both the 1AB and 2AB interactions become less stabilising with increasing pressure and the 2AB in particular becomes destabilising. Given that neither H-bond is observed to become unfavourably short further highlights the importance of dispersion interactions in stabilising organic crystals that have weak H-bonds.

5.4.5 Phase II → I transition

The unit cell dimensions of phase I at 150 K (a=21.6354(8) Å, b=5.8253(2) Å, c=8.33002(3) Å and β=101.069(3) °) are similar to those of the structure obtained at 0.8 GPa (a=8.1757(14) Å, b=5.6902(3) Å and c=20.9980(9) Å). This similarity led to the initial hypothesis that phase II could be transformed to phase I by slow decrease of pressure as phase I has a larger molecular volume (128.79 Å^3) than the orthorhombic cell (122.11 Å^3). The use of pressure to obtain denser crystal polymorphs has been successfully demonstrated previously; for example in serine monohydrate, ammonium perchlorate and 1,1,2,2-tetrachloroethane.[47-49]

Reflections corresponding to phase I could not be indexed in the single-crystal sample, where the crystal eventually melted on decompression at *ca.* 0.27 GPa. The lowest pressure for which 3-D data were collected and a model refined was 0.5 GPa, however the crystal was still unambiguously the phase II polymorph. The crystal became visibly cracked over the period of decompression, as shown in Figure 5.8, accompanied by deterioration in the quality of the diffraction pattern. This was interpreted as the crystal structure attempting to undergo an evidently reconstructive phase transition, but destroying itself in the process.

The neutron powder diffraction experiment allowed the transition to be observed, where the powder pattern at 0.33 GPa could be indexed as a mixture of both phases. The respective diffraction patterns of the two phases are very similar to each other, making it hard to distinguish the appearance of phase I. Identification of two small peaks, unaccounted for by phase II, were attributed to overlapping reflections of phase I; the [4-1-3], [113], [4-1-1] and [311] reflections. These peaks are shown in Figure 5.10 in a magnified region of the refined powder pattern at 0.33 GPa.

After recompression and re-crystallisation of the aniline sample following the melting transition below *ca.* 0.3 GPa, the powder pattern could only be indexed on a monoclinic cell. This phase persisted up to at least 1.04 GPa where it was not investigated further owing to experimental time constraints. The existence of phase I to this pressure identifies a region on the aniline phase diagram where both polymorphs are stable.

5.4.6 Suggested transformation pathways

The non-superimposable layers between phase I and II are displaced by a half-unit cell translation along the *a*-axes and *b*-axes (with respect to phase II). The transition only appears possible through one of two potential rearrangements. Either the layers could slide across each other in the *ab* direction by *ca.* 5 Å or all the molecules within one layer could be rotated by *ca.* 130° about an axis aligned between the *a*- and *c*-directions. However, in order for layer-sliding to occur, the hydrogen bonds would all have to be broken and remade. Secondly, short H···H contacts could result as the amino groups of molecules in neighbouring layers slide past each other. If this were the case, slight expansion of the *c*-axis could be required. The phenomenon of negative compressibility in cell dimensions has been reported before but it is uncommon. If the transition proceeded via molecular rotation instead, the hydrogen bonds could remain intact. However, each molecule would have to rotate in the opposite direction with respect to its neighbours along the *a*-axis, probably resulting in unfavourably short intermolecular contacts.

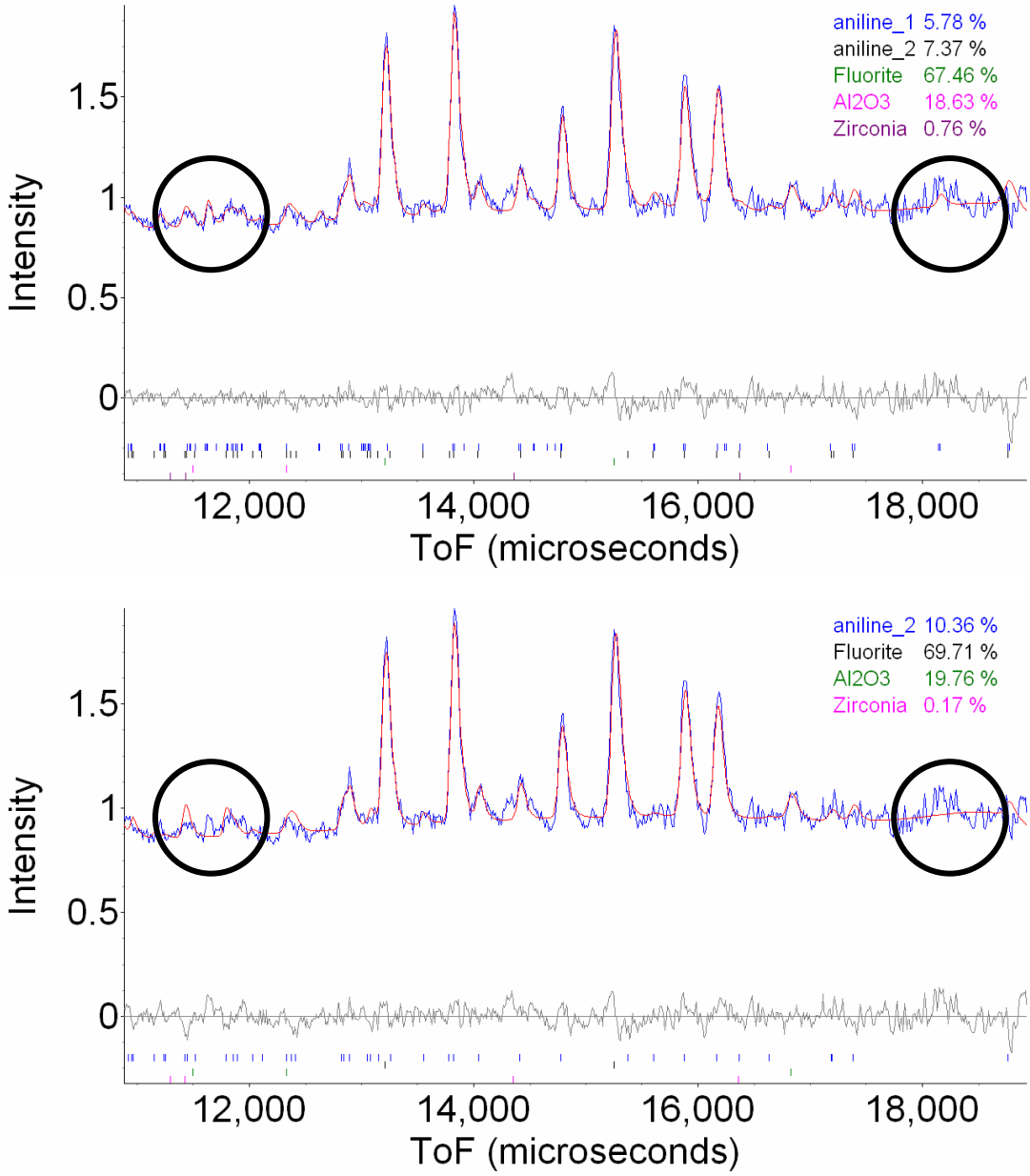

Figure 5.10. Magnified region of the refined powder pattern for mixed phase aniline at 0.33 GPa (top). The circled regions indicate the peaks that are solely attributed to phase I. The pattern at the bottom shows the fit when modelled as phase II only.

5.4.7 The relative stabilities of phases I and II

The thermodynamic relationship between phases I and II, at 0.84 and 0.87 GPa respectively, was estimated from statistical frequencies calculated using plane-wave DFT. The BLYP functional has been reported to reproduce the experimental spectra

of aniline better than other DFT functionals and so it was used to perform the calculations here.[14] Both structures were geometry optimised in DMOL using space group symmetry and then allowed to relax in *P*1 prior to frequency calculation in *P*1. Unit cell dimensions were held fixed to experimental values.

Polymorph stability is determined by Gibbs free energy, $G = U + PV - TS$, where the symbols have their usual thermodynamic meanings. Frequently, the calculated lattice energy is used to rationalise relative polymorph stabilities.[50, 51] However, it has been shown that it is important to also consider the effect of temperature on free energy; the role of entropy (which becomes significant above 0 K) in molecular systems should not be ignored.[2] The polymorph stability has been calculated here on the basis of DFT energy, zero point energy, vibrational enthalpy, and the *PV* and *TS* terms. The total free energy and a breakdown into the individual contributions are given in Table 5.3.

The calculations suggest that phase I is actually more stable by 2.4 kJ mol^{-1} at *ca.* 0.85 GPa and 298 K. This is contrary to the experimental observation that phase II is obtained on application of pressure to the liquid phase. The energy difference between the two forms is relatively small, showing that they are both competitive under low pressure conditions. Experimentally this is the case at the slightly lower pressure of 0.3 GPa where the phase II→I transition occurs. The most likely explanation for the incorrect prediction of polymorph stability is that dispersive interactions are not being taken into account by the DFT optimisations. The PIXEL calculations reported here show that these are in fact the most important intermolecular interactions in the crystal structure.

Table 5.3. Calculated thermodynamic energy terms for phases I and II

Energy contribution per molecule	Phase I, 0.84 GPa	Phase II, 0.87 GPa
DFT / kJ mol^{-1}	-755064.06	-755063.05
Zero point energy / kJ mol^{-1}	308.02	307.63
Vibrational enthalpy / kJ mol^{-1}	17.69	17.75
***TS* / kJ mol^{-1}**	34.77	34.94
***PV* / kJ mol^{-1}**	61.56	63.49
Free energy / kJ mol^{-1}	-754711.55	-754709.12

5.5 Conclusions

The effect of pressure on aniline has been explored up to 7.37 GPa using both high-pressure neutron powder diffraction and high-pressure single-crystal X-ray diffraction. The structure of aniline at 100 K and 150 K has also been obtained using low-temperature single-crystal X-ray diffraction.

Aniline has been crystallised in the orthorhombic space group $Pna2_1$ through in-situ growth at *ca.* 0.6 GPa. The structure of the high-pressure phase (II) is very closely related to that of the low-temperature form (I) at 252 K which has the space group $P2_1/c$. Neutron powder diffraction data show that phase II transforms to the less dense phase I on decompression at 0.33 GPa. Phase I could not be obtained with decompression of the single-crystal sample, which instead begins to break up – seen both visually on the surface of the crystal and also in the deteriorating quality of the diffraction pattern. We interpret this as the crystal attempting to undergo the transition which must be reconstructive in nature. This view is consistent with a comparison of the phase I and II structures which suggests that an unfavourable distortion of the lattice must take place in order for the transition to proceed.

PIXEL calculations show that dispersive forces in phase II are more dominant than H-bonds, which become destabilising as pressure is increased. The calculated lattice energies for both phases show that the main contribution comes from the dispersive forces. An attempt has been made to identify the relative free energies of phase I and II from statistical frequencies, calculated by periodic DFT. However, they contradict experimental observations by suggesting that phase I is more stable at 0.84 GPa than phase II at 0.87 GPa by 2.43 kJ mol^{-1}. This inconsistency is likely due to improper treatment of dispersion by DFT, which has been shown by PIXEL to be the most important type of intermolecular interaction in the structure.

The bulk modulus has been determined for phase II from an extensive set of data, where K_0 = 6.980(19) GPa and K' = 9.16(4), indicating a very compressible crystal structure.

5.6 References

1. N. P. Funnell, W. G. Marshall and S. Parsons, *CrystEngComm*, 2011, **13**, 5841-5848.
2. R. D. L. Johnstone, A. R. Lennie, S. F. Parker, S. Parsons, E. Pidcock, P. R. Richardson, J. E. Warren and P. A. Wood, *CrystEngComm*, 2010, **12**, 1065-1078.
3. P. A. Wood, D. Francis, W. G. Marshall, S. A. Moggach, S. Parsons, E. Pidcock and A. L. Rohl, *CrystEngComm*, 2008, **10**, 1154-1166.
4. S. A. Moggach, W. G. Marshall and S. Parsons, *Acta Crystallographica, Section B: Structural Science*, 2006, **B62**, 815-825.
5. A. Gavezzotti, *Molecular Aggregation: Structure Analysis and Molecular Simulation of Crystals and Liquids*, Oxford University Press, Oxford, UK, 2007.
6. S. Crawford, M. T. Kirchner, D. Blaeser, R. Boese, W. I. F. David, A. Dawson, A. Gehrke, R. M. Ibberson, W. G. Marshall, S. Parsons and O. Yamamuro, *Angewandte Chemie, International Edition*, 2009, **48**, 755-757.
7. D. R. Allan, W. G. Marshall, D. J. Francis, I. D. H. Oswald, C. R. Pulham and C. Spanswick, *Dalton Transactions*, 2010, **39**, 3736-3743.
8. F. P. A. Fabbiani, D. R. Allan, A. Dawson, D. J. Francis, W. G. Marshall and C. R. Pulham, *Inorganica Chimica Acta*, 2008, **361**, 487-494.
9. M. Podsiadlo and A. Katrusiak, *Acta Crystallographica, Section B: Structural Science*, 2006, **B62**, 1071-1077.
10. M. Yamashita, S. Inomata, K. Ishikawa, T. Kashiwagi, H. Matsuo, S. Sawamura and M. Kato, *Acta Crystallographica, Section E: Structure Reports Online*, 2007, **E63**, o2762-o2764.
11. I. D. H. Oswald, A. Hamilton, C. Hall, W. G. Marshall, T. J. Prior and C. R. Pulham, *Journal of the American Chemical Society*, 2008, **130**, 17795-17800.
12. G. N. R. Tripathi, *Journal of Chemical Physics*, 1980, **73**, 5521-5530.
13. T. Takagi, *Review of Physical Chemistry of Japan*, 1978, **48**, 10-16.
14. M. A. Palafox, M. Gill, N. J. Nunez, V. K. Rastogi, L. Mittal and R. Sharma, *International Journal of Quantum Chemistry*, 2005, **103**, 394-421.

15. M. Fukuyo, K. Hirotsu and T. Higuchi, *Acta Crystallographica, Section B: Structural Crystallography and Crystal Chemistry*, 1982, **B38**, 640-643.
16. L. Merrill and W. A. Bassett, *Review of Scientific Instruments*, 1974, **45**, 290-294.
17. S. A. Moggach, D. R. Allan, S. Parsons and J. E. Warren, *Journal of Applied Crystallography*, 2008, **41**, 249-251.
18. G. J. Piermarini, S. Block, J. D. Barnett and R. A. Forman, *Journal of Applied Physics*, 1975, **46**, 2774-2780.
19. Agilent, Crysalis PRO, Agilent Technologies, Yarnton, England, 2010.
20. W. G. Marshall and D. J. Francis, *Journal of Applied Crystallography*, 2002, **35**, 122-125.
21. R. J. Angel, *Journal of Physics: Condensed Matter*, 1993, **5**, L141-L144.
22. ISIS, ISIS 96-ISIS Facility Annual Report 1995-96, Rutherford Appleton Laboratory, 1996, RAL-TR-96-050, 61-62.
23. ISIS, ISIS 97-ISIS Facility Annual Report 1996-7, Rutherford Appleton Laboratory, 1997, RAL-TR-97-050, 28-29.
24. R. J. Angel, D. R. Allan, R. Miletich and L. W. Finger, *Journal of Applied Crystallography*, 1997, **30**, 461-466.
25. A. Coelho, *TOPAS-Academic: General Profile and Structure Analysis Software for Powder Diffraction Data. Version 4.1*, 2007.
26. S. J. Clark, M. D. Segall, C. J. Pickard, P. J. Hasnip, M. I. J. Probert, K. Refson and M. C. Payne, *Zeitschrift fuer Kristallographie*, 2005, **220**, 567-570.
27. R. Boese and M. Nussbaumer, *In Situ Crystallisation Techniques*, Oxford University Press, Oxford, UK, 1994.
28. Bruker-Nonius, *SAINT version 7, Program for integration of area detector data*, 2006.
29. G. M. Sheldrick, *SADABS Version 2008-1* 2008, University of Göttingen, Germany.
30. A. Altomare, G. Cascarano, C. Giacovazzo, A. Guagliardi, M. C. Burla, G. Polidori and M. Camalli, *Journal of Applied Crystallography*, 1994, **27**, 435.

31. P. W. Betteridge, J. R. Carruthers, R. I. Cooper, K. Prout and D. J. Watkin, *Journal of Applied Crystallography*, 2003, **36**, 1487.

32. J. P. Perdew, K. Burke and M. Ernzerhof, *Physical Review Letters*, 1996, **77**, 3865-3868.

33. H. J. Monkhorst and J. D. Pack, *Physical Reviews B: Solid State*, 1976, **13**, 5188.

34. S. Grimme, *Journal of Computational Chemistry*, 2006, **27**, 1787-1799.

35. B. Delley, *Journal of Chemical Physics*, 1990, **92**, 508-517.

36. A. D. Becke, *Physical Review A: Atomic, Molecular, and Optical Physics*, 1988, **38**, 3098-3100.

37. C. Lee, W. Yang and R. G. Parr, *Physical Review B: Condensed Matter and Materials Physics*, 1988, **37**, 785-789.

38. M. H. Herzog-Cance, D. J. Jones, R. El Mejjad, J. Roziere and J. Tomkinson, *Journal of the Chemical Society, Faraday Transactions*, 1992, **88**, 2275-2281.

39. M. J. Frisch, G. W. Trucks, H. B. Schlegel, G. E. Scuseria, M. A. Robb, J. R. Cheeseman, G. Scalmani, V. Barone, B. Mennucci, G. A. Petersson, H. Nakatsuji, M. Caricato, X. Li, H. P. Hratchian, A. F. Izmaylov, J. Bloino, G. Zheng, J. L. Sonnenberg, M. Hada, M. Ehara, K. Toyota, R. Fukuda, J. Hasegawa, M. Ishida, T. Nakajima, Y. Honda, O. Kitao, H. Nakai, T. Vreven, J. A. Montgomery Jr., J. E. Peralta, F. Ogliaro, M. Bearpark, J. J. Heyd, E. Brothers, K. N. Kudin, V. N. Staroverov, R. Kobayashi, J. Normand, K. Raghavachari, A. Rendell, J. C. Burant, S. S. Iyengar, J. Tomasi, M. Cossi, N. Rega, J. M. Millam, M. Klene, J. E. Knox, J. B. Cross, V. Bakken, C. Adamo, J. Jaramillo, R. Gomperts, R. E. Stratmann, O. Yazyev, A. J. Austin, R. Cammi, C. Pomelli, J. W. Ochterski, R. L. Martin, K. Morokuma, V. G. Zakrzewski, G. A. Voth, P. Salvador, J. J. Dannenberg, S. Dapprich, A. D. Daniels, Ö. Farkas, J. B. Foresman, J. V. Ortiz, J. Cioslowski and D. J. Fox, *Gaussian 09 , Revision B.01, Gasussian, Inc.*, 2009.

40. A. Gavezzotti, *OPiX: A computer program package for the calculation of intermolecular interactions and crystal energies*, 2003.

41. C. F. Macrae, I. J. Bruno, J. A. Chisholm, P. R. Edgington, P. McCabe, E. Pidcock, L. Rodriguez-Monge, R. Taylor, J. van de Streek and P. A. Wood, *Journal of Applied Crystallography*, 2008, **41**, 466-470.

42. R. J. Angel, *EOSFIT version 5.2*, 2002, Virginia Tech, Blackburg, VA, USA.

43. N. P. Funnell, A. Dawson, D. Francis, A. R. Lennie, W. G. Marshall, S. A. Moggach, J. E. Warren and S. Parsons, *CrystEngComm*, 2010, **12**, 2573-2583.

44. F. Birch, *Journal of Geophysical Research, B*, 1986, **91**, 4949-4954.

45. A. Gavezzotti, *Zeitschrift fuer Kristallographie*, 2005, **220**, 499-510.

46. P. A. Wood, J. J. McKinnon, S. Parsons, E. Pidcock and M. A. Spackman, *CrystEngComm*, 2008, **10**, 368-376.

47. R. D. L. Johnstone, D. Francis, A. R. Lennie, W. G. Marshall, S. A. Moggach, S. Parsons, E. Pidcock and J. E. Warren, *CrystEngComm*, 2008, **10**, 1758-1769.

48. S. Hunter, A. J. Davidson, C. A. Morrison, C. R. Pulham, P. Richardson, M. J. Farrow, W. G. Marshall, A. R. Lennie and P. J. Gould, *Journal of Physical Chemistry C*, 2011, **115**, 18782-18788.

49. M. Bujak, D. Blaeser, A. Katrusiak and R. Boese, *Chemical Communications (Cambridge, United Kingdom)*, 2011, **47**, 8769-8771.

50. G. M. Day, T. G. Cooper, A. J. Cruz-Cabeza, K. E. Hejczyk, H. L. Ammon, S. X. M. Boerrigter, J. S. Tan, R. G. Della Valle, E. Venuti, J. Jose, S. R. Gadre, G. R. Desiraju, T. S. Thakur, B. P. van Eijck, J. C. Facelli, V. E. Bazterra, M. B. Ferraro, D. W. M. Hofmann, M. A. Neumann, F. J. J. Leusen, J. Kendrick, S. L. Price, A. J. Misquitta, P. G. Karamertzanis, G. W. A. Welch, H. A. Scheraga, Y. A. Arnautova, M. U. Schmidt, J. van de Streek, A. K. Wolf and B. Schweizer, *Acta Crystallographica. Section B, Structural Science*, 2009, **65**, 107-125.

51. D. A. Bardwell, C. S. Adjiman, Y. A. Arnautova, E. Bartashevich, S. X. M. Boerrigter, D. E. Braun, A. J. Cruz-Cabeza, G. M. Day, R. G. Della Valle, G. R. Desiraju, B. P. van Eijck, J. C. Facelli, M. B. Ferraro, D. Grillo, M. Habgood, D. W. M. Hofmann, F. Hofmann, K. V. J. Jose, P. G. Karamertzanis, A. V. Kazantsev, J. Kendrick, L. N. Kuleshova, F. J. J.

Leusen, A. V. Maleev, A. J. Misquitta, S. Mohamed, R. J. Needs, M. A. Neumann, D. Nikylov, A. M. Orendt, R. Pal, C. C. Pantelides, C. J. Pickard, L. S. Price, S. L. Price, H. A. Scheraga, J. van de Streek, T. S. Thakur, S. Tiwari, E. Venuti and I. K. Zhitkov, *Acta Crystallographica, Section B: Structural Science*, 2011, **B67**, 535-551.

Chapter 6

The Crystalline-Plastic Phase Transition in Cyclohexane Examined by Neutron Total Scattering*

*Nicholas P. Funnell, Martin T. Dove, Simon Parsons and Matthew G. Tucker, *in preparation*

6.1 Introduction

In a typical crystal structure determination, only the long-range average structure, derived from the intensity and position of Bragg peaks, is determined from a scattering pattern and the remaining background is discarded. However, by considering the long-range structure only, important features in the local environment can be missed. The implications of this can be understood by considering a hypothetical structure where 30% of the atomic sites are vacant as shown in Figure 14.3 in Ref. 1 (image originally created by Thomas Proffen), reproduced here in Figure 6.1. Bragg diffraction is insensitive as to whether the vacancies are randomly distributed or correlated on a local scale; the same pattern is observed in both cases as, on average, they are identical. However the diffraction pattern corresponding to the correlated structure contains significantly more diffuse scattering.

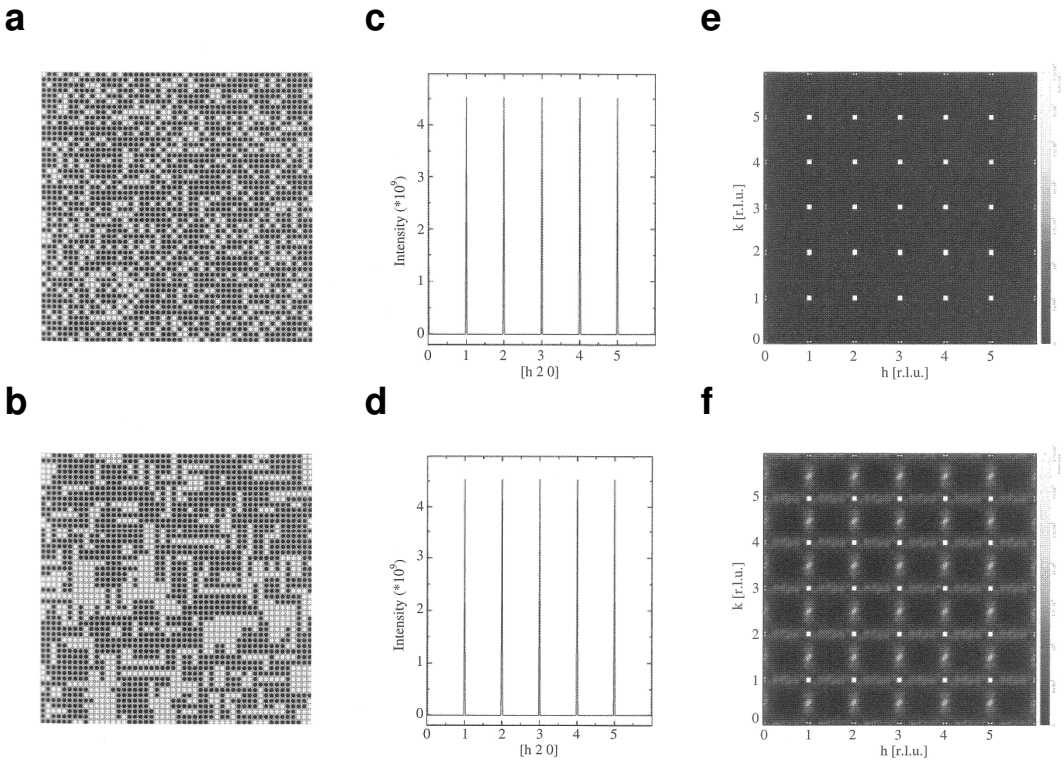

Figure 6.1. Hypothetical crystal structures where 30% of the atomic sites are randomly vacant **(a)** and where the vacancies are correlated **(b)**. The corresponding powder diffraction patterns are shown in **(c)** and **(d)** respectively and the single crystal patterns in **(e)** and **(f)**. The Figure is taken from Ref. 1 and was originally created by Thomas Proffen.

Total scattering is a technique that accounts for the local structure, namely interatomic distances, contained in diffuse scattering. Although the method was originally intended for structural determination of liquids and amorphous solids, which lack any long-range order, the application of total scattering to crystalline systems yields additional benefits that Rietveld refinement cannot provide. By simultaneously modelling both the long-range order and local correlations using Reverse Monte Carlo (RMC) refinements, an 'instantaneous snapshot' of the crystal can be obtained, where the molecules appear disordered on a local scale but the average atomic coordinates reproduce the ordered structure seen by Bragg scattering. This is a more accurate depiction of a real crystal structure and makes the use of total scattering particularly appealing for studying disorder. Total scattering has previously been successfully used to study several different systems including nickel cyanide chains, silica, zeolites and metal-organic framework materials.[2-5] Recently, more challenging applications of total scattering have been described which include in-situ experiments at high pressure and fingerprinting pharmaceutical products.[6, 7] So far molecular systems have not been investigated to a great extent; SF_6 and CBr_4 are part a very small collection of experiments that have focussed on these systems.[8, 9]

Cyclohexane is known to undergo a thermally induced transition at 186 K between two solid phases. Below 186 K, it possesses an ordered crystalline structure (*C*2/*c*, phase II) and between 186 K and 280 K it is a plastic solid, where the molecules are rotationally disordered about the lattice points of a face-centred cubic unit cell. Kahn *et al* determined the packing arrangement of both these phases through X-ray diffraction of single crystal samples (single-crystals of the plastic phase were obtained by growth near the transition point, using a zone melting technique).[10] Two disorder models were tested for phase I – one where the molecule was isotropically disordered, being treated as a sphere of electron density and another where the molecule adopted 24 different orientations about the FCC lattice point. The latter model was found to give better agreement with the experimental data.

Raman scattering, molecular dynamics (MD) simulations and NMR experiments have all been performed with the aim of identifying the precise nature of the disorder in phase I and the liquid phase. Although there does not appear to be a

definitive consensus, most of the studies conclude that the molecular motion is more complex than uncorrelated isotropic tumbling.[11-16]

Examination of the phase behaviour in cyclohexane using neutron total scattering has already been carried out by Farman *et al*. where it was concluded that the characteristics of the pair distribution function (PDF) in the plastic phase were more consistent with a disordered FCC lattice model rather than a molecule undergoing unhindered isotropic rotation.[17] However, owing to instrument limitations at the time, data were only collected to Q_{max} = 16 Å^{-1}. Modern diffractometers are now capable of collecting data at much higher resolution – *ca.* Q_{max} = 60 Å^{-1}, which reduces the effect of Fourier truncation, making assignment of 'real' peaks corresponding to intra and intermolecular contacts and bond distances much more straightforward.

Modelling the PDF from total scattering data using a Reverse Monte Carlo approach appears to be an ideal way to probe the disorder in cyclohexane. The RMC process is, in principle, completely driven by the experimental data. The authors of Ref 17 suggest that RMC modelling could be a direction with which this research could proceed, although they point out that it cannot provide a unique fit to the data and that, frequently, chemically unrealistic atomic configurations are generated. Following advances in RMC software over the last couple of decades, the latter is readily prevented with judicious use of geometry restraints, although the former issue remains, as it is inherent to the method.

We report our observations for the crystalline-plastic phase transition in cyclohexane-d_{12} using RMC modelling of total scattering data, to a much higher resolution of Q_{max} = 45 Å^{-1}.

6.2 Experimental

6.2.1 Sample preparation

Cyclohexane-d_{12}, obtained from CDN Isotopes, was frozen with liquid nitrogen and cold-ground into a homogenous powder at 77 K, in a nitrogen atmosphere.[18]

6.2.2 Neutron total scattering

The cyclohexane sample was packed into a thin-walled vanadium can and mounted on a CCR device to control the sample temperature. Total scattering data were collected on the General Materials Diffractometer (GEM) at the ISIS pulsed spallation source using the neutron time-of-flight (ToF) method.[19] Data were collected to Q_{max} = 60 Å^{-1} at the following temperatures, 13, 75, 126, 176, 206 and 266 K. The measured differential cross-section data were processed using GUDRUN, producing total scattering structure factor data, $F(Q)$ to a useable $Q_{\max}$ of 45 Å^{-1}, and the corresponding total radial distribution functions, $G(r)$, after correcting for background scattering, multiple scattering, Placzek inelasticity and beam attenuation by the sample container. The measured $G(r)$ data at 13, 176 and 266 K are shown in Figure 6.2. A thorough comparison of commonly used total scattering terminology and the relationship between the differential cross-section, $F(Q)$ and $G(r)$ data is given by Keen.[20]

The Bragg peaks in the total scattering pattern were refined in TOPAS Academic using data collected on the detector bank 2θ = 91°.[21] The refined model was then used in GSAS with data from the detector bank 2θ = 63° in order to obtain the necessary data files for refinement by RMCProfile.[22-24] The phase I Bragg data were refined against the Frenkel model described by Kahn *et al.*[10] Rietveld fits to the data at 13K, 176 K and 266 K using GSAS are shown in Figure 6.3. Crystal structure refinement details for these temperatures are given in Table 6.1

6.2.3 Reverse Monte-Carlo modelling

Crystal structure refinements in TOPAS and MD simulations were used to generate starting configurations, in a 6x6x6 supercell for each dataset. The program RMCProfile was used to simultaneously fit calculated $F(Q)$, $G(r)$ and $I(t)$ (the Bragg profile fitted as a function of time of flight) data to the experimental observations by randomly moving atoms in the configuration. Moves are accepted based on minimisation of the function

$$\chi^2 = \sum_j \left(y_j^{\exp} - y_j^{calc} \right) / \sigma_j^2$$

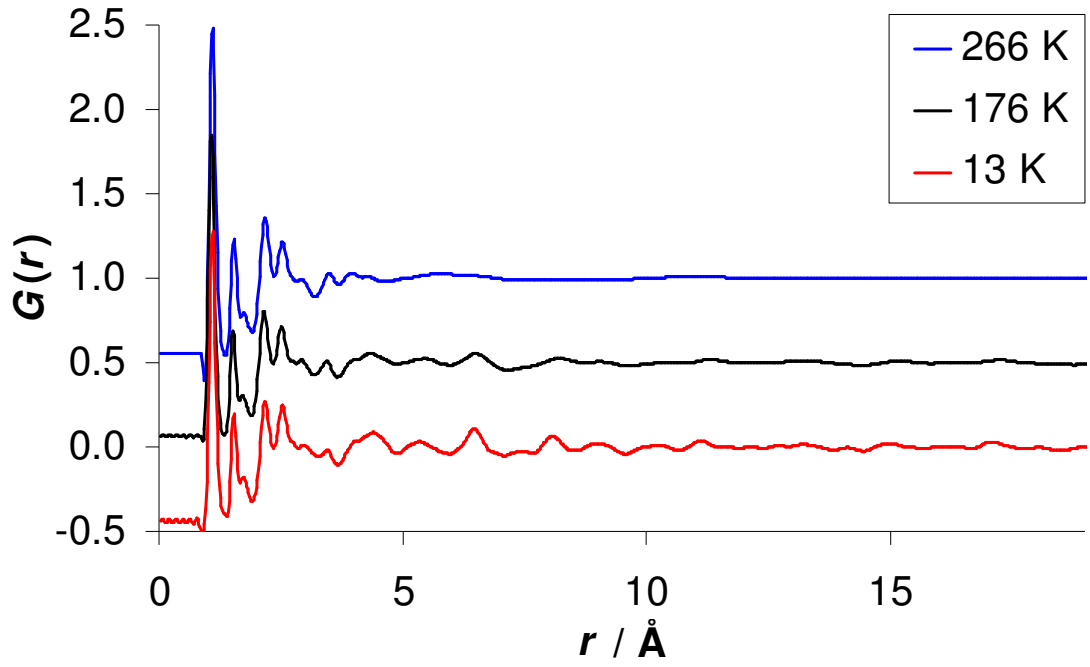

Figure 6.2 Experimental *G*(*r*) plots for phase II data at 13 K and 176 K and phase I data at 266 K

Moves that increase the value of χ^2 are accepted within the probability limit

$$P = \exp\left(-\Delta \chi^2 / 2\right)$$

to avoid being trapped in a false minimum. Molecular mechanics-based restraints were used to maintain chemically sensible connectivity of the molecules; these are discussed in more detail in Section 6.3.1. Refinement of the phase I and II datasets were carried until no further improvements in the value of χ^2 were seen.

6.2.4 Molecular dynamics simulations

Molecular dynamics simulations were performed with the DISCOVER software package implemented in Accelrys Materials Studio. The cvff forcefield was used with an NPT ensemble.[25] Simulations were carried out for 20 ps at intervals of 0.5 fs using a Berendsen thermostat and a Parrinello barostat.[26, 27]

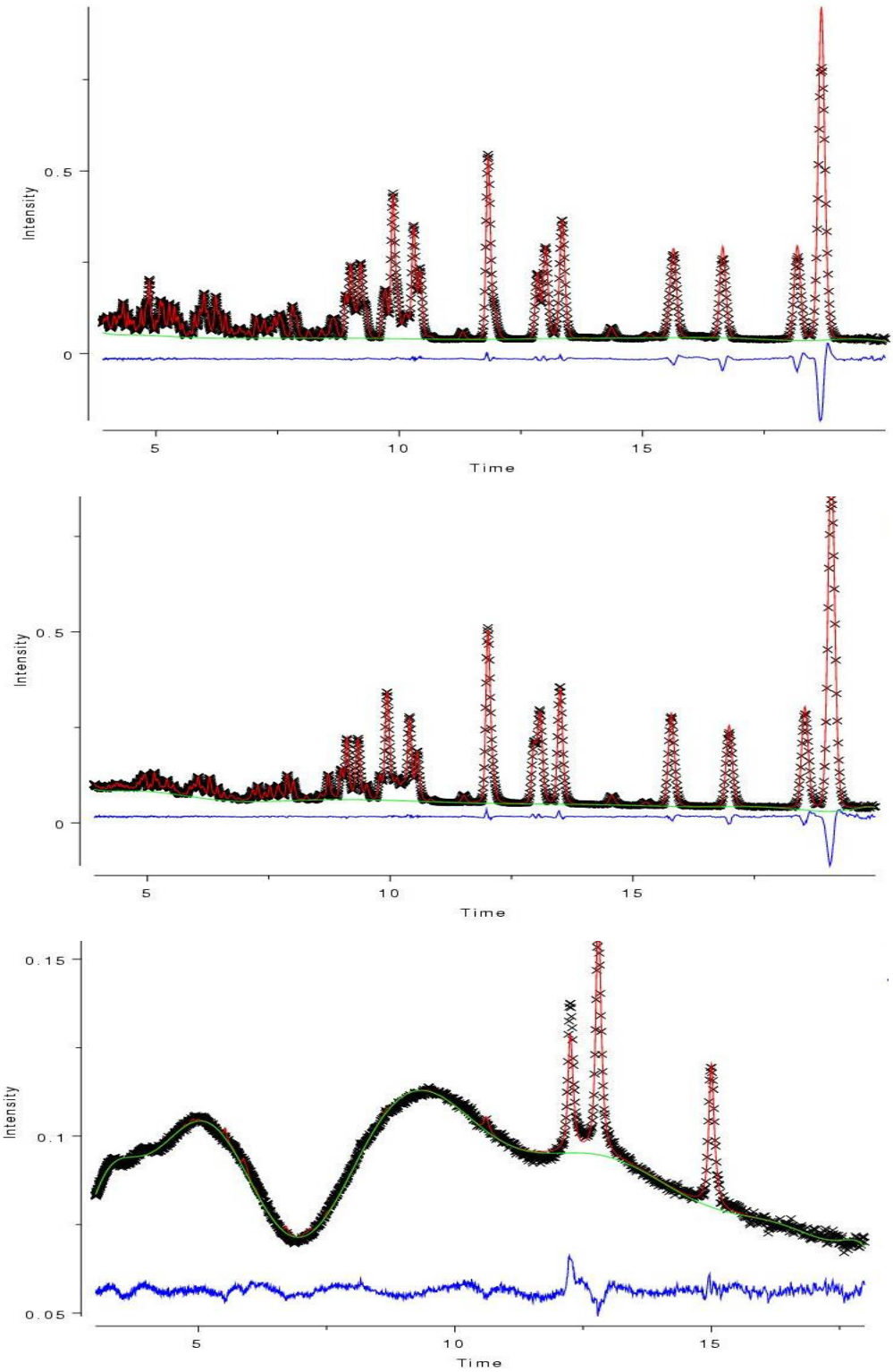

Figure 6.3. Refined powder patterns of cyclohexane at 13, 176 and 266 K. Experimental data are shown in black, the calculated structure in red and the difference in blue. The minimum and maximum d-spacing used are 0.8 and 4.1 Å for the 13 K and 176K data. The minimum and maximum d-spacing used for the 266 K data are 0.6 and 3.7 Å

Table 6.1. Crystal structure refinement details for selected datasets from the detector bank $2\theta = 63°$

Temperature / K	**13**	**176**	**266**
Sample type and radiation used	Neutron, powder	Neutron, powder	Neutron, plastic
Chemical formula	C_6D_{12}	C_6D_{12}	C_6D_{12}
M_r / g mol^{-1}	96.06	96.06	96.06
Cell setting, space group	Monoclinic, *C*2/*c*	Monoclinic, *C*2/*c*	Cubic, *Fm*3*m*
a / Å	11.23875(9)	11.32426(14)	8.6861(4)
b / Å	6.36785(5)	6.45096(8)	8.6861(4)
c / Å	8.07527(8)	8.26274(10)	8.6861(4)
β / °	108.7097(5)	108.9088(7)	90(0)
V / Å^3	547.381(11)	571.039(17)	655.36(8)
Z	4	4	4
D_c / Mg m^{-3}	1.17	1.12	0.97
d_{max}, d_{min} / Å	4.1, 0.8	4.1, 0.8	3.7, 0.6
R_{wp}	0.0191	0.0142	0.0142
Reflection/Profile data	2044	2044	2242

6.3 Results and discussion

6.3.1 RMCProfile geometric restraints

Forcefield-based distance and angle restraints were used to ensure the configurations were chemically realistic as RMCProfile does not take this into account. The forms of these restraints are detailed in the RMCProfile manual.[28] The energy terms, bond distances and angles used are given in Table 6.2. As cyclohexane is a relatively rigid molecule, the time-averaged covalent bond distances and angles are not expected to change significantly as a function of temperature. A 'temperature' parameter controlling the weight of the restraints was fixed at 10 K for all phase II datasets. Use of the real temperature caused a large proportion of the atoms in the configuration to deviate from their ideal coordination numbers. This problem was not as prevalent in the phase I data and so real temperatures of 206 and 266 K were used. Minimum

approach distances were employed to prevent atoms getting too close together. For D-D, C-D and C-C atom pairs, the closest distances allowed were 1.4, 0.9 and 1.3 Å respectively. These distances are below the realistic closest approach distances seen experimentally (1.7, 1.1 and 1.5 Å) in order to avoid introducing bias into the model.

Table 6.2. Parameters used for geometric restraints

Parameter	Dist. / Å or Angle / °	Energy / eV
C-C	1.524	2.155
C-D	1.100	2.275
C-C-C	110.83	8.364
C-C-D	109.17	7.365
D-C-D	106.06	7.365

6.3.2 Initial starting models

For each dataset, two different starting models were used. The purpose of this was to test the reproducibility of the RMC refinements – to see if similar final atomic configurations were obtained. The first model was a completely ordered configuration; a supercell of the time-average crystal structure. This was only possible for the phase II data. An equivalent model was made for the phase I data by constructing an artificial cell, with all molecules in the same orientation, centred on the lattice points of a FCC cell with dimensions obtained from a Pawley fit. The models that are ordered prior to RMC refinement are hereafter referred to as model 'A'.

The second starting model was obtained via molecular dynamics simulations, performed at each experimental temperature, where the starting coordinates and cell dimensions for phase II were obtained from the 13 K crystal structure. The phase I configurations were constructed using the following procedure: molecules were placed on the FCC lattice points of a cell with *P*1 symmetry and dimensions corresponding to the plastic crystal at 206 K. The molecules were arbitrarily orientated in positions that visually appeared to be sterically favourable. The

geometry was coarsely optimised (final $\Delta E = 4 \times 10^{-5}$ Ha) and then MD simulations on a 6×6×6 supercell were performed. The purpose of the geometry optimisation was to relieve instabilities in the initial cycles of the MD simulation which were observed if the geometry was not optimised. This provided a set of coordinates sufficient to serve as a starting point for the dynamics simulation. The resulting supercells for both phases were then manually adjusted to those of the relevant crystal structure supercell before undergoing RMC modelling. The dynamics-derived models will be hereafter referred to as model 'B'.

The initial fits of the two starting models to the $G(r)$ data before any RMC refinement are shown for the 13 and 266 K datasets in Figures 6.4 and 6.5 respectively. For all the initial fits shown, Model B shows markedly better agreement between the raw data and the RMC fit at $r > 5$ Å, particularly for phase I. The poor fit at low r in model B, relative to the high r region, is a consequence of the MD simulations preserving 'ideal' covalent bond lengths, an indication that the bond stretching and bending force constants are too high.

6.3.3 RMCProfile refinement of the total scattering data: Phase II

The final RMC fits at 13, 176 and 266 K for models A and B to the $G(r)$, $F(Q)$ and $I(t)$ data are shown in Figures 6.6, 6.7 and 6.8 respectively. It is clear from the Figures that there is very little difference between the two models in terms of the final fit obtained for the phase II data.

The PDF's at $r \leq 5$ Å change very little as a function of temperature as the major contribution to these peaks comes from intra-atomic contacts which are not expected to vary significantly. Only a very small degree of broadening is present here, reflecting the effect of the thermal energy on the magnitude of bond stretching. Interatomic contacts start to contribute to the PDF above *ca.* 1.8 Å (see Section 6.3.4). Peak broadening on increasing temperature can be seen above *ca.* 5 Å as this region is due to intermolecular contacts only (the longest intramolecular D···D contact is *ca.* 5 Å). The broadening at 176 K relative to 13 K shows the molecules are disordering to a greater extent from their equilibrium positions as they are heated.

In phase I, the PDF becomes very diffuse in the intermolecular region, indicating a wide range of contact distances, consistent with the nature of the expected disorder.

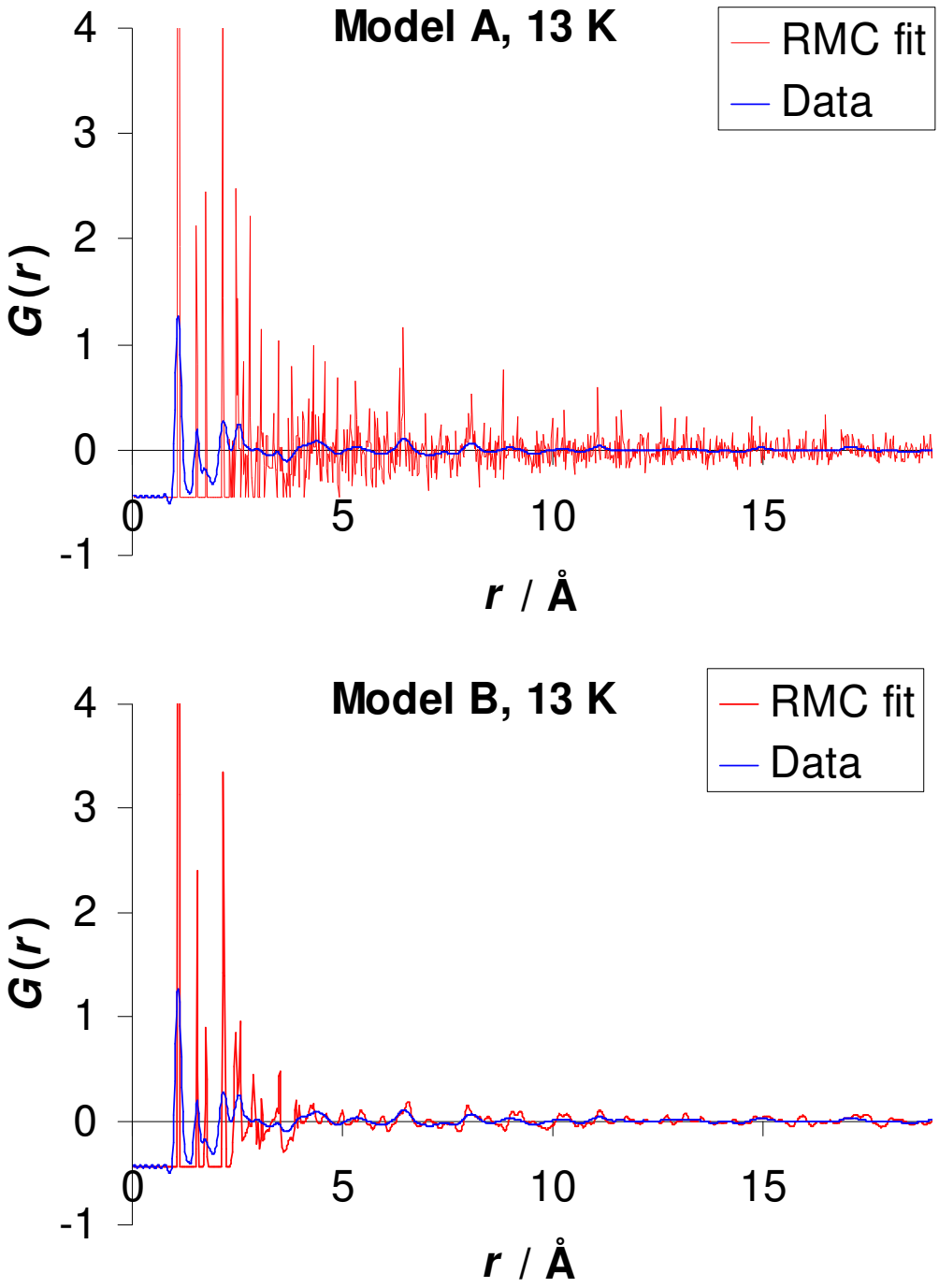

Figure 6.4. Initial fits of the atomistic configuration to experimental data at 13 K using models A and B, before RMC refinement. The y-axis has been truncated at '4' for sake of clarity.

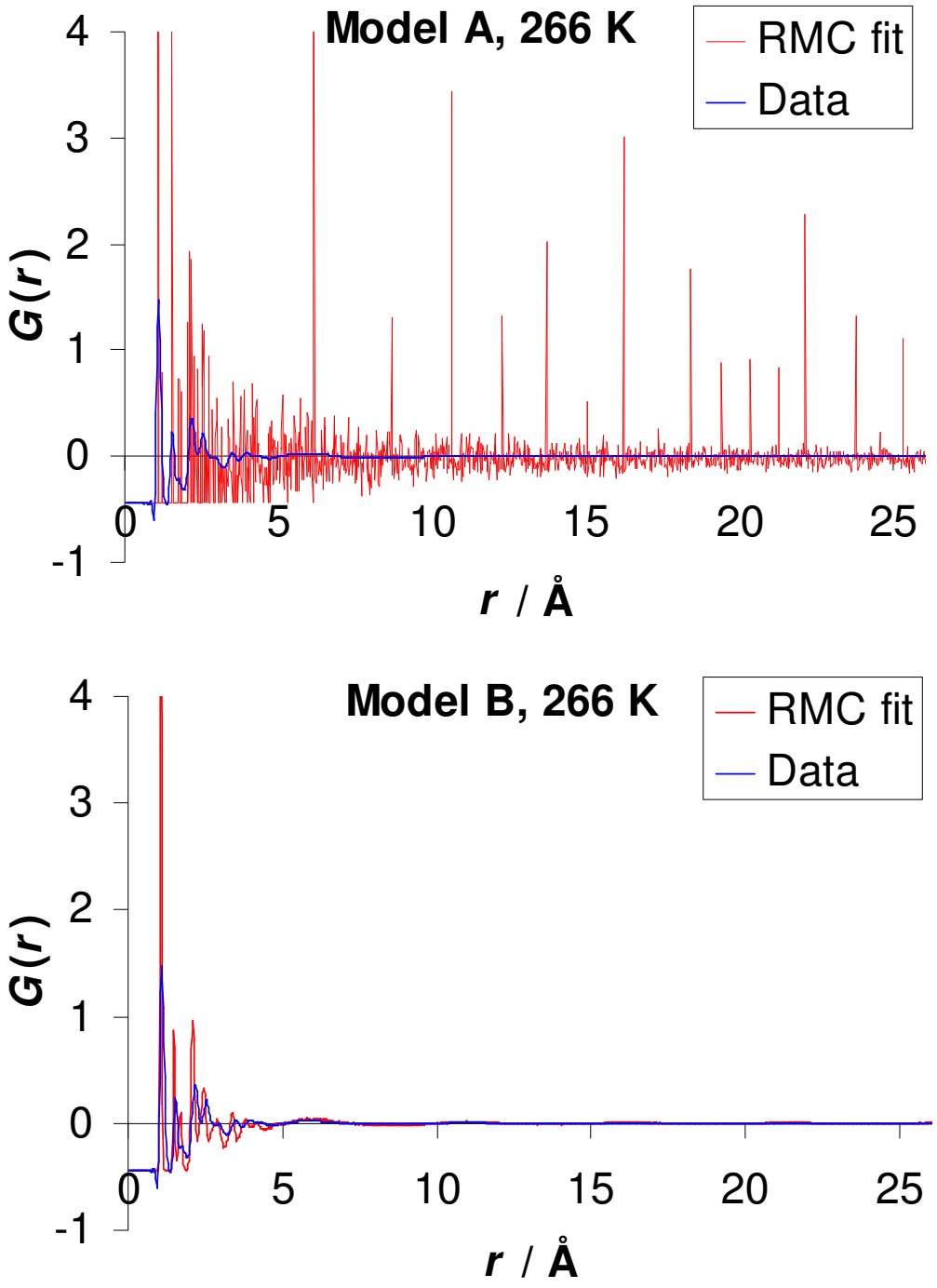

Figure 6.5. Initial fits of the atomistic configuration to experimental data at 266 K using models A and B, before RMC refinement. The y-axis has been truncated at '4' for sake of clarity.

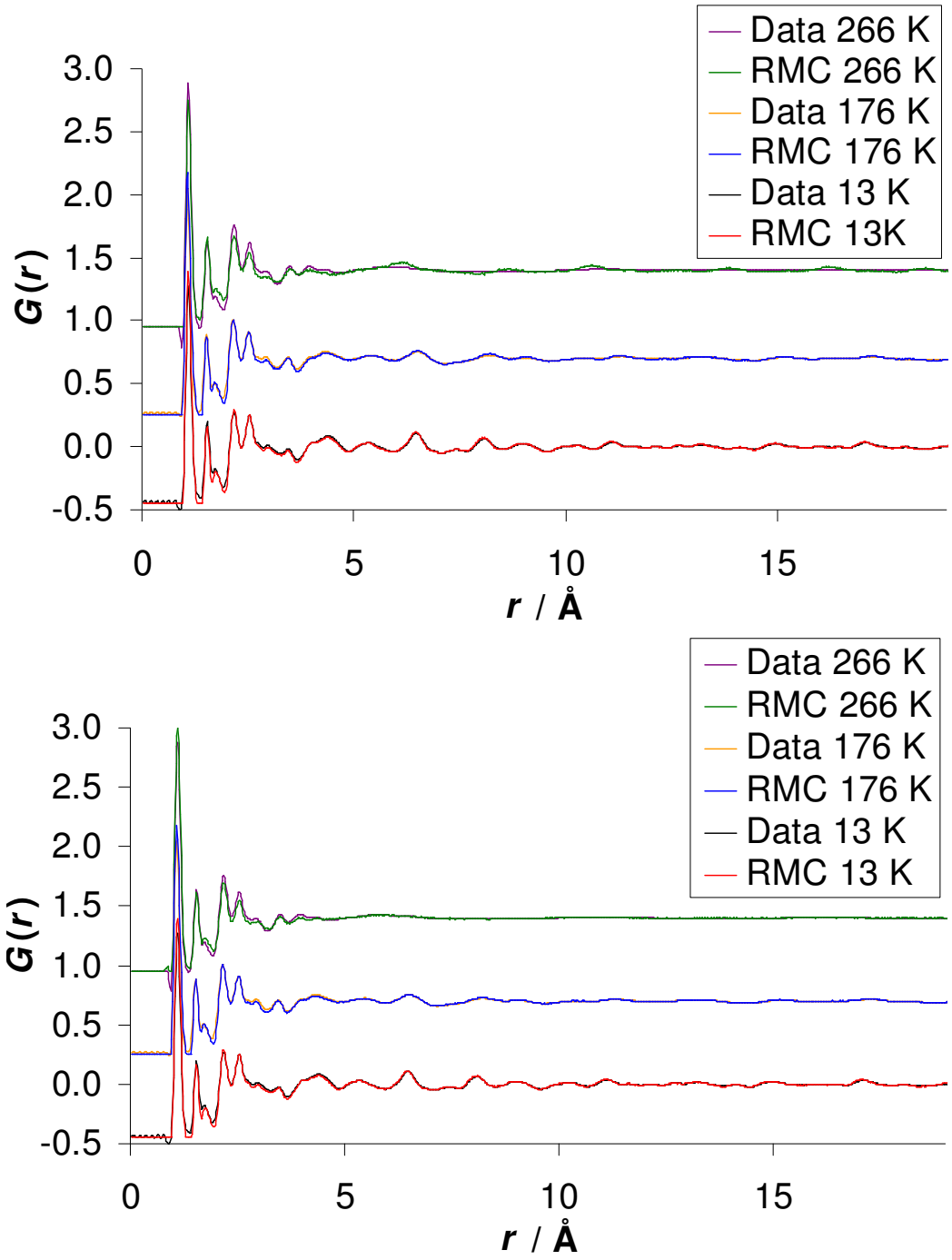

Figure 6.6. Final RMC fits to the *G*(*r*) data for model A (top) and model B (bottom).

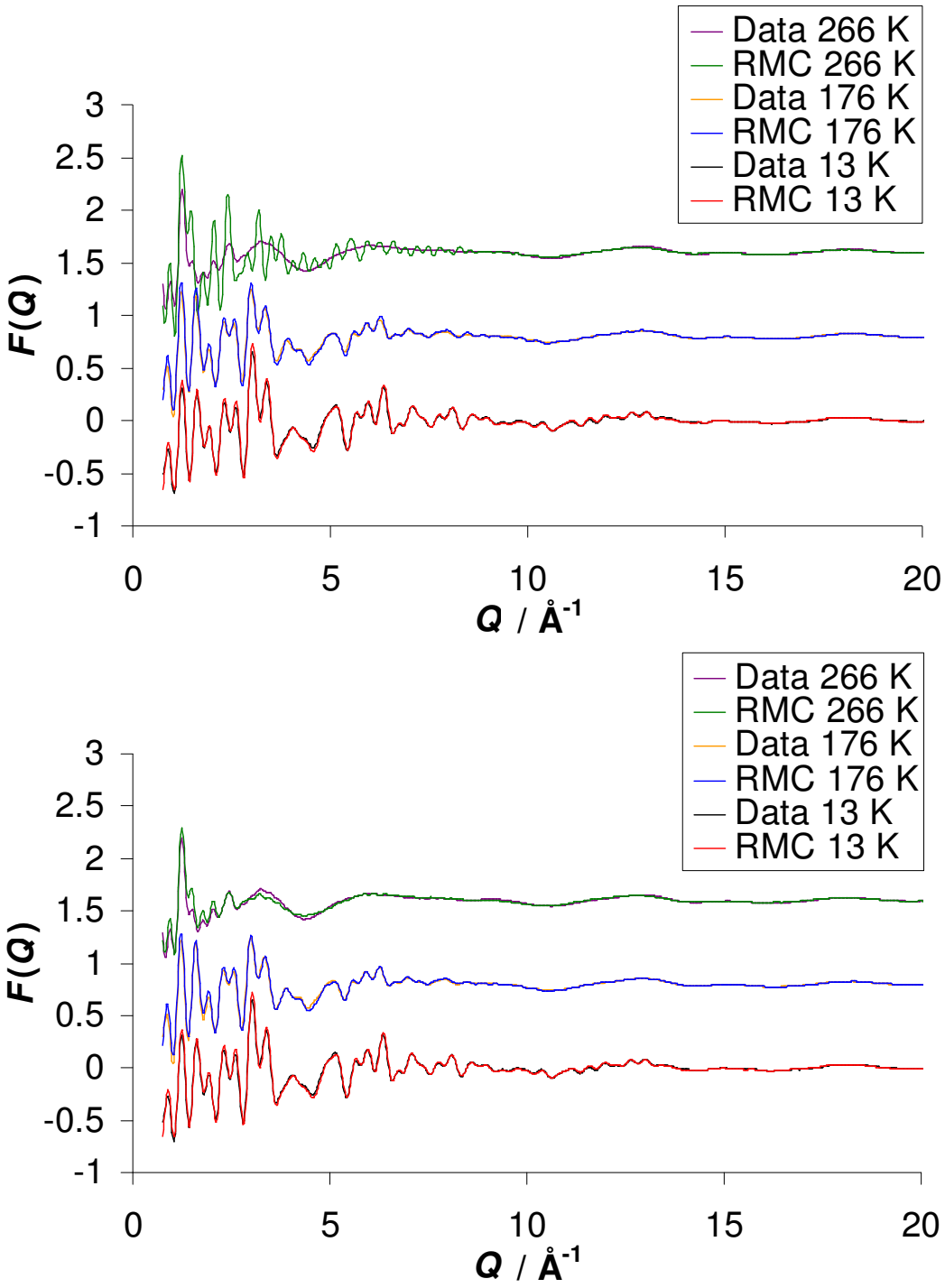

Figure 6.7. Final RMC fits to the *F*(*Q*) data for model A (top) and model B (bottom). The x-axis has been truncated at 20 to show the low-*Q* region more clearly

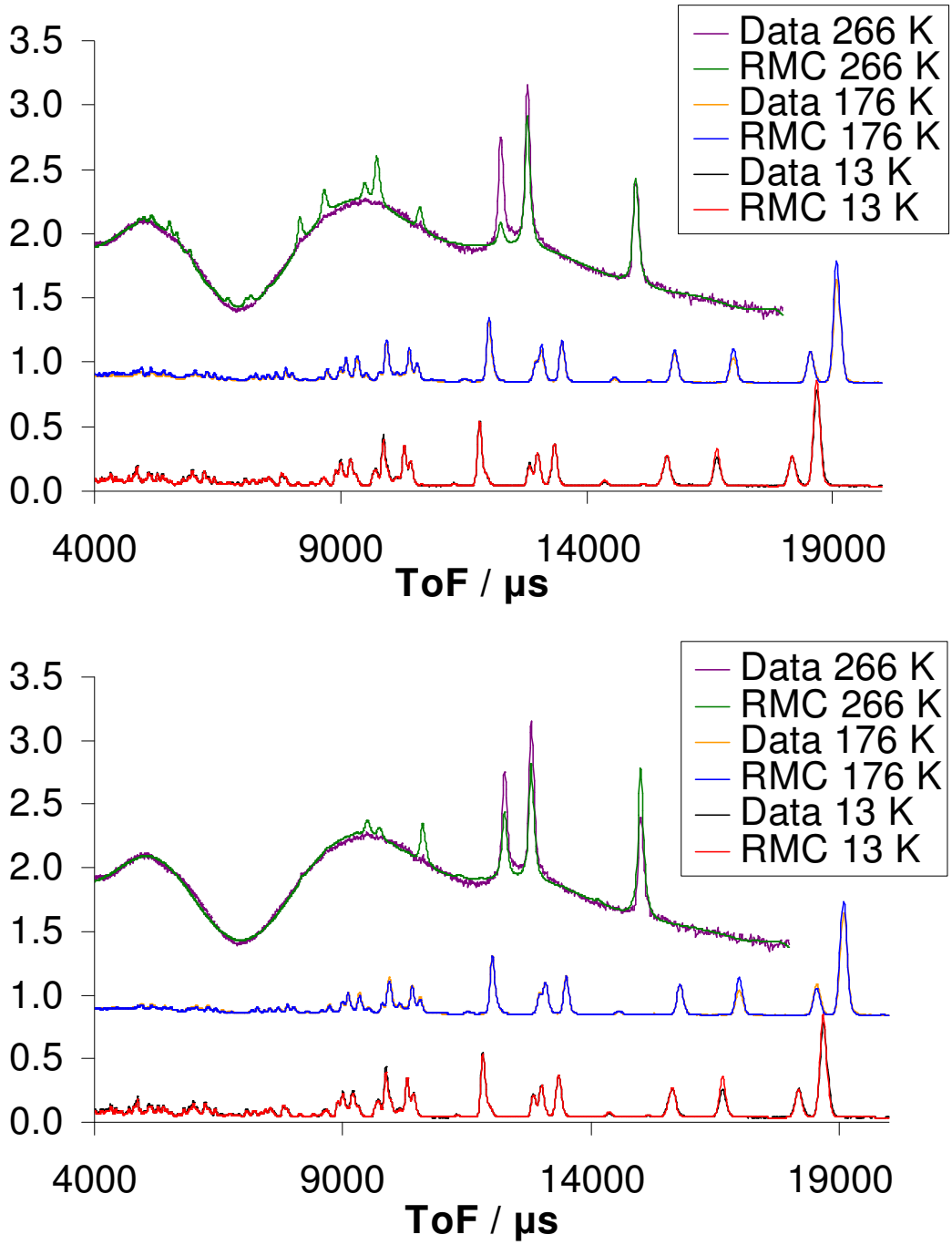

Figure 6.8. Final RMC fits to the *I*(*t*) data for models A (top) and B (bottom). The intensities for the 266 K data have been scaled by a factor of 20 to show the fit more clearly.

The effect of temperature on the instantaneous structure can be seen in Figure 6.9, which shows the final atomic configurations at 13, 176, 206 and 266 K for models A and B condensed back down onto a single unit cell (using a combination of 9 configurations has been used to improve coverage statistics where the configurations were all derived in an identical manner, as detailed in the *Experimental* section). The Figure also shows the average crystal structure for comparison of the thermal ellipsoids with the instantaneous positions as seen by total scattering.

6.3.4 RMCProfile refinement of the total scattering data: Phase I

The phase I data were initially modelled without the $I(t)$ data as the only information contained in the diffraction pattern, after the background was discarded, were the unit cell dimensions and the effective dimensions of the 'sphere' of density corresponding to the average molecular coordinates. The cell dimensions are not refined by RMCProfile and it was thought that the dimensions of the molecular 'sphere' would be dealt with by the $G(r)$ data.

The fits to the $G(r)$ and $F(Q)$ data were excellent for both models (Figure 6.10) despite the final two atomic configurations being very different, shown in Figure 6.11. The distribution of the carbon positions in phase I show that whereas RMC refinement of model B results in isotropic disorder, in model A the molecules show significantly more disorder about the molecular C_3 axis rather than any tumbling motion.

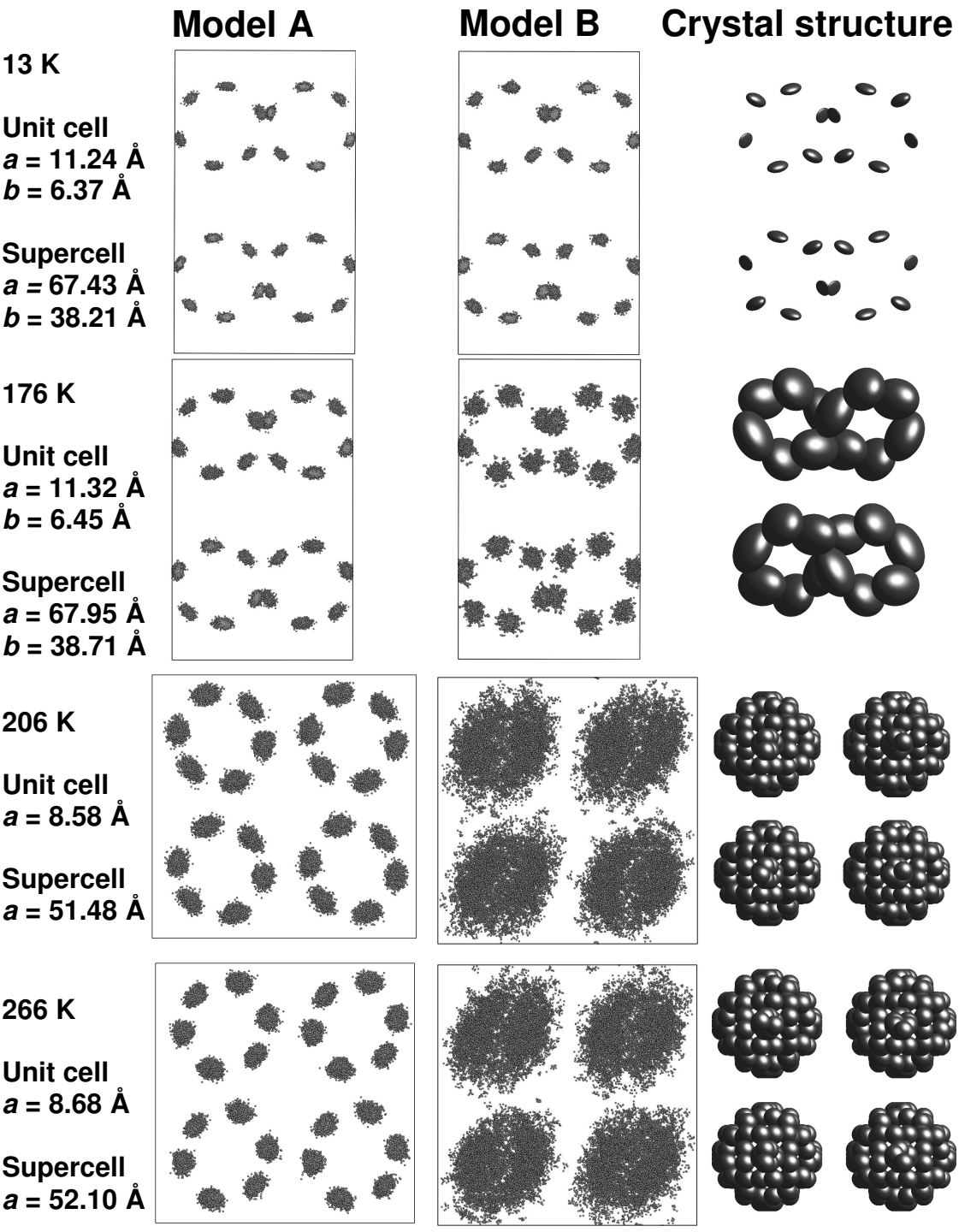

Figure 6.9. Condensed supercells of model A, B and the average crystal structure at selected temperatures. The crystal structures for 206 and 266 K have been refined isotropically. Thermal ellipsoids are plotted at the 100% probability level. Deuterium atoms are omitted for clarity. Unit cell and supercell dimensions are given at each temperature for the cell axes that are visible (note $a = b = c$ for the phase I structures at 206 and 266 K).

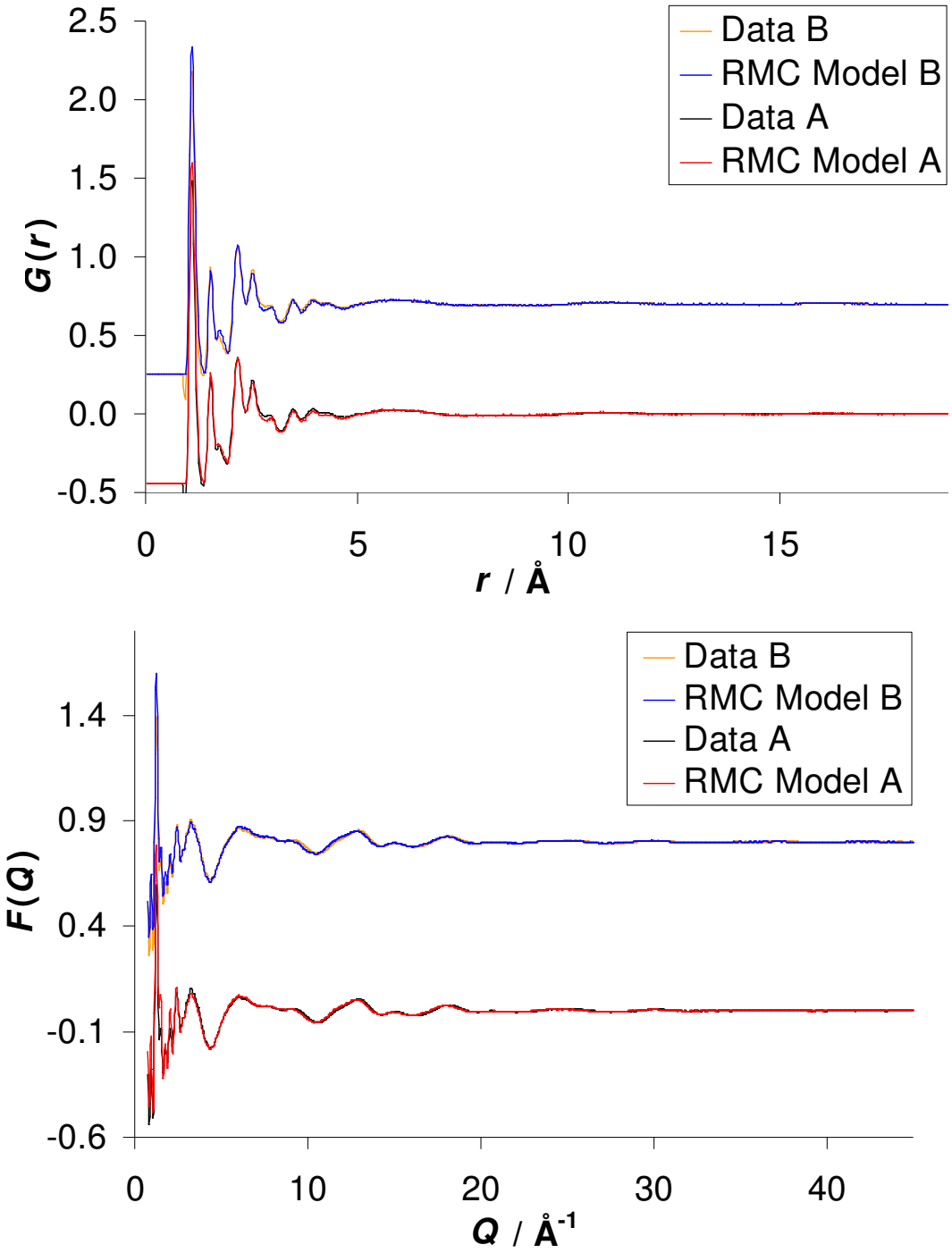

Figure 6.10. Final RMC fits to the *G*(*r*) data (top) and *F*(*Q*) data (bottom) in the absence of *I*(*t*) data.

However, the anisotropic molecular motion seen in model A means that the model does not fulfil the symmetry requirements of an FCC cell, despite giving a perfectly good fit to the $G(r)$ and $F(Q)$ data. Therefore, $I(t)$ data were subsequently included in a new set of refinements, with the aim of increasing disorder in the model so that the structure, on average, reproduced the cubic symmetry of the FCC cell. The final models obtained (Figure 6.9) show that the RMC refinements have not driven the molecules in model A to adopt an isotropic tumbling motion – the structure is relatively ordered, which is evident in the RMC fit to the $I(t)$ data where several extra erroneous peaks are present. This shows that model A is not adequate for the phase I data – a fact that may have been missed if the average structure had not been taken into account.

By comparison, the fit to the $I(t)$ data for model B is better in terms of the number of peaks present. Although there are a few erroneous peaks still present in the data, indicating that the cubic symmetry is not being exactly reproduced, it is clear that the $I(t)$ fit for model B is markedly better than that of Model A. The fits to the $G(r)$ and $F(Q)$ data are excellent for model B but are relatively poor for model A. Therefore, it would seem that model B gives the best overall agreement with the experimental data, showing that the molecules undergo isotropic motion in the plastic phase.

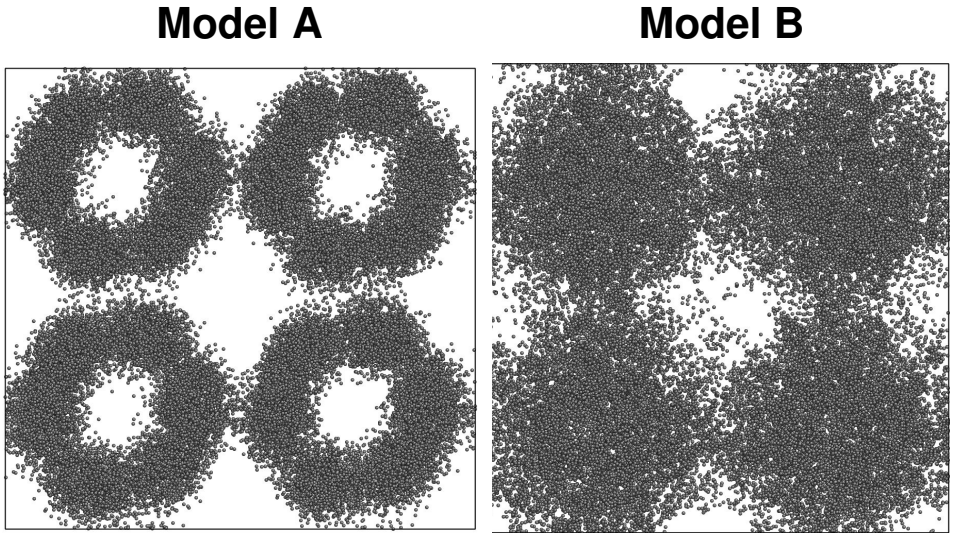

Figure 6.11. Final atomic configurations for models A and B at 266 K in the absence of $I(t)$ data. Deuterium atoms are omitted for clarity.

6.3.5 Intermolecular D···D contacts

Many of the previous investigations on cyclohexane have sought to understand the nature of the disorder in the plastic phase, where it has been suggested that the molecules should not be able to tumble independently of each other - there is insufficient space to do so.[10, 17] In order for one molecule to tumble, its neighbours must make room for it. An advantage of fitting an atomistic model to total scattering data presents itself here - the extent of molecular correlation can be assessed through the frequency of, short D···D contacts. If a molecule should fail to spatially accommodate its neighbour then a short D···D contact would result. Wood *et al* have identified a minimum approach distance of 1.7 Å for intermolecular H···H contacts in small organic molecules up to pressures of 10 GPa.[29]

The closest D···D approach distance permitted by the constraints in the RMC refinement is 1.4 Å – well below the limit of 1.7 Å. Figure 6.12 shows histograms of intermolecular D···D contacts for models A, and B at 13 K, 176 K and 266 K. The inadequacy of model A for phase II can be seen here as short D···D contacts are formed – the shortest distance seen is 1.23 Å. By contrast, the shortest contact distance seen in model B is 1.9 Å; another indication that this model is a more accurate representation of the disorder in phase I. The shortest distance observed in the results of the MD simulations is 1.84 Å at 266 K. With the exception of model A (which is clearly incorrect anyway), none of the observed contact distances approach the 1.7 Å limit, thus confirming the argument based on spatial limitations that the molecular motion is correlated.

6.3.6 Preferred axes of rotation in phase II

The atomistic models obtained through RMC refinement show that as the sample is warmed towards the transition at 186 K, the molecules start to show increasing thermal motion, effectively preparing to undergo the transition (Figure 6.9). Whether this is an entirely random process or one that shows a discernable trend as a function of temperature can be investigated by recording the angles the molecules make with each cell axis. In order to do this each molecule has been defined by three C-C vectors that pass through the molecular centroid. Figure 6.13 shows how each vector

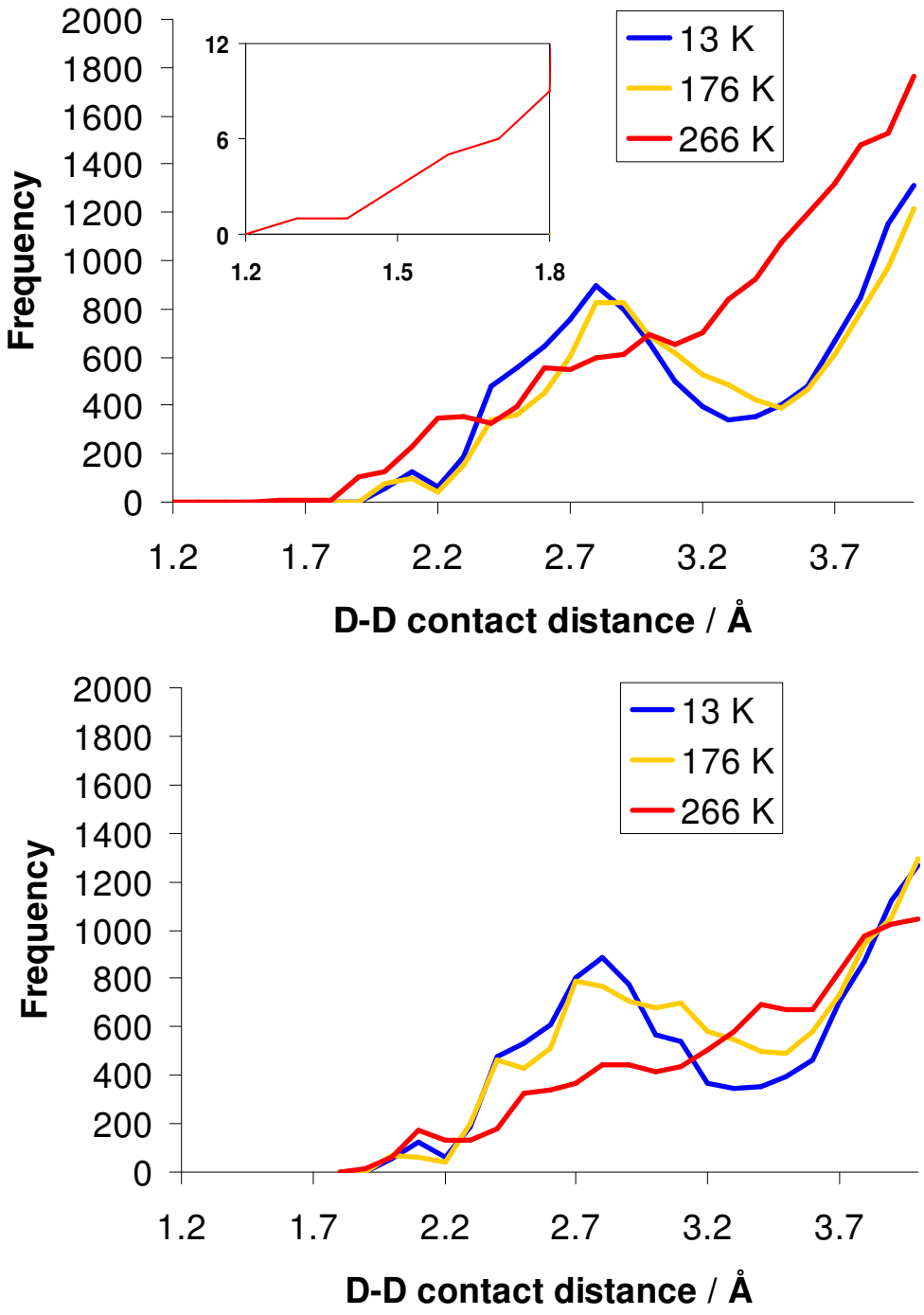

Figure 6.12. Shortest intermolecular D···D contact distances in model A (top) and model B (bottom). The inset plot for model A shows the 1.2-1.8 Å region in more detail.

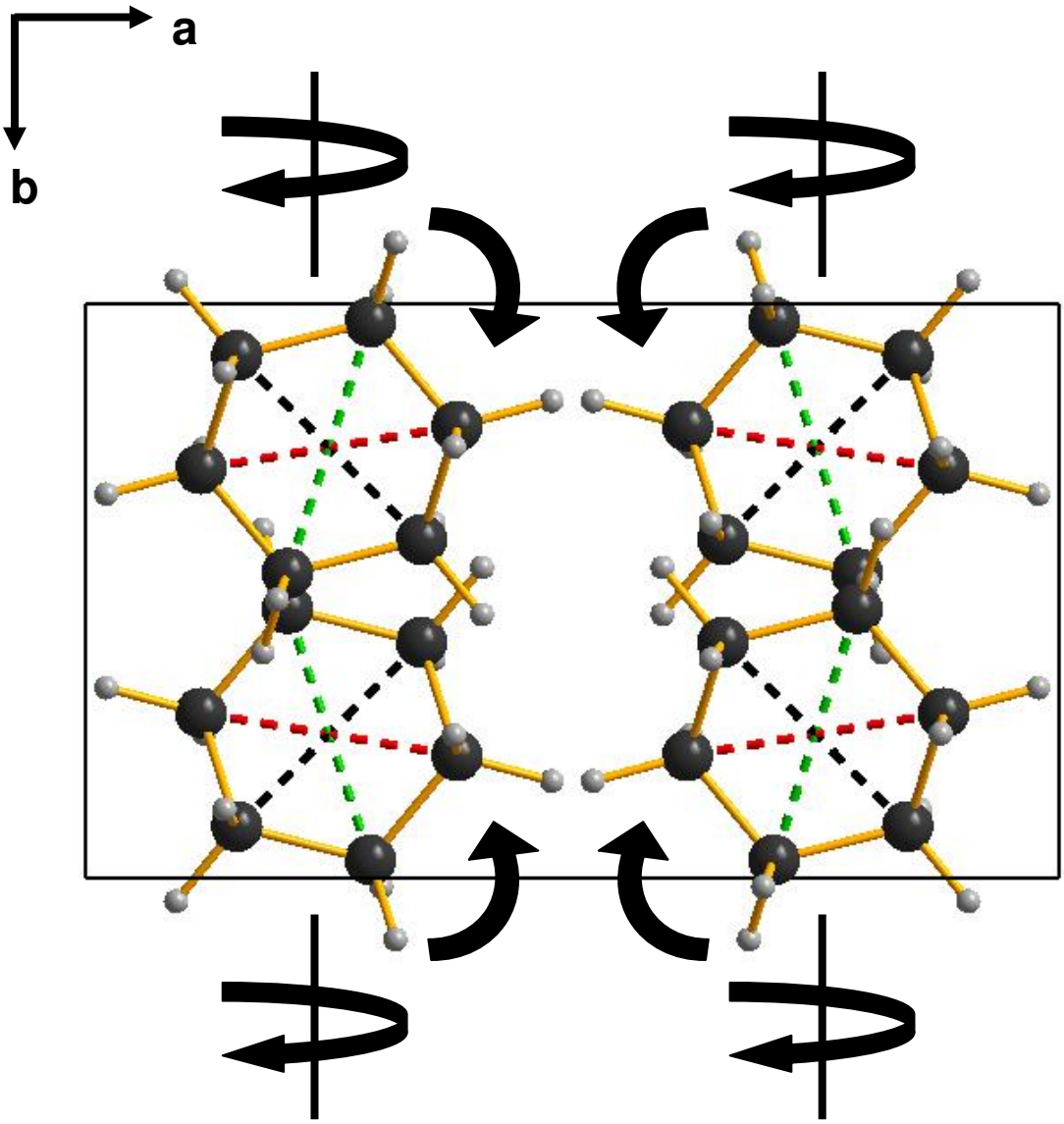

Figure 6.13. View along the *c*-axis showing the three vectors used to describe each molecule. Vectors 1, 2 and 3 are shown in red, green and black dotted lines respectively. The thick black arrows indicate the approximate motion of the cyclohexane molecules on heating to 176 K.

has been defined. At higher temperatures, an increasing number of C-C vectors deviate further from the mean angle they make with a particular axis, reflecting the greater thermal energy the molecules possess. Some vector angle/axis plots show a definite trend as a function of temperature and these are shown in Figure 6.14 and 6.15 for models A and B respectively. Vector 2 is roughly perpendicular to the *c*-axis and so the fact it makes a smaller angle with **a** and a larger angle with **b** at 176 K than at 13 K suggests that the molecules are rotating, approximately, about the

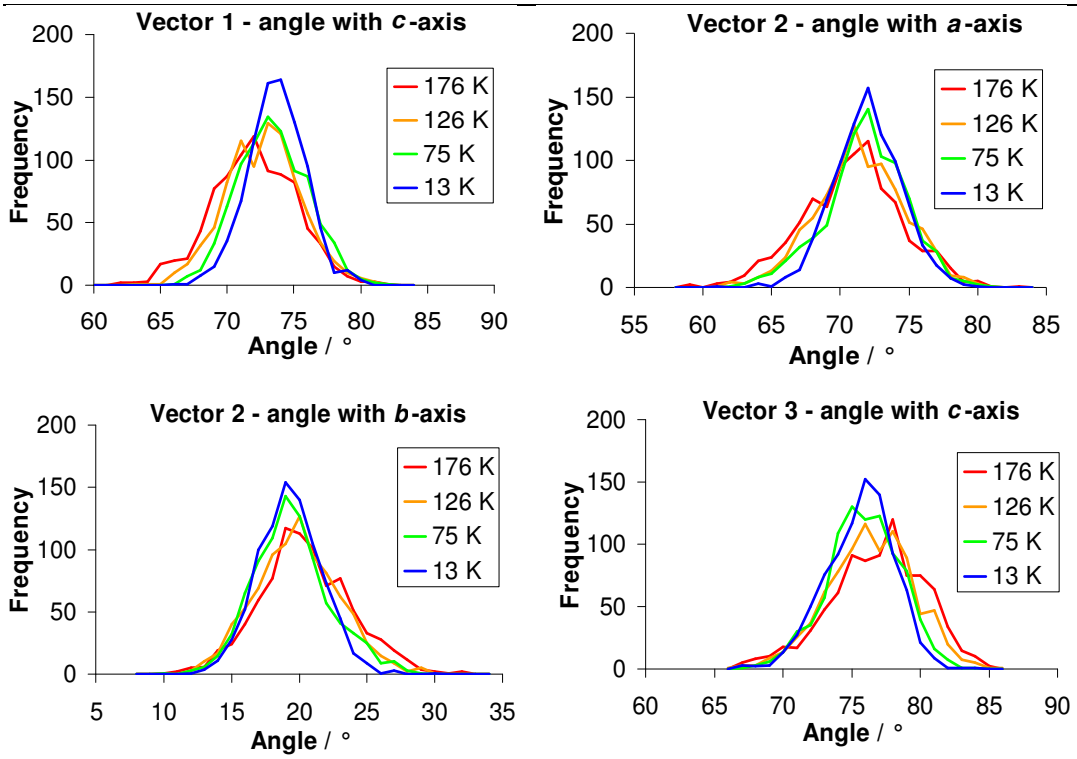

Figure 6.14. Selected vector-axis angle histograms for all phase II data using model A.

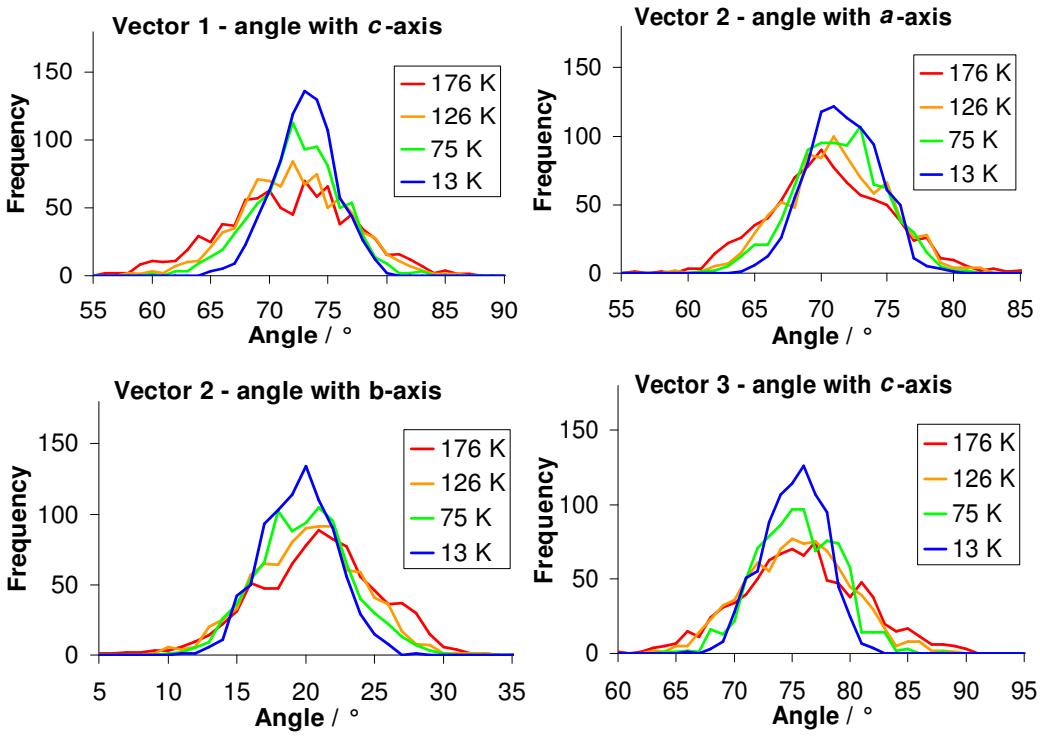

Figure 6.15. Selected vector-axis histograms for all phase II data using model B

molecular C_3 axis. Similarly, decreasing and increasing angles with the *c*-axis made by vectors 1 and 3 respectively, suggest that the molecules are also rotating about the *b*-axis. The approximate molecular motion is shown diagrammatically in Figure 6.13.

These trends are also present in the structures seen by Rietveld refinement, although the angular changes are very small - the largest change is seen is 0.63° (vector 1 with **a**). The effect of temperature on the vector-axis angles is much more prominent in the RMC models, where the angular change falls in the range *ca.* 2-3° for each vector. Although this is still a small change, it is sufficient to show that a large proportion of the molecules are undergoing correlated rotation. This is the case in particular for the relationship between vectors 1 and 3 with the *c*-axis (corresponding to rotation about the *b*-axis) where the respective histogram peaks clearly shift, whereas those for vector 2 with the *a*- and *b*-axes do not; the tail of the histogram increases in one direction. This suggests that the overall orientation of the molecules, with respect to rotation about **b**, shows a gradual change whilst a greater degree of freedom is allowed for rotation about the C_3 axis as a function of increasing temperature. These observations concur with deuterium NMR results by McGrath and Weiss which indicate that molecular motion in phase II is more complex than C_3 rotations alone.[14] They also report that a large fraction of the sample is undergoing this complex rotation which is consistent with the observations made here.

These rotational trends are only partially reproduced by the MD simulations (prior to any RMC refinement), as shown in Figure 6.16. The most striking difference between Figures 6.14 and 6.16 is that a far narrower range of angles are observed between the vectors and axes at 13 K (*ca.* 7° compared with *ca.* 15° after RMC refinement) in the simulations. A small temperature-induced shift in the peak positions (*ca.* 3°) can be seen in the histograms corresponding to the angles made with the *a*- and *b*-axes by vector 2, moving to smaller and larger angles respectively. However, any temperature related trends for vectors 1 and 3 are not as obvious. This shows that whilst the MD simulations can reproduce the rotational behaviour about the C_3 axis to some extent, the correlated motion of the molecules about the *b*-axis has not been predicted.

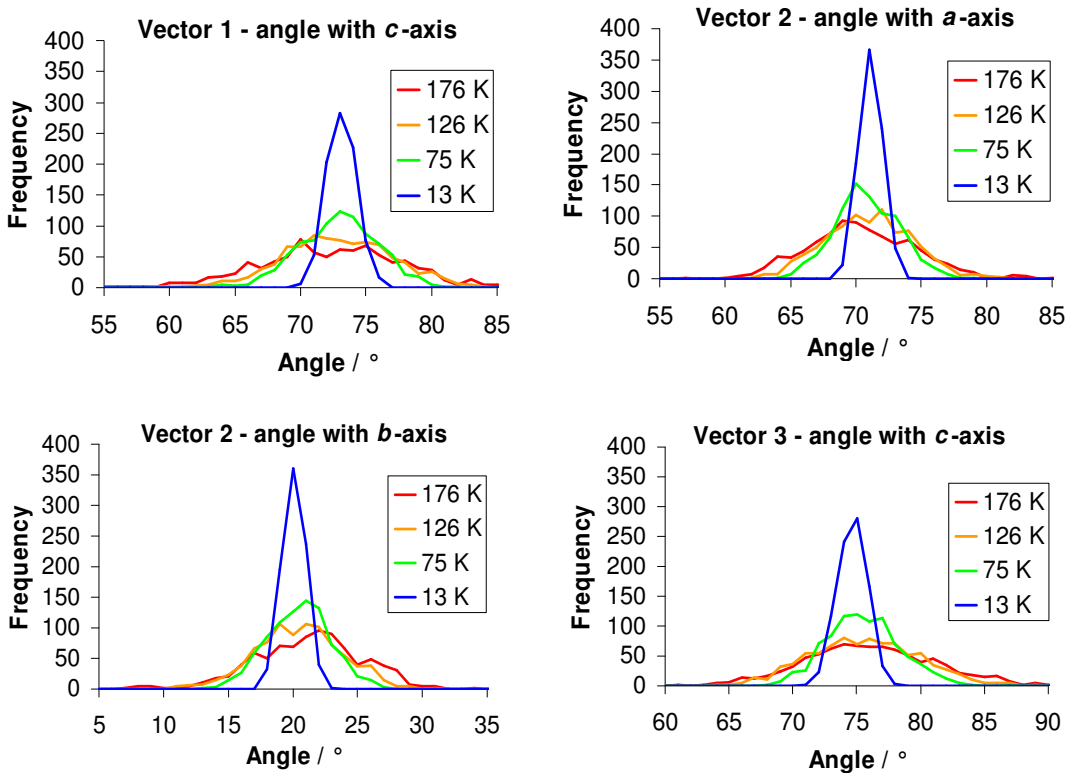

Figure 6.16. Selected vector-axis angle histograms for all phase II data from MD simulations, prior to RMC refinement

6.4 Conclusions

The effect of temperature on the structure of cyclohexane has been explored using high resolution neutron total scattering and Reverse Monte Carlo modelling. The two models that were trialled show that use of either one results in a good fit to the phase II experimental data. Only model B shows good fits to the data for phase I as model A violates the symmetry requirements of the FCC cell - shown in the fit to the $I(t)$ data in the form of additional peaks. Although there a few extra peaks in the $I(t)$ fit for Model B, it clearly reproduces the cubic symmetry much better than Model A.

The RMC fits of models A and B to the phase I $G(r)$ and $F(Q)$ data are both excellent if the $I(t)$ data are removed from the refinement, despite giving two very different final atomic configurations. This demonstrates the importance of considering the long-range structure, even for plastic phases.

The isotropic model, B, shows that short D···D contacts below 1.7 Å do not develop. Therefore the molecules must be spatially accommodating each other by correlating their rotational motion.

In phase II, clear trends can be seen in the development of the rotational disorder on heating to 176 K. Analysis of intramolecular C-C vectors through the molecular centroid show that the molecules rotate about their C_3 axes in the opposite direction to their nearest neighbours whilst all rotating in the same direction about an axis aligned with the *b*-direction.

6.5 References

1. A. J. Blake, W. Clegg, J. M. Cole, J. S. O. Evans, P. Main, S. Parsons and D. J. Watkin, *Crystal Structure Analysis: Principles and Practice*, 2009.
2. A. L. Goodwin, M. T. Dove, A. M. Chippindale, S. J. Hibble, A. H. Pohl and A. C. Hannon, *Physical Review B: Condensed Matter and Materials Physics*, 2009, **80**, 054101/054101-054101/054107.
3. M. G. Tucker, M. T. Dove and D. A. Keen, *Journal of Physics: Condensed Matter*, 2000, **12**, L723-L730.
4. J. E. Readman, P. M. Forster, K. W. Chapman, P. J. Chupas, J. B. Parise and J. A. Hriljac, *Chemical Communications (Cambridge, United Kingdom)*, 2009, 3383-3385.
5. T. D. Bennett, A. L. Goodwin, M. T. Dove, D. A. Keen, M. G. Tucker, E. R. Barney, A. K. Soper, E. G. Bithell, J.-C. Tan and A. K. Cheetham, *Physical Review Letters*, 2010, **104(11)**, 115503/1-115503/4
6. K. W. Chapman, P. J. Chupas, G. J. Halder, J. A. Hriljac, C. Kurtz, B. K. Greve, C. J. Ruschman and A. P. Wilkinson, *Journal of Applied Crystallography*, 2010, **43**, 297-307.
7. T. Dykhne, R. Taylor, A. Florence and S. J. L. Billinge, *Pharmaceutical Research*, 2011, **28**, 1041-1048.
8. M. T. Dove, M. G. Tucker and D. A. Keen, *European Journal of Mineralogy*, 2002, **14**, 331-348.

9. L. Temleitner and L. Pusztai, *Physical Review B: Condensed Matter and Materials Physics*, 2010, **81**, 134101/134101-134101/134108.
10. R. Kahn, R. Fourme, D. Andre and M. Renaud, *Acta Crystallographica, Section B: Structural Crystallography and Crystal Chemistry*, 1973, **29**, 131-138.
11. M. L. Bansal and A. P. Roy, *Molecular Physics*, 1979, **38**, 1419-1426.
12. A. Brodka and T. W. Zerda, *Journal of Chemical Physics*, 1992, **97**, 5669-5675.
13. V. Ehrenberg, C. Hoheisel and A. Würflinger, *Physics and Chemistry of Liquids*, 1992, **25**, 27-36.
14. K. J. McGrath and R. G. Weiss, *Langmuir*, 1997, **13**, 4474-4479.
15. A. V. Chadwick and J. N. Sherwood, *Journal of the Chemical Society, Faraday Transactions 1: Physical Chemistry in Condensed Phases*, 1972, **68**, 47-50.
16. E. M. Hampton and J. N. Sherwood, *Journal of the Chemical Society, Faraday Transactions 1: Physical Chemistry in Condensed Phases*, 1976, **72**, 2398-2403.
17. H. Farman, L. O'Mard, J. C. Dore and M. C. Bellissent-Funel, *Molecular Physics*, 1991, **73**, 855-871.
18. R. M. Ibberson, *Journal of Applied Crystallography*, 1996, **29**, 498-500.
19. W. G. Williams, R. M. Ibberson, P. Day and J. E. Enderby, *Physica B: Condensed Matter (Amsterdam)*, 1998, **241-243**, 234-236.
20. D. A. Keen, *Journal of Applied Crystallography*, 2001, **34**, 172-177.
21. A. Coelho, *TOPAS-Academic: General Profile and Structure Analysis Software for Powder Diffraction Data. Version 4.1*, 2007.
22. B. H. Toby, *Journal of Applied Crystallography*, 2001, **34**, 210-213.
23. M. G. Tucker, D. A. Keen, M. T. Dove, A. L. Goodwin and Q. Hui, *Journal of Physics: Condensed Matter*, 2007, **19**, 335218/335211-335218/335216.
24. A. C. Larson and R. B. von Dreele, *General Structure Analysis System (GSAS), Los Alamos National Laboratory*, 2000.

25. P. Dauber-Osguthorpe, V. A. Roberts, D. J. Osguthorpe, J. Wolff, M. Genest and A. T. Hagler, *Proteins: Structure, Function, and Genetics*, 1988, **4**, 31-47.

26. H. J. C. Berendsen, J. P. M. Postma, W. F. Van Gunsteren, A. DiNola and J. R. Haak, *Journal of Chemical Physics*, 1984, **81**, 3684-3690.

27. M. Parrinello and A. Rahman, *Journal of Chemical Physics*, 1982, **76**, 2662-2666.

28. M. Tucker, A. Goodwin and M. Dove, *RMCProfile User Manual, Version 6.4.7*, 2010.

29. P. A. Wood, J. J. McKinnon, S. Parsons, E. Pidcock and M. A. Spackman, *CrystEngComm*, 2008, **10**, 368-376.

Chapter 7

A Neutron Total Scattering Study of Crystalline Oxalyl Chloride*

*Nicholas P. Funnell, Martin T. Dove, Simon Parsons and Matthew G. Tucker

7.1 Introduction

It is desirable to understand why phase transformations in the solid state occur as this can lead to the ability to design and control the physical and/or chemical properties of functional materials and pharmaceuticals through selective polymorph growth. Whilst polymorph stability can often be explained through thermodynamic analysis, it is less well-understood how molecules in a structure actually prepare to undergo a transition. An ideal experimental method for investigating this is neutron total scattering. Total scattering experiments measure diffraction patterns which not only describe the time-average crystal structure but also provide information on local atomic environments. These data can be modelled using Reverse Monte Carlo (RMC) refinement to create atomistic models representative of the structure at any instantaneous moment in time. A more detailed overview of the advantages presented by total scattering is given in Chapter 6. This technique has been successfully applied to several inorganic extended structures including silica, strontium titanate, mixed-ratio zirconium and titanium phosphates and metal-organic frameworks but so far relatively few investigations have focussed on molecular materials.[1-4]

Oxalyl chloride (Scheme 7.1) is planar in the solid-state, but in the gas phase it exists as a mixture of planar and gauche conformers.[5] Several studies have been conducted that aim to identify the vibrational modes and relative stabilities of the different conformers.[6-9]

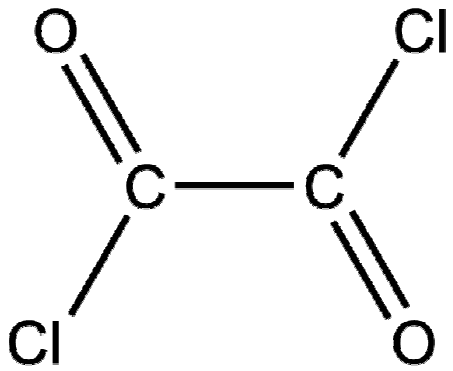

Scheme 7.1. The molecular structure of oxalyl chloride.

Oxalyl chloride freezes when cooled to 260 K into a disordered solid phase in the space group *Pbca* (phase-I), first determined by Groth and Hassel, although the authors did not report any disorder.[10] Unpublished results from the High Resolution Powder Diffractometer (HRPD) at the ISIS pulsed neutron spallation source, collected by R. M. Ibberson and S. Parsons, show that when cooled below 250 K, the structure undergoes a transition to an ordered solid phase in $P2_1/c$ (phase-II). The same experiment showed that it is possible to super-cool phase I to temperatures as low as 2 K (See Figure 7.1). Differential scanning calorimetry (DSC) traces have shown that this transformation is quite broad on cooling but on warming the transition is sharp and easy to discern (unpublished data, S. Parsons). The phase II structure is very similar to that of oxalyl bromide, also determined by Groth and Hassel (*a*=6.18, *b*=5.46, *c*=7.80 Å and β=112.4° in oxalyl bromide *c.f.* *a*=6.24, *b*=5.36, *c*=7.35 Å and β=114.11 in oxalyl chloride phase II at 245 K). All the molecules are arranged in layers such that they are perpendicular to their immediate neighbours. The HRPD data suggest that in phase-I *ca.* 85% of the molecules rotate about the normal to the C-C bond, whilst the remaining 15% remain in the same orientation as phase-II forming a minor component of the crystal structure. The two structures are shown in Figure 7.2.

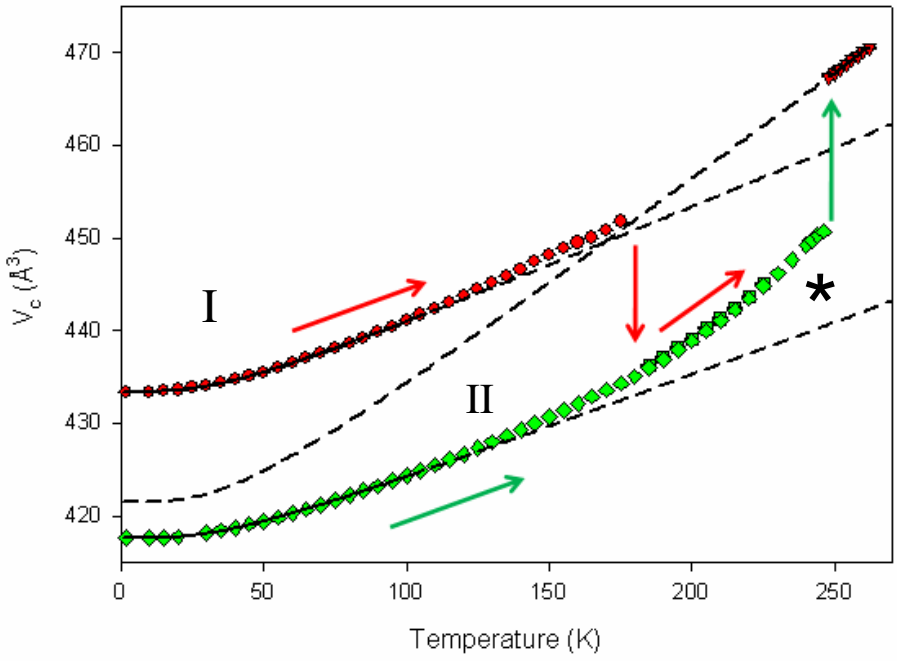

Figure 7.1: HRPD data showing variation of the volume of phases I and II with temperature. The star indicates the region where the sample shows departure from ideal behaviour. The dotted lines indicate ideal thermal expansion curves based on a Debye model. [S.Parsons and R. M. Ibberson, Unpublished data from HRPD, ISIS]

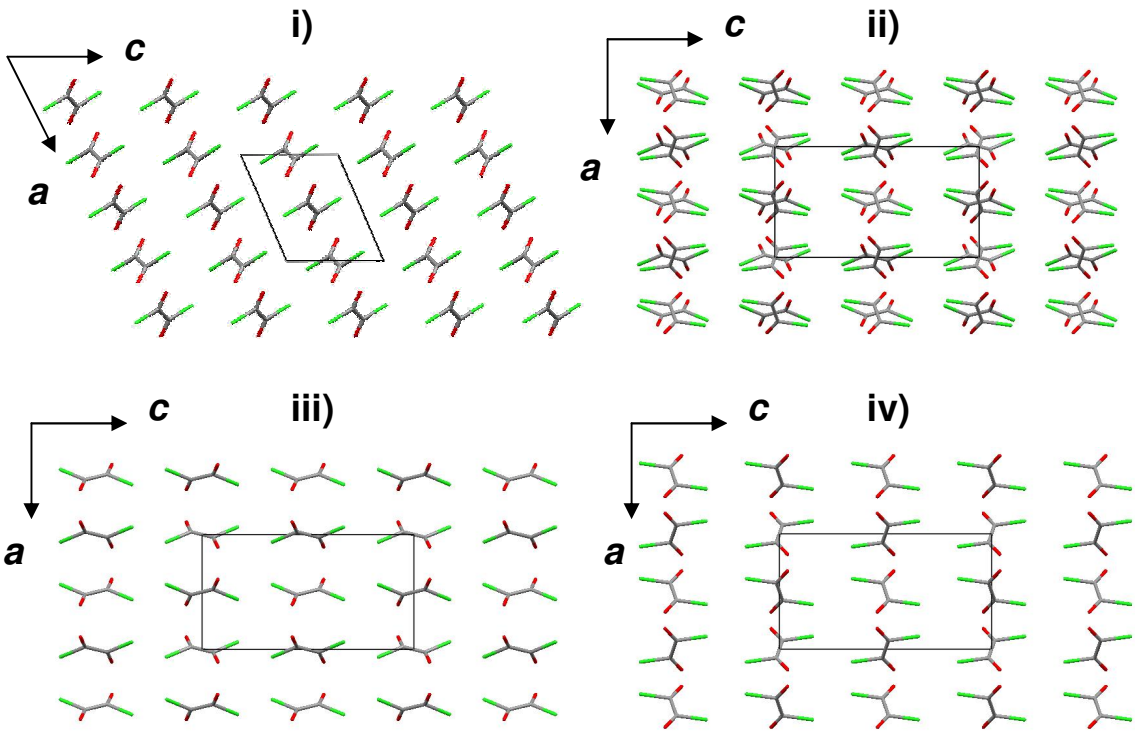

Figure 7.2. Packing arrangement of oxalyl chloride molecules in **i)** Phase II and **ii)** Phase I, as seen by Rietveld refinement. The overlapping molecules in **ii)** are partially occupied. **iii)** and **iv)** show the individual major and minor components of phase I respectively. Oxygen atoms are coloured red and chlorine in green.

The variation of the unit cell volumes of the two phases with temperature was found to deviate from ideal Debye behaviour, particularly for phase II between *ca.* 180-250 K, shown in Figure 7.1. The departure from ideal behaviour becomes more prominent as temperature increases, showing that the sample is preparing to undergo the transition at 250 K. The transition may proceed via layer formation of the minor component in localised regions of the lattice. If a molecule in the minor orientation lies within a layer of the major component then short intermolecular Cl-Cl contacts of *ca.* 2.7 Å would be observed if it were not spatially accommodated by the surrounding molecules. This contact distance is well below 3.5 Å - the sum of the van der Waals radii for two Cl atoms. Formation of layers containing only molecules in the minor orientation would prevent these unfavourable contacts from developing.

The precise nature of this disorder, in terms of whether it occur randomly or if it is ordered on a local scale, cannot be determined by Rietveld refinement as both the ordered and disordered possibilities would have the same average structure (a

more detailed explanation of this is given in Chapter 6). The aim of this investigation is to use total scattering and molecular dynamics (MD) simulations to observe the extent of local ordering in oxalyl chloride leading up to, and above the transition at 250 K. Of particular interest is the distribution of Cl-Cl contacts for the reasons stated above.

Owing to a lack of consistency used in total scattering nomenclature, our definitions follow those outlined by Keen.[11]

7.2 Experimental

7.2.1 Sample preparation

Oxalyl chloride, obtained from Sigma-Aldrich, was frozen with liquid nitrogen and cold-ground into a homogenous powder at 77 K, in a nitrogenous atmosphere.[12]

7.2.2 Neutron total scattering

Owing to difficulties with temperature control the total scattering experiment was performed twice. The data reported here are derived from both experiments. In both investigations, the sample was packed into a thin-walled vanadium can and was mounted on a CCR device in the first experiment and on a cryostat in the second. Total scattering data were collected on the General Materials Diffractometer (GEM) at the ISIS pulsed spallation source using the neutron time-of-flight (ToF) method.[13] Data were collected to Q_{max} = 60 Å^{-1}. Data collections in the first experiment were carried out at the following temperatures 13, 53, 106, 158, and 208 K. In the second experiment, data were collected at 245, and 255 K; either side of the transition point. The measured differential cross-section data were processed using GUDRUN, producing total scattering structure factor data, $F(Q)$ to a useable $Q_{\max}$ of 50 Å^{-1}, and the corresponding total radial distribution functions, $G(r)$, after correcting for background scattering, multiple scattering, Placzek inelasticity and beam attenuation by the sample container.

The Bragg diffraction data (detector bank 79-106°), contained in the total scattering pattern were refined against a Z-matrix model of oxalyl chloride in TOPAS Academic, using a dummy atom at the centre of the molecule, constraining it to be centrosymmetric.[14] The model was then used as a starting point in GSAS with

data from the detector bank 50-74° in order to obtain the necessary data files for refinement by RMCProfile.[15] Rietveld fits to the data at 13, 245 and 255 K using GSAS are shown in Figure 7.3. Crystal structure refinement details for these data are given in Table 7.1.[16, 17]

7.2.3 Reverse Monte-Carlo modelling

The crystal structures refined in TOPAS were used to generate an initial atomic configuration, in a 10x10x10 supercell for all phase II datasets and a 10x10x5 supercell for phase I refinements, both consisting of 2000 molecules. The method used by RMCProfile fits calculated $F(Q)$, $G(r)$ and $I(t)$ data to the experimental observations by moving atoms in the configuration at random. More detail on this procedure is given in Chapter 6. Geometric constraints were employed to maintain the connectivity of the molecules – these are discussed in Section 7.3.1. Refinement proceeded until there were no further improvements in the value of χ^2.

7.2.4 Molecular dynamics simulations

Molecular dynamics simulations were carried out using the program Forcite, implemented in the Accelrys Materials Studio suite. The cvff forcefield was used with an NPT ensemble.[18] Simulations were carried out for 20 ps at intervals of 0.5 fs using an NHL thermostat and a Parinello barostat.[19, 20]

7.2.5 Frequency calculations

Statistical frequency calculations within a harmonic approximation were carried out using DMOL implemented in the Accelrys Materials Studio suite on the crystal structure of oxalyl chloride at 13 K.[21] The structure was initially geometry optimised in $P2_1/c$ where the cell dimensions were held fixed. The structure was then allowed to relax in $P1$ prior to calculation of frequencies. The PBE exchange-correlation functional was used with a DNP basis set. Dispersion was accounted for using the TS semi-empirical dispersion correction scheme. Brillouin zone integrations were performed by Monkhorst-Pack k-point sampling at intervals of 0.07 $Å^{-1}$. The total energy convergence was 10^{-5} Ha per atom, the maximum force tolerance was 0.002 Ha $Å^{-1}$ and the maximum displacement was 0.005 Å.

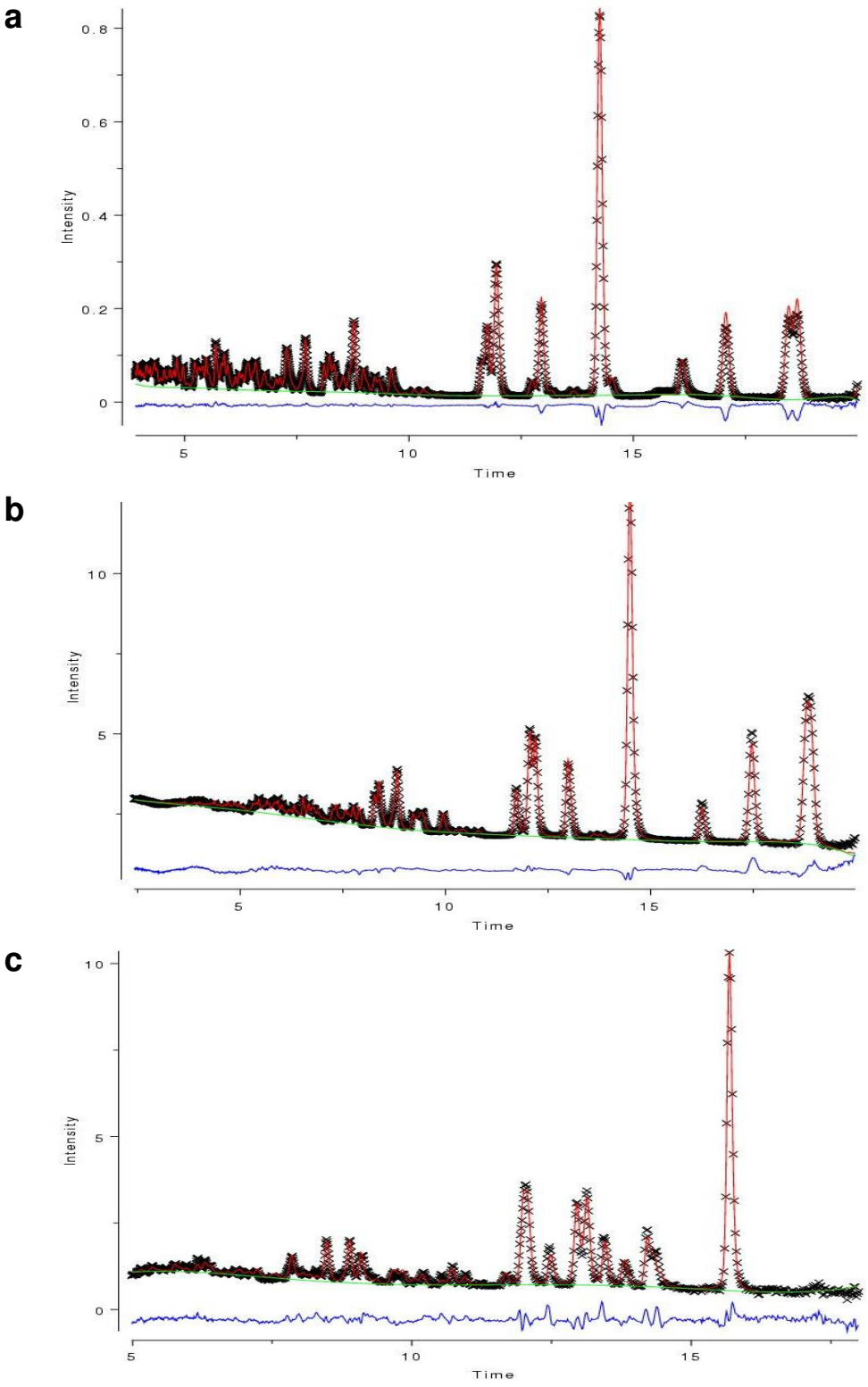

Figure 7.3. Rietveld refinements of the crystal structures at **a)** 13 K, **b)** 245 K and **c)** 255 K. Experimental data are shown in black, the calculated fit in red and the difference in blue. The patterns are plotted as a function of time-of-flight. The d-spacing ranges shown in the patterns above are 0.8-4.1 Å for the 13 K data, 0.5-4.1 Å for the 245 K data and 0.7-3.9 Å for the 255 K data.

Table 7.1. Crystal structure refinement details for selected datasets from the detector bank 2θ = 50-74°. The high value of χ^2 indicates an underestimation of the errors

Temperature / K	**13**	**245**	**255**
Sample type and radiation used	Neutron, powder	Neutron, powder	Neutron, powder
Chemical formula	$C_2O_2Cl_2$	$C_2O_2Cl_2$	$C_2O_2Cl_2$
M_r / g mol^{-1}	126.93	126.93	126.93
Cell setting, space group	Monoclinic, $P2_1/c$	Monoclinic, $P2_1/c$	Orthorhombic, *Pbca*
a / Å	5.99043(6)	5.24418(14)	6.4360(13)
b / Å	5.29850(5)	5.35899(11)	6.0407(12)
c / Å	7.15751(7)	7.34897(14)	11.9332(9)
β / °	113.0431(7)	114.0978(18)	90(0)
V / Å^3	209.054(2)	224.484(4)	465.89(5)
Z	2	2	4
D_c / Mg m^{-3}	2.02	1.88	1.80
d_{max}, d_{min} / Å	4.1, 0.8	4.1, 0.5	3.9, 0.7
R_{wp}	0.0405	0.0189	0.0996
X^2	16.16	16.84	13.86
Reflection/Profile data	2044	1890	1462

7.3 Results and Discussion

7.3.1 RMCProfile geometric restraints

There was a need to place restraints on the intra- and intermolecular geometry of the molecules as RMCProfile would otherwise generate an unrealistic atomic configuration. The restraints used were based on a simple forcefield model, which is detailed in the RMCProfile manual.[22] The distances and angles used for the intramolecular geometry for each dataset were obtained from the refined crystal structures. For the phase II refinements, the 'temperature' parameter, controlling the weight of the restraints was set to 20 K above the experimental temperature. Although the real temperature could also be used, this was not the case for the 13 K dataset, where insufficient broadening was seen in the partial radial distribution functions for the covalent bonds. Increasing the temperature parameter by 20 K solved this problem and so the same procedure was performed for all phase II data

for sake of consistency. The closest approach distances permitted for the atom pairs C-C, C-O, C-Cl, O-O, O-Cl and Cl-Cl in phase II were 1.4, 1.0, 1.6, 2.0, 2.0, and 2.0 Å respectively. Although the 2.0 Å distances seem physically unreasonable, they were set at this value to prevent inducing bias into the model, so that the refinement could be driven by the experimental data as much as possible. Refinement of the phase I data at 255 K was problematic as unrealistically short Cl-Cl contacts below 3 Å developed and the connectivity of a significant portion of molecules was not preserved. Therefore it was necessary to set the minimum Cl-Cl approach distance to 3.0 Å. The use of the closest approach distance induced a 'spike' in the partial radial distribution function, $g(r)$, corresponding to the Cl-Cl distance at 3.0 Å, an example of which is shown in Figure 7.4. This is a commonly-encountered problem when using closest-approach restraints, which are better designed to cope with relatively rigid polyhedral systems, whereas oxalyl chloride is more flexible.[15, 23] The Cl-Cl spike in the phase I data shows that the final models generated are unrealistic and that no firm conclusions should be drawn from them. The difficulty in dealing with flexible molecular systems using RMC is discussed in Section 7.3.4.

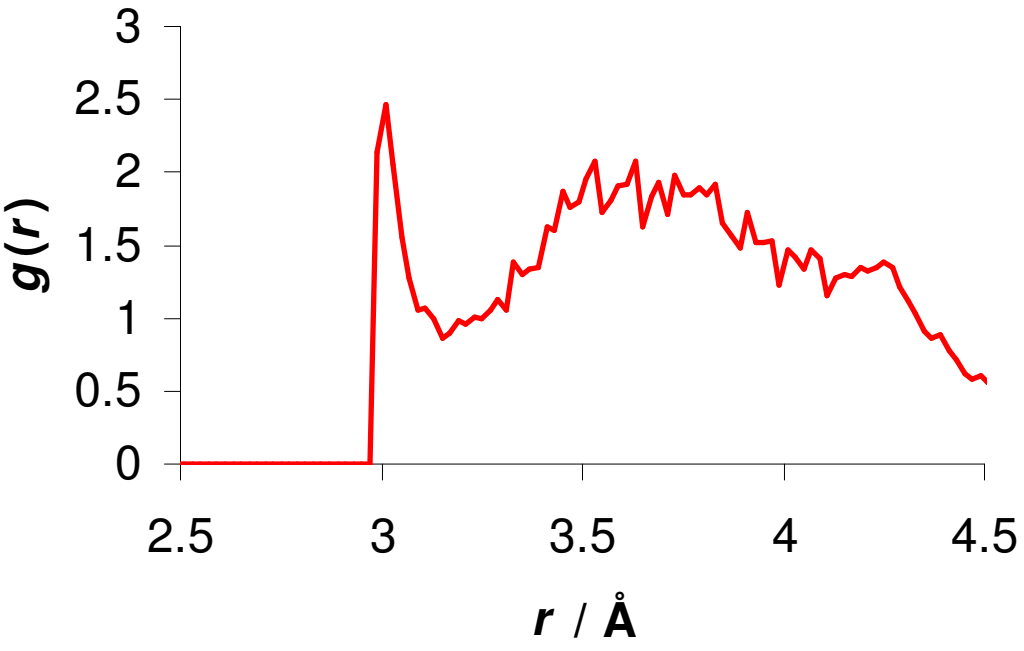

Figure 7.4. Partial $g(r)$ for Cl-Cl contacts in phase I. The use of a closest approach constraint results in the sharp peak at 3 Å.

7.3.2 Initial starting models

Similarly to the starting models used for cyclohexane in Chapter 6, initial atomic configurations for phase II were derived from the ordered crystal structure at each temperature (model IIA) and molecular dynamics simulations (model IIB). The refined crystal structure at 13 K was used as the starting point for each MD simulation of phase II.

Generating a suitable starting model for phase I at 255 K was less straightforward and so four different starting models were trialled. However as each of these required the use of the 3 Å minimum approach constraint for the Cl-Cl contacts, these will not be discussed in any more detail.

The initial RMC fits of models IIA and IIB to the data at 13 K, prior to refinement are shown in Figure 7.5. It is immediately apparent that the dynamics-derived model (IIB) gives a better fit to the PDF above *ca.* 3 Å in terms of being more disordered than IIA, although the agreement between peak positions is not particularly good. Above *ca.* 3 Å, intermolecular contacts start to contribute to the PDF and beyond *ca.* 4.5 Å the intermolecular contacts are the sole contributor to the PDF. The relatively poor fit at low r in IIB is a consequence of the MD simulations preserving 'ideal' covalent bond lengths, an indication that the bond stretching and bending force constants are too high. Thus neither of the initial starting models used show particularly good agreement with the experimental data prior to any refinement.

7.3.3 RMCProfile refinement of the phase II total scattering data

The final RMC fits at 13 K and 245 K for models IIA and IIB to the $G(r)$, $F(Q)$ and $I(t)$ data are shown in Figure 7.6. Both models IIA and IIB generally show good fits to all data, although at 13 K model IIA appears to be slightly better than IIB. This is particularly evident in the $G(r)$ in the range $3 < r < 10$ Å which suggests that model IIB contains too much disorder for the data. This is also reflected in the slightly worse fit to the $I(t)$ data for model IIB. The extent of disorder in the two models is evident in the atomic configurations; Figures 7.7 and 7.8 show the final atomic configurations for all phase II data, condensed back down onto a single unit cell.

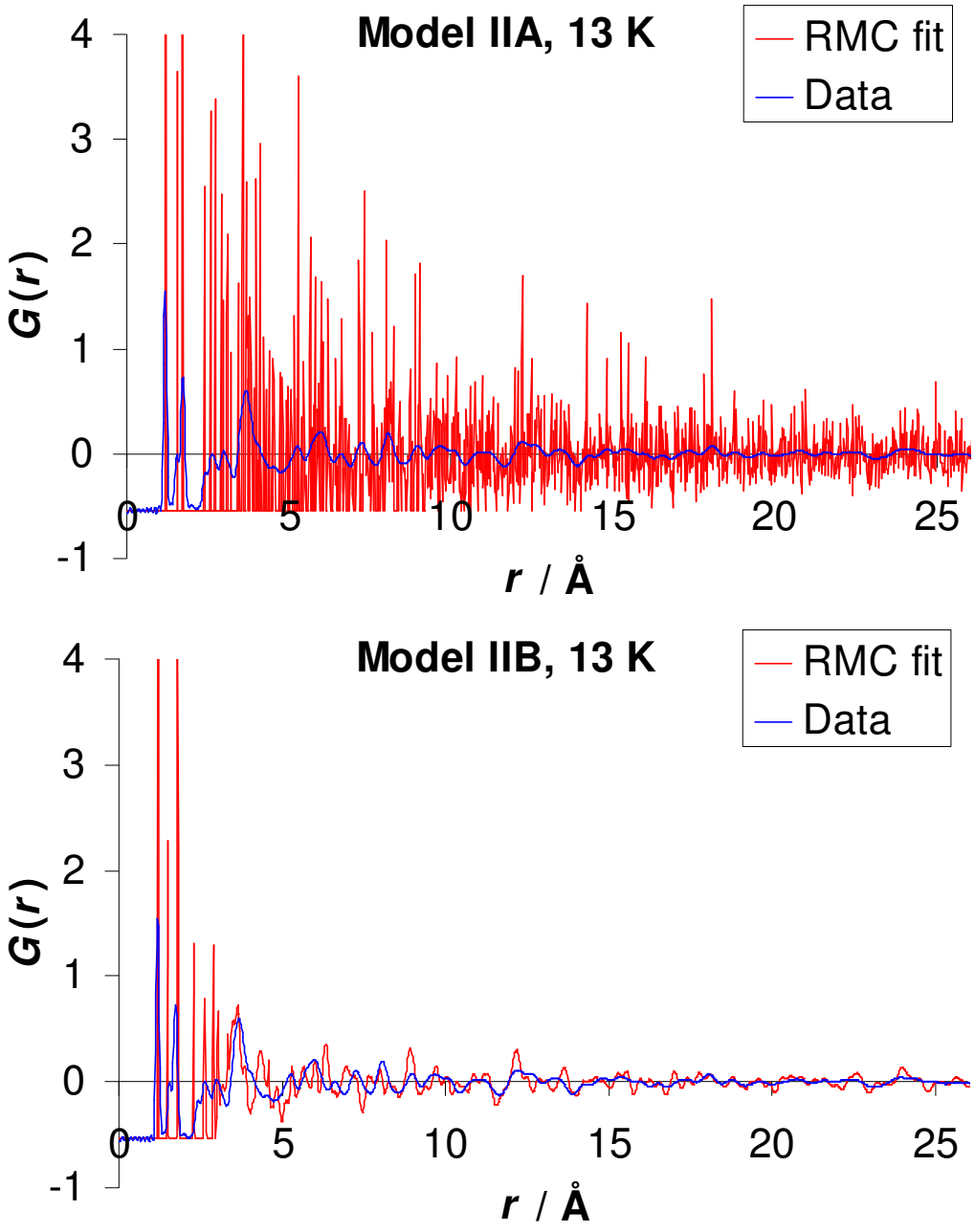

Figure 7.5. Initial fits of the atomistic configuration to experimental data at 13 K using models IIA and IIB before RMC refinement. The y-axis has been truncated at '4' for sake of clarity

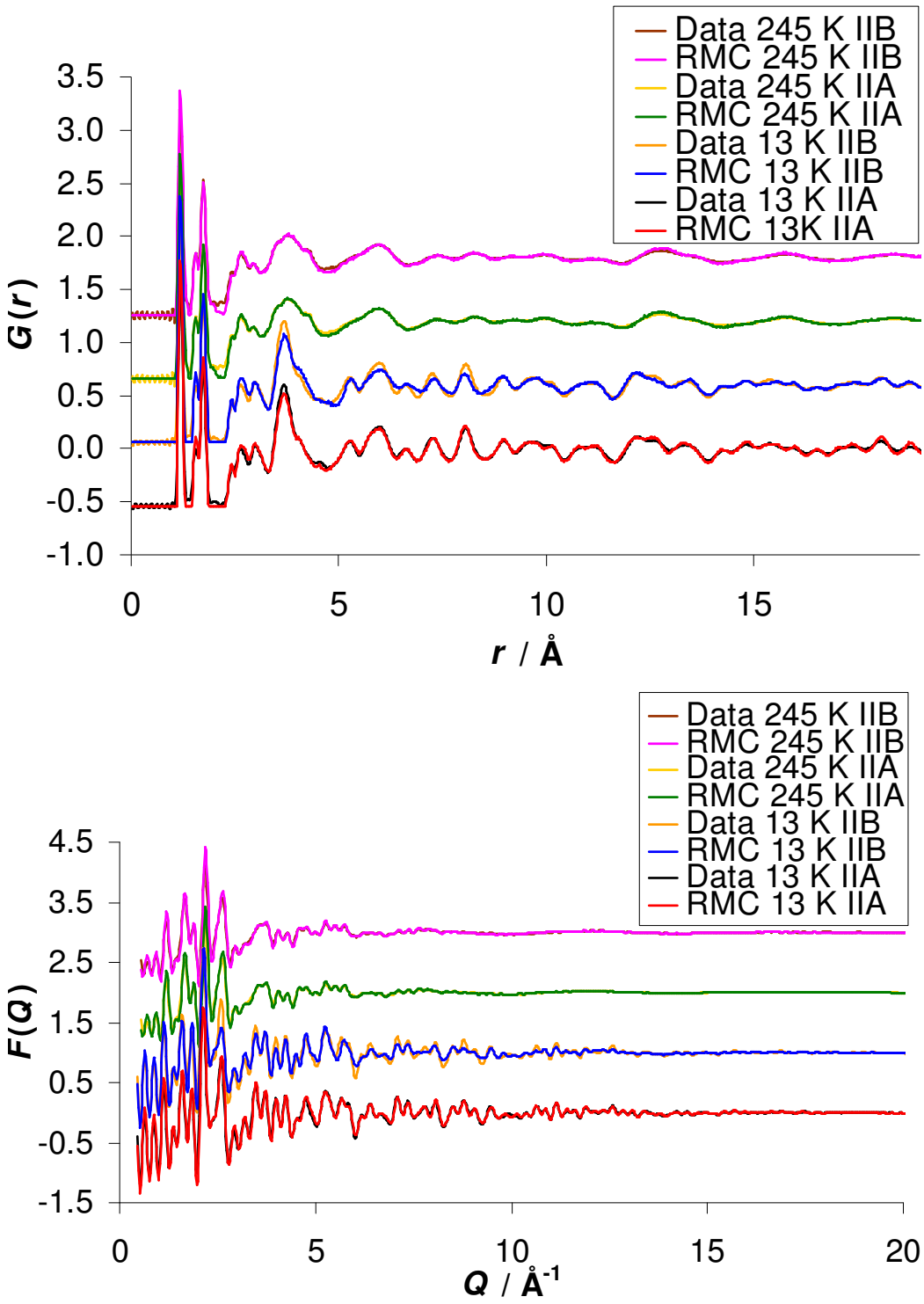

Figure 7.6. Final RMC fits to the *G*(*r*), *F*(*Q*) and $I(t)$ data for 13 and 245 K using models IIA and IIB. *Q* has been truncated at 20 in the F(Q) fits to show the low *Q* more region clearly. An excellent fit is seen for all data between *Q* = 20-50 Å^{-1}.

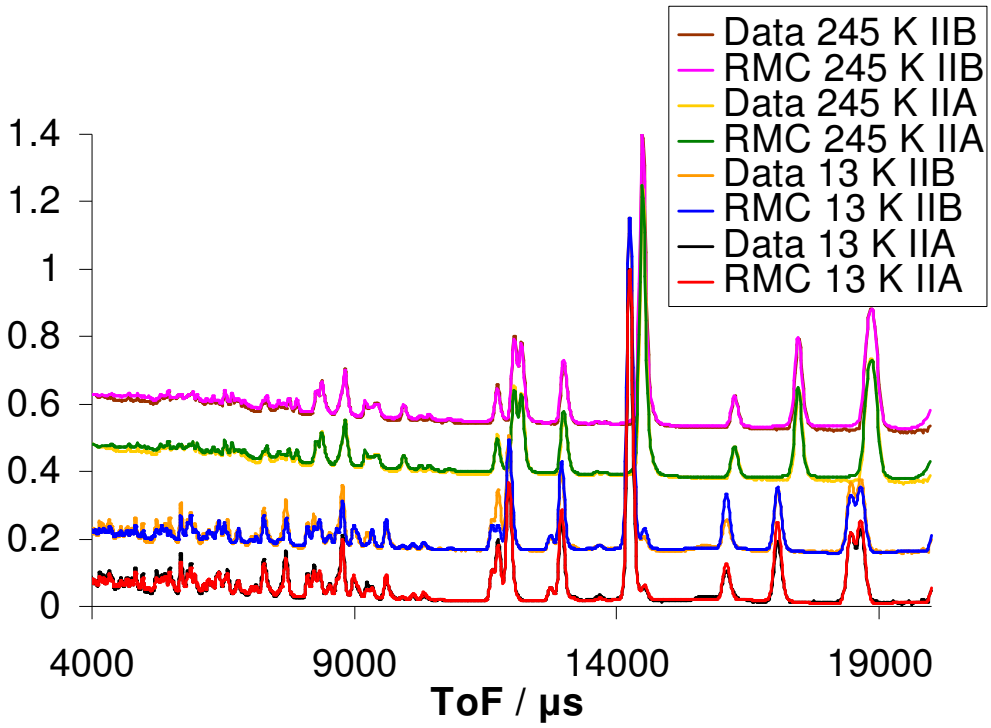

Figure 7.6 continued

Each unit cell in the Figures is orientated so the view is along the C-C bond of the lower molecule in the cell. The configurations for IIA and IIB show that on warming to 208 K, the atoms tend to vibrate in a direction perpendicular to the plane of the molecule. By viewing the structure along a C-C bond, the out-of-plane thermal motion is emphasised. The anisotropic motion of the Cl and O atoms can be easily rationalised through torsional vibrations about the C-C bond. The out-of-plane motion of the C atoms can be achieved through a combination of vibrational motions. Three examples are illustrated in Figure 7.9, corresponding to low energy vibrations calculated (DMOL) at 51.67, 71.58 and 96.48 cm^{-1}.

At 245 K, the atomic thermal motion becomes much more isotropic – a feature also observed in cyclohexane on heating (Chapter 6). This may be due to the molecules gaining enough room to vibrate more freely, experiencing reduced steric restriction from their neighbours as a result of the expanding unit cell. This additional freedom may also facilitate the molecular rotation necessary for the phase transition at 250 K. The onset of increased thermal motion can also be seen in the

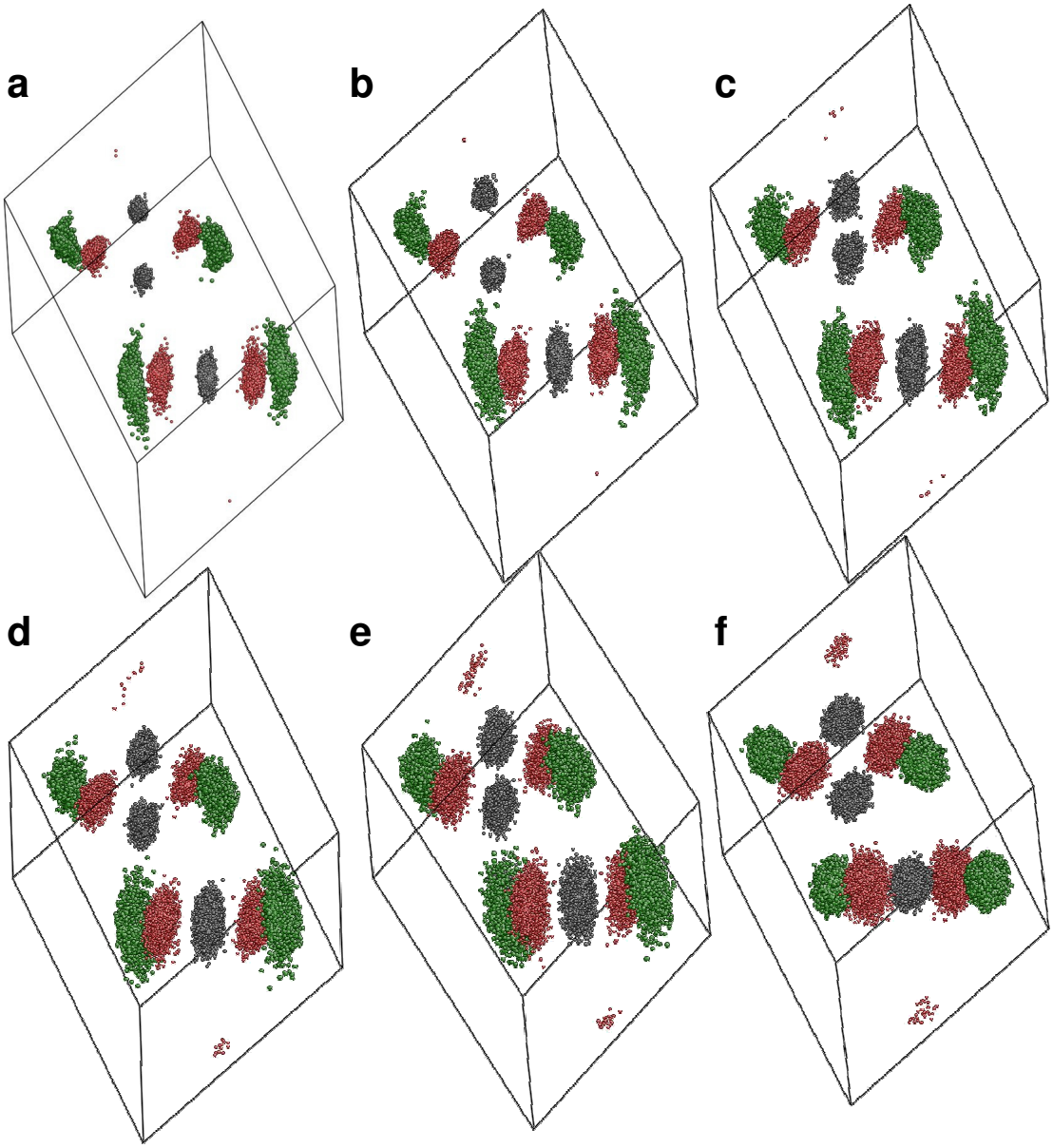

Figure 7.7. The distribution of atomic positions in the model A supercell condensed back onto a single unit cell at **a)** 13 K, **b)** 53 K, **c)** 106 K, **d)** 158 K, **e)** 208 K and **f)** 245 K. In all cases, the cell has been orientated so the view is along the C-C vector of the lower molecule in each unit cell. The molecule at the top of each cell is split over two unit cells. Carbon atoms are shown in grey, chlorine atoms in green, and oxygen atoms in red.

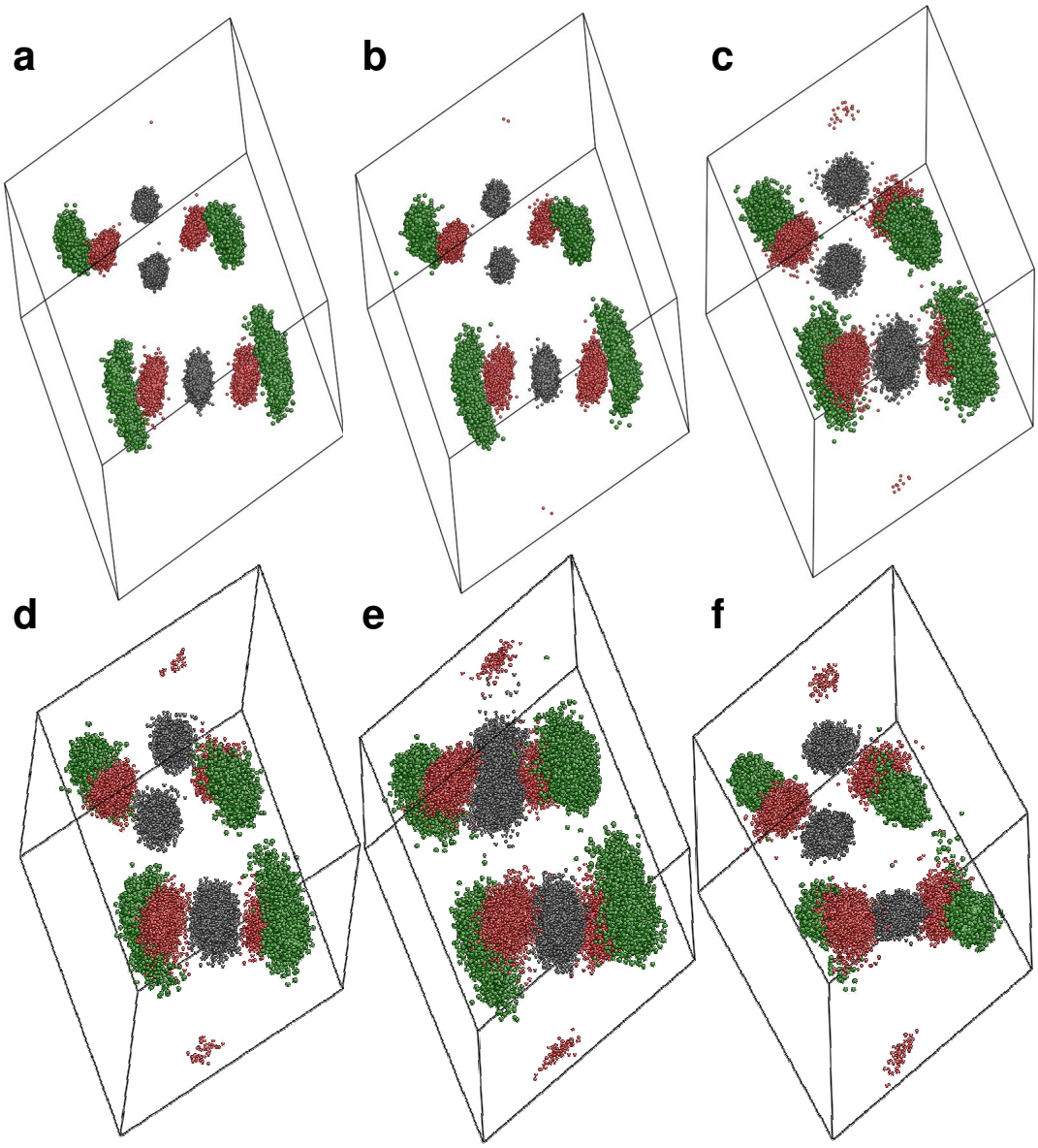

Figure 7.8. The distribution of atomic positions in the model B supercell condensed back onto a single unit cell at **a)** 13 K, **b)** 53 K, **c)** 106 K, **d)** 158 K, **e)** 208 K and **f)** 245 K. In all cases, the cell has been orientated so the view is along the C-C vector of the lower molecule in each unit cell. The molecule at the top of each cell is split over two unit cells. Carbon atoms are shown in grey, chlorine atoms in green, and oxygen atoms in red.

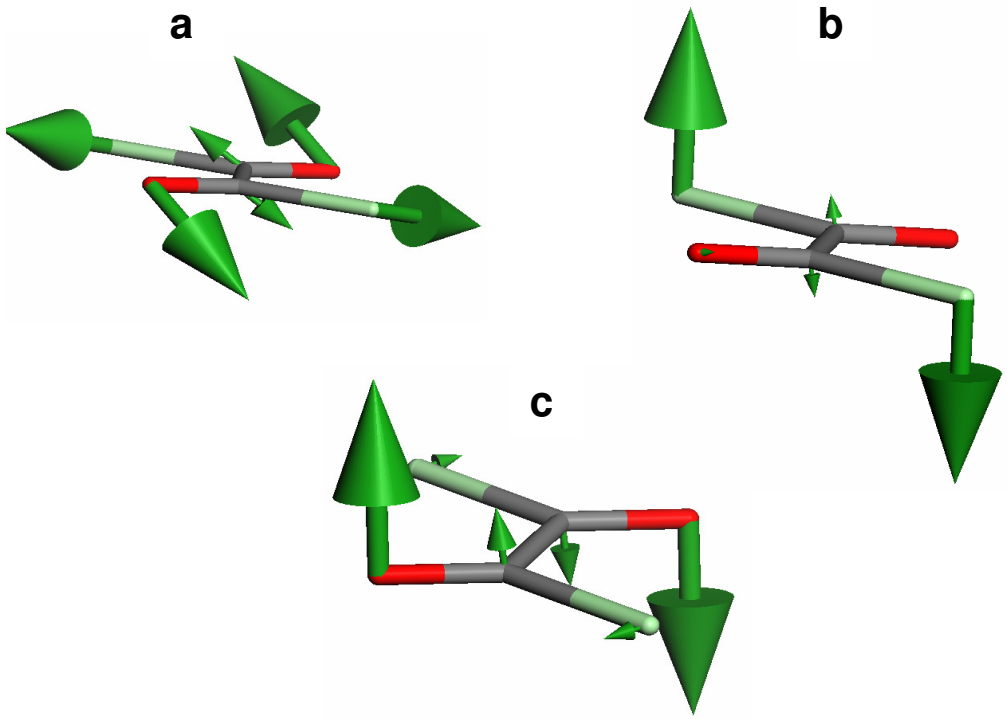

Figure 7.9. Low-energy vibrations at **a)** 51 cm^{-1}, **b)** 71 cm^{-1} and **c)** 96 cm^{-1} showing possible vibrations that account for the anisotropic distribution of the C atoms.

G(*r*) plots above *ca.* 3 Å where the peaks that were once sharply defined at 13 K show reduced intensity by 245 K and become much broader. This behaviour is also evident in the time-average crystal structures, determined by Rietveld refinement, shown in Figure 7.10. The structures for 13 and 53 K have not been included as these could not be refined anisotropically; the atomic displacement parameters became non-positive definite when refined. A discrepancy between the instantaneous and time-average structures is that the magnitude of thermal motion in chlorine is much greater than oxygen in the former but the latter suggests that the oxygen atom experiences greater displacement. Nevertheless, the time-average structure still clearly shows a conversion to isotropic atomic thermal behaviour in the structure at 245 K.

The data do not show that any of the molecules completely undergo the transition to phase I – they only suggest that the molecules are preparing to transform. As temperature increases, short Cl-Cl contacts start to develop – the tail

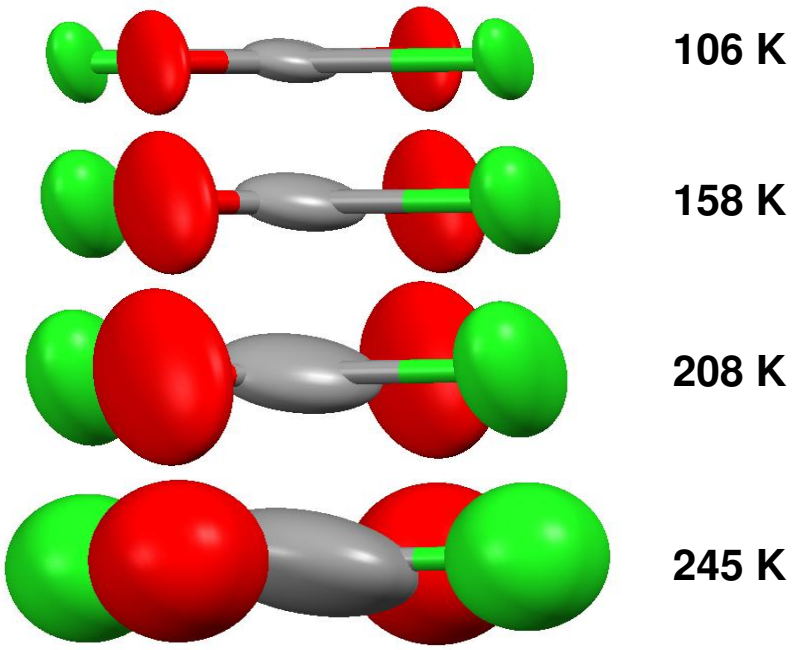

Figure 7.10. Crystal structure of oxalyl chloride, determined by Rietveld refinement, viewed along the C-C bond. Structures are not given for 13 and 53 K as these could not be refined anisotropically. Ellipsoids are drawn at the 100% probability level

end of the partial $g(r)$ corresponding to these distances lies at *ca.* 2.9 Å. Figure 7.11 shows the Cl-Cl partial $g(r)$'s at 13 and 245 K, derived from model IA and a histogram of Cl-Cl contacts from the Cambridge Structural Database. The agreement between the database search and the distribution of contacts observed here is rather good. It is clear that as temperature is increased, shorter contacts become more numerous. The intensity between *ca.* 2.5-2.9 Å is due to Cl atoms from molecules that have not been successfully held together, although this has only occurred for 46 Cl atoms out of a total 4000.

7.3.4 Difficulty with RMCProfile refinement of Phase I

The need to prevent the development of close Cl-Cl contacts using closest approach constraints in phase I is unfortunate as it shows that the data (albeit with the aid of forcefield-based molecular restraints) are insufficient to drive the model to a chemically reasonable configuration. Therefore it cannot be determined whether the relief of short, yet chemically reasonable, Cl-Cl contacts that develop in phase II

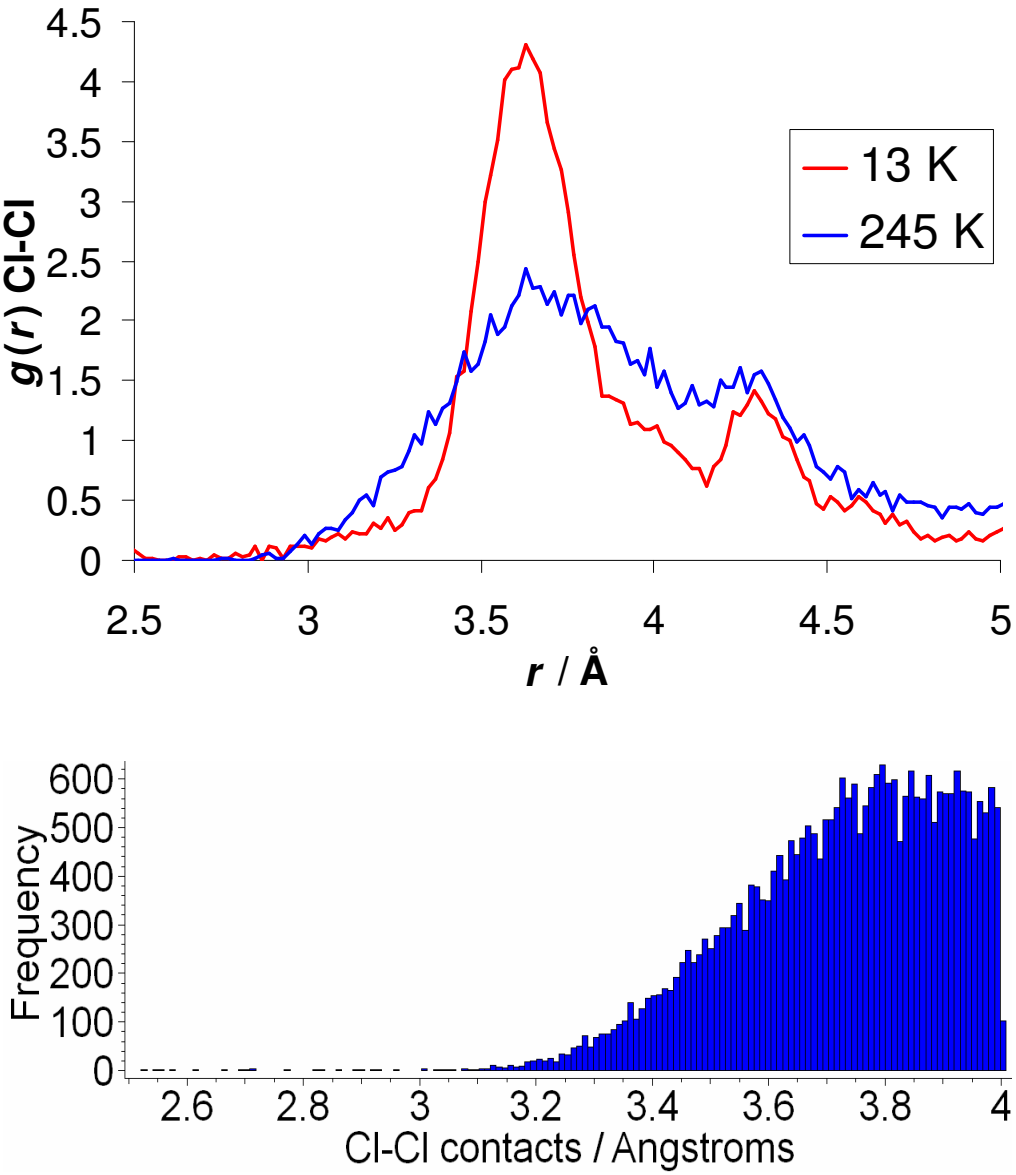

Figure 7.11. Partial *g*(*r*) for Cl-Cl contacts, taken from model IA at 13 and 245 K (top) and histogram of Cl-Cl contacts in the Cambridge Structural Database (bottom)

occur, as the models generated are clearly inaccurate due to the Cl-Cl 'spike' seen at 3 Å. However if the minimum approach distance restraint had not been applied then there would be no impetus for the onset of disorder to occur in layers anyway as neighbouring molecules would not be identified as being unfavourably close.

A difficulty may lie in the possibility that oxalyl chloride is simply too complex a system to study via the RMC method as it currently stands. The molecule

is comprised of three atom types and therefore possesses six different atom-atom partial $g(r)$'s, which combine to give the overall $G(r)$. The flexibility in the packing arrangement of small molecules, held together by relatively weak intermolecular forces compared with covalent bonds could lead to many different combinations of the partial $g(r)$'s that ultimately give the same $G(r)$. In the case of oxalyl chloride seen here, the spike in the partial g(r) for Cl-Cl contacts was readily accommodated into the overall $G(r)$ with no apparent ill-effects on the fit. Flexibility in packing arrangement has not been identified as a significant problem in other molecular systems such as SF_6 and CBr_4 (although disorder in cyclohexane could not be elucidated in the absence of $I(t)$ data – see Chapter 6) but these are relatively rigid molecules whereas oxalyl chloride possesses rotational freedom about the C-C bond.[24, 25] Similarly, other systems with three or more atoms including $SrTiO_3$, $SrSnO_3$ and $H_3Co(CN)_6$ have all undergone RMC refinement without the difficulties encountered here but these are, again, relatively rigid molecules by comparison.[3, 26, 27] The authors of Ref. 3 did anticipate that the $SrTiO_3$ system would present more of a challenge (than systems with one or two atom types) as it possessed three different atoms.

7.3.5 The onset of disorder in phase I in the molecular dynamics simulation

The onset of disorder in phase I was partially predicted by the MD simulations, without the aid of experimental data. Figure 7.12 shows one layer of oxalyl chloride molecules from the final time-step of the MD simulation at 255 K. While the vast majority of the molecules remain in the starting orientation used for the simulation – the major component, one of the molecules has rotated by *ca.* 90° relative to its neighbours (highlighted by the white circle in the Figure). Another molecule, shown by the orange circle in the Figure also appears to have rotated significantly from its starting position. Similar behaviour was seen when the simulation temperature was increased to 275 K and 293 K. The crystal structure refinements in GSAS suggest that approximately one third of the molecules adopt the minor phase – a far greater quantity than that seen in the simulations. However, when an artificially created crystal structure where the major component consisted of 75% of the molecules and the minor, 25%, was used as a starting point for the simulation, the crystal collapsed

into a liquid. This may be indicative of a route through which the disordered crystal can transform into the liquid phase. Once a significant quantity of the molecules adopt the minor phase orientation, the long-range order breaks down and the crystal melts. However, given that the disorder in phase I cannot be elucidated by total scattering it is doubtful that the melting transition can be structurally assessed by this technique.

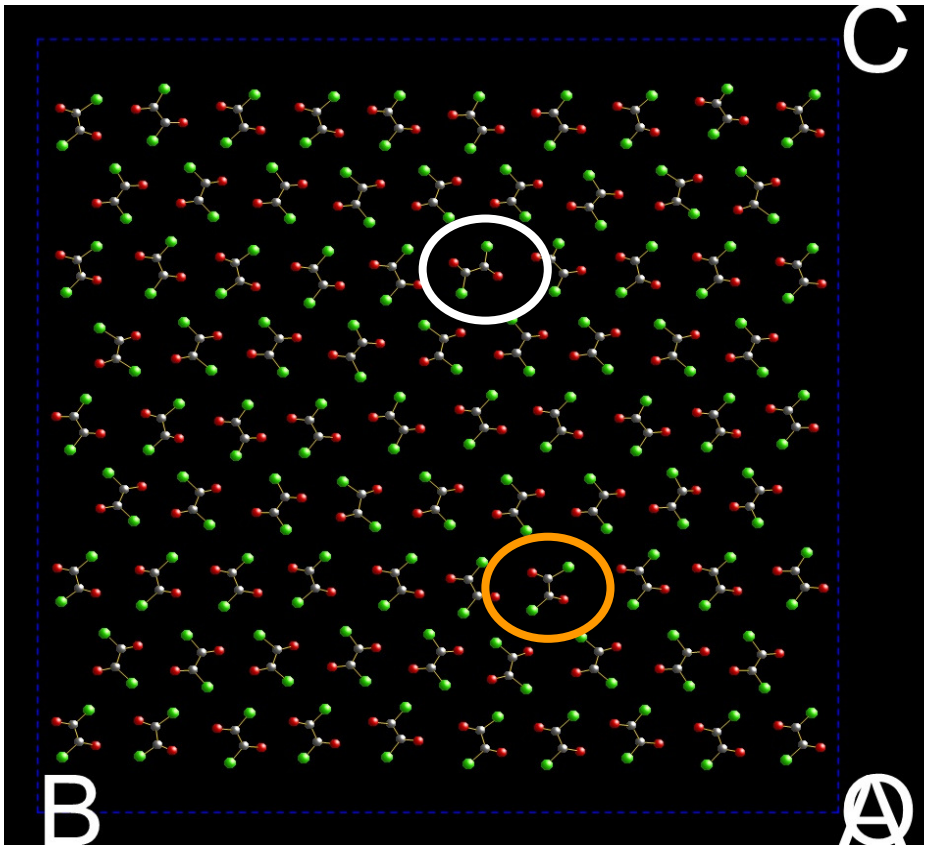

Figure 7.12. One layer of the structure generated by the MD simulation at 255 K. The white circle indicates a molecule that has adopted the orientation of the minor component of the disordered phase. The orange circle shows a molecule that appears to significantly deviate from the orientation of the major component.

7.4 Conclusions

The effect of temperature on the solid phases of oxalyl chloride has been explored using high resolution neutron total scattering and Reverse Monte Carlo modelling. The RMC refinements show that the molecular motion is mostly confined within the plane of the molecule between 13 and 208 K. At 245 K, the atomic thermal motion

becomes significantly more isotropic and it is possibly this behaviour that enables the molecules to rotate by 90° in order to undergo the phase transition to phase I.

The RMC method has not been able to deduce the nature of the disorder of phase I. The need to prevent unrealistically short intermolecular Cl-Cl contacts with a closest-approach constraint induces a unrealistic quantity of these contacts at 3 Å, meaning that the models are inaccurate. That this feature can be incorporated into the overall $G(r)$ shows there are many equivalent ways that the molecules can arrange themselves in that fit the total scattering data that give rather different atomic configurations. This problem may also apply to other flexible molecular systems with more than 2 different atom types.

The onset of disorder in phase I has partially been seen with molecular dynamics simulations without the aid of any experimental data. From an initial starting model consisting of all molecules adopting the orientation of the major component of phase I, a very small proportion of the molecules were observed to rotate 90° to their neighbours, forming the minor component.

7.5 References

1. T. D. Bennett, A. L. Goodwin, M. T. Dove, D. A. Keen, M. G. Tucker, E. R. Barney, A. K. Soper, E. G. Bithell, J.-C. Tan and A. K. Cheetham, *Physical Review Letters*, 2010, **104(11)**, 115503/1-115503/4
2. M. G. Tucker, M. T. Dove and D. A. Keen, *Journal of Physics: Condensed Matter*, 2000, **12**, L723-L730.
3. Q. Hui, M. G. Tucker, M. T. Dove, S. A. Wells and D. A. Keen, *Journal of Physics: Condensed Matter*, 2005, **17**, S111-S124.
4. V. A. Burnell, J. E. Readman, C. C. Tang, J. E. Parker, S. P. Thompson and J. A. Hriljac, *Journal of Solid State Chemistry*, 2010, **183**, 2196-2204.
5. D. D. Danielson, L. Hedberg, K. Hedberg, K. Hagen and M. Traetteberg, *Journal of Physical Chemistry*, 1995, **99**, 9374-9379.
6. J. R. Durig, J. F. Davis and A. Wang, *Journal of Molecular Structure*, 1996, **375**, 67-81.
7. J. R. Durig and S. E. Hannum, *Journal of Chemical Physics*, 1970, **52**, 6089-6095.

8. S. Gutierrez-Oliva and A. Toro-Labbe, *Chemical Physics Letters*, 2004, **383**, 435-440.
9. S. Kim, S. E. Wheeler, N. J. DeYonker and H. F. Schaefer, III, *Journal of Chemical Physics*, 2005, **122**, 234313/234311-234313/234314.
10. P. Groth and O. Hassel, *Acta Chemica Scandinavica*, 1962, **16**, 2311-2317.
11. D. A. Keen, *Journal of Applied Crystallography*, 2001, **34**, 172-177.
12. R. M. Ibberson, *Journal of Applied Crystallography*, 1996, **29**, 498-500.
13. W. G. Williams, R. M. Ibberson, P. Day and J. E. Enderby, *Physica B: Condensed Matter (Amsterdam)*, 1998, **241-243**, 234-236.
14. A. Coelho, *TOPAS-Academic: General Profile and Structure Analysis Software for Powder Diffraction Data. Version 4.1*, 2007.
15. M. G. Tucker, D. A. Keen, M. T. Dove, A. L. Goodwin and Q. Hui, *Journal of Physics: Condensed Matter*, 2007, **19**, 335218/335211-335218/335216.
16. B. H. Toby, *Journal of Applied Crystallography*, 2001, **34**, 210-213.
17. A. C. Larson and R. B. von Dreele, *General Structure Analysis System (GSAS), Los Alamos National Laboratory*, 2000.
18. P. Dauber-Osguthorpe, V. A. Roberts, D. J. Osguthorpe, J. Wolff, M. Genest and A. T. Hagler, *Proteins: Structure, Function, and Genetics*, 1988, **4**, 31-47.
19. S. Nose, *Progress of Theoretical Physics Supplement*, 1991, **103**, 1-46.
20. M. Parrinello and A. Rahman, *Journal of Chemical Physics*, 1982, **76**, 2662-2666.
21. B. Delley, *Journal of Chemical Physics*, 1990, **92**, 508-517.
22. M. Tucker, A. Goodwin and M. Dove, *RMCProfile User Manual, Version 6.4.7*, 2010.
23. A. L. Goodwin, F. M. Michel, B. L. Phillips, D. A. Keen, M. T. Dove and R. J. Reeder, *Chemistry of Materials*, 2010, **22**, 3197-3205.
24. M. T. Dove, M. G. Tucker and D. A. Keen, *European Journal of Mineralogy*, 2002, **14**, 331-348.
25. L. Temleitner and L. Pusztai, *Physical Review B: Condensed Matter and Materials Physics*, 2010, **81**, 134101/134101-134101/134108.

26. A. L. Goodwin, S. A. T. Redfern, M. T. Dove, D. A. Keen and M. G. Tucker, *Physical Review B: Condensed Matter and Materials Physics*, 2007, **76**, 174114/174111-174114/174111.

27. D. A. Keen, M. T. Dove, J. S. O. Evans, A. L. Goodwin, L. Peters and M. G. Tucker, *Journal of Physics: Condensed Matter*, 2010, **22**, 404202/404201-404202/404207.

Chapter 8

Conclusion

8.1 Conclusion

The aim of this project was to identify and rationalise phase transitions in the solid state in terms of how and why they occur. The thermodynamic analyses carried out on the materials in Chapters 2-5 showed that the *PV* term is generally the most influential for directing crystal packing at non-ambient pressures. Assessment of the other thermodynamic variables, *U* and *TS* has also shown that these terms should not always be neglected when considering polymorphism, which is particularly evident in Chapter 4. The total scattering investigations in Chapters 6 and 7 were partially successful in identifying how materials prepare to undergo a phase transformation although the studies described here form very early work on this particular application of total scattering to molecular systems.

The crystal structure of L-alanine-d_7 was shown to persist up to 13.6 GPa before undergoing amorphisation at 15 GPa. The transition was due to volume collapse of the structure, mediated by the lack of remaining interstitial voids to take up the effects of compression. PIXEL calculations do not indicate the formation of destabilising contacts and thus the transition is driven by minimisation of the *PV* term. This is the first amino acid known to undergo a transition of this type and the data collected here are at a higher pressure than any other diffraction data collected on an amino acid. The molecular topology became increasingly body-centred cubic as pressure was applied, resembling the crystal packing of a typical BCC material such as tungsten. The high level of compressibility seen in this system was ascribed to the approximately spherical shape of the molecule. The bulk modulus was determined from an extensive set of pressure-volume data and was found to be 13.1(6) GPa.

A new monoclinic polymorph of the 4-methylpyridine pentachlorophenol co-crystal was theoretically predicted on the basis of *PV* minimisation and subsequently obtained by in situ crystallisation at high pressure. This phase had only been seen previously for the mono-deuterated analogue of this material. The monoclinic crystal could be reliably recovered to ambient pressure where it was observed to be stable. So far, this is the only known route to obtaining this polymorph thus demonstrating the potential for pressure in crystal engineering. Further predictions were made

towards the experimental conditions which favour growth of the mono-deuterated co-crystal in a triclinic polymorph. A combined analysis of theoretical lattice energy, zero point energy, vibrational enthalpy and the *PV* and *TS* terms suggest that growth of this phase requires low temperature conditions. Experiments aiming to obtain this are ongoing.

Pressure-induced crystallisation of aniline at 0.7 GPa yields an orthorhombic phase ($Pna2_1$), the structure of which was shown to persist to 7.37 GPa by high-pressure neutron powder diffraction. The bulk modulus was determined as being 6.980(19) GPa from an extensive set of pressure-volume data. On decompression to 0.33 GPa the sample transforms to a less dense monoclinic phase which has previously only been obtained at low temperature and ambient pressure. This transition is not observed in a high-pressure single-crystal X-ray diffraction experiment where the crystal breaks up on decompression instead. This is interpreted as the crystal attempting to undergo the evidently reconstructive transition. PIXEL calculations on the orthorhombic phase show that dispersive forces contribute the most to lattice stability, even more so than the hydrogen bonds, one of which becomes destabilising at higher pressure.

The thermally induced crystalline → plastic phase transition in cyclohexane-d_{12} has been measured by neutron total scattering and modelled using a Reverse Monte Carlo approach. On heating towards the transition temperature at 176 K, each molecule prepares to transform through rotating about its molecular C_3 axis in the opposite direction to its nearest neighbours. At the same time, all the molecules rotate in the same direction about an axis aligned with the *b*-direction. The RMC fits to the long-range and local structure data show that the molecules tumble isotropically in the plastic phase. The $I(t)$ data are shown to be essential as their removal results in the RMC method being unable to identify the type of disorder that is present. The isotropic tumbling motion for each molecule is shown to be correlated with that of its neighbour as short D···D contacts below 1.7 Å are not seen to develop.

Reverse Monte Carlo modelling of neutron total scattering data has been used to explore the structural behaviour of oxalyl chloride in its ordered and disordered solid phases. The refinements show that when warmed towards the transition point at

250 K, the atoms show increasing thermal motion perpendicular to the plane of the molecule. Just below the transition temperature, the atomic thermal motion becomes significantly more isotropic showing the reduced steric restriction on the movement of each molecule. The transition between the two phases was partially observed in molecular dynamics simulations, where a small proportion of molecules rotated by *ca*. 90° relative to their neighbours thus forming the disordered component of the high temperature phase. Analysis of the high-temperature solid phase above 250 K was not performed as satisfactory RMC models could not be obtained; an unrealistic quantity of short Cl-Cl contacts was observed. Through this study, oxalyl chloride has been identified as a system that may be too complex for investigation by RMC owing to a combination of intramolecular flexibility and a large number of partial $g(r)$'s that arise from the presence of three different atom types.

The work described in this Thesis has demonstrated that application of extreme condition environments to single crystal and powdered samples of organic molecular crystals is an effective method for investigating crystal structure stability. The results of the high-pressure studies carried out here all show the need for molecules to pack efficiently in the solid state – something that becomes more important as pressure is increased. Despite the exertion of very high pressures, abnormally short hydrogen bonds are not seen and short intermolecular H···H contacts (less than 1.7 Å) do not develop when interstitial voids are compressed. The PIXEL method is particularly useful in quantifying the energies of these interactions, showing that as they begin to reach their closest approach limit, they become increasingly destabilising, preventing the occurrence of abnormally short contacts. These features of molecular organic crystals form criteria that should be fulfilled when predicting crystal structure stability.

Although relative lattice energies are frequently used to rationalise polymorph stability, it is more correct to consider Gibbs free energy instead. Inclusion of the *PV*, *TS*, *ZPE* and E_{vib} terms gives a more realistic depiction of a chemical system and thus it is more likely that structural predictions will be correct. This has been clearly demonstrated for MP-PCP and also to some extent for aniline. Given the difference in intermolecular interactions seen in these systems, i.e. MP-PCP possesses strong intermolecular H-bonding whereas aniline molecules mainly

interact via dispersive forces, it seems that a thorough assessment of Gibbs free energy to determine stability should be generally applicable to many other organic systems. However, caution should still be taken when drawing conclusions from analysis by statistical thermodynamics as assumptions are made; namely that the system can be adequately described by a harmonic approximation. For instance in the case of aniline, although the phase transition was correctly predicted by the *PV* term, the relative stability of the two polymorphs was not reproduced by the calculated Gibbs free energy.

Thermodynamic analysis is extremely important in crystal structure prediction but this does not account for kinetic effects, which can sometimes lead to the existence of metastable crystalline phases. The total scattering work described here is a step towards understanding the role of kinetic factors in phase transitions, although this area is clearly at an early stage of development. The investigation into the phase transitions in cyclohexane and oxalyl chloride revealed the extent of molecular mobility on a local scale, leading up to the thermally-induced transitions. Knowing the degree of molecular mobility within a 'stable region' of a phase diagram for a given material is of utmost importance, in particular for the pharmaceutical industry, where excess molecular motion can lead to undesirable transformation from one state of matter to another. Thus atomistic modelling of total scattering data appears to be a promising technique with which phase stability (including non-crystalline phases) can be assessed.